Understanding mixing processes in stars using hydrodynamic simulations

Internal gravity waves in stellar interiors

University *of* Exeter

Arthur Le Saux

Submitted by Arthur Le Saux to the University of Exeter as thesis for the degree of

Doctor of Philosophy in Physics

September 2023

Acknowledgements

It's a pleasure to write these few lines, which mark the culmination of the first chapter in my career as an astrophysicist. This chapter began when I first came to Exeter in May 2017 to spend 3-months as a summer student. This first glimpse of astrophysics was revealing, and I would like to start by thanking Isabelle, who enabled me to complete this internship. More than six years later, this chapter is coming to an end, with my graduation from the University of Exeter. It has been enriching from a scientific point of view, of course, but also in many other ways. Once more, I would like to thank Isabelle, who enabled me to carry out this thesis in the best possible conditions and helped me to give the best of myself. I had the opportunity to lead my research into the physics of waves in stellar interiors, which turned out to be fascinating. The best part being that there is still a lot to discover. One last thanks to Isabelle as coach of the SWRR training sessions.

Next, I would like to say a big thank you to Thomas, whose help and advice have been invaluable. Most of the hard work I have done for this thesis has been made easier thanks to our discussions. In particular, I will always remember with pleasure the endless debates about 4π factors.

During my graduate years, I had the chance to collaborate and to be guided by two (former) post-docs, Lisa Bugnet and Earl Bellinger. Thanks to both of you, I discovered asteroseismology, a field perfectly complementary to the main topic of research of my PhD. Congratulations on your new permanent positions at ISTA and Yale! Also, a special thanks to Lisa for inviting me to CCA and ISTA, it was a great experience.

I am very pleased to have integrated the MUSIC team, who provided a perfect environment to explore the world of multidimensional simulations. Dimitar Vlaykov, Tom Constantino, Adrien Morison, Tom Goffrey and Jane Pratt it is a pleasure to work in such a good company. I am pleased to think that this is the start of a fruitful collaboration.

After spending so much time there, it is a bit difficult to leave the Astro Group of the University of Exeter. Thank you to everyone I met there, it has been a pleasure. I would like to thank as well my second home institution, the CRAL at the ENS Lyon, for the warm welcome extended on every visit. In addition, I would like to thank those with whom I have been lucky

enough to collaborate with over the last few years : Sarbani Basu, Sacha Brun, Victor Réville, Rafael García, Savita Mathur, Sébastient Lebonnois and Itziar Garate-Lopez.

I am grateful to Matt Browning and Michel Rieutord, examiners for my thesis, for being patient enough to read my thesis. We had some very interesting discussions on the morning of 1 June 2023!

Lastly, I can't thank enough my family, and particularly my parents, Agnès and Jean-Michel, for their unfailing support during my (long) years of study. It is thanks to them that I am able to pursue an exciting career. Cheers to my brother, Victor, for being the awesome one. And of course thank you to Alix for having put up with the distance and for cheering me on these last few years! It hasn't always been easy, but we've succeeded and I'm looking forward to new adventures with you.

Abstract

Waves that propagate in stellar interiors are essential to stellar physics for two reasons. First, the interiors of stars are studied by detection of global modes of oscillations resulting from wave interference. Secondly, waves are involved in various transport phenomena. In stars, there are two main types of waves: acoustic and gravity. This duality of waves as observational tools and physical processes impacting stellar structure makes them a crucial field of study in astrophysics.

In this thesis, we focus on internal gravity waves (IGWs), which are well known for transporting angular momentum, energy and chemical elements in stably stratified media. Despite observations of very high precision, detection of IGWs is still challenging and their properties in stellar interiors remain poorly understood and/or constrained. This is mostly because IGWs are inherently 3D, non-linear and anisotropic phenomena. Consequently, multidimensional modelling is a great tool to study these waves. However, stellar hydrodynamics faces important challenges such as numerical stability and thermal relaxation. To face them, an artificial increase of the stellar luminosity and of the thermal diffusivity by several orders of magnitudes is a commonly used tactic. Using two-dimensional simulations of a solar-like model, we quantify the impact of such a technique on IGWs. Our results suggest that this technique affect the excitation of IGWs, because of an impact on convective motions and overshooting, but also their damping.

Main-sequence intermediate-mass stars, with $M \gtrsim 2M_{\odot}$, possess a convective core and a radiative envelope. It remains unclear if waves generated at the edge of the convective core should be able to propagate up to the stellar surface. In this context, we have carried out an analysis of IGWs in simulations of 5 $M_{\odot}$ star model. Our results show that low frequency waves excited by core convection are strongly impacted by radiative effects as they propagate. In the upper layers of the simulation domain, we observe an increase of the temperature, likely due to heat added in these layers by IGWs damped by radiative diffusion. We show that non-linear effects linked to large amplitude IGWs may be relevant just above the convective core. Both these effects are intensified by the artificial enhancement of the luminosity and radiative diffusivity. Our results also highlight that direct comparison between numerical simulations with enhanced luminosity and observations must be made with caution.

Table of contents

List of figures

List of tables

Chapter 1

Introduction

A star may be defined in simple terms as a self-gravitating plasma that radiates a large amount of energy generated in its core by thermonuclear reactions. Despite its apparent simplicity, this definition is relatively recent and has been difficult to establish since we can only observe the surface of stars. For decades, stellar interiors have thus only been studied theoretically, because very few observational constraints have been available. However, the study of stars is essential as it benefits most areas of astrophysical research. Most, if not all, stars host planetary systems whose properties are highly dependent on those of the host star, such as its mass, radius and evolutionary state (e.g. Huber et al., 2013). Massive stars produce the heaviest chemical elements in the universe and die in huge explosions that disperse these elements and feed the surrounding interstellar medium (e.g. Thielemann et al., 1996). This will influence and drive the evolution and dynamics of galaxies (e.g. Kennicutt and Evans, 2012; Nomoto et al., 2006). There is still much to be learned about the stars, and each step forward raises new questions. Among these questions, those concerning the structure and dynamics of stellar interiors are among the most complex. What we do know for sure is that the internal structure changes as the star evolves (e.g. Kippenhahn and Weigert, 1990). These changes are described by the theory of stellar structure and evolution, which is briefly introduced in Chapt. 2. However, we know from observations that many details about the structure and dynamics of stellar interiors remain unexplained by this theory. In stellar physics, many complex phenomena linked to rotation, magnetism and mixing remain poorly understood and/or constrained. Among these phenomena that current theories fail to explain, we can cite the following examples: the solid rotation of the solar core (Thompson et al., 2003), the observed surface abundance of Lithium in low-mass stars (Baraffe et al., 2017) and in Red Clump stars (Kumar et al., 2020), the slow rotation rate of the core of evolved stars (e.g. Marques et al., 2013), the lifetime of hydrogen-burning stars which require additional mixing at the edge of convective region (e.g. Castro et al., 2014) or the enhanced mass loss measured in progenitors of supernovae (e.g. Quataert and Shiode, 2012).

And these are just a few of them.

The discovery of waves propagating in the stellar interiors seems to be a promising way to solve these mysteries. These waves make stars oscillate in normal modes, causing variations in the volume of a given star that can be observed as periodic variations in its luminosity. This discovery marked a turning point in stellar physics because the properties of an oscillation mode depend on the structure of the star. Consequently, the analysis of these modes offer an incredible insight into stellar internal structure and dynamics (Aerts et al., 2010). The science that studies the interior of stars thanks to their oscillations is called asteroseismology. This is the subject of Chapt. 3. The study of stellar oscillations, in the the case of the Sun, is called helioseismology. In the late 20th century, development of new methods based on observations of solar oscillations have allowed to get a good understanding of the structure of the Sun (see the reviews by Basu, 2016; Christensen-Dalsgaard, 2002). In 2006, when the CoRoT satellite (Auvergne et al., 2009) was launched, asteroseismology underwent a revolution. For the first time, it was possible to have accurate photometric data on thousands of stars at different stages of evolution. This allowed to test stellar evolution theory with many more constraints. Since then, the satellites *Kepler* (Borucki et al., 2010) and TESS (Ricker et al., 2015) have provided observations of many more stars.

Interpreting correctly the observations of oscillations modes requires a good understanding of the physics of the associated waves. This is essential to analyse the data already available but also to prepare for future missions such as PLATO, an ESA project scheduled for the end of 2026 (Rauer et al., 2014). Furthermore, most of the unexplained phenomena that occur inside stars suggest the need for additional transport mechanisms, and waves could be one of them. This makes two essential reasons to study waves that propagate in stellar interiors. The first obvious way to understand the physics of these waves is from a theoretical point of view. To do this, astrophysicists draw on the geoscience community. Indeed, it has long been known that waves propagate in the Earth's atmosphere and in oceans (e.g. Nansen and Sverdrup, 1897). In such media, two main types of waves exist and are studied. First, there are acoustic waves whose restoring force is the pressure gradient. Second, there are internal gravity waves (IGWs) whose restoring force is buoyancy. The latter are suggested to play a role in the transport of energy, chemical elements and angular momentum. The main properties of IGWs are described in Chapt. 4. In the Earth's atmosphere, they can change the temperature, wind direction or the movement and concentration of particles (see the book of Sutherland, 2010, for a complete review on the subject). For instance, they are suggested as the driving mechanism of the Quasi-Biennal Oscillation, a 28-month periodic reversal of the wind direction occurring in the stratosphere near the equator (e.g. Baldwin et al., 2001). In the oceans, they are involved in vari-

ous mixing phenomena, which may, for example, be responsible for the thermohaline circulation (e.g. Nikurashin and Ferrari, 2013). These waves are most likely present in the atmosphere of other planets or moons in the solar system. Characteristic signatures of their presence have been observed in the atmospheres of Venus (e.g. Peralta et al., 2008), Saturn (e.g. Fuller et al., 2014), Jupiter (e.g. Young et al., 1997) and Titan (e.g. Lorenz et al., 2014). In addition, they are also often invoked to explain observed phenomena in planetary atmospheres. For instance, in Venus atmosphere, they could explain the zonal wind profile measured by Venera and Pioneer Venus probes (Lebonnois et al., 2019, 2016). They have also been suggested as a possible origin of the temperature variability observed in Neptune's stratosphere (Uckert et al., 2014). The presence of these waves in such a wide range of systems suggests that they could also be present in the atmospheres of exoplanets. This could have important impacts on the atmospheric dynamics of hot exoplanets, i.e. gaseous giant planets with short orbital period (e.g. Watkins and Cho, 2010).

Internal gravity waves can also be modelled in experimental set-ups (e.g. Le Bars et al., 2015; Townsend, 1966). In their remarkable study, Plumb and McEwan (1978) managed to model experimentally an analogue of the QBO in an annulus of salt-stratified water. Furthermore, such experiments with a controlled configuration allow for a parameterisation study. Thus, although the configuration is generally simplified compared to real natural phenomena, it provides a very good understanding of the physics underlying the phenomena being modelled.

Another interesting way of studying these waves, and the internal structure of stars in general, is through hydrodynamical simulations. It consists of numerically solving the equations of hydrodynamics to predict the behaviour of the internal dynamics of stars. This allows the theory to be tested directly and is an effective tool to guide observations. Simulations can also be used to get new information on phenomena that are too complex to be modelled analytically, such the differential rotation of the Sun (e.g Hotta and Kusano, 2021). The last decades have shown that it is possible to model realistic IGWs in multidimensional simulations of stellar interiors, allowing to get new insights on their physics (e.g. Alvan et al., 2014; Rogers and Glatzmaier, 2005a). However, stellar hydrodynamical simulations are extremely complex due to the wide range of time and lengths scales characterising stellar interiors. They must deal with physical and numerical challenges that make them computationally expensive. Therefore, they are performed using simplifying assumptions and/or numerical artefacts that could have an impact on physical processes, as explained in Chapt. 5.

In this context, the work presented in this thesis has two main objectives. The first one aims at improving our understanding of the physics of IGWs, and their impact on stellar interiors. The interest of these results may go beyond stellar physics. As mentioned, IGWs are present in a wide variety of systems, and testing their properties in different conditions will help to

improve their understanding in general. The second objective is to improve the efficiency of the interpretation of results from hydrodynamical simulations. In particular, it is important to be able to differentiate between effects resulting from physical phenomena and those resulting from numerical effects. We will see that running a simulation, although very complicated, is not the only challenge. The analysis that follows also requires a lot of investment. To achieve these objectives, we have run two sets of two-dimensional simulations using the fully compressible time implicit code MUSIC (Geroux et al., 2016; Goffrey et al., 2017; Viallet et al., 2013). The first one is composed of four simulations of a solar-like model, and its analysis is presented in Chapt. 6. The second one is a set of four simulations of a 5 solar mass star model and is the subject of Chapt. 7. Finally, after presenting in Chapt. 8 current projects that follow on from the work presented in this thesis, we conclude and discuss our results in Chapt. 9.

Chapter 2

An overview of stellar structure and evolution

The theory of stellar structure and evolution is now generally accepted, and new observations help either confirming it or improving it. This first chapter will only give a brief overview of it to set up the context of this thesis. Over the last century, a lot of textbooks have presented this theory in great details, and we refer the reader to them if needed. Some of these books have become classics such as Chandrasekhar (1939), Schwarzschild (1958) or Kippenhahn and Weigert (1990). This first section is mostly based on Kippenhahn and Weigert (1990).

2.1 Characteristic timescales

Before getting to the stellar structure and evolution theory, let's first introduce the timescales associated with a star of mass $M_\star$, radius $R_\star$ and luminosity $L_\star$. This will give a first insight on the complexity of stellar modelling.

The shortest timescale is the time needed for the star to collapse under gravity if all pressure forces are removed. The equation of motion in that case will be

$$\frac{\partial^2 r}{\partial t^2} = -\frac{\mathrm{Gm}}{r^2}, \tag{2.1}$$

with r the radial coordinate, t the time, G the gravitational constant [1] and $m = m(r)$ the mass enclose in a sphere of radius r. We can then define a dynamical timescale τ_{dyn} associated with

[1] $\mathrm{G} = 6.67430 \times 10^{-11}\ \mathrm{m^3 kg^{-1} s^{-2}}$

the collapse as

$$\frac{R_\star}{\tau_{\rm dyn}^2} \simeq \frac{\partial^2 r}{\partial t^2}. \tag{2.2}$$

Then, using Eq. (2.1) we obtain an expression for the dynamical timescale

$$\tau_{\rm dyn} \simeq \left(\frac{R_\star^3}{\mathrm{G}M_\star}\right)^{1/2} \simeq \left(\frac{1}{\mathrm{G}\bar{\rho}}\right)^{1/2}, \tag{2.3}$$

with $\bar{\rho}$ the mean density in the star. For a star in hydrostatic equilibrium, this is the typical time on which the star reacts to a slight perturbation of hydrostatic equilibrium. A typical value for this timescale is $\tau_{\rm dyn} \sim 27$ min in the case of the Sun[2]. [3]

In the case of stars, the timescale needed to reach a thermal equilibrium can be estimated using the Kelvin-Helmholtz timescale. It is defined as the ratio of gravitational energy available in the star, $E_{\rm g}$, and the energy that is radiated away per unit of time, which is the luminosity of the star, L. This is the time a star would survive if its only energy source was its available gravitational energy. Then, this timescale $\tau_{\rm KH}$ is written as

$$\tau_{\rm KH} = \frac{|E_{\rm g}|}{L_\star}. \tag{2.4}$$

The gravitational energy can be expressed as

$$|E_{\rm g}| \simeq \frac{\mathrm{G}M_\star^2}{2R_\star}. \tag{2.5}$$

Consequently, the Kelvin-Helmholtz timescale is defined as

$$\tau_{\rm KH} \simeq \frac{\mathrm{G}M_\star^2}{2R_\star L_\star}. \tag{2.6}$$

A typical value for this timescale is $\tau_{\rm KH} \sim 1.6 \times 10^7$ years for the Sun.

The last timescale that needs to be introduced is the nuclear timescale $\tau_{\rm nuc}$. This is the characteristic lifetime for a star and correspond to the time to consume the energy available in the nuclear fusion reactions of hydrogen into helium, $E_{\rm n}$. It is defined as

$$\tau_{\rm nuc} = \frac{E_{\rm n}}{L_\star}. \tag{2.7}$$

[2] In the case of the Sun we have $1M_\odot = 1.989 \times 10^{30}$ kg, with the subscript $\odot$ indicating solar reference value.
[3] with $1R_\odot = 6.957 \times 10^{10}$ cm and $1L_\odot = 3.828 \times 10^{33}$ erg.s^{-1}.

For the Sun, its typical value is $\tau_{\rm nuc} \sim 10^{10}$ years.

From the estimation computed for the Sun it appears that these three timescales compare as

$$\tau_{\rm nuc} \gg \tau_{\rm KH} \gg \tau_{\rm dyn} \tag{2.8}$$

which is actually valid for most of the life of stars. These inequalities will be really useful to simplify equations when looking at a given phenomenon. Also, it is because the dynamical timescale is much smaller than the two others that it is possible to assume hydrostatic equilibrium for a star. However, these inequalities are not valid throughout the entire life of a star; particularly as the star evolves the three timescales become comparable.

2.2 Internal structure of stars

According to the theory of stellar structure, stars are self-gravitating objects made of ionised gas. Their structure is modelled with the description of spatial and temporal variations of thermodynamics variables such as density ρ, temperature T or pressure p, and of its fractional composition in hydrogen X, helium Y and heavier elements Z. In this chapter we neglect rotation, mass loss, interactions with another star and magnetism, so spherical symmetry may be assumed. Therefore, in this section, all functions depend only on two independent variables: radius r and time t.

2.2.1 Equations of stellar structure

The equations of stellar structure consist of three conservation equations, which are conservation of mass, momentum and energy. These equations need to be completed with conditions required for thermal equilibrium, a description of the energy generation mechanism and of energy transport phenomena. The three main transport mechanisms are radiation, convection and conduction. Finally, it is possible to add the evolution of chemical abundances, which determines stellar evolution.

Mass conservation

Let's introduce $m(r,t)$ the mass contained in a sphere of radius r at a given time t. The conservation of mass in that sphere can be expressed by the equation

$$\mathrm{d}m = 4\pi r^2 \rho \mathrm{d}r - 4\pi r^2 \rho \mathrm{v} \mathrm{d}t, \tag{2.9}$$

where v is the radial velocity of the mass flow coming out of the sphere. The first term on the right-hand side represents a variation of mass induced by a variation in radius of the sphere, and the second term takes into account mass exchanges with the surrounding.

Momentum conservation

The equation expressing momentum conservation is basically resulting from Newton's second law. Due to our assumptions to neglect for now all external forces, the only forces acting inside the stars are the pressure gradient (towards the surface) and gravity (towards the centre). If we consider that these two forces are in balance, the conservation of momentum is given by the condition of hydrostatic equilibrium, and it is expressed as

$$\frac{\partial p}{\partial r} = -\rho g = -\frac{\mathrm{G}m}{r^2}\rho, \tag{2.10}$$

with g the acceleration due to gravity.

Energy conservation

As mentioned, the main source of energy in stars is nuclear reactions that occur in the innermost part of a star. These are quantified by the nuclear energy released per unit mass per unit time ϵ_{nuc}, which depend on chemical composition, temperature and density. We can define the net energy L_r flowing through a shell of radius r

$$\frac{\partial L_r}{\partial m} = \epsilon_{\mathrm{nuc}} - \epsilon_\nu + \epsilon_g, \tag{2.11}$$

where ϵ_ν represents the energy lost in the form of neutrinos and ϵ_g is the gravo-thermal energy, which is a source term in case of compression and a sink term in case of expansion of the star. It can be defined using the specific entropy s as

$$\epsilon_g = -T\frac{\partial s}{\partial t}. \tag{2.12}$$

This term is computed using an equation of state (EoS), i.e. an equation that links thermodynamic variables to each other, the opacities and nuclear reactions rates. The conditions in stellar interiors make it complex and expensive to compute this term, so we use interpolation from precomputed tables. In the context of this thesis, we use the Opacity Project at Livermore (OPAL) EOS from Rogers and Nayfonov (2002).

To complete these equations, efficient energy transport processes are needed. Three mechanisms share the transport in stellar interiors: radiation, conduction and convection. Which one dominates depend on the value of temperature gradient, as we will see in the next section.

2.2.2 Energy transport in stellar interiors

It has been known for a long time that the structure of stars depends on the transport of energy (Eddington, 1916). The energy generated by nuclear reactions near the centre of the star has to travel all the way to the surface to be radiated and to balance gravity. Transport by conduction is the result of collisions between particles. Generally, these particles are much slower than photons, making conduction an inefficient transport process in stars (see Chapter 5 of Kippenhahn and Weigert, 1990, for more details). Therefore, it is common to consider that there are two dominant transfers of energy in stellar interiors: radiation and convection. The relative efficiency of these two transport processes depends on the temperature gradient and can be expressed by the Schwarzschild criterion (Schwarzschild, 1958), which is expressed as

$$\nabla_{ad} = \left(\frac{\mathrm{d}\ln T}{\mathrm{d}\ln p}\right)_{\mathrm{ad}} < \left(\frac{\mathrm{d}\ln T}{\mathrm{d}\ln p}\right) = \nabla. \tag{2.13}$$

This means that if the local temperature gradient become larger than the adiabatic temperature gradient, the region is dynamically unstable and convective motions start. In most cases, this is caused either by a too high energy flux that has to be transported or by a large value of the opacities in a given region. Indeed, these induce an increase of the local temperature gradient.

The Schwarzschild criterion can also be expressed with the Brunt-Väisälä, or buoyancy, frequency N. This frequency characterise the maximum frequency for vertical oscillations under gravity of a fluid parcel around its equilibrium position (Lighthill, 1978). It is defined as

$$N^2 := g\left(\frac{1}{\Gamma_1}\frac{\mathrm{d}\ln p}{\mathrm{d}r} - \frac{\mathrm{d}\ln \rho}{\mathrm{d}r}\right), \tag{2.14}$$

with Γ_1 the first adiabatic exponent defined by

$$\Gamma_1 := \left(\frac{\partial \ln \rho}{\partial \ln p}\right)_{\mathrm{ad}}. \tag{2.15}$$

The Brunt-Väisälä frequency can also be expressed as

$$N^2 = \frac{g\delta}{H_p}(\nabla_{\mathrm{ad}} - \nabla), \tag{2.16}$$

where we have introduced $\delta = -\left(\frac{\partial \ln \rho}{\partial \ln T}\right)_{ad}$ and the pressure scale height in the case of hydrostatic equilibrium [4]

$$\mathrm{H}_p = \frac{p_0}{\rho_0 g_0} \,, \tag{2.17}$$

where p_0, ρ_0 and g_0 are the reference state pressure, density and acceleration of gravity. The expression given by Eq. (2.16) makes it easier to relate the Brunt-Väisälä frequency to the Schwarzschild criterion. Indeed, if $N^2 < 0$ we can infer that N is imaginary and then instead of oscillating the fluid parcel will move away exponentially [5], i.e. the convective instability arises. On the other hand, when $N^2 > 0$, that particle oscillates around its equilibrium position and the region is stably stratified. Then the fluid motions are mainly horizontal, and the buoyancy force always act in the opposite direction to a vertical displacement of a fluid particle.

Before describing these two zones, convective and radiative, it is important to specify for this work that stellar interiors are stratified. This means the pressure, density and temperature vary with depth. Consequently, a given mass element of fluid will need some energy to move radially against the direction of gravity.

Transport by radiation

The first mechanism that transport efficiently energy is radiation. Consequently, a given stellar layer is called a radiative region if the dominant process that transport energy is radiation. Under this mechanism, heat is transferred by emission, absorption and scattering of photons. Between emission and absorption, a photon mean free path is estimated by

$$l_{\mathrm{ph}} = \frac{1}{\kappa \rho}, \tag{2.18}$$

where κ is the mean absorption coefficient, which we consider to be the *Rosseland mean* opacities in this work (see Sect. 5.1.3 of Kippenhahn et al., 2013, for more details). If we estimate its value for the Sun, as in Kippenhahn and Weigert (1990), using $\kappa \simeq 1\ \mathrm{cm^2 g^{-1}}$ and the mean density of the Sun $\overline{\rho_\odot} \simeq 1.4 \mathrm{gcm^{-3}}$, we find that $l_{ph} \simeq 2$ cm. This distance is tiny compare to the radius of the Sun that is approximately $R_\odot = 6.957 \times 10^{10}$ cm. This means that the distance over which one particle will transport energy is very small compare to the total distance over which the energy has to be transported. Moreover, the temperature change over 2 cm is only of the order of 3×10^{-4} K (Kupka and Muthsam, 2017). In this case the *diffusion approximation* is justified, and the radiative energy flux may be expressed as a heat conduction

[4] The general definition of the pressure scale height is $\mathrm{H}_p := -\left(\frac{\mathrm{d} \ln p}{\mathrm{d}r}\right)^{-1}$.

[5] This is because the displacement of a fluid particle is of the form $\xi = \xi_0 e^{i\omega t}$, as it will be explained in Chapt. 3.

equation by

$$\mathbf{F}_{\text{rad}} = -\chi \nabla T, \tag{2.19}$$

where is introduced the radiative conductivity

$$\chi = \frac{4ac}{3} \frac{T^3}{\kappa \rho} \tag{2.20}$$

with c is the velocity of light and $a = 7.57 \times 10^{-15}$ erg cm^{-3}K^{-4} is the *radiation density constant*.

Note that the *diffusion approximation* is no longer valid close to the surface of the star, as the photon mean free path becomes comparable to the remaining distance to the surface.

Transport by convection

Convective transport, the second mechanism, is characterised by an exchange of energy between different layers within a star by macroscopic motions of matter from hot regions to cold ones. Even today, the theoretical description of convective motions and the related energy transport remain very complex, particularly because the medium is turbulent. This is why many models are using the Mixing Length Theory (MLT) of Prandtl (1925) and its expansion to stellar convection (Böhm-Vitense, 1958; Gough, 1977; Spiegel, 1963). According to this theory, hot 'bubbles' of matter will move upward into cold regions and cold ones move downward into hot regions, allowing heat transfer between different layers of the star.

The MLT assumes only one size of convective element that travels at an average velocity over an average distance called the mixing length, Λ, defined as a fraction of the pressure scale height.

$$\Lambda = \alpha_{\text{MLT}} \text{H}_p, \tag{2.21}$$

with α_{MLT} a free parameter and H_p the pressure scale height, as defined in equation (2.17). Thus, 'bubbles' of matter will move radially over distance Λ before mixing the transported heat and material with the surrounding and then lose their identity.

We will see that MLT is not enough for the purposes of this work because we need to consider different sizes of convective elements that travel on different distances. Particularly, MLT neglects all the contributions from small convective elements. However, even if MLT can not allow the study of convective element dynamics, it can give a good approximation of the convective flux and the total energy transport. This is because of its free parameter α_{MLT}, which can be adjusted to match predictions and observations. However, this free parameter is also a weakness of the theory, as it can compensate for inaccuracies or missing physics in the theory of stellar convection.

Usually, the local convective flux is estimated by (Kippenhahn and Weigert, 1990)

$$\mathbf{F}_{\rm conv} = \rho {\rm v}_{\rm conv} c_P {\rm D}T \tag{2.22}$$

where $\rm v_{conv}$ is typical velocity of convective motions, c_P is the specific heat capacity at constant pressure and DT the excess temperature of the considered 'bubbles' of matter over its surroundings.

2.3 Stellar evolution

Stellar evolution is the science that focuses on the life of stars, from birth to death, including all their major stages of evolution. This evolution may be graphically summarized on a Hertzsprung-Russell diagram, which presents the luminosity of the star $L_\star$ as a function of its effective temperature[6] $T_{\rm eff}$. In Fig. 2.1 is presented the Hertzsprung-Russell diagrams for a $1M_\odot$ and a $5M_\odot$ stellar models. The evolution of these two stellar models were computed using the MESA stellar evolution code (version mesa-r15140) (Paxton et al., 2011, 2013, 2015, 2018, 2019). This two kind of stars will be studied in Chapt. 6 and 7. On this plot, the main stages of stellar evolution can be identified, as we will show in the next paragraphs.

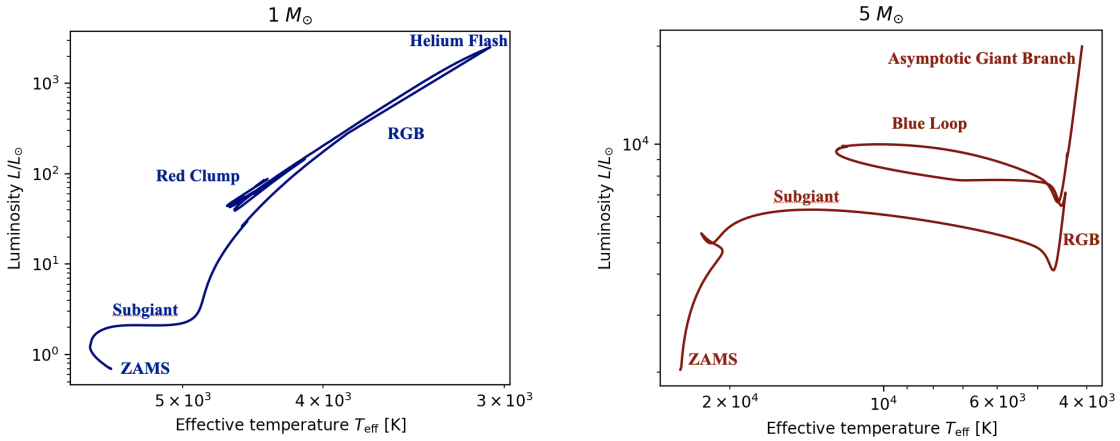

Fig. 2.1 Evolutionary path of a $1M_\odot$ (left) and a $5M_\odot$ (right) models computed with the MESA stellar evolution code. The main stages of their evolution are indicated on the plots.

[6]The effective temperature of a star of radius R is the temperature that would have a *black body* with the same luminosity L as the star and is given by the Stefan-Boltzmann law $L = 4\pi R^2 \sigma T_{\rm eff}^4$, with $\sigma = 5.67 \times 10^8$ W m^{-2}K^{-4} the Stefan-Boltzmann constant.

Stars form within large molecular gas clouds that collapse on themselves due to a gravitational instability. This instability appears when the gravity overcomes pressure. This results in an adiabatic contraction phase, during which the densest area accretes matter from the surrounding. At this stage, the object is a *protostar*. During this contraction, part of the gravitational energy is converted to internal energy, causing the gas to heat up, and some is radiated away as luminosity.

Once the accretion stops, the object becomes a *pre-main-sequence* star, whose main source of energy is still the gravitational contraction. On the Hertzsprung-Russell diagram, this stage is characterised by an almost vertical line known as the Hayashi track (Hayashi, 1961) (not shown in Fig. 2.1). The luminosity of the star decreases rapidly because it becomes fully convective. The convection increases the transport rate of energy and consequently the loss of energy is more important. However, in the meantime the star is still contracting, such that its central density and temperature keep increasing. At some point, radiation becomes more efficient to transport energy than convection and a radiative core starts developing. When this core is large enough, stars more massive than 0.5 $M_\odot$ enter the Henyey track (Henyey et al., 1955), which is horizontal on the Hertzsprung-Russell diagram (not represented in Fig. 2.1). The effective temperature of the star increases, whereas its luminosity remains almost constant. This formation stage lasts about one Kelvin-Helmoltz timescale, $\tau_{\rm KH}$ (see Eq. 2.6 for its definition) and it ends with the ignition of nuclear reactions in the core of the star.

This step is called the *Zero-Age Main-Sequence* (ZAMS in Fig. 2.1) and indicate the beginning of the *main-sequence*. The main-sequence is defined as the phase when the star burns hydrogen in its core and is in hydrostatic equilibrium. Indeed, during this period, the nuclear fusion of hydrogen into helium makes it possible to counterbalance the contraction due to gravity. This stable phase is the longest in the life of a star and lasts for approximately one nuclear timescale, the duration of which depends strongly on the mass of the star, as highlighted by Eq. (2.7). The more massive a star is, the faster it will consume its hydrogen and the shorter its lifetime on the main-sequence. Stars leave the main-sequence when they have consumed almost all their central hydrogen supply. For a 1 $M_\odot$ star, this step lasts approximately $\tau_{\rm nuc} \sim 10$ billion years.

As explained in Sect. 2.2.2, convective and radiative zones are distinct in stellar interiors. Stars like the Sun, i.e. low-mass stars, have a radiative core and convective envelope. It is the opposite for more massive stars ($M \gtrsim 2\ M_\odot$), which have a convective core and a radiative envelope. This mass limit between these two types of stars is not clearly defined. Indeed, stars with mass between 1.2 and 2 $M_\odot$ may already present a convective core but also still have a relatively thick convective envelope, with a radiative zone separating the two. This is for instance the case of F type stars.

Following the main-sequence, the star enters the *subgiant* phase and hydrogen burning in the core of the star stops. With no nuclear reaction in the core, the internal pressure of the core decreases sharply and gravity no longer encounters any obstacles. The core of the star contracts and heats up, while the envelope expands due to the layered fusion of the hydrogen and its temperature decreases. This phenomenon causes the stars to turn red because the lower temperature induces a red shift in their colour. During the beginning of this phase, the star consists of an inert core of helium (the result of hydrogen fusion during the main sequence) surrounded by a layer of burning hydrogen that will increase the mass of the core. This is the Red Giant Branch (RGB in Fig. 2.1) phase. During the RGB, the star will lose some of its mass. For stars with mass M $> 0.5 M_{\odot}$, once the core is sufficiently massive, i.e. when the temperature and pressure become sufficiently high, helium can start burning. There are two different cases for this ignition. In stars with mass M $< \lesssim 2.3 M_{\odot}$, the ignition of helium is rather short and explosive. This is the *Helium flash* which leads the star to settle in the Red Clump (see Fig. 2.1). In this phase, convective transport remains the dominant energy transport. In stars with M $\gtrsim 2.3 M_{\odot}$, the helium fusion is stable and the surface temperature of the star will increase, causing its colour to tend towards blue. This is called the Blue Loop (see Fig. 2.1) because of its path on the Hertzsprung-Russell diagram. This stage is followed by the Asymptotic Giant Branch phase, which marks the end of helium fusion. The core, composed of carbon and oxygen (C-O), contracts and heats up, while the envelope expands and cools.

After the star runs out of helium in its core, it will end its life as a white dwarf, neutron star or black hole depending on its mass. However, despite being very interesting, these late stages of evolution are not relevant for the work presented in this thesis, thus we will not describe them. These are detailed in the book of Kippenhahn and Weigert (1990).

Chapter 3

Theory of stellar oscillations

Stellar oscillations can be observed as variability in their luminosity. The first observation of such stellar variability goes back to the 16th century, when David Fabricius reported the fading and reappearance of a star (e.g. Catelan and Smith, 2015). This star was later named *Mira* by Hevelius and Horrocks (1662), which gave its name to the stars that pulsate in the same way. In the centuries that followed, other types of variable stars were observed, such as the Cepheids discovered in 1784 by John Goodricke (e.g. Leavitt and Pickering, 1912) or δ-Scuti in 1935 by Edward Fath (Fath, 1935). The pulsations of these types of stars are of large amplitude, which is why they were observed so early. They are part of a group of stars known today as classical pulsators. The pulsations of these stars originate from a readjustment of their internal structure, and each type of pulsation characterise a particular type of stars. In this thesis, we are interested in a different type of oscillations excited by turbulent convection discovered in the second half of the last century. These turbulent motions generate acoustic and gravity waves that propagate in the interior of stars and may become stationary due to the interference phenomenon. These stationary waves are global oscillations modes of stars. The properties of these modes and associated waves are described in this chapter.

3.1 Stellar seismology

In their pioneering paper, Leighton et al. (1962) reported the detection of vertical motions with *a striking repetitive time correlation, with a period* $T = 296 \pm 3$ *sec* in the solar atmosphere. This detection was confirmed a few months later by Evans and Michard (1962) and interpreted as global mode of oscillations of the Sun by Ulrich (1970) and Leibacher and Stein (1971). First, these global modes of oscillations were observed as bright ridges in frequency-wavenumber diagram by Deubner (1975) and Rhodes et al. (1977). A few years later, Claverie et al. (1979) clearly identified individual peaks equally spaced in frequency in the power spectrum of the

Sun, corresponding to actual low degree global modes of oscillations. These modes were rapidly identified as stable standing acoustic waves (e.g. Ando and Osaki, 1975). In these studies, the excitation mechanism responsible for these modes was not clearly identified. It is Goldreich and Keeley (1977), who first showed that turbulent convection could generate them.

In the last decades, analysis of these modes of oscillations has proven to be very powerful to study the solar interior. For instance, we got very strong constraints on the sound speed and density profile of the Sun (e.g. Antia and Basu, 1994), the rotation profile down to 25% of the solar radius (e.g. Brown and Morrow, 1987; García et al., 2007; Thompson et al., 2003) or the neutrino flux emanating from the Sun (e.g. Couvidat et al., 2003). Two main methods exist to get information on solar interior. The first one is *seismic modelling*, also called "forward modelling", which consist in building evolutionary models of the Sun and compare their properties with current observations. The idea is to tune these numerical models until there is good match with the observed properties such as radius, luminosity, effective temperature, surface abundances, age and pulsation frequencies. With this method, we thus also have information on the evolutionary path of the solar model. A limitation of this method is that it is restricted to the parameters space chosen to tune the model. Consequently, solutions depends strongly on the assumptions used. The second method is *seismic inversion* and consist in building static models of the Sun based on its observed oscillations frequencies. When comparing these frequencies to eigenfrequencies of a one-dimensional numerical model, the overall agreement is relatively good, but there are some discrepancies. This is a hint that the modelled structure of the Sun is incorrect, at least in details. We know from the theory of stellar oscillations that the oscillations frequencies of a star depends on its internal structure (see Sect. 3.3). Therefore, using the discrepancies between the observed and modelled frequencies, we can determine the structure of the Sun. The main advantage of this method is that it does not depend on a restricted set of parameters (details on inversion methods are given in Sect. 8.1). This will highlight the incorrectly modelled or missing physics of the initial model. In the last decades, inversion methods have been intensively applied to the Sun, revealing many features of the solar interiors. For instance, they allowed to probe the location of the interface between the radiative and convective zones (Christensen-Dalsgaard et al., 1991), the helium abundance if the convective envelope (Däppen et al., 1991), the efficiency of chemical diffusion (Christensen-Dalsgaard et al., 1993) and the rotation profile of the solar interior (Howe, 2009). More details on global helioseismology may be found in the reviews by Basu (2016); Buldgen et al. (2019); Christensen-Dalsgaard (2002); Kosovichev (2011)

Asteroseismology started much later due to the technical challenge to observe stars other than the Sun with high precision photometry, even if it was suspected from long time that other stars should oscillate in a solar-like way (e.g. Christensen-Dalsgaard, 1984). The first

confirmed detection of solar-like oscillations in a star other than the Sun goes back to Martić et al. (1999) and was rapidly followed by others (e.g. Bedding et al., 2001; Bouchy and Carrier, 2001; Buzasi et al., 2000). These detections were rapidly limited by technical constraints, such the impact of Earth rotation on ground-based observations. With the arrival of CoRoT in 2006 (Auvergne et al., 2009) and *Kepler* in 2009 (Borucki et al., 2010), some of these technical constraints were lifted and asteroseismology underwent a revolution. Thanks to the precision of the observations of these satellites, it was then possible to probe the interior of stars other than the Sun. The number of these observations is continuously increasing thanks to NASA's TESS satellite (Ricker et al., 2015), which has been operating since April 2018, and will continue to increase with the launch of the PLATO mission from ESA, scheduled for late 2026 (Rauer et al., 2014). Those observations include both main-sequence and red giant stars. As the oscillations observed in these stars are similar to the ones of the Sun, methods of forward and inverse modelling may also be applied to them. This would be extremely valuable to get information on stars at different evolutionary stages. However, in practice this is much more difficult because only low angular degrees modes of oscillations are observed for stars other than the Sun. Therefore, there are way less constraints to apply these methods. Current inverse methods have been applied to main-sequence solar-like stars (e.g. Bellinger et al., 2017) but are still failing when applied to evolved stars. This will be the subject of Sect. 8.1.

Similarly, as those stars oscillate due to standing acoustic waves, we should expect them to oscillate due to standing gravity waves. However, there is still no confirm detections of such oscillations modes in stars. In the Sun, the search for these gravity modes has been a long-standing quest (see Belkacem et al., 2022, for a recent review). The main difficulty lies in the fact that gravity waves propagate in the radiative interior of the Sun, and are evanescent in its convective envelope. Consequently, the resulting oscillations modes are expected to have very low amplitude at the surface of the Sun. Therefore, higher mass stars with convective cores and radiative envelopes should be more suitable targets for observing gravity waves excited by turbulent convection. But today, there is no confirmed detection in this type of stars either. Therefore, additional constraints on the properties of gravity waves, such as their amplitude and excitation spectrum, are needed to contribute to this quest. This motivates us to study the properties of these waves with hydrodynamical simulations.

3.2 Equations of hydrodynamics

The gas that makes up stars is predicted to be stratified, both in temperature and densities. Densities range from $\sim 10^0 - 10^2$ g cm^{-3} near the centre of the star and fall to $\sim 10^{-8}$ g cm^{-3} close the surface. Similarly, temperature ranges from $\sim 10^7$ K in the central regions, down to

$\sim 10^3 - 10^4$ K at the surface. These values are typical for main-sequence stars and can evolve during stellar evolution. With these temperatures and densities, the mean-free-path of particles is much smaller than the characteristic scales on which thermodynamic quantities vary (of the order of the radius of stars). Thus, it is possible to consider stellar matter as fluid and to describe it using the equations of hydrodynamics. In the work presented in this thesis, rotation and magnetic fields are not considered. We can thus assume stars as spherically symmetric.

First, let us introduce some properties of the stellar medium: the local pressure $p(\mathbf{r},t)$, the local density $\rho(\mathbf{r},t)$ and the velocity $\mathbf{v}(\mathbf{r},t)$, with $\mathbf{r}$ the position vector. These quantities are linked by the hydrodynamic equations, which, as for the equations of stellar structure introduced in Sect. 2.2.1, express the conservation of mass, momentum and energy.

In the case assumed here of spherical symmetry, the conservation of mass may be expressed by differentiating the first term on the right-hand-side (RHS) of Eq. (2.9) with respect to r, the second term with respect to t and equating the two

$$\frac{\partial \rho}{\partial t} + \frac{1}{r^2}\frac{\partial \rho \mathrm{v}_r}{\partial r} = 0. \tag{3.1}$$

This equation is called the continuity equation and is expressed in the general case as

$$\frac{\partial \rho}{\partial t} + \nabla \cdot (\rho \mathbf{v}) = 0, \tag{3.2}$$

with $\nabla\cdot$ the divergence operator.

The second conservation law expresses the conservation of momentum. In Sect. 2.2.1 we considered only a static case with two forces: gravity and pressure gradient. For a fluid in motion with velocity $\mathbf{v}(\mathbf{r},t)$, we need to consider how particles of fluids interact. These interactions can be modelled by the viscous stress tensor σ defined as

$$\sigma = \mu\left(\nabla\mathbf{v} + (\nabla\mathbf{v})^T - \frac{2}{3}\nabla\cdot\mathbf{v}\mathbb{I}\right) + \zeta\nabla\cdot\mathbf{v}\mathbb{I}, \tag{3.3}$$

with the superscript T that denotes the transpose, μ is the dynamic viscosity, ζ the bulk viscosity and $\mathbb{I}$ is the identity matrix. In this case the momentum equation is

$$\rho\left(\frac{\partial \mathbf{v}}{\partial t} + \mathbf{v}\cdot\nabla\mathbf{v}\right) = -\boldsymbol{\nabla} p + \rho\mathbf{f} + \nabla\cdot\sigma - \rho\mathbf{g}, \tag{3.4}$$

where $\mathbf{f}$ are the external body forces per unit mass. This equation is also called the Navier-Stokes equation.

The last conservation equation, the one for energy expresses the first principle of thermodynamics for a fluid particle and is given in its local form by

$$\frac{\partial \rho E}{\partial t} + \nabla \cdot [(\rho E + p)\mathbf{v}] = Q - \rho \mathbf{v} \cdot \mathbf{g} + \nabla \cdot (\sigma \mathbf{v}) - \nabla \cdot \mathbf{F} + \rho \mathbf{v} \cdot \mathbf{f}, \tag{3.5}$$

where $E = \frac{1}{2}\mathbf{v}^2 + e$ is the total specific energy, sum of kinetic and internal specific energies, Q represents the sources and sinks of heat and corresponds to the RHS of Eq. (2.11) and $\mathbf{F}$ is the surface density of heat flux. Equation (3.5) expresses the conservation of total energy, with contribution from the kinetic and internal energies. The evolution of kinetic energy is governed by the momentum equation, by taking the scalar product of the Eq. (3.4) with the velocity $\mathbf{v}$. Then, if we subtract the evolution of kinetic energy from Eq. (3.5), we can obtain an equation that only described the evolution of internal energy (Rieutord, 2015)

$$\frac{\partial \rho e}{\partial t} + \nabla \cdot (\rho e \mathbf{v}) = Q + \sigma \cdot \nabla \mathbf{v} - \nabla \cdot \mathbf{F} - p \nabla \cdot \mathbf{v}. \tag{3.6}$$

An alternative that has proven to be useful is to work with the entropy s instead of the internal energy e. These two quantities are linked with the thermodynamic relation

$$\mathrm{d}e = T\,\mathrm{d}s - p\mathrm{d}\mathcal{V}, \tag{3.7}$$

with $\mathcal{V}$ the volume. Using the continuity equation Eq. (3.2) and the relation Eq. (3.7), we can rewrite the internal energy conservation as

$$\rho T \left(\frac{\partial}{\partial t} + \mathbf{v} \cdot \nabla \right) s = Q + \sigma \cdot \nabla \mathbf{v} - \nabla \cdot \mathbf{F}. \tag{3.8}$$

The equations introduced above are the general equations of hydrodynamics. In the context of oscillations in stellar interiors, a few approximations can be made to simplify these equations. First, all terms involving viscosity are supposed to be small and may be neglected. The surface density of heat flux $\mathbf{F}$ is reduced in our case to the radiative flux F_{rad} given by Eq. (2.19) as the diffusion approximation is valid in stellar interiors. As we neglect all external body forces, such as the ones linked to magnetic field or rotation, we can consider $\mathbf{f} = 0$. Finally, we will work with the equations of hydrodynamics written in the form

$$\frac{\partial \rho}{\partial t} + \nabla \cdot (\rho \mathbf{v}) = 0, \tag{3.9}$$

$$\rho \left(\frac{\partial}{\partial t} + \mathbf{v} \cdot \nabla \right) \mathbf{v} = -\boldsymbol{\nabla} p - \rho \mathbf{g}, \tag{3.10}$$

$$\rho T\left(\frac{\partial}{\partial t}+\mathbf{v}\cdot\nabla\right)s=\mathcal{Q}-\nabla\cdot\mathbf{F}_{\rm rad}. \tag{3.11}$$

In order to form a complete set, supplementary equations are needed to close the system. First, the acceleration due to gravity is defined as $\mathbf{g}=-\nabla\Phi$, with Φ the gravitational potential that satisfy Poisson's equation

$$\nabla^2\Phi=4\pi\mathrm{G}\rho, \tag{3.12}$$

where ∇^2 is the Laplacian operator. Second, the other equations that are needed are an equation of state which link pressure p, entropy s, density ρ and temperature T together and an equation for the opacity $\kappa(\rho,T)$ for a given chemical composition. To describe stellar interior these two types of equations are complex and most of the time the solutions are interpolated from already computed tables such as the OPAL (Iglesias and Rogers, 1996) and OPAL EOS (Rogers and Nayfonov, 2002) tables, which are mostly valid for main-sequence stars. Finally, we need to specify the source term $\mathcal{Q}$can be assumed to have only one component that is relevant for our work, which is the nuclear energy generation rate $\epsilon_N(\rho,T)$.

3.3 Linear adiabatic non-radial oscillations equations

3.3.1 Perturbations in spherical coordinates system

A usual practice to study stellar oscillations is to consider them as small perturbations around a static equilibrium state. For a variable f, we denote the corresponding equilibrium state with the subscript 0, i.e. f_0. There are two kinds of perturbations: the Eulerian and Lagrangian perturbations. The former is defined as a perturbation at a given location $\mathbf{r}$ and denoted by the subscript f_1 and the latter as the perturbation of a given fluid element, denoted by δf. Therefore, a thermodynamic quantity f may be written as:

$$f(\mathbf{r},t)=f_0(\mathbf{r})+f_1(\mathbf{r},t), \tag{3.13}$$

or

$$f(\mathbf{r},t)=f_0(\mathbf{r}_0)+\delta f(\mathbf{r},t), \tag{3.14}$$

The two kinds of perturbations are linked by the relation

$$\delta f(\mathbf{r},t)=f_1(\mathbf{r},t)+\xi\cdot\nabla f_0(\mathbf{r}), \tag{3.15}$$

where $\xi=\mathbf{r}-\mathbf{r}_0$ is the displacement of the fluid induced by the perturbation. Note that in this work we do not consider rotation or any other mean flow, thus we have for the velocity field

$\mathbf{v} = \mathbf{v}_0 + \mathbf{v}_1 = \mathbf{v}_1$. From Eq. (3.15) it appears that in this case the two velocity perturbations are equal $\delta\mathbf{v} = \mathbf{v}_1$. For simplicity, in the following the subscript 1 is not used for the velocity field.

Assuming the spherical symmetry of the equilibrium model, we will expand the Eulerian perturbation in the form

$$f_1(r,\theta,\phi,t) = \sum_{\ell,m} a_{\ell,m} f_1(r) Y_\ell^m(\theta,\phi) e^{i\omega t}, \tag{3.16}$$

where ω is the angular frequency of the oscillation, Y_ℓ^m is a spherical harmonic function and $a_{\ell,m}$ a normalization factor. The spherical harmonics form an orthonormal basis of eigenfunctions of the Laplacian operator on the unit sphere (more details on the spherical harmonics can be found in Cohen-Tannoudji et al., 1986; Courant and Hilbert, 1966). A spherical harmonic function is defined as

$$Y_\ell^m(\theta,\phi) = (-1)^m c_{\ell m} P_\ell^m(\cos\theta) e^{im\phi}\ , \tag{3.17}$$

where $P_\ell^m(\cos\theta)$ is a Legendre polynomial and $c_{\ell m}$ is a normalization coefficient. In this thesis, we chose it such that the integral of $|Y_\ell^m|^2$ over the unit sphere is 1. We thus have,

$$\int_{\mathcal{S}} Y_{\ell,m}(\theta,\phi) Y_{\ell',m'}(\theta,\phi) \sin\theta \mathrm{d}\theta \mathrm{d}\phi = \delta_{\ell,\ell'}\delta_{m,m'} \tag{3.18}$$

A spherical harmonic is defined by its angular degree $\ell \geq 0$ and azimuthal order m with $-\ell \leq m \leq \ell$. For vector fields, it is usually more convenient to use the vectorial spherical harmonics basis $(\mathbf{R}_{\ell,m}, \mathbf{S}_{\ell,m}, \mathbf{T}_{\ell,m})$ defined in the spherical basis $(\mathbf{e}_r, \mathbf{e}_\theta, \mathbf{e}_\phi)$ as (Rieutord, 1987)

$$\begin{cases} \mathbf{R}_{\ell,m}(\theta,\phi) = Y_{\ell,m}\mathbf{e}_r \\ \mathbf{S}_{\ell,m}(\theta,\phi) = \nabla_\mathrm{h} Y_{\ell,m} = \frac{\partial}{\partial\theta} Y_{\ell,m}\mathbf{e}_\theta + \frac{1}{\sin\theta}\frac{\partial}{\partial\phi} Y_{\ell,m}\mathbf{e}_\phi \\ \mathbf{T}_{\ell,m}(\theta,\phi) = \nabla_\mathrm{h} \times \mathbf{R}_{\ell,m} = \frac{1}{\sin\theta}\frac{\partial}{\partial\phi} Y_{\ell,m}\mathbf{e}_\theta - \frac{\partial}{\partial\theta} Y_{\ell,m}\mathbf{e}_\phi \end{cases} . \tag{3.19}$$

The displacement vector associated with a wave can thus be written as

$$\xi(r,\theta,\phi,t) = \sum_{\ell,m} \left[\xi_{R;\ell,m}(r)\mathbf{R}_{\ell,m}(\theta,\phi) + \xi_{S;\ell,m}(r)\mathbf{S}_{\ell,m}(\theta,\phi) + \xi_{T;\ell,m}(r)\mathbf{T}_{\ell,m}(\theta,\phi)\right] e^{i\omega t}. \tag{3.20}$$

Using this decomposition and the momentum equation Eq. (3.4), we obtain that $\xi_{T;\ell,m}(r) = 0$ (see for example Alvan, 2014). Finally, the displacement vector may be expressed as

$$\xi(r,\theta,\phi,t) = \left[\xi_r(r); \xi_\mathrm{h}(r)\frac{\partial}{\partial\theta}; \xi_\mathrm{h}(r)\frac{1}{\sin\theta}\frac{\partial}{\partial\phi}\right] Y_\ell^m(\theta,\phi) e^{i\omega t}, \tag{3.21}$$

where we have changed the notation $\xi_r = \xi_{R;\ell,m}$ and $\xi_\mathrm{h} = \xi_{S;\ell,m}$ for simplicity. We can then identify the former as the radial component and the latter as the horizontal component of the displacement vector. The horizontal one can be expressed as (Unno et al., 1989)

$$\xi_\mathrm{h} = \frac{1}{\omega^2 r}\left(\frac{p_1}{\rho} + \Phi_1\right) \tag{3.22}$$

Using these expansions, the equations of hydrodynamics given by Eq. (3.9) - (3.11), and the Poisson's equation, Eq. (3.12) are linearised by expanding them in perturbations and retaining only terms of order 0 and 1. For clarity, the subscript 0 will dropped for equilibrium quantity, unless if there is an ambiguity. We intentionally omit the details of the calculations here, but one can refer to the chapter 3 of Unno et al. (1989) for more details. In the case of adiabatic oscillations, the specific entropy is conserved during oscillations and the linearised equations reduce to

$$\frac{1}{\rho}\frac{\mathrm{d}p_1}{\mathrm{d}r} + \frac{g}{\rho c_s^2}p_1 + \left(N^2 - \omega^2\right)\xi_r = -\frac{\mathrm{d}\Phi_1}{\mathrm{d}r}, \tag{3.23}$$

$$\frac{1}{r^2}\frac{\mathrm{d}}{\mathrm{d}r}\left(r^2\xi_r\right) - \frac{g}{c_s^2}\xi_r + \left(1 - \frac{L_\ell^2}{\omega^2}\right)\frac{p_1}{\rho c_s^2} = \frac{\ell(\ell+1)}{\omega^2 r^2}\Phi_1, \tag{3.24}$$

$$\frac{1}{r^2}\frac{\mathrm{d}}{\mathrm{d}r}\left(r^2\frac{\mathrm{d}\Phi_1}{\mathrm{d}r}\right) - \frac{\ell(\ell+1)}{r^2}\Phi_1 = 4\pi\mathrm{G}\rho\left(\frac{p_1}{\rho c_s^2} + \frac{N^2}{g}\xi_r\right). \tag{3.25}$$

where $c_s = (\Gamma_1 p/\rho)^{1/2}$ is the sound velocity. We have also introduced two characteristic frequencies, the Brunt-Väisälä frequency N and the Lamb frequency L_ℓ. The former has already been defined in Eq. (2.14) and the latter is defined by

$$L_\ell^2 := \frac{\ell(\ell+1)c_s^2}{r^2}. \tag{3.26}$$

with ℓ the angular harmonic degree. The evolution of the Lamb S_l and Brunt-Väisälä N frequencies as functions of normalised radius is presented in Fig. 3.1 in the cases of a solar and a $5M_\odot$ star models.

The system formed by Eq. (3.23) - (3.25) is still difficult to solve analytically. In order to simplify it, let us introduce the Cowling approximation (Cowling, 1941) that neglect any perturbations to gravitational potential $\Phi_1 = 0$. This approximation supposes that the contribution of one part of the medium to the gravitational potential perturbation is largely cancelled in non-radial oscillations by the contribution of another part of the medium (Unno et al., 1989). This is justified for modes with large radial order n and/ or angular degree ℓ. This approximation

allows us to neglect Eq. (3.25). Using the change of variable,

$$\begin{cases} \tilde{\xi}_r := r^2 \xi_r \exp\left(-\int_0^r \frac{g}{c_s^2} \mathrm{d}r\right) \\ \tilde{\eta} := \frac{p_1}{\rho} \exp\left(-\int_0^r \frac{N^2}{g} \mathrm{d}r\right) \end{cases}, \tag{3.27}$$

we can write Eq. (3.23) and (3.24) into a canonical form,

$$\frac{\mathrm{d}\tilde{\xi}_r}{\mathrm{d}r} = h(r) \frac{r^2}{\rho c_\mathrm{s}^2} \left(\frac{L_l^2}{\omega^2} - 1\right) \tilde{\eta}, \tag{3.28}$$

$$\frac{\mathrm{d}\tilde{\eta}}{\mathrm{d}r} = \frac{1}{r^2 h(r)} (\omega^2 - N^2) \tilde{\xi}_r. \tag{3.29}$$

where

$$h(r) := \exp\left[\int_0^r \left(\frac{N^2}{g} - \frac{g}{c_\mathrm{s}^2}\right) \mathrm{d}r\right] > 0. \tag{3.30}$$

The two equations given by Eq. (3.28) and (3.29) are called the linear adiabatic non-radial oscillations equations.

3.3.2 Local solution

For oscillations of high radial order n, the eigenfunctions ξ_r and ξ_h vary much more rapidly than the equilibrium quantities (Aerts et al., 2010). Therefore, it allows us to neglect the coefficients of ξ_r in Eq. (3.23) and the coefficients of p_1 in Eq. (3.24). In this context, our calculations are restricted to a local analysis. By deriving Eq. (3.28) with respect to r and eliminating p_1 from the resulting equation, we obtain the following equation for non-radial oscillations (Christensen-Dalsgaard, 2014)

$$\frac{\mathrm{d}^2 \tilde{\xi}_r}{\mathrm{d}r^2} + K(r) \tilde{\xi}_r = 0 \,, \tag{3.31}$$

where $K(r)$ is:

$$K(r) = \frac{\omega^2}{c_\mathrm{s}^2} \left(\frac{N^2}{\omega^2} - 1\right) \left(\frac{L_l^2}{\omega^2} - 1\right) . \tag{3.32}$$

We identify K with the square of the radial component k_r of the wave vector, $K = k_r^2$. Thus, Eq. (3.32) is a dispersion relation, i.e. a relation that links the wavenumber and the frequency. The nature of the solutions of Eq. (3.31) will depend on the sign of K and thus on the two characteristic frequencies L_ℓ and N. We can distinguish two cases:

- $\omega^2 > N^2, L_\ell^2$ or $\omega^2 < N^2, L_\ell^2$: in this case $K > 0$ thus k_r is real and ξ_r is locally an oscillating function of r

$$\xi_r \propto \exp\left(\pm i \sqrt{K} \mathrm{d}r\right), \tag{3.33}$$

- $N^2 > \omega^2 > L_\ell^2$ or $L_\ell^2 > \omega^2 > N^2$: in that case $K < 0$ thus k_r is purely imaginary and ξ_r is evanescent in the corresponding region

$$\xi_r \propto \exp\left(\pm \sqrt{|K|} \mathrm{d}r\right), \tag{3.34}$$

These conditions restrict the radial propagation of a given wave to specific regions, which will depends on the angular degree ℓ and the frequency ω of the wave. This is illustrated by the blue and red shaded area on Fig. 3.1. The two shaded areas indicate the regions where the solutions to the wave equation are oscillatory for the considered wave (ω, ℓ). There is a clear distinction between low frequency waves satisfying $\omega^2 < N^2, L_\ell^2$ (blue area) and high frequency waves satisfying $\omega^2 > N^2, L_\ell^2$ (red area). The former are gravity waves and the latter acoustic waves. In regions where waves oscillates, they propagate back and forth in the cavity to form standing waves, which are non-radial global modes of oscillations. Modes associated with internal gravity waves are gravity, or g, modes and the ones associated with acoustic waves are acoustic, or p, modes. These two types of modes are described in the next section.

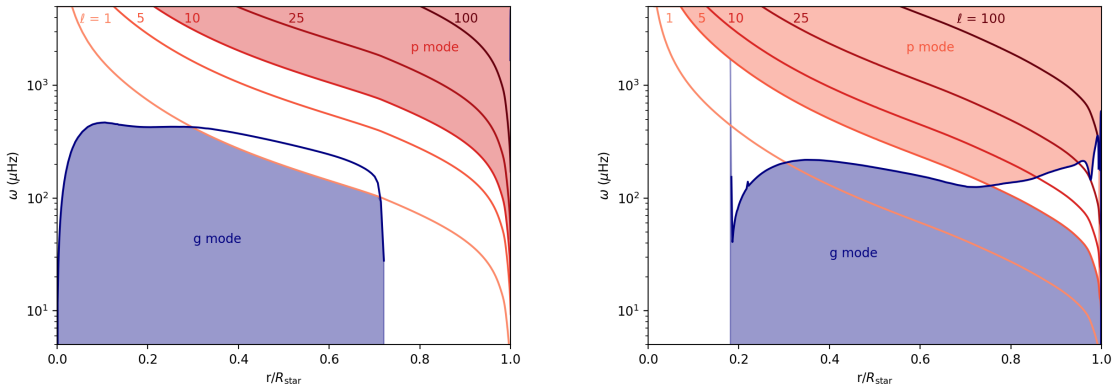

Fig. 3.1 Evolution of the Brunt-Väisälä N (blue line) and the Lamb frequencies for $\ell = 1$, 5, 10, 25 and 100 (red lines) for solar (left panel) and a 5 $M_\odot$ (right panel) model. The containment regions are shown for g modes (blue shaded area) and p modes (red shaded area). For the solar model, these cavities are plotted for g modes and p modes of angular degree $\ell = 1$ and $\ell = 10$ respectively. For the 5 $M_\odot$ model, they are plotted for g modes and p modes with angular degree $\ell = 5$.

3.4 General solution to the oscillation equations

3.4.1 Asymptotic method

The local method introduced in the previous section present the advantage of giving a simple understanding of modes trapping in stellar interiors. However, it can not be used to compute the eigenfunctions of the oscillations equations. In this section we present an asymptotic method to globally study modes of oscillations, i.e. without considering equilibrium quantities as constant. We will intentionally give only the main steps of the calculation, but more details are given in Unno et al. (1989) or Christensen-Dalsgaard (2014). Note that this method is only valid for high radial orders[1] n. In this limit, we can still work in the context of the Cowling approximation. First, Eq. (3.28) - (3.29) can be combined into

$$\frac{\mathrm{d}^2\tilde{\xi}_r}{\mathrm{d}r^2} - \frac{\mathrm{d}\ln|P|}{\mathrm{d}r}\frac{\mathrm{d}\tilde{\xi}_r}{\mathrm{d}r} - k_r^2\tilde{\xi}_r = 0, \tag{3.35}$$

where

$$P(r) = \frac{r^2}{c_s^2}\left(\frac{L_\ell^2}{\omega^2} - 1\right)h(r). \tag{3.36}$$

and $h(r)$ was introduced in Eq. (3.30).

The second order equation given by Eq. (3.35) can be rewritten in a form without the first derivative in $\tilde{\xi}_r$ with the following change of variable

$$\Xi = \tilde{\xi}_r|P|^{-1/2}\rho_c^{1/2} = \rho^{1/2}c_s r\left(|1 - \frac{L_\ell^2}{\omega^2}|\right)^{-1/2}\xi_r, \tag{3.37}$$

with ρ_c the density at the centre of the star. Then,

$$\frac{\mathrm{d}^2\Xi}{\mathrm{d}r^2} + \left[k_r^2 - f(P)\right]\Xi = 0 \tag{3.38}$$

where we have introduced the function,

$$f(x) := |x|^{1/2}\frac{\mathrm{d}^2|x|^{-1/2}}{\mathrm{d}r^2}. \tag{3.39}$$

Note that this function f is generally small compared to k_r^2 (Christensen-Dalsgaard, 2014), thus it is neglected in the following. In that case, Eq. (3.38) is equivalent to Eq. (3.31), except that the equilibrium quantities are not considered constant any more. As shown by

[1] For low radial orders numerical methods should be used.

Shibahashi (1979), solutions to Eq. (3.38) can be obtained with the JWKB method, which is commonly used in quantum mechanics to solve the Schrödinger equation (see for example Cohen-Tannoudji et al., 1986). This method assumes that the solutions varies rapidly compare to the equilibrium quantities. In this context the solutions may be expressed in the form

$$\Xi = a(r)\exp\left[i\Psi(r)\right], \tag{3.40}$$

with $a(r)$ the amplitude which is a function slowly varying with radius whereas $\Psi(r)$ is rapidly varying such as

$$k_r = \frac{\mathrm{d}\Psi}{\mathrm{d}r}. \tag{3.41}$$

Injecting Eq. (3.40) in Eq. (3.38) and from what has been shown in Sect. 3.3.2, it is straightforward that the solutions will take two different forms depending on the sign of k_r^2. If $k_r^2 > 0$ the solution is oscillatory and if $k_r^2 < 0$ the solution is exponentially decaying with radius. Assuming that $k_r^2 > 0$ for radii r between r_1 and r_2, with $r_1 < r_2$ and that $k_r^2 < 0$ if r $< r_1$ or r $> r_2$, the solutions are (Unno et al., 1989)

$$\Xi(r) = \begin{cases} \frac{A}{\sqrt{\pi}}\frac{1}{\sqrt{k_r}}\exp\left(-\int_{r_1}^{r}|k_r|\mathrm{d}r\right), & \text{if } r \ll r_1 \\ \frac{A}{\sqrt{\pi}}\frac{1}{\sqrt{k_r}}\cos\left(\int_{r_1}^{r}k_r\mathrm{d}r - \frac{\pi}{4}\right), & \text{if } r_1 \ll r \ll r_2 \\ \frac{A}{\sqrt{\pi}}\frac{(-1)^n}{\sqrt{k_r}}\exp\left(-\int_{r}^{r_2}|k_r|\mathrm{d}r\right), & \text{if } r \gg r_2. \end{cases} \tag{3.42}$$

with A a constant. The two radii r_1 and r_2 are the inner and outer turning points respectively. They correspond to locations where $k_r = 0$. At a turning point, a propagating wave is reflected. The solutions given by Eq. (3.42) must fulfil the quantization condition

$$\int_{r_1}^{r_2} k_r \mathrm{d}r = \left(n - \frac{1}{2}\right)\pi \tag{3.43}$$

with n the radial order of the corresponding oscillation mode.

We will now consider two cases: low frequencies corresponding to g modes and high frequencies to p modes.

3.4.2 Gravity modes

Gravity modes, or g modes, results from the interference of propagating internal gravity waves trapped in radiative zones. For these waves we usually have $\omega \ll L_\ell$ therefore we can use for

Eq. (3.32) the approximation

$$k_r^2 \simeq \left(\frac{N^2}{\omega^2} - 1\right)\frac{l(l+1)}{r^2}. \tag{3.44}$$

A mode is trapped between its two turning points r_1 and r_2, which in this case are defined as the location where $\omega = N$. Considering Eq. (3.43), we can express the eigenfrequencies of g modes of low degree and high radial order as (Tassoul, 1980)

$$\omega_{n,\ell} = \frac{\sqrt{\ell(\ell+1)}\int_{r_1}^{r_2} N\frac{\mathrm{d}r}{r}}{\pi(n+\ell/2+\alpha_g)}, \tag{3.45}$$

where α_g is a phase constant, depending on the inner and outer turning point of the mode (Christensen-Dalsgaard, 2014). The values of these eigenfrequencies as a function of angular degree computed for the Sun are presented on Fig. 3.2. In this figure is also presented the f mode, or fundamental mode, which is a surface gravity mode, but we will not consider it in the present work.

We can see from Eq. (3.45) that the frequencies of g modes are inversely proportional to their radial order n. This is an important property of g modes, which is equivalent to stating that modes of consecutive radial orders are equally spaced in period. This will help us to identify g modes in hydrodynamical simulations. This period spacing $\Delta\Pi$ is given by

$$\Delta\Pi = \frac{1}{\omega_{n,\ell}} - \frac{1}{\omega_{n+1,\ell}} = \frac{\pi}{\sqrt{\ell(\ell+1)}\int_{r_1}^{r_2}\frac{N}{r}\mathrm{d}r} \tag{3.46}$$

Indeed this equation is independent of n, implying the constant period spacing of modes of a given angular degree ℓ. From Eq. (3.37) and (3.42), we can express the eigenfunction of a given g mode (n,ℓ), i.e. the radial displacement associated with this mode in the region where it is oscillating

$$\xi_r(r) \simeq B\left(\frac{\sqrt{\ell(\ell+1)}}{\omega}\right)^{1/2}\rho^{-1/2}r^{-3/2}\left|\frac{N^2}{\omega^2}-1\right|^{-1/4}\cos\left[\int_{r_1}^{r}\left(\frac{N^2}{\omega^2}-1\right)^{1/2}\frac{\mathrm{d}r'}{r'} - \frac{\pi}{4}\right] \tag{3.47}$$

with B a constant that fixes the amplitude. In order to get the eigenfunctions $\xi_{r;n,\ell}$ and eigenfrequencies $\omega_{n,\ell}$, we will solve the associated system numerically with the oscillations code GYRE (Townsend et al., 2018; Townsend and Teitler, 2013). We will then be able to compare their theoretical predictions to measurements made in hydrodynamical simulations presented in Chapt. 6 and 7.

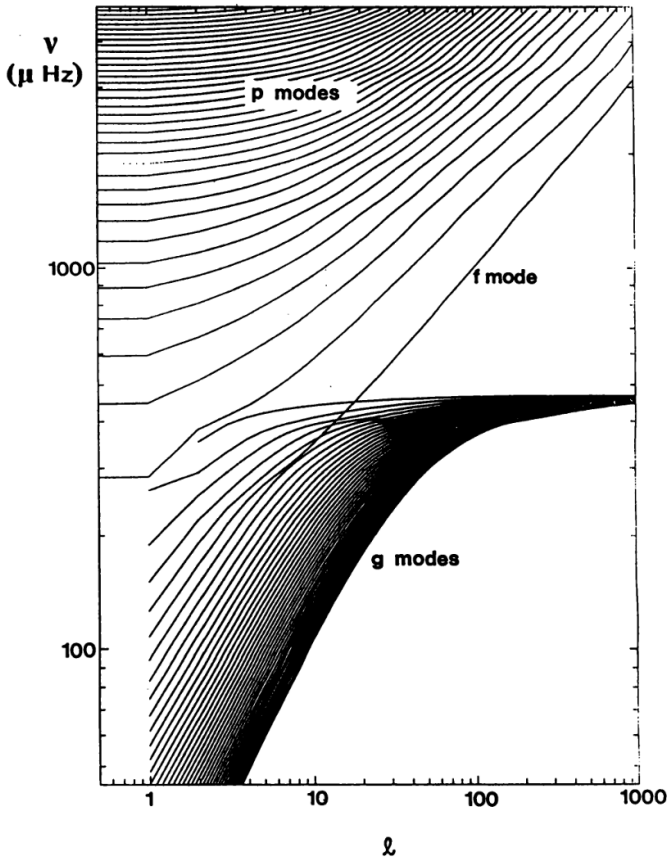

Fig. 3.2 Adiabatic oscillation frequencies for a normal model of the present Sun, as functions of angular degree ℓ. For clarity, points corresponding to modes with a given radial order have been connected by straight lines. Only g modes with radial order less than 40 have been included. Credits:Christensen-Dalsgaard (1988)

3.4.3 Acoustic modes

Acoustic modes, or p modes, are formed by superposition of progressive acoustic waves for which the restoring force is the pressure gradient. These waves propagate between an inner r_1 and an outer r_2 turning points. In this case, the inner turning point is reached when the wave frequency is equal to the local Lamb frequency, $\omega = L_\ell(r_t)$. The outer one is generally close to the photosphere (Unno et al., 1989) so we set $r_2 \simeq R_{\rm star}$. This is the reason why global acoustic modes can be easily observed as *5 minutes oscillations*, as it was initially done for the Sun by Leighton et al. (1962). As already mentioned in Sect. 3.3.2, the frequency of p modes is larger than the Lamb and Brunt-Väisälä frequencies. We can assume that $\omega \gg N$ and therefore reduce

Eq. (3.32) to

$$k_r^2 \simeq \frac{1}{c_s^2}\left(L_\ell^2 - \omega^2\right). \tag{3.48}$$

As for g modes, we can thus determine an expression for the eigenfrequencies of high order p modes. However, Eq. (3.43) can not be used directly because the formulation given by Eq. (3.38) fails at $\omega = L_\ell$. As detailed in Sect 7.5 of Christensen-Dalsgaard (2014), a similar expression may be derived for p modes with the same method, but we will not derive it here for simplicity. The eigenfrequencies of p modes are given by (Tassoul, 1980)

$$\omega_{n,\ell} = \frac{\left(n + \ell/2 + 1/4 + \alpha_p\right)\pi}{\int_0^{R_{\rm star}} \frac{\mathrm{d}r}{c_s}} \tag{3.49}$$

with α_p a phase constant. The values of these eigenfrequencies as a function of angular degree computed for the Sun are presented on Fig. 3.2. This expression highlights that the eigenfrequencies of p modes of consecutive radial order are equally spaced in frequency. This frequency spacing is given by

$$\Delta\omega_\ell = \omega_{n+1,\ell} - \omega_{n,\ell} = \pi\left[\int_0^{R_{\rm star}} \frac{\mathrm{d}r}{c_s}\right]^{-1}. \tag{3.50}$$

For the radial mode $\ell = 0$, the frequency spacing is usually called the *large frequency separation* and is written $\Delta\nu$. Note that a maximal frequency for p modes exists and is defined as the cut-off frequency $\nu_{ac} \propto g/\sqrt{T_{\rm eff}}$ above which the atmosphere is not able to trap the modes and propagating waves are not reflected and keep travelling in the stellar atmosphere (Hekker and Mazumdar, 2014).

With this asymptotic method, we can also infer an asymptotic expression for the eigenfunctions of high order p modes when assuming $\omega^2 \gg L_\ell^2$

$$\xi_r \simeq C\rho^{-1/2}c^{-1/2}r^{-1}\cos\left[\omega\int_r^{R_{\rm star}} \frac{\mathrm{d}r'}{c_s} - (\frac{1}{4} + \alpha)\pi\right] \tag{3.51}$$

with C a constant fixing the amplitude. Interestingly, we can see from this expression that the eigenfunctions of p modes are independent of their angular degree ℓ in the approximation $\omega^2 \gg L_\ell^2$.

3.4.4 Mixed modes

Mixed modes are formed by coupling between acoustic and gravity modes. Therefore, a mixed mode with frequency ω will present properties of a g mode in regions where $\omega^2 < N^2, L_\ell^2$, and

the ones of a p mode in regions where $\omega^2 > N^2, L_\ell^2$. For this coupling to happen requires two conditions: p and g modes should have similar frequencies and the evanescent region between their respective resonant cavities should not be too large, allowing the oscillations to reach the other cavity before being damped out. In that case, p and g modes with similar frequencies and angular degrees will interact. This will affect their frequencies by a process known as *avoided crossing* (e.g. Aizenman et al., 1977). This phenomenon is well known in atomic physics (von Neuman and Wigner, 1929). It has been suggested by Christensen-Dalsgaard (2014) that it may be understood as the coupling of two oscillators $y_1(t)$ and $y_2(t)$. In this formalism, the system is described by the equations (Deheuvels and Michel, 2010)

$$\frac{\mathrm{d}^2 y_1}{\mathrm{d}t^2} + \omega_1^2 y_1 - \alpha_{1,2} y_2 = 0 \tag{3.52}$$

$$\frac{\mathrm{d}^2 y_2}{\mathrm{d}t^2} + \omega_2^2 y_2 - \alpha_{1,2} y_1 = 0 \tag{3.53}$$

where ω_1 and ω_2 are the eigenfrequencies of each oscillator respectively and $\alpha_{1,2}$ represents the coupling between the two oscillators. When uncoupled ($\alpha_{1,2} = 0$), the oscillators cross at $\omega_1 = \omega_2 = \omega_0$. When coupled, the eigenfrequencies of the system formed by Eq. (3.52) and (3.53) are given by

$$\omega_\pm = \frac{\omega_1^2 + \omega_2^2}{2} \pm \left[\left(\omega_1^2 - \omega_2^2 \right)^2 + 4\alpha_{1,2}^2 \right]^{1/2} \tag{3.54}$$

In the case when the coupling factor is small compared to the difference between the eigenfrequencies, $\alpha_{1,2} \ll |\omega_1^2 - \omega_2^2|$, the eigenfrequencies of the system are close to ω_1 and ω_2. On the other hand, if it is large, $\alpha_{1,2} \gg |\omega_1^2 - \omega_2^2|$, the eigenfrequencies are estimated by $\omega_\pm^2 \simeq \omega_0^2 \pm \alpha_{1,2}$. In that case, the two oscillators "avoid" the frequency ω_0 and the eigenmodes are mixed modes, one with dominant properties from ω_1 and the other one from ω_2 (Hekker and Mazumdar, 2014).

The above method gives a good understanding of what are mixed modes, but we can use an asymptotic method as in Sect. 3.4.1 to obtain the actual eigenfunctions and eigenfrequencies corresponding to mixed modes. An important difference is that mixed modes have four turning points, which are basically two from the g mode component, r_1 and r_2, and two for the p mode one, r_3 and r_4. This is illustrated on the propagation diagram of a 1.3 $M_\odot$ red giant star in Fig. 3.3.

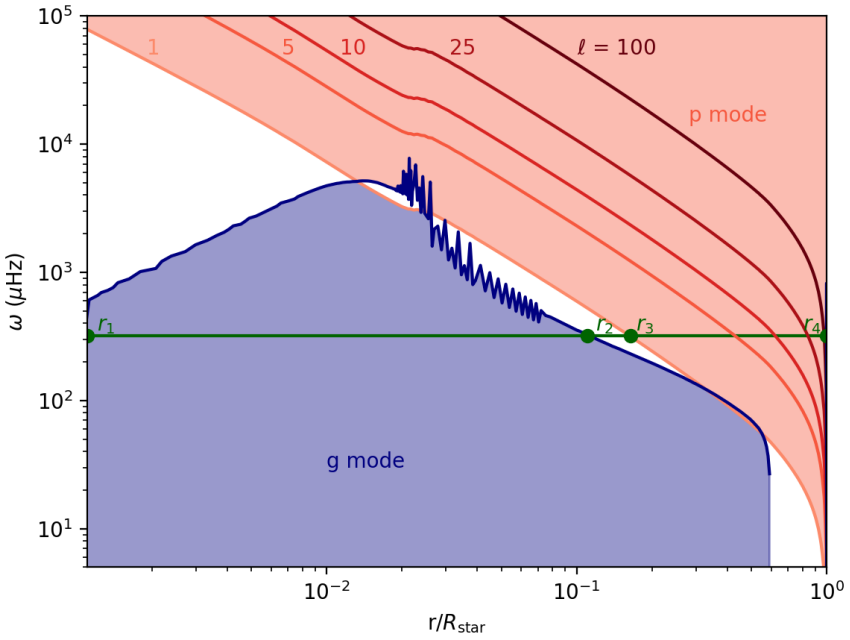

Fig. 3.3 Evolution of the Brunt-Väisälä N (blue line) and the Lamb frequencies for $\ell = 1$, 5, 10, 25 and 100 (red lines) for a 1.3 $M_\odot$ Red Giant star model. The containment regions are also shown for g modes (blue shaded area) and p modes (red shaded area) of angular degree $\ell = 1$ and frequency $\omega = 320$ μHz.

The eigenfunctions are given by (Unno et al., 1989)

$$\xi_r(r) = \begin{cases} \frac{A_1}{c_s r\sqrt{\pi\rho k_r}}\left(|1-\frac{L_\ell^2}{\omega^2}|\right)^{1/2}\cos\left(\int_{r_1}^{r} k_r \mathrm{d}r - \frac{\pi}{4}\right), & \text{if } r_1 \ll r \ll r_2 \\ \frac{A_1}{c_s r\sqrt{\pi\rho k_r}}\left(|1-\frac{L_\ell^2}{\omega^2}|\right)^{1/2}[\frac{1}{\sqrt{2}}\sin\left(\int_{r_1}^{r_2} k_r \mathrm{d}r\right)\exp\left(-\int_{r_2}^{r}|k_r|\mathrm{d}r\right) & \\ \quad +\cos\left(\int_{r_1}^{r_2} k_r \mathrm{d}r\right)\exp\left(\int_{r_2}^{r}|k_r|\mathrm{d}r\right)], & \text{if } r_2 \ll r \ll r_3 \\ \frac{A_2}{c_s r\sqrt{\pi\rho k_r}}\left(|1-\frac{L_\ell^2}{\omega^2}|\right)^{1/2}\cos\left(\int_{r}^{r_4} k_r \mathrm{d}r - \frac{\pi}{4}\right), & \text{if } r_3 \ll r \ll r_4. \end{cases} \tag{3.55}$$

where A_1 and A_2 are constants. For radii smaller than r_1 or larger than r_4, the eigenfunctions are exponentially decaying with distance, i.e. waves are evanescent. The solution given by Eq. (3.55) imply a condition for the eigenvalues that can be express as (Mosser et al., 2012)

$$\tan\theta_p = q\tan\theta_g \tag{3.56}$$

where $\tan\theta_p$ and $\tan\theta_g$ are the acoustic and gravity waves phases. The dimensionless coefficient q is called *coupling factor* and quantify the level of coupling between p and g modes. It is

equivalent to the coefficient $\alpha_{1,2}$ mentioned in the simple analogy with the two oscillators. This factor q is supposed to have values in the range $[0, 1/4]$ (Unno et al., 1989). Its actual value depends on the properties of the g and p modes cavities, and particularly on the thickness of the evanescent region between the two cavities (Takata, 2016). Finally, the condition Eq. (3.56) gives the asymptotic expression for eigenfrequencies (Bugnet, 2020)

$$\omega_{n,\ell} = \omega_p + \frac{\Delta\omega_p}{\pi} \arctan\left[q \tan\left(\pi\left[\frac{1}{\omega\Delta\Pi_\ell} - \frac{1}{\omega_g\Delta\Pi_\ell}\right]\right)\right]. \tag{3.57}$$

with ω_p and ω_g the frequencies of the associated p and g modes and $\Delta\omega_p$ and $\Delta\Pi_\ell$ are the frequencies and periods spacing given by Eq. (3.50) and (3.46) respectively.

Chapter 4

Properties of internal gravity waves

In stably stratified fluids, it is now generally accepted that internal gravity waves (IGW) can transport energy, chemical elements and angular momentum between distant regions. Those waves have been well studied and observed in the Earth's oceans and atmosphere (see Sutherland (2010) for a complete review). It is in the oceans that they were first observed, although indirectly, through the dead-water phenomenon by Nansen and Sverdrup (1897). This phenomenon arises when a boat sailing over a stratified fluid is slowed down in comparison to a homogeneous case (Fourdrinoy et al., 2020). In his PhD thesis, Ekman (1904) explained that IGWs generated by the boat and propagating at the interface between saline and fresh water could produce this effect. In the atmosphere, IGWs were observed later, but they are now invoked to explain various phenomena. For instance, they are proposed as the mechanism driving the Quasi Biennial Oscillation (QBO) by transporting angular momentum upward (see for example Baldwin et al., 2001). The QBO is a reversal of the direction of the winds in the stratosphere, with a period of approximately two years. These waves have also been studied and/ or observed in the atmospheres of other planets of the solar system such as Mars, Venus, Jupiter and Titan[1]. Compared to the Earth's atmosphere and oceans, the study of IGWs in stars is relatively recent, where they have been first studied theoretically in the solar atmosphere (Stein, 1967) and then its interior. Nowadays, they are assumed to play a role in almost every star, particularly related to angular momentum transport and chemical mixing. Consequently, there is a lot to learn from the atmospheric science community.

[1]Titan is actually a moon of Saturn, but its atmospheric dynamics is similar to the one of rocky planets.

4.1 Propagation

Internal gravity waves' restoring force is buoyancy i.e. gravity, this is the reason why they can only propagate in stably stratified media. In literature, it is common to find a distinction between two types of gravity waves: surface and internal gravity waves. In this work, we will focus on internal gravity waves, but the surface ones are just a particular case of internal waves propagating at a discontinuity of density in the medium (Vallis, 2017).

In Sect. 3.3.2 we have identified the radial component k_r of the wave vector $\mathbf{k} = (k_r, k_\theta, k_\phi)$. A common practice when studying waves is to group together the two components perpendicular to the radial one to define a horizontal wave vector $\mathbf{k}_\mathrm{h} = (k_\theta, k_\phi)$. The norm of these vectors are defined as $k^2 = k_r^2 + k_\theta^2 + k_\phi^2$ and $k_\mathrm{h}^2 = k_\theta^2 + k_\phi^2$. Assuming the local plane wave approximation, we can express the horizontal wavenumber k_h as a function of spherical harmonic degree ℓ and radius r with the relation

$$k_\mathrm{h} = \frac{\sqrt{\ell(\ell+1)}}{r}. \tag{4.1}$$

Then we can rewrite the dispersion relation Eq. (3.44) for IGWs as

$$\frac{\omega^2}{N^2} = \frac{k_\mathrm{h}^2}{k^2}. \tag{4.2}$$

Alternatively we can also express the frequency ω of an IGW in terms of the angle α between the 3D wave vector $\mathbf{k}$ and the horizontal one $\mathbf{k}_\mathrm{h}$

$$\omega = \pm N \cos\alpha, \tag{4.3}$$

with $\cos\alpha = \pm k_h/k$. According to Eq. (4.3), the frequency of an IGW is only a function of N and α. Therefore, if these quantities are given, the frequency of a wave does not depend on its wavelength (Holton, 2004). The angle α is represented on Fig. 4.1. In this two-dimensional schematic, we do not consider the ϕ-direction, therefore $k_\mathrm{h} = k_\theta$. This angle α can help to estimate the frequency of dominant waves when looking at a snapshot from a hydrodynamical simulation. This dispersion relation imposes the condition already mentioned in Sect. 6.4.3 on the frequency of an IGW

$$\omega \leq N \tag{4.4}$$

The maximal frequency of an IGW, $\omega = N$ corresponds to a wave propagating vertically, i.e. radially in our case.

Using the dispersion relation given by Eq. (4.3), we can now retrieve the expressions of the phase velocity $\mathbf{u}_\mathrm{p}$ and the group velocity $\mathbf{u}_\mathrm{g}$ associated with an IGW. For the phase velocity we

have

$$\mathbf{u}_\mathrm{p} = \frac{\omega}{k}\frac{\mathbf{k}}{k} = \frac{Nk_h}{k^3}(k_r, k_\mathrm{h}). \tag{4.5}$$

From this relation it appears that the phase velocity depends on the wave vector, therefore IGWs are dispersive waves. The group velocity is given by

$$\mathbf{u}_\mathrm{g} = \frac{\partial\omega}{\partial\mathbf{k}} = \frac{Nk_r}{k^2}\left(-\frac{k_h}{k}, \frac{k_\theta k_r}{k_h k}, \frac{k_\phi k_r}{k_h k}\right). \tag{4.6}$$

Then the magnitude of the group velocity is

$$|\mathbf{u_g}| = \frac{N}{k}\sin\alpha. \tag{4.7}$$

In Chapt. 6 and 7, using the group velocity, we will be able to estimate how fast energy is transported radially by IGWs via measurement of the wave energy flux in simulations.

An interesting property of IGWs is that their group velocity and wave vector are perpendicular

$$\mathbf{u_g}.\mathbf{k} = 0. \tag{4.8}$$

The group velocity is therefore parallel to the motions of the fluid parcels, i.e. IGWs are transverse waves, as illustrated on Fig. 4.1. In addition, this also implies that the group velocity, which corresponds to the velocity and direction of transport of energy, is perpendicular to the phase velocity, i.e. to the direction of phase propagation. Particularly, we can see from Eq. (4.5) and (4.6) that the phase and group velocities have opposite signs in the radial direction. This implies that if the wave crests move outward, the energy moves inward, and vice versa (see Sect. 7.3.4 in Vallis, 2017).

From the dispersion relation Eq. (4.3) and Eq. (4.8) it appears that the group velocity, which describes the propagation of energy, is radial when the phase propagation is horizontal. In other words, the closer the frequency ω of the wave is to the Brunt-Väisälä frequency N, the more radially the energy propagates.

4.2 Damping by radiative diffusion

As they propagate, IGWs are dissipated by radiative and viscous effects. Both can be considered as diffusive damping. In order to determine which one is dominant, we use the Prandtl number P_r that compares the intensity of these two effects. It is expressed as

$$P_r = \frac{\nu}{\kappa_\mathrm{rad}}, \tag{4.9}$$

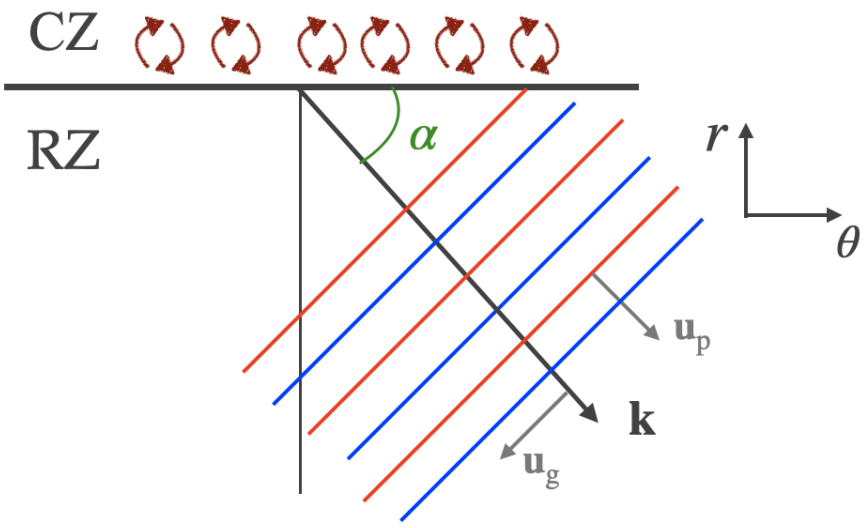

Fig. 4.1 An internal wave propagating in the direction **k**. For the wave shown k_r is negative and k_θ is positive. The solid coloured lines show crests and troughs of the perturbation due to an IGW. The motion of the fluid parcels is along the lines of constant phase, as shown, and is parallel to the group velocity and perpendicular to the phase speed. Figure adapted from Vallis (2017)

.

with ν the kinetic viscosity and $\kappa_{\rm rad}$ the radiative diffusivity defined as

$$\kappa_{\rm rad} = \frac{\chi}{c_p \rho} \tag{4.10}$$

with χ the radiative conductivity already introduced in Sect. 2.2.2 in Eq. (2.20). In stars, radiative effects largely dominate over viscous ones, therefore the Prandtl number is usually very small, typically $Pr \sim 10^{-7}$. We will thus consider that in stellar interiors, radiative diffusion is the main dissipative effect for IGWs. This is of major interest as it is through damping that waves can transport angular momentum, energy and chemical elements. As we will see in Chapt. 6, modelling a realistic radiative diffusion is not trivial in hydrodynamical simulations. Therefore, these transport properties of IGWs should be studied with caution.

In order to take into account damping by radiative diffusion, we need to rewrite Eq. (3.38) to consider non-adiabatic effects. To avoid long calculation, we will introduce a new form of this equation, which is derived by Press (1981) for a perfect gas in a Boussinesq case with a plane parallel symmetry. The Boussinesq approximation neglects all density variations, except in the buoyancy term $\rho \mathbf{g}$ of the momentum equation. Note that within this approximation, the diffusion coefficients are assumed constant (Rieutord, 2015). This non-adiabatic wave equation

reads

$$\frac{\partial^2\Psi}{\partial r^2}+\left(\frac{N^2}{\omega^2}-1\right)k_{\rm h}^2\Psi+\frac{i\kappa_{\rm rad}}{\omega}\left(\frac{\partial^2}{\partial r^2}-k_{\rm h}^2\right)^2\Psi=0 \tag{4.11}$$

with i is the imaginary unit and

$$\Psi:=\rho_0^{1/2}k_{\rm h}^{-2}{\rm v}_r, \tag{4.12}$$

where ρ_0 is assumed to be constant. To derive Eq. (4.11), the dispersion relation for IGWs given by Eq. (3.44) has been used.

In Eq. (4.11) the last term corresponds to the non-adiabatic effects. As in Sect. 3.4, we can use the JWKB method to solve this equation and obtain for the vertical component of the velocity

$${\rm v}_r=Ck_{\rm h}^{3/2}\rho_0^{-1/2}\left(\frac{N^2}{\omega^2}-1\right)^{-1/4}\exp\left(i\int k_r{\rm d}r-i\omega t\right)\exp\left(-\tau/2\right) \tag{4.13}$$

where C is a constant fixing the amplitude and the last exponential term represents the effect of radiative damping. The parameter τ is defined as

$$\tau(r,\ell,\omega)=[\ell(\ell+1)]^{3/2}\int_{r_{\rm e}}^{r}\kappa_{\rm rad}\frac{N^3}{\omega^4}\left(\frac{N^2}{N^2-\omega^2}\right)^{1/2}\frac{{\rm d}r}{r^3}, \tag{4.14}$$

where $r_{\rm e}$ is the radius at which the waves are excited.

In presence of a gradient of chemical composition, Zahn et al. (1997) have shown that this parameter τ is slightly modified to

$$\tau(r,\ell,\omega)=[\ell(\ell+1)]^{3/2}\int_{r_{\rm e}}^{r}\kappa_{\rm rad}\frac{NN_t^2}{\omega^4}\left(\frac{N^2}{N^2-\omega^2}\right)^{1/2}\frac{{\rm d}r}{r^3}, \tag{4.15}$$

with N_t the thermal part of the Brunt-Väisälä frequency. Indeed, due to the chemical gradient, the expression of the Brunt-Väisälä frequency is slightly modified compared to Eq. (2.16). In that case it is given by

$$N^2=N_t^2+N_\mu^2=\frac{g\delta}{H_p}\left(\nabla_{ad}-\nabla+\frac{\phi}{\delta}\nabla_\mu\right), \tag{4.16}$$

with ∇_μ the compositional gradient and ϕ defined as

$$\phi:=\left(\frac{\partial\ln\rho}{\partial\ln\mu}\right). \tag{4.17}$$

In absence of a gradient of composition $\nabla\mu=0$ and $N=N_t$ as in Eq. (2.16).

4.3 Generation mechanisms

Generally speaking, any perturbation to a stably stratified radiative region can generate IGWs. In this work, we consider that the main waves' excitation mechanism is turbulent convection. There are other mechanisms that could generate oscillations (κ and ϵ mechanisms, linked respectively to opacities and nuclear reactions, or also excitation by tidal forces) but we are not interested in them in the context of this thesis. Excitation by turbulent convection allows generating IGWs in, or at the edge of, a convective region that will propagate in an adjacent radiative zone. To date, the actual wave spectrum generated by this mechanism in stars remains uncertain. There are some predictions from analytical models, as we will see, but none has been observationally confirmed and hydrodynamical simulations do not always agree on this (see for example Couston et al., 2018; Rogers et al., 2013). However, it is generally admitted that this excitation mechanism has two distinct components:

- excitation by turbulent eddies, usually called Reynold's stress, which generates waves by turbulence in the bulk of convective zones.
- excitation by penetrative convection, when convective motions cross the convective boundary and penetrate into the adjacent radiative region. These convective motions, often referred to as plumes, produce a mechanical and thermal perturbations of the stable zone.

These two generation mechanisms are described in the next sections.

4.3.1 Excitation by turbulent eddies

Convective regions are composed of chaotic, unsteady motions described as turbulence. This produces pressure and density perturbations that can generate waves.

Inhomogeneous wave equation

To analytically predict the wave spectrum, a common method is to derive an inhomogeneous wave equation from the momentum and the mass conservation equations. Once more, we consider oscillations as small perturbations around a static equilibrium state, but unlike in Chapt. 3, we keep the quadratic terms in eulerian perturbations. These non-linear terms are considered as source terms in the inhomogeneous wave equation, which will take the form of a forced oscillation's equation

$$\frac{\partial^2 \xi}{\partial t^2} + \mathcal{L}(\xi) = \mathcal{S} \tag{4.18}$$

where $\mathcal{L}$ is a linear operator and $\mathcal{S}$ the considered non-linear source term. This method applied to wave excitation by turbulence was initially developed by Lighthill (1952). In this pioneering work, the authors study the sound generated by fluid motions in a turbulent homogeneous medium.

The study by Lighthill (1952) was then extended to an isothermal stratified fluid by Stein (1967), which allows considering the excitation of gravity waves. The main conclusion from this work is that the excitation results from two source terms: turbulent Reynolds stress and turbulent entropy fluctuations. The authors also show that the gravity waves emission is proportional to the size of the largest eddies, the ones which bear the bulk of the energy. Assuming a Kolmogorov spectrum for the turbulent flow (Kolmogorov, 1941) and an isothermal stratified atmosphere, the total upward gravity waves flux is given by

$$F_{\text{wave}} \simeq 10^2 \frac{\rho_0 \mathrm{v}_{\text{conv}}^3}{H} \left(\frac{H}{H_p} \right)^5 \tag{4.19}$$

where v_{conv} is the turbulent convective velocity scale, H is the characteristic length scale of the largest eddies and H_p is the pressure scale height already introduce with Eq. (2.17). The term $\rho_0 \mathrm{v}_{\text{conv}}^3$ is a good approximation for the convective flux that can be derived from MLT arguments (Biermann, 1932). The authors finally highlight that gravity waves emission is very efficient, as the ratio H/H_p comes close to 1.

Twenty years later, Goldreich and Kumar (1990) get back to the study of waves generation by turbulent convection using a similar methodology but more suited to a stellar case. In this work, the authors solve the fully compressible inhomogeneous wave equation with the divergence of the turbulent Reynold's stress as the source term. Their aim is to estimate the efficiency of the transfer of energy from the turbulent medium into the trapped modes and the propagating waves. In this study also, the turbulence spectrum is approximated with a Kolmogorov spectrum. They conclude that the amount of energy transferred from the turbulent medium to propagating gravity waves scales as

$$F_{\text{wave}} \propto \rho_0 \mathrm{v}_{\text{conv}}^3 \mathcal{M}_t, \tag{4.20}$$

where $\mathcal{M}_t$ is the turbulent Mach number defined as

$$\mathcal{M}_t = \frac{\mathrm{v}_{\text{conv}}}{c_{\text{s}}}, \tag{4.21}$$

and we usually have $\mathcal{M}_t \ll 1$ for stellar convective region. It appears that this result quantitatively differs from Stein (1967). This can be explained by different assumptions in the model used. In Stein (1967), the authors considered an isothermal atmosphere, whereas in

Goldreich and Kumar (1990) they considered a two-layer atmosphere, the upper one also isothermal, but the lower one adiabatic with the turbulent convection confined in it. They also explained that the excitation mainly occurs in the upper part of the convection zone, where the turbulent Mach number $\mathcal{M}_t$ is maximal. Here, it is worth mentioning a remark from Lecoanet and Quataert (2013): it looks like there are some ambiguities in the derivation of the wave amplitude equation of Goldreich and Kumar (1990). The latter seem to assume that the pressure perturbation terms, p_1 are orthogonal under the weighting function $1/c_\mathrm{s}^2$ and they used the normalization $\int \mathrm{d}z\rho c_\mathrm{s}^{-2}|p_1|^2 \sim 1$. These two assumptions are true for acoustic waves, but not for gravity waves. For internal gravity waves, the pressure perturbations are orthogonal under the weighting function 1 and $\int \mathrm{d}z\rho c_\mathrm{s}^{-2}|p_1|^2 \sim \mathcal{M}_t$.

Based on the work for the p modes excitation by Reynold's stress from Goldreich et al. (1994), Kumar et al. (1999) derive an expression for the wave flux per unit frequency in waves just below the convective envelope of the Sun which is

$$F_\mathrm{wave} = \frac{\omega^2}{4\pi}\int \mathrm{d}r \frac{\rho^2}{r}\left[\left(\frac{\partial \xi_r}{\partial r}\right)^2 + \ell(\ell+1)\left(\frac{\partial \xi_\mathrm{h}}{\partial r}\right)^2\right]\exp\left[-\frac{h_\omega^2 \ell(\ell+1)}{2r^2}\right]\frac{\mathrm{v}^3 L^4}{1+(\omega\tau_L)^{15/2}}, \tag{4.22}$$

where L is the radial size of an energy bearing turbulent eddy, $\tau_L \simeq L/\mathrm{v}$ is the characteristic convective time, and h_ω is the size of the largest convective eddy of frequency ω at the radius r. Once integrated over frequency and horizontal wavenumber they obtain the same expression for the gravity waves flux as Goldreich and Kumar (1990) (see Eq. (4.20)). However, they seem to use different assumptions than Goldreich et al. (1994) to model the correlation function of convective eddies and waves, but they do not say it explicitly. In Kumar et al. (1999), it is the Gaussian function in Eq. (4.22) that models the spatial correlation of waves and convective eddies. In Goldreich et al. (1994), this correlation is modelled by a parameter of order unity that describes the ratio of the horizontal to vertical correlation lengths of turbulent eddies. Concerning the time correlation, Goldreich et al. (1994) interpolate between the contributions of eddies with different sizes using the function

$$\chi_k(\omega) = \frac{1+(\omega H/\mathrm{v}_\mathrm{conv})^p}{1+(\omega H/\mathrm{v}_\mathrm{conv})^{15/2+p}}, \tag{4.23}$$

with p a free parameter. Goldreich et al. (1994) set its value to 10 to get a good agreement with observations whereas Kumar et al. (1999) fix it to 0, but the reason for this is not clear.

This method of solving an inhomogeneous wave equation was extended in a more complete way by Belkacem et al. (2009) for IGWs. It is based on a work on p modes excitation by Samadi and Goupil (2001) which generalised the contribution from Reynolds stress and entropy fluctuations for any kind of energy spectrum, and not only the Kolmogorov one as assumed in

previous works. In particular, it allows using an energy spectrum generated with hydrodynamic simulations. The other main focus of that paper is to consider two different contributions in the entropy fluctuations. The first one is the Lagrangian entropy fluctuations, and the second is the one due to the advection of entropy by the turbulent velocity field. In the case of IGWs, Belkacem et al. (2009) show that the entropy source term may be neglected as it is small compared to the Reynolds stress one, whereas it is the opposite for acoustic modes (Goldreich et al., 1994). The final expression for the excitation rate P of g modes, as derived by Belkacem et al. (2009), is

$$P = \frac{\pi^3}{2I} \int_0^M dm \rho_0 R(r) \int_0^{+\infty} dk \mathcal{S}_k, \tag{4.24}$$

with

$$\mathcal{S}_k = \frac{1}{k^2} \int_{-\infty}^{+\infty} d\omega E^2(k) \chi_k(\omega + \omega_0) \chi_k(\omega), \tag{4.25}$$

where m is the local mass of fluid, $E(k)$ the spatial kinetic energy spectrum, $\chi_k(\omega)$ the eddy-time correlation function. $R(r)$ depends on the eigenfunction and is not given for simplicity. However, the main benefit of Eq. (4.24) is that it remains very general. With some well-chosen assumptions, it is possible to retrieve an equivalent formulation of previous works for the excitation rate. This also implies that it is possible to use any energy spectrum $E(k)$ and time correlation function $\chi_k(\omega)$ as input. Belkacem et al. (2009) suggest that it is better to use a Lorentzian function for $\chi_k(\omega)$ instead of the Gaussian function usually considered.

All the studies presented above did not consider different possibilities for the shape of the temperature gradient at the convective-radiative interface. This problem was addressed for the first time by Lecoanet and Quataert (2013) as they focused particularly on this transition region. The authors derived an expression for the IGW flux spectrum using a different approach to solve the inhomogeneous wave equation. Instead of the mode projection formalism commonly used, they solved their equation using a Green's function approach. The source term they consider is the Reynold's stress that they split into three components: a convection-convection interaction term, as well as wave-convection and wave-wave interaction terms. They assume that the convection-convection term, $\nabla \cdot (\mathrm{v_{conv}} \mathrm{v_{conv}})$, is dominant compared to the other two. They characterise the transition region between the convective and radiative zones by its width d and the vertical (or radial) profile of the buoyancy frequency N^2, or equivalently of the temperature gradient, in this region. If d is small, the waves see a discontinuous transition. In this case, Lecoanet and Quataert (2013) predict for the wave flux

$$\frac{\mathrm{d}F^{\mathrm{D}}_{\mathrm{wave}}}{\mathrm{d}\ln\omega \mathrm{d}\ln k_{\mathrm{h}}} \propto \rho \mathrm{v}^3_{\mathrm{conv}} \mathcal{M}_t (H k_{\mathrm{h}})^4 \left(\frac{\omega}{\omega_{\mathrm{conv}}} \right)^{-13/2}, \tag{4.26}$$

with H the size of the largest convective eddies. If d is large, the waves see a smooth convective-radiative transition and their flux depends on the profile of N^2 in the transition region. Lecoanet and Quataert (2013) consider two smooth cases: first, an abrupt but continuous transition described by a piecewise linear profile for N^2, which yields the scaling relation

$$\frac{\mathrm{d}F^{\mathrm{L}}_{\mathrm{wave}}}{\mathrm{d}\ln\omega\mathrm{d}\ln k_{\mathrm{h}}} \sim \rho \mathrm{v}^3_{\mathrm{conv}} (Hk_{\mathrm{h}})^4 \left(\frac{\omega}{\omega_{\mathrm{conv}}}\right)^{-41/6} (k_{\mathrm{h}}d)^{1/3}. \tag{4.27}$$

They also consider a smoother transition given by a tanh profile for N^2, which yields

$$\frac{\mathrm{d}F^{\mathrm{T}}_{\mathrm{wave}}}{\mathrm{d}\ln\omega\mathrm{d}\ln k_{\mathrm{h}}} \sim \rho \mathrm{v}^3_{\mathrm{conv}} \left(H_p k_{\mathrm{h}}\right)^4 \left(\frac{\omega}{\omega_{\mathrm{conv}}}\right)^{-15/2} (k_{\mathrm{h}}d). \tag{4.28}$$

In these three cases the IGWs spectrum is predicted to follow a power law whose steepness vary with the shape of the temperature gradient at the interface. Once integrated over frequency and horizontal wavenumber, the spectrum in the discontinuous case predicts a wave flux equivalent to Eq. (4.20) from Goldreich and Kumar (1990) but they are different for the two smooth cases. In the linear case it is

$$F^{\mathrm{L}}_{\mathrm{wave}} \sim \rho \mathrm{v}^3_{\mathrm{conv}} \mathcal{M}_t^{2/3} \left(\frac{d}{H_p}\right)^{1/3}, \tag{4.29}$$

and in the tanh profile, it is

$$F^{\mathrm{T}}_{\mathrm{wave}} \sim \rho \mathrm{v}^3_{\mathrm{conv}} \left(\frac{d}{H_p}\right). \tag{4.30}$$

Finally, this model predicts that the wave flux increase as the transition gets smoother. They conclude that the real interface in the Sun should be intermediate between the smooth ones considered, and thus predict a larger wave flux than previous estimations. This work implies that waves of different frequency, i.e. with more or less large wavelength, will not see the transition with the same steepness. Consequently, the IGWs spectrum in radiative zones of stars does not only depend on the source but also on that transition region. To take into account both these effects, we will compare the results of our hydrodynamical simulations with the three cases of Lecoanet and Quataert (2013).

Other methods

Press (1981) developed an alternative method to determine the wave flux generated by convective eddies. This model is based on the assumption of continuity of pressure perturbations at the interface between the radiative and convective zones. In the case of an incompressible medium, which is valid for low frequency IGWs, i.e. $\omega \ll N$, it is possible to assume for an

IGW that $\mathrm{v_h} \gg \mathrm{v}_r$. Then using the dispersion relation for IGWs, Press (1981) assume that

$$\mathrm{v_h} \simeq \frac{N}{\omega}\mathrm{v}_r. \tag{4.31}$$

Assuming an equipartition of the energy of an IGW between its kinetic E_k and potential E_p components, they estimate the total energy density $\mathcal{E}$ of an internal waves with

$$\mathcal{E} = \rho\left(\frac{N}{\omega}\right)^2 \mathrm{v}_r^2. \tag{4.32}$$

Multiplying this expression by the group velocity given by Eq. (4.6), they obtain an expression for the radial energy flux of a single wave (ω, ℓ)

$$F_{\mathrm{wave}} = \frac{\rho(N^2-\omega^2)^{-1/2}}{k_{\mathrm{h}}}\mathrm{v}_r^2. \tag{4.33}$$

In this model, Press (1981) consider that waves are excited by eddies with only one frequency ω_{conv} and horizontal wavenumber $k_{\mathrm{h,conv}}$. Then, by matching the pressure perturbation on both sides of the convective interface, they obtain

$$\mathrm{v}_r \sim \frac{\omega}{k_r}. \tag{4.34}$$

The velocity associated with convective eddies is $\mathrm{v_{conv}} = \omega_{\mathrm{conv}}/k_{\mathrm{h,conv}}$. Then the wave flux becomes

$$F_{\mathrm{wave}} \sim \rho \mathrm{v}_{\mathrm{conv}}^3 \frac{\omega}{(N^2-\omega^2)^{1/2}} \tag{4.35}$$

A decade later, Garcia Lopez and Spruit (1991) used a similar method but instead of assuming the continuity of turbulent pressure at the interface, they consider that the turbulent pressure fluctuations linked to convective eddies matches the waves density energy at the interface between the convective and radiative regions. Another difference with Press (1981) is that they consider convective eddies of different sizes for which the associated velocities $\mathrm{v_{eddies}}$ are related with a Kolmogorov type law,

$$\mathrm{v_{eddies}}(\lambda) = \mathrm{v_{conv}}\left(\frac{\lambda}{H}\right)^{1/3} \tag{4.36}$$

with λ the size of an eddy and H the size of the energy bearing eddies. The authors also consider the decay of the flux amplitude resulting from the damping of waves by radiative diffusion as

they propagate. Their expression for the wave flux is written

$$F_{\text{wave}} = \frac{\rho}{2\pi} \frac{(N^2-\omega^2)^{1/2}}{N^2} \frac{\mathrm{v}^2\omega^2}{k_{\text{h}}} \exp\left[-\frac{r-r_{\text{e}}}{L_d(\omega,k_{\text{h}})}\right] \tag{4.37}$$

with r_{e} the radius at which waves are excited and $L_d(\omega,k_{\text{h}})$ is the damping length of a wave characterised by (ω, ℓ). It is defined as

$$L_d(\omega,k_{\text{h}}) = \frac{u_{\text{g},r}}{k_r^2 \kappa_{\text{rad}}} \tag{4.38}$$

with $u_{\text{g},r}$ the radial component of the group velocity defined in Eq. (4.6).

4.3.2 Excitation by penetrative convection

Wave generation by convective plumes that penetrate into the radiative region has received less attention for the moment. Nevertheless, this excitation mechanism is more studied in atmospheric sciences (see for example Townsend, 1966) and had already been observed in simulations (see for example Dintrans et al., 2005). A first model was derived by Montalbán and Schatzman (2000), based on the turbulent plume model of Rieutord and Zahn (1995). For this model, Montalbán and Schatzman (2000) consider that the plumes penetrating in the radiative zone create a turbulent shear flow just below the convective boundary. They derive an expression for the velocity field in that layer based on the turbulent plume model of Rieutord and Zahn (1995). The IGWs spectrum they obtain present a Gaussian dependence in frequency and horizontal wavenumber

$$F_{\text{wave}} \propto \exp\left(-\ell^2 b^2 - \omega^2 \tau_p^2\right) \tag{4.39}$$

with b the width of a plume and τ_p the timescale associated with a plume in the penetration region.

This model was then revisited by Pinçon et al. (2016), who consider plumes as having their own identity in time and space and that they are independent of one another. They derive the velocity field associated with one plume and first consider the excitation of waves by a single plume. Once again, their method is based on solving an inhomogeneous wave equation like Eq. (4.18) where the source term takes a form similar to a Reynold's stress term

$$\mathcal{S} = \nabla \cdot \left(\mathbf{V_p} \otimes \mathbf{V_p}\right), \tag{4.40}$$

where $\mathbf{V_p}(\mathbf{r})$ is the velocity associated with a convective plume. Assuming that a plume is localised in space and time, they use the velocity field proposed by Townsend (1966) for a

single plume

$$\mathbf{V_p}(\mathbf{r}) = V_0(r)\exp\left(-\frac{S_h^2}{2b^2}\right)\exp\left(-\frac{t^2}{\tau_p^2}\right)\mathbf{e}_r, \tag{4.41}$$

with $\mathbf{e}_r$ the unit radial vector and S_h the distance on the sphere from the centre of the plume.The characteristic radius b and radial velocity field in the penetration zone $V_0(r)$ are derived from the Rieutord and Zahn (1995) model of turbulent plumes. The expression for the radius is

$$b = \frac{z_0}{\sqrt{2}}\frac{3\alpha_E(\Gamma_1 - 1)}{2\Gamma_1 - 1}, \tag{4.42}$$

with z_0 the thickness of the convective zone and $\alpha_E = 0.083$ an entrainment coefficient whose value is taken from Turner (1986). From Zahn (1991), the vertical plume velocity is

$$V_0(r) = V_b\left[1 - \left(\frac{z}{L_p}\right)^2\right]^{1/3} \tag{4.43}$$

where $z = r_{\rm conv} - r$ with $r_{\rm conv}$ the radius of convective boundary defined by the Schwarzschild's criterion (see Eq. (2.13)) and V_b the initial vertical velocity field of the plume in the penetration region defined as

$$V_b = \left(\frac{2L_{\rm star}}{\pi\rho_{\rm conv}r_{\rm conv}^2}\right)^{1/3}, \tag{4.44}$$

with $\rho_{\rm conv}$ the mean density at the base of the convective zone. In Eq. (4.43), the parameter L_p is the penetration length or overshooting distance. In their model, Pinçon et al. (2016) consider it as a free parameter, because its value is not well-defined. Indeed, theoretical estimation (Zahn, 1991) and observations (Basu, 1997; Christensen-Dalsgaard et al., 2011) do not agree on its value. However, they show that wave excitation is more efficient for smaller L_p.

Finally, considering a total of $\mathcal{N}$ independent plumes, the expression for the wave energy flux per unit frequency is

$$F_{\rm wave}(r,\omega,\ell,m) \sim \frac{1}{4\pi r^2}\frac{\mathcal{N}S_p}{2}\frac{\rho_{\rm conv}V_b^3}{2}F_{R,\ell}\frac{\mathrm{e}^{-\omega^2/4\nu_{\rm p}^2}}{\nu_p}\mathrm{e}^{-\mathrm{k}_{\rm h,conv}^2\mathrm{b}^2/2}, \tag{4.45}$$

where $S_p = \pi b^2$ is the area occupied by a single plume, $k_{\rm h,conv} = \sqrt{\ell(\ell+1)}/r_b^2$ is the horizontal wavenumber at the convective boundary and $\nu_p = 1/\tau_p$ is the frequency associated with a plume lifetime. The Froude number at the base of the convective zone $F_{R,\ell}$ is defined as

$$F_{R,\ell} = \frac{V_b k_{\rm h,conv}}{N_0}, \tag{4.46}$$

where N_0 is the value of the Brunt-Väisälä frequency at the bottom of the transition region, in the sense of Zahn (1991), i.e. the region just below the penetration zone where thermal diffusion dominates advection.

In their study, Pinçon et al. (2016) compare their prediction for the wave flux, Eq. (4.45) to the model of Kumar et al. (1999), Eq. (4.22). Figure 4.2 shows this comparison. It appears that the two mechanisms present a similar efficiency at exciting IGWs in terms of amplitude of the wave flux. However, the plumes' excitation seems to be more efficient at low frequency between 1 and 5.5 $\times 10^{-6}$rad s^{-1}, whereas the excitation by convective eddies takes over at higher frequencies $\omega > 5.5 \times 10^{-6}$rad s^{-1}. At very low frequencies, $\omega < 10^{-6}$rad s^{-1} $\sim 0.16\mu$Hz,

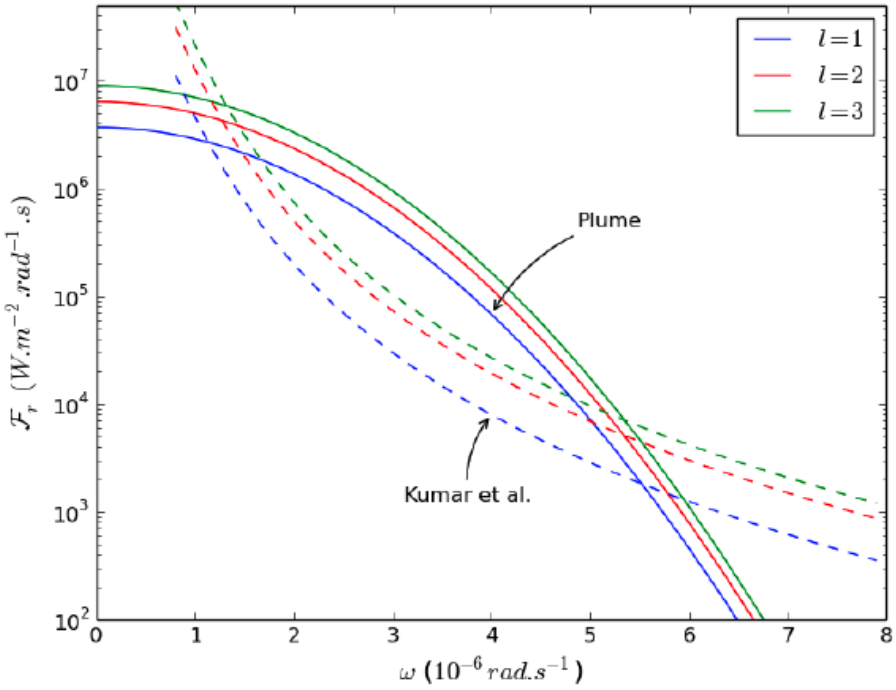

Fig. 4.2 Mean radial wave energy flux per unit of frequency at the top of the radiative zone as a function of the radian frequency, for any azimuthal number m and angular degrees $\ell = 1$; 2 and 3, in the case of the plume-induced waves (solid lines) and the one of turbulence-induced waves from the formalism of Kumar et al. (1999) (dashed lines). Credits: Pinçon et al. (2016)

.

it is unclear which process dominates, but in this thesis we will not study such low frequency waves as it would require very high resolution simulation (see Sect. 6.7 for more details on the problem of spatial resolution of IGWs). We will use these different models to compare their predictions to results from hydrodynamical simulations (see Chapt. 6 and 7).

Chapter 5

Numerical modelling of stellar interiors

Observations of global modes of oscillations of stars allow us to probe their internal structure, but also to get information about their mass, radius and age.In order to interpret correctly and accurately these observations, we need to have a correct and precise description of the properties of these modes and associated waves. Thanks to these observations, it is possible to confirm or refute theoretical predictions concerning the internal structure and dynamics of stars. However, a lot of phenomena occurring in stellar interiors are inherently three-dimensional, non-linear and anisotropic, making them very difficult to model analytically. It is thus necessary to use assumptions to develop theoretical models, which will then described physical phenomena in a simplified way. Hydrodynamical simulations thus offer a great intermediate solution between the unknown physics occurring in actual stars and the simplified description of theoretical models. In the last decades, multidimensional simulations have proven to be very efficient to test theoretical models and guide observations. However, as it will be explained in Chapt. 7, direct comparison between multidimensional simulations and observations is not straightforward. To ease this comparison, we can adapt results from two- and three-dimensional simulations into one-dimensional parametrisation to implement them into evolutionary one-dimensional models.

5.1 One-dimensional model

One dimensional modelling is the most common way of studying numerically stellar internal structure and evolution. Its strength lies in the fact that it can model a star through almost its entire evolution. This type of numerical modelling is not only used in the stellar physics community, but also for the study of galaxies evolution or exoplanets atmospheres, for instance.

To model a star on evolutionary time scales, one dimensional models solve the equations of stellar structure given in Sect. 2.2.1. The first stellar evolution codes were developed in the

1960s (e.g. Kippenhahn et al., 1967). Today the method remains broadly the same, but it has greatly benefitted from an increased precision in computation of opacities and equations of state tables as well as nuclear reaction rates. In addition, parametrisation describing dynamical processes linked to rotation, magnetism and some mixing processes have been clearly improved. As a result, one-dimensional modelling combined with observations of high precision has allowed to build realistic models of the Sun, known as standard or seismic models depending on the type of observations used as described in Sect. 3.1 (see also Christensen-Dalsgaard, 2021, for a recent review on solar modelling.). Figure 5.1 shows the relative difference in squared sound speed c_s^2 (left panel) and density ρ (right panel) between model S and observations. The Standard Solar Model known as model S is described in Christensen-Dalsgaard et al. (1996) and is considered as a reference solar model. The relative differences are tiny, less than 0.5% for the squared sound speed and less than 2% for the density. This highlights the success of one-dimensional modelling, but also the quality of the observation we can get for the Sun.

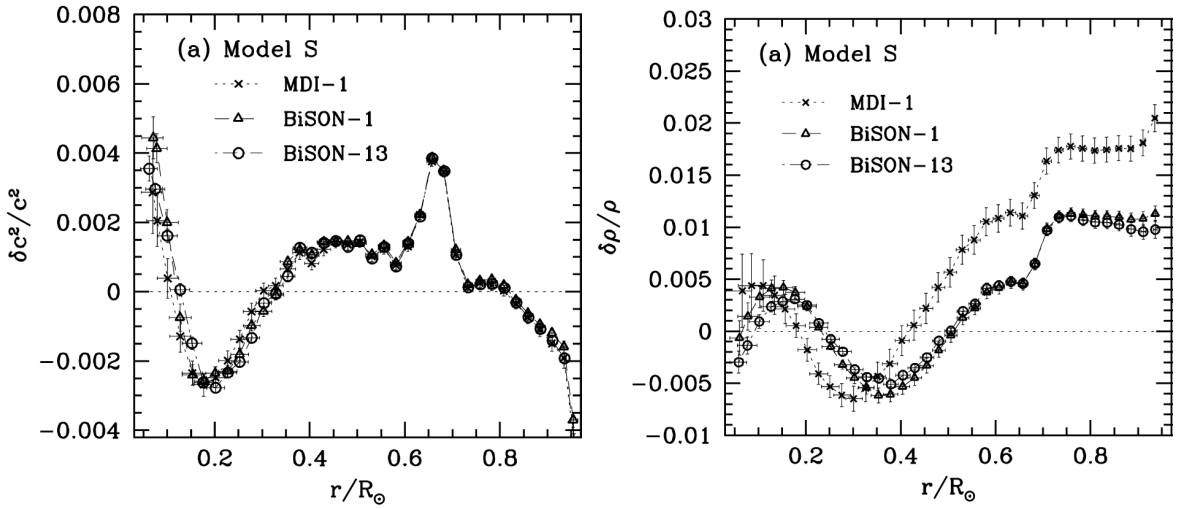

Fig. 5.1 Relative difference in sound speed (left panel) and density (right panel) between observational data of the Sun and Model S. Figure adapted from Basu et al. (2009).

However, Fig. 5.1 also reflects the limitations of one-dimensional modelling. Indeed, one-dimensional models can not give any insight on the physical phenomena responsible for the remaining discrepancies. The main reason for that is because this type of modelling require assumptions that limit the complexity of the physics that could be involved. Particularly, one-dimensional models are assumed quasi-static and dot no consider dynamical processes. For instance, convection is modelled with the Mixing Length Theory, which only consider eddies of one size and do not take into account convective penetration. Stars are assumed spherically symmetric, which do not allow modelling fast rotators. The impact of waves, rotation and magnetic fields on the stellar structure is only parametrised, forcing users to

make crude approximations and to use free parameters. For instance, the transport of angular momentum and the chemical mixing induced by IGWs is described using the JWKB method introduced in Sect. 3.4 (see for example Talon and Charbonnel, 2005), which we know to present limitations. In order to study and explain these discrepancies, it is necessary to develop a new theory or to improve an existing one. A complementary method is to use multidimensional (magneto-)hydrodynamical ((M)HD) modelling. We will present it in the next sections.

5.2 Multidimensional simulations and their challenges

5.2.1 Hydrodynamical simulations

Numerical simulations in two and three dimensions are used to solve the equations of (M)HD. This makes it possible to study and analyse non-linear dynamical processes in a wide range of astrophysical contexts. Indeed, these simulations are run to model stellar interiors and atmospheres but also accretion disks, galaxy formations or (exo-)planetary atmospheres for instance. The main differences between these applications are the temporal and spatial scales characterising the modelled system, as well as the physical characteristics of the flows involved.

In the context of this thesis, we are only interested in hydrodynamical processes, so magnetic field is neglected. Thus, the equations we would like to solve are the ones given by Eq. (3.9) - (3.11). Unfortunately, there are no known general analytical solutions to these non-linear equations, and we don't even know if such a solution exists. This is why numerical simulations are valuable tools, they can give approximate solutions to the equations of hydrodynamics. A method to do this numerically consists in spatially discretizing the equations on a grid and to evolve an initial solution over a given time in discrete time steps.

However, it is not that simple, solving numerically these equations is computationally very expensive. A certain number of approximations are needed in order to run simulations and get the results in a reasonable amount of time. The nature and number of these approximations depends on the problem studied. First, it is possible to make assumptions about the spatial scales that will be resolved. This is the distinction between Direct Numerical Simulations (DNS) and Large Eddy Simulations (LES). In DNS, all scales of motions are resolved, from the largest structure, which is typically the size of the system, down to the dissipation scale l_D. This implies that the size of a unit grid cell should be at most half the dissipation scale. In stellar interiors, this dissipation scale is typically $l_D \sim 1$ cm in the convection zone (Canuto, 2009). Thus, running a DNS of the whole solar convective zone would require almost 10^{33} grid points (Kupka and Muthsam, 2017). This is far from possible with current computational resources.

The second approach, LES, aims to ignore the smallest scales, and can be viewed as a kind of averaging of the hydrodynamical equations over a certain volume. Typically, most of the inertial range associated with flow is resolved. This scale is much smaller than the largest structure, at least one order of magnitude smaller. The inertial range is typically the scale at which the non-linear advection dominates over everything. The LES approach allows modelling the properties of the equations of hydrodynamics on grids with moderate resolutions. This type of simulation needs a model for the small scales that are not resolved by the grid. The model can be explicit, by adding extra terms to the equations that are solved. Or it can be implicit, and the numerical viscosity has the role of representing the physical dissipation happening at scales smaller than the grid. In that case, there is no need to add any extra terms in the equations. The latter case is known as Implicit LES, or ILES and is the kind of simulations we are using for the work presented in this thesis.

5.2.2 Spatial resolution

To have an idea of what can be achieved in terms of resolution with an LES, Kupka and Muthsam (2017) states that at that time the highest resolution LES has been run by Muthsam et al. (2011) and has a resolution of ~ 3 km. This is more than 5 orders of magnitude larger than the viscous dissipation scale l_D. Nevertheless, this is still well below the driving scale, which is typically the largest convective eddies in stars, generally assumed to be the size of the convective zone. For a given simulation, the required spatial resolution depends on the system studied. In the context of stellar hydrodynamical simulations, the wide range of length scales involved is a major challenge. Indeed, the largest length scale correspond to the size of the system, i.e. the radius of the star. The reference stellar radius is the one of the Sun. The value adopted by the International Astronomical Union is $R_\odot \simeq 6.957 \times 10^8$ m and has been measured by (Haberreiter et al., 2008). In theory, the smallest scales that should be resolved are the viscous dissipation scale and the photon mean-free-path, both of the order of the centimetre. There is more than 10 orders of magnitude difference between these largest and smallest scales. In addition, the characteristic length scale associated with a given thermodynamic quantity can vary by order of magnitudes depending on the location within a star where it is measured.

Figure 5.2 presents the radial profile of the density in model S (Christensen-Dalsgaard et al., 1996). The value of the density at the centre of the Sun is close to 10^2 g cm^{-3} and decrease to almost 10^{-6} g cm^{-3} at the solar surface. Consequently, in order to model the whole Sun, it would be necessary to consider variations in density of approximately 8 orders of magnitude. This drop in density is particularly important close to the surface of the Sun. This is one of the main reason why extension of the numerical domain to the photosphere is an open challenge for stellar hydrodynamical simulations.

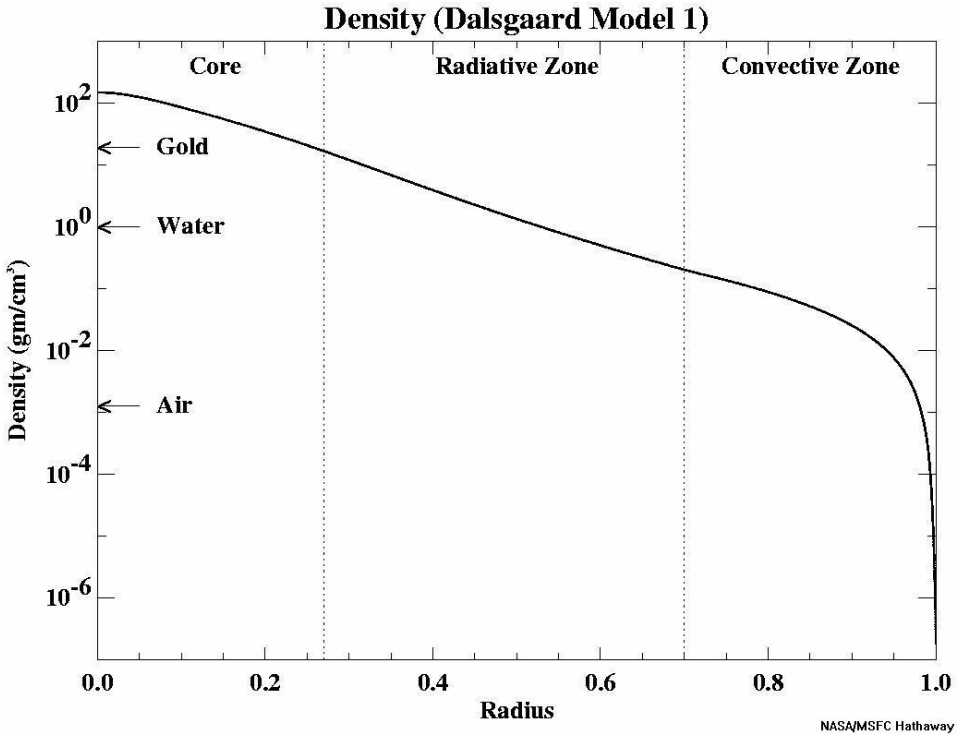

Fig. 5.2 Radial profile of the density for the reference solar Model S. Credits: solar-science.msfc.nasa.gov

.

5.2.3 The problem of timescales

Similar issues exist with the time scales involved. As described in Sect. 2.1, the lifetime of a star on the main sequence is set by the nuclear timescale $\tau_{\rm nuc}$, given by Eq. (2.7), for which a typical order of magnitude is 10^{10} years for low-mass stars. In the case of the Sun, other relevant time scales for multidimensional simulations are the thermal timescale set by the Kelvin-Helmholtz time $\tau_{\rm KH}$, see Eq. (2.6), which is about 10^7 years, the magnetic cycle period $\tau_{\rm cycle} \simeq 11$ years, the rotation period of about 1 month, the convective timescale $\tau_{\rm conv}$ which of the order of ten days or time scales associated with waves $\tau_{\rm waves}$ which range from five minutes to a few days. This is illustrated on Fig. 5.3. The difference between the longest, $\tau_{\rm nuc}$, and the shortest, $\tau_{\rm waves}$, is more than 15 orders of magnitude! It is clear that all of them can not be studied at the same time. Therefore, we distinguish two types of numerical models. On the one hand, evolutionary timescale, of the order of $\tau_{\rm nuc}$, are studied with one-dimensional modelling, which neglect all dynamical processes (see Sect. 5.1). On the other hand, all time scales of the order of a few years or shorter (in blue on Fig. 5.3), which are in principle related to dynamical processes, are studied with (magneto-)hydrodynamical simulations. In

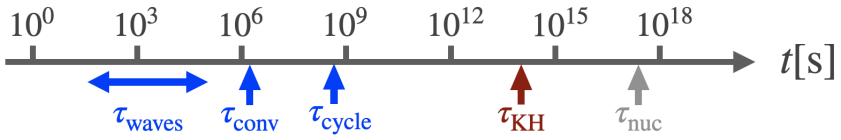

Fig. 5.3 Schematic visualisation of the timescales relevant to stellar interiors. Adapted from Käpylä et al. (2013).

.

this context, it is possible to consider that nuclear reactions are stationary and thus neglect the nuclear timescale (in grey on Fig. 5.3).

The thermal timescale τ_{KH}, in red in Fig. 5.3, deserves a special discussion. Although much larger than a year, it is relevant and even very important for multidimensional simulations. It is the time required for the system to reach a thermally relaxed state. Rigorously, all simulations should be run for at least a few thermal times before starting any analysis. In practice, this is far beyond reach. The time step Δt_{step} of a simulation is usually set by the Courant-Friedrichs-Lewy (CFL) limit (Courant et al., 1928). It defines an upper limit for the time step with the criterion

$$\Delta t_{\text{step}} = C \min(\Delta \mathbf{x}) / \max(|\mathbf{u}|), \tag{5.1}$$

with C a constant depending on the temporal and spatial discretisation scheme used (Kupka and Muthsam, 2017) and $\Delta \mathbf{x}$ the vector representing a unit grid cell. Thus, $\min \Delta \mathbf{x}$ is the minimal length associated with a grid cell in a given direction. At the denominator, the velocity $\mathbf{u}$ can be any velocity involved in the simulation, such as the velocity of the flows $\mathbf{v}$ or the sound speed c_s. The CFL criterion ensures that any perturbation in the simulation can not cross more than one cell in a one time step. To give an order of magnitude, the resulting typical time step in a simulation of stellar interiors is usually several seconds. It would thus require to run a simulation of the Sun for at least 10^{14} time steps to achieve thermal relaxation. The computational cost needed to evolve the model for that long is too expensive. This issue of thermal relaxation is actually an open problem for stellar hydrodynamical simulations (see Chapt. 6).

5.3 Modelling waves with multidimensional simulations

5.3.1 Time integration

As mentioned in the previous section, solving numerically the equations of hydrodynamics require discretising them, both spatially and temporally. Concerning the temporal discretisation, computing the solution from one time step to the next one require to integrate all the terms involved in the equations. The method to do that is called a time integration scheme. In this work, we consider low-Mach flows, i.e. velocity associated with fluid flows v are much smaller than the sound speed c_s. The Mach number Ma is defined as

$$\mathrm{Ma} = \frac{\mathrm{v}}{c_s} \tag{5.2}$$

with v a velocity associated with the flow, which in the convective zone we can assume to be $\mathrm{v} = \mathrm{v}_{\mathrm{conv}}$. Then in the convective zone we have $\mathrm{Ma} = \mathcal{M}_{\mathrm{t}}$, the turbulent Mach number defined by Eq. (4.21). Generally, in the simulations considered in this work, we have $\mathrm{Ma} \lesssim 10^{-3}$. For such flow, the efficiency of the time integration method is a challenge. In most of the existing codes, the equations of hydrodynamics are solved with an explicit time integration scheme. This means that the solver uses the information at the current and previous time steps to compute the value of a variable at the next time step. For instance, let's consider the equation

$$\frac{\partial u}{\partial t} = F(u), \tag{5.3}$$

with u any variable and F an arbitrary function of u. An explicit method will compute the value of u at the step $n+1$ with

$$u_{n+1} = u_n + \Delta t F(u_n) \tag{5.4}$$

with Δt the computational time step and u_i the value of u at step $i = n, n+1$. This kind of time integration offers the main advantage of being relatively simple to implement, but it adds a more severe constraint on the size of the time step (Glatzmaier, 2013). With explicit methods, all relevant velocities involved in the simulations have to be taken into account in the CFL limit, which is a condition for numerical stability (see Eq. 5.1). In the case of low-Mach flows, the largest velocity is the sound speed, therefore in Eq. (5.1) we have $\mathbf{u} = c_s$ This new limit really imposes a very short computational time step as in that case $c_s \gg \mathrm{v}$.

One possible solution to avoid this strong constraint is to use an implicit time integration scheme. For this method, the solver uses the information of current and next time steps to update the value of a variable. To make this possible, the idea is to define a function G that

depends on both the current and next values of the variable, such as

$$G(u_{n+1}, u_n) = \frac{u_{n+1} - u_n}{\Delta t} - F(u_{n+1}), \tag{5.5}$$

and then to solve

$$G(u_{n+1}, u_n) = 0. \tag{5.6}$$

These functions are generally complex to define and computationally expensive to solve. However, with this method, the numerical time step is not limited by numerical stability. It is limited by the relevant physical phenomena in the simulations. For convenience, it is usual to also use the CFL criterion, but the velocity at the denominator may be chosen by the user depending on the desired accuracy. For instance, in simulations of convection, we can use the CFL criterion for advection (see Eq. (5.1)), which is significantly larger than the one limited by the sound speed in the case of low-Mach flows. Using explicit or implicit method or the other depends on the problem studied. The hydrodynamical code used in this thesis is based on a time implicit method (see Sect. 6.2.1).

5.3.2 Waves in hydrodynamical simulations

In the context of stellar hydrodynamics, the two types of waves described in Chapt. 3, i.e. acoustic and internal gravity waves, can be modelled numerically. In order to accurately model a given wave, it is essential to use a numerical time step $\Delta t_{\rm step}$ much smaller than the period T of this wave, i.e. $\Delta t_{\rm step} \ll T$. Acoustic waves are high frequency waves and thus require a very short computational time step. Another issue related to the high frequency of acoustic waves is the precision of the time integration, which arise in both explicit and implicit time integration. This is different from the CFL limit, as it does not depend on the spatial grid. When temporally resolving a wave with a period comparable to the time step, this will lead to integration errors when solving the non-linear terms of the equations. With an explicit scheme the errors will grow exponentially and with an implicit one the wave will be numerically damped out.

Internal gravity waves have received much more attention from the stellar hydrodynamical community. The main reason for that is because the computational cost to model IGWs is less than for acoustic waves. Indeed, to study IGWs it is possible to use the anelastic approximation, which only allows subsonic flows. In order for anelastic approximation to be valid, perturbations in density and temperature need to be small (Gough, 1969). This allows to rewrite the equations of hydrodynamics in such a way that there is no acoustic wave solution (see Rieutord, 2015, for more details on this approximation) The anelastic approximation is less restrictive than the

Boussinesq one mentioned in Sect. 4.2, which is only valid for shallow motions. Then, it allows including IGWs while filtering out the acoustic waves. One advantage from this approximation is that it allows to use the CFL limit for advection given by Eq. (5.1). It is then computationally less expensive to study phenomena over longer timescale.

The first observation of IGWs in hydrodynamical simulations goes back to Hurlburt et al. (1986). Their two-dimensional simulations were run to study convective penetration, so they do not analyse waves properties in many details. They at least confirm with a numerical experiment that convection excites a broad spectrum of IGWs in stellar interiors. Shortly thereafter, studies focusing specifically on the analysis of IGWs were published by Andersen (1994). Using simulations with a cartesian geometry in two dimensions, they measure a spectrum for IGWs excited by convection. Two years later, Andersen (1996) use similar simulations to estimate the amplitude of g modes at the solar surface. In the early 2000s, Kiraga et al. (2003, 2005) compare the wave energy flux measured in two and three dimensions. They conclude that two-dimensional simulations overestimate the wave energy flux compared to analytical predictions. In a series of papers, Rogers and Glatzmaier (2005a,b, 2006); Rogers et al. (2006) present simulations of an equatorial slice of the Sun with a more realistic stratification of the radiative region which allows studying the interactions of waves with their environment, particularly the transport of angular momentum through radiative damping. The degree of realism has been further increased in the three-dimensional spherical simulations of Alvan et al. (2014, 2015). In Alvan et al. (2014), the authors study the amplitude of waves in their model and found a relatively good agreement with theoretical predictions. They emphasise the relevance of using simulations as complement to observations. Alvan et al. (2015) isolate and study individual waves to highlight the importance of running three-dimensional simulations to study IGWs. All these studies presented above were focusing on solar model with the hope to get new insights in the quest of solar g modes. However, there is still no confirmed detection yet (Belkacem et al., 2022).

Stars more massive than approximately $2M_\odot$ possess a convective core and a radiative envelope. Internal gravity waves are thus excited near the centre of the star and propagate toward the surface. In principle, this should offer a better opportunity to observe IGWs and then get constraints on the internal structure and dynamics of these stars, which are not very well known. Interestingly, in these stars internal gravity waves propagate towards the surface through a medium of decreasing density, which tend to increase their amplitude. These waves are also damped by radiative diffusion as they travel, and are suggested to transport energy and angular momentum and mix chemical elements through this mechanism (Schatzman, 1993). Thus, the evolution of IGWs amplitude will depend on the interplay between growth due to

decreasing density and decay due to radiative damping. It remains unclear if these waves should be able to propagate up to the surface.

Ten years ago, Rogers et al. (2013) started to run simulations of these more massive stars with the aim of focusing on IGWs. In their work, the authors focus on the relation between rotation and IGWs using two-dimensional simulations of an equatorial slice of $3M_\odot$ star model. They show that such waves are efficient at transporting angular momentum over large distance on relatively short timescales. A few years later, Rogers and McElwaine (2017) use Lagrangian particle tracers in similar simulations to study the transport of chemical elements by IGWs. They show that in their simulations such mixing can be treated as a diffusive process, as was already suggested in the literature (see for example Montalbán and Schatzman, 2000). The generation and propagation of IGWs in radiative envelopes are studied in three-dimensional simulations by Edelmann et al. (2019). As already suggested by Rogers et al. (2013), they describe the spectrum of IGWs as a double power law, relatively flat at low frequencies and steeper at larger ones. They conclude that their IGWs spectrum is significantly flatter than the analytical predictions of Lecoanet and Quataert (2013), and could be compatible with the plumes' excitation model of Pinçon et al. (2016). The authors also suggest that IGWs could be able to propagate up to the surface of the star and thus be observed by photometry.

Most of the studies presented above ran simulations with anelastic codes. Recently, Horst et al. (2020) presented a fully compressible two-dimensional simulation of a $3M_\odot$ star model, which makes it possible to observe acoustic waves. They show that a time-implicit fully compressible set up allows to model IGWs of much lower frequencies than it is possible with time-explicit anelastic simulations. The IGWs spectra they observe is relatively flat, like the one described by Edelmann et al. (2019).

All the simulations presented until here are global stellar simulations, i.e. a large portion of a star is modelled. However, it is also possible to run simulations with different set-up to study IGWs. Indeed, as mentioned in Chapt. 4, these waves may be present in all stratified medium. Recently, Couston et al. (2018) and Lecoanet et al. (2021) run simulations in cartesian geometry to study IGWs generation by turbulent convection from a general fluid dynamics perspective, not only in stellar interiors. In Couston et al. (2018), they are modelling this phenomenon using a three-dimensional cartesian DNS. In these simulations, the convective layer is beneath the radiative zone. On top of this radiative zone is added an absorption layer that damp IGWs to avoid reflection. Therefore, they do not observe g modes. The authors distinguish two energy quantities. There is the kinetic energy per unit surface area and unit (thermal) time K defined as

$$K(z) = \int \frac{|\mathbf{v}|}{2} \frac{\mathrm{d}x\mathrm{d}y\mathrm{d}t}{L^2 T_s} \tag{5.7}$$

where L is the size of the box in the x and y directions and T_s is the period over which results are integrated in time. This quantity is used to characterize the convection zone. Then there is the z-dependent vertical energy flux F expressed as

$$F(z) = \int \mathrm{v}_r p \frac{\mathrm{d}x\mathrm{d}y\mathrm{d}t}{L^2 T_s} \tag{5.8}$$

This expression is usually called the acoustic flux and is often used to quantify the energy flux associated with IGWs in fluid dynamics (Lighthill, 1978). When measuring the vertical energy flux F in their simulations, they obtain a similar dependence on frequency and wavenumber than the wave flux given by Eq. (4.26) from Lecoanet and Quataert (2013). Because of the presence of overshooting plumes near the convective boundary, they measure the wave flux in their DNS results away from the interface and then interpolate it to have an expression of the spectrum at the boundary. The wave flux then reads

$$\frac{dF}{d\log\omega\, d\log k_h} \sim F_c \mathcal{M}_t (k_\mathrm{h} H)^4 \left(\frac{\omega}{\omega_c}\right)^{-13/2} \mathrm{e}^{-2\gamma(\mathrm{z}-\mathrm{z_i})}\,, \tag{5.9}$$

where z_i is the vertical coordinate of the interface and $\gamma = k_h^3 N^3 \omega^{-4}$ is a damping coefficient that could result either from viscous or radiative effects, as the Prandtl number is set to 1 in these simulations. We can notice that the two expressions (4.26) and (5.9) are equal at the interface. Lecoanet et al. (2021) run simulations with the same configurations but in two dimensions and obtain similar results. They particularly insist on the point that it is surprising to find such a good agreement in two dimensions. Indeed, the theory from Lecoanet and Quataert (2013) is not supposed to be applicable for their two-dimensional simulations. They suggest there may be an alternative explanation for this, but do not investigate further.

Chapter 6

Artificial luminosity enhancement in hydrodynamical simulations of a solar-like model

Thermal relaxation of simulations is one of the greatest open challenge in multidimensional hydrodynamical modelling. The reasons for this were outlined in Sect. 5.2. The main physical reason is that stars are very massive systems and consequently their thermal relaxation time, given by Eq. (2.6) is extremely long compare to dynamical processes. It is thus computationally impossible to reach thermal relaxation for a global simulation of a star just by running it one time step after another. Several methods have been developed to face this problem (see Anders et al., 2018, and reference there in) but all have their flaws. One tactic is to artificially increase the stellar luminosity by several orders of magnitude. The aim of the work presented in this chapter is to study the impact of such a technique on the internal structure and dynamics of a stellar model. To do this, we performed two-dimensional fully compressible time-implicit simulations of a solar-like model with different luminosities. We particularly focus on internal gravity waves.

6.1 Facing the problem of thermal relaxation with a boost

To overcome numerical difficulties inherent to stellar hydrodynamics, particularly thermal relaxation, an artificial increase in the stellar luminosity by several orders of magnitude is a commonly used tactic. The reason for this is that the Kelvin-Helmholtz timescale is inversely proportional to the luminosity of the star (see Eq. (2.6)). This technique, known as *boosting* a stellar model, is widely use in the community (see for examples Brun et al., 2011, 2017;

Cristini et al., 2017; Horst et al., 2020; Meakin and Arnett, 2007; Rogers and Glatzmaier, 2005a, 2006; Rogers et al., 2013; Tian et al., 2009). The enhancement factors take values starting at 10 and going up to 10^7 for stars with a radiative zone (Edelmann et al., 2019) and even 10^9 for the less luminous stars which are fully convective (Käpylä, 2021). An important condition, when artificially increasing the luminosity of a simulation, is to also increase the thermal diffusivity by the same amount. This is in order to preserve the structure of the star. Indeed, the structure of the radiative zone depends on the temperature gradient, which can be written using Eq. (2.19)

$$\nabla T \propto -\frac{L_{\rm star}}{\chi} \tag{6.1}$$

with $L_{\rm star}$ the luminosity of the star which we can assume to be given by $L_{\rm star} = 4\pi r^2 F_{\rm rad}$ in the radiative zone.

Another reason sometimes mentioned to defend the usage of this method is related to numerical stability. The extra input of energy in the model makes it is possible to reach higher convective velocities and thus to increase the Mach number of the simulations. Indeed, running simulations with low Mach number is still a challenge for fully compressible set up (e.g. Miczek et al., 2015).

At first glance, this tactic may seem justified: enhancing the luminosity adds more energy to the simulation, and enhancing the thermal diffusivity increases the rate at which this energy is transported. However, to our knowledge, no studies have been carried out to ensure that this does not have an impact on the internal structure and dynamics of the stellar model. Recently, Käpylä (2019) showed that an artificial modification of the heat conductivity in the radiative and overshooting regions could impact the overshooting process. The question concerning the impact on the properties of IGWs was raised by Lecoanet et al. (2019), but they did not study it.

6.2 Numerical simulations

6.2.1 The MUSIC code

To run simulations, we use the Multidimensional Stellar Implicit Code (MUSIC). A detailed description of the code and of the time implicit integration method is available in Goffrey et al. (2017); Viallet et al. (2011, 2016). Here, we provide a brief description of its main characteristics. MUSIC solves the inviscid Euler equations in the presence of external gravity and thermal diffusion. In other words, it solves the continuity and momentum equations given by Eq. (3.9) and (3.10) respectively. Concerning the energy equations, MUSIC works with the internal energy e so it solves Eq. (3.6). For the stellar simulations considered in this work, the

major heat transport that contributes to thermal conductivity is radiative transfer characterised by the radiative flux $F_{\rm rad}$, given within the diffusion approximation by Eq. (2.19). MUSIC uses five variable that are the three components of the velocity field $\mathbf{v}$ (or two components in two dimensions), the density ρ and the internal energy e.

The opacities are interpolated from the OPAL tables (Iglesias and Rogers, 1996) for solar metallicity and the equation of state is based on the OPAL tables of (Rogers and Nayfonov, 2002), which are appropriate for the description of main-sequence stars interior structures.

MUSIC offers the possibility to run simulations in two and three dimensions, either in cartesian and spherical geometry. In order to provide the initial structures for the multidimensional simulations, MUSIC needs an initial radial profile of density and internal energy computed with a 1D evolutionary model. In this work, we use the 1D Lyon stellar evolution code (Baraffe et al., 1998; Baraffe and El Eid, 1991), using the same opacities and equation of state as MUSIC. Different boundary conditions can be defined, but we will use the following unless otherwise stated. The radial boundary conditions for the density correspond to a constant radial derivative of the density (Pratt et al., 2016). The energy flux at the inner and outer radial boundaries are set to the value of the energy flux at that radius in the 1D stellar evolution model. At the boundaries in θ, because of the extension of the angular domain to the poles, reflective boundary conditions for the density and the energy are used (i.e. the values are mirrored at the boundary). For the velocity, we impose reflective conditions at the radial and polar boundaries, corresponding to

- $\mathrm{v}_r = 0$ and $\frac{\partial \mathrm{v}_\theta}{\partial r} = 0$ at $r_{\rm in}$ and $r_{\rm out}$,
- $\frac{\partial \mathrm{v}_r}{\partial \theta} = 0$ and $\mathrm{v}_\theta = 0$ at $\theta = 0$ and $\theta = \pi$.

6.2.2 Reference model

To initiate MUSIC simulations we use a radial profile structure close to the one of the Sun, that is a solar mass star on the main-sequence with a convective envelope covering $\sim 30\%$ of the stellar radius. The motivation is to use an initial structure as close as possible to a realistic stellar interior structure, as has been done in previous studies using MUSIC (see Pratt et al., 2017, 2016). However, care should be taken, as the aim is to build a model that can be boosted. Indeed, in the Sun the convection zone is not exactly adiabatic but slightly superadiabatic. The superadiabaticity is defined as ∇ - $\nabla_{\rm ad}$, the difference between the temperature gradient and the adiabatic gradient, which are defined in Eq. (2.13). In the bulk of the convective region the superadiabaticity is very small, typically smaller than 10^{-4} but at its outer edge the superadiabaticity can be larger than 10^{-2}. The outer structure is thus very sensitive to any change of the opacity (and thus of the thermal diffusivity) and of the luminosity, as such changes

will modify the superadiabaticity and thus the temperature stratification. Therefore, in order to avoid a readjustment of the model structure when starting a hydrodynamical simulation using MUSIC with enhanced luminosity and thermal diffusivity, the profile of the stellar structure model must be adiabatic. We have thus constructed an artificial solar-like model, with our stellar evolution code enforcing a very small superadiabaticity ($<10^{-8}$) throughout the convective zone. In this case, an increase in the luminosity and of the radiative diffusivity (or a decrease of the opacity by the same factor) has no impact on the model structure (in terms of density and temperature radial profiles). This yields a reference initial model slightly more compact and hotter than a Standard Solar Model calculated with the MLT using $\alpha_{\rm MLT} = 1.9$ (see Eq. 2.21), an initial helium abundance $Y = 0.28$ and metallicity $Z = 0.02$. Our adiabatic solar-like model thus have a radius $R_{\rm star} = 0.798 R_\odot$ and luminosity $L_{\rm star} = 1.074 L_\odot$. The model is build to ensure $M_{\rm star} = 1 M_\odot$. The left panel of Fig. 6.1 shows how these structural modifications impact the density and radiative diffusivity profiles in the adiabatic model. These two quantities are relevant for the study of IGWs as they drive the evolution of their amplitude (see Eq. 4.13). In addition to these changes, a shift of the Schwarzschild boundary towards smaller

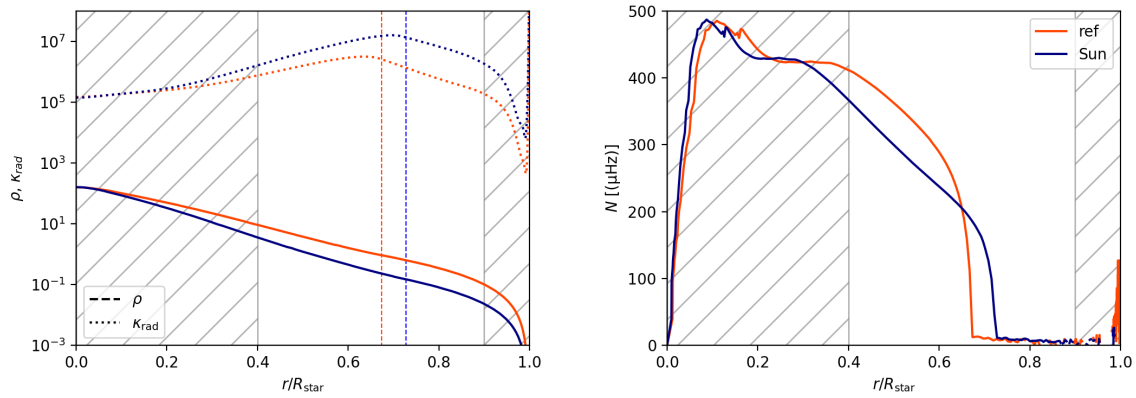

Fig. 6.1 Radial profiles of the density ρ [gcm^{-3}] and radiative diffusivity $\kappa_{\rm rad}$ [cm^{2}s^{-1}] (left panel) and of the Brunt-Väisälä frequency [μHz](right panel) for our solar model (blue) and adiabatic model (orange). Vertical dashed lines with the same colour code on the left panel indicates the interface between convective and radiative zones as defined by the Schwarzschild criterion. The hatched regions are not considered in the two-dimensional simulations.

radii happens in the adiabatic model. It is shifted from $r_{\rm conv} = 0.728 R_{\rm star}$ in the solar model to $r_{\rm conv} = 0.6734 R_{\rm star}$ in the adiabatic model. The criterion for convective stability is based on the temperature gradient (see Eq. 2.13) thus its modification near the interface probably result in this shift of the convective boundary. This is also the reason why the model is more compact and luminous. The shape of the profile away from the boundary is different in the two models, resulting in the modification of the region where a given monochromatic wave

can propagate. However, more importantly, the shape of N close to the boundary appears to be conserved. Indeed, the radial profile of N in this region plays an important role for the excitation of IGWs, as shown by the analytical work of Lecoanet and Quataert (2013) who found that the IGW flux at the interface can vary by orders of magnitude depending on the steepness of the Brunt-Väisälä profile at the boundary (see Sect. 4.3.1). This effect was also suggested by Rogers (2015) and confirmed by the numerical simulations of Couston et al. (2017) showing that increasing the stiffness of the interface (i.e. stronger stratification) decreases the IGW flux.

Using this adiabatic model, we can set up MUSIC simulations. Our reference simulations for this study, named model *ref*, is a two-dimensional simulation of this adiabatic solar-like model in a spherical shell using spherical coordinates, namely the radius r and the colatitude θ, and assuming azimuthal symmetry in the ϕ-direction. In multidimensional simulations of stellar interiors, it is usual to refer to a direction perpendicular to the radial one as the horizontal direction. In the following, we identify the horizontal direction as corresponding to the co-latitude (θ). The radial domain extends from $r_{\rm in} = 0.4R_{\rm star}$ to $r_{\rm out} = 0.9R_{\rm star}$, and the one in the co-latitudinal direction ranges from 0 to π, including the full hemisphere. We use a uniform grid resolution of $N_r \times N_\theta = 512 \times 512$ cells. This provides a good resolution of the pressure scale height at the Schwarzschild boundary $H_{p,\rm conv}/\Delta r \sim 92$, with $\Delta r = 550$ km the radial grid spacing. In the θ-direction, the typical size of a grid cell is 2300 km. The choice of the resolution in the θ-direction is set by the requirement to preserve a good aspect ratio of the grid cells on the whole domain on a spherical grid.

6.2.3 Boosted simulations

To artificially boost simulations, we use the following method. The energy flux, and equivalently the luminosity, at the radial boundaries is multiplied by an enhancement factor, and the Rosseland mean opacities κ in MUSIC are decreased by the same factor. In this work we analyse the impact of enhancing the luminosity and thermal diffusivity by factors 10, 10^2 and 10^4. These three simulations are named *boost1d1*, *boost1d2* and *boost1d4* respectively. As already mentioned, larger values of the boosting factor have been used in the literature, but our range is sufficiently large to quantify the impact of the boost on penetrative convection and IGWs. In order to quantify a dynamical timescale associated with a simulation, we define the convective turnover time $\tau_{\rm conv}$ as

$$\tau_{\rm conv} = \left\langle \int_{r_{\rm conv}}^{r_{\rm out}} \frac{{\rm d}r}{{\rm v}_{\rm rms}(r,t)} \right\rangle_t = \omega_{\rm conv}^{-1}, \tag{6.2}$$

Table 6.1 Summary of the two-dimensional simulations.

Simulation	$L/L_{\rm star}$	$\tau_{\rm conv}^{(a)}$ (s)	$N_{\rm conv}^{(b)}$	$\omega_{\rm conv}^{(c)}$ (μHz)
ref	1	8×10^5	565	1.25
boost1d1	10^1	3.6×10^5	375	2.78
boost1d2	10^2	1.7×10^5	450	5.88
boost1d4	10^4	3.5×10^4	530	28.57

[a] Convective turnover time (see Eq. (4.14) for its definition), measured from our simulations.
[b] Number of convective turnover times used for this work.
[c] Convective turnover frequency associated with $\tau_{\rm conv}$

with $v_{\rm rms}$ the root-mean-square velocity. The brackets $\langle . \rangle_t$ denote a time average, and it is defined in Eq. (A.1). In Eq. (6.2) we also define the convective turnover frequency $\omega_{\rm conv}$ by the frequency associated with the characteristic timescale $\tau_{\rm conv}$. We identify this frequency with the characteristic frequency associated with convective eddies used in the various theoretical models introduced in Sect. 4.3. The values of $\tau_{\rm conv}$ and $\omega_{\rm conv}$ for our four simulations are summarised in Table 6.1.

6.3 Velocities

6.3.1 Root-mean-square velocity

One of the main effects of artificially enhancing the luminosity of a numerical model is to increase the fluid velocities. This is readily seen by looking at the root-mean-square (rms) velocities, which we compute in this work as a mass-weighted squared velocity defined by Eq. (A.3). We are using this definition for the $v_{\rm rms}$ as it is the most relevant for comparison with analytical models (see details in Appendix A).

Figure 6.2 shows the radial profile of the rms velocity (left panel) and of the rms velocity normalised by the luminosity enhancement factor to a power 1/3 (right panel). For each simulation the profile is computed over $\sim 375\tau_{\rm conv}$ and the corresponding value of $\tau_{\rm conv}$ is given in Table 6.1. Our numerical simulations reproduce the expected scaling of $v_{\rm rms}$ in the convective zone with the luminosity

$$v_{\rm rms} \propto L^{1/3}. \tag{6.3}$$

This relation is expected from theoretical arguments based on the MLT (Biermann, 1932) and confirmed by many hydrodynamical simulations (Andrassy et al., 2020; Edelmann et al., 2019;

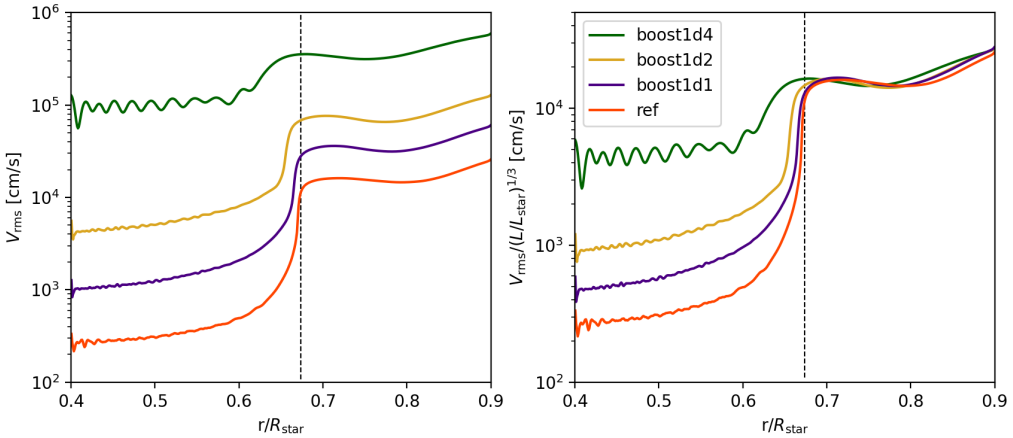

Fig. 6.2 Radial evolution of the rms velocity for the four simulations *ref*, *boost1d1*, *boost1d2*, and *boost1d4*. The convective boundary corresponding to the Schwarzschild criterion from the one-dimensional initial model is indicated by the vertical dashed line.

Porter and Woodward, 2000; Viallet et al., 2013, e.g.). The rms velocities observed in the radiative zone are mainly due to the propagation of internal waves. The left panel of Fig. 6.2 shows that the rms velocity amplitude of the oscillatory motions increases with the luminosity enhancement factor.

Figure 6.2 also shows deeper penetration of the convective motions below the convective boundary and larger overshooting depth with increasing luminosity (see Baraffe et al., 2021, for a detailed study of penetrative convection in these simulations.). The extension of the overshooting length with increasing luminosity is expected from theory (Rempel, 2004; Zahn, 1991) and has also been reported in previous numerical simulations (see for example Hotta, 2017; Käpylä, 2019). Larger velocities in the convective zone and in the overshooting layer with enhanced luminosity factor will impact IGWs as they are excited by turbulent convection in the convective zone and by penetrating flows across the convective boundary. This will be studied in Sect. 6.5.

6.3.2 Radial velocity

The excitation of waves at the convective boundary and their propagation in the stably stratified region is well illustrated in Fig. 6.3, which displays the normalised radial velocity in the two-dimensional plane for the four simulations. The radial velocity v_r is normalised by the rms radial velocity, $v_{r,\mathrm{rms}}(r)$, for better visualisation, as the amplitude of the velocity in the radiative zone can be several orders of magnitude smaller than its typical value in the convective zone (see Fig. 6.2). In the convective envelope, we can clearly see upward (red) and downward

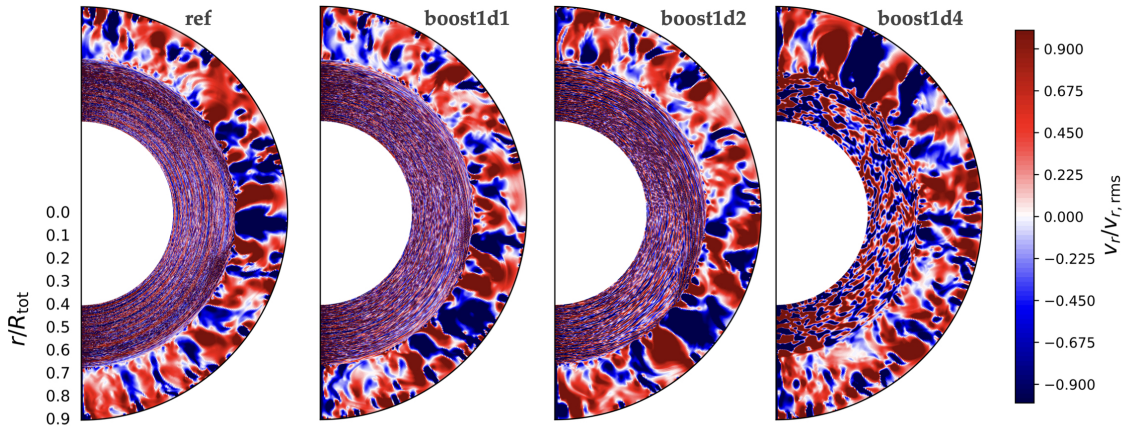

Fig. 6.3 Visualisation of the radial velocity for the four stellar simulations *ref*, *boost1d1*, *boost1d2,* and *boost1d4* as a function of radius r and co-latitude θ. The radial velocity is normalised by the rms radial velocity.

(blue) flows characterising the convective motions, and these patterns are quite similar in the four simulations. Whereas in the radiative region ($r < 0.6734 R_{\rm star}$) the patterns are different with different luminosity enhancement factors. In model *ref*, the thin concentric circles are characteristics of IGW wavefronts. These circular wavefronts are in fact spirals, and their inclination with respect to the convective boundary reflects the frequency of the wave (Stein, 1967). This is a consequence of the dispersion relation for IGWs given by Eq. (4.3). Therefore, the higher the frequency, the smaller the angle α and the less horizontal the wavefront. This is known as the St. Andrews cross (Sutherland, 2010).

For *boost1d1* and *boost1d2*, it can be seen in Fig. 6.3 that the inclination of the wavefronts increases compared to *ref*. This suggests that the dominant waves have higher frequencies. We confirm this pattern in Sect. 6.5. For the most boosted simulation *boost1d4*, the characteristic spiral structures in the radiative zone are not visible any more.

6.4 Radial kinetic energy spectra

Given that IGWs result from the dynamical interaction between the convective and radiative zones, the radial kinetic energy spectra in both regions are useful diagnostics to analyse the properties of waves. Since waves are periodic phenomena in space and time, our analysis is performed in the spectral domain, both spatially and temporally. In the following, we use a temporal Fourier transform of the radial velocity $\mathrm{v}_r(r,\theta,t)$ to obtain a dependence in frequency

ω, $\tilde{\mathrm{v}}_r(r,\theta,\omega)$. We then perform a projection on the spherical harmonics basis to obtain $\hat{\mathrm{v}}_r(r,\ell,\omega)$, where ℓ is the spherical harmonic degree. The definition we are using for spherical harmonics and Fourier transform are given in Appendix B.

6.4.1 Convective zone

We first analyse the power spectrum of the radial velocity in the convective zone for all simulations. An important quantity in this context is the convective turnover timescale, τ_{conv} (see Eq. (4.14)), which defines a characteristic frequency ω_{conv} associated with the convection. Equations (4.14) and (6.3) imply the scaling relation $\omega_{\mathrm{conv}} \propto L^{1/3}$. The values of ω_{conv} for each simulation are provided in Table 6.1. As we will see in the following, the characteristic convective turnover frequency is particularly relevant for present analysis.

Figure 6.4 shows the power spectrum of the radial velocity $P[\hat{\mathrm{v}}_r^2]$ (see Eq. (B.5) for its definition), at a radius $r = 0.762R_{\mathrm{tot}}$, which is located in the bulk of the convective envelope for the four numerical models. We note that the power spectrum barely depends on the location r within the convection zone, as long as r is far enough from the top and bottom boundaries. Based on the scaling relations for the velocities and the convective frequency with the luminosity enhancement factor, the power spectra displayed in Fig. 6.4 are calculated with the velocity divided by $(L/L_{\mathrm{star}})^{1/3}$. For all simulations, the power spectrum values range between 10^{-5} and 10^{2} $\mathrm{cm^2 s^{-2}}$. By also dividing the frequency ω by ω_{conv}, providing the same range of normalised frequency for all four simulations between 0 to ~ 35 (see right y-axis in Fig. 6.4), one obtains very similar spectra for all simulations. All numerical models show a significant amount of energy for frequencies up to $\omega/\omega_{\mathrm{conv}} \sim 5$ and for harmonic degree ℓ between 0 and 100. It is thus interesting to find that a proper rescaling can provide similar power spectra independently of the luminosity enhancement factor. But the actual frequency range is very different for each simulation, with an increase of power in high frequencies for larger luminosity enhancement factors. The normalised frequency value $\omega/\omega_{\mathrm{conv}} \sim 5$ corresponds to $\sim 6\,\mu\mathrm{Hz}$ for the *ref* simulation, $\sim 14\,\mu\mathrm{Hz}$ for *boost1d1*, $\sim 30\,\mu\mathrm{Hz}$ for *boost1d2* and $\sim 145\,\mu\mathrm{Hz}$ for *boost1d4*. Thus, the higher the boost, the larger the energy in convective eddies of high frequencies.

6.4.2 Radiative zone

We now analyse the power spectra of the radial velocity in the radiative zone. Figure 6.5 shows the power spectra of the radial velocity at radius $r = 0.494R_{\mathrm{tot}}$, which is approximately at two pressure scale heights $H_{p,\mathrm{conv}}$ from the convective boundary.

At such a depth, located far away from the convective boundary, one can reasonably assume that the waves are the main contributor to the velocity and that the contribution from penetrative

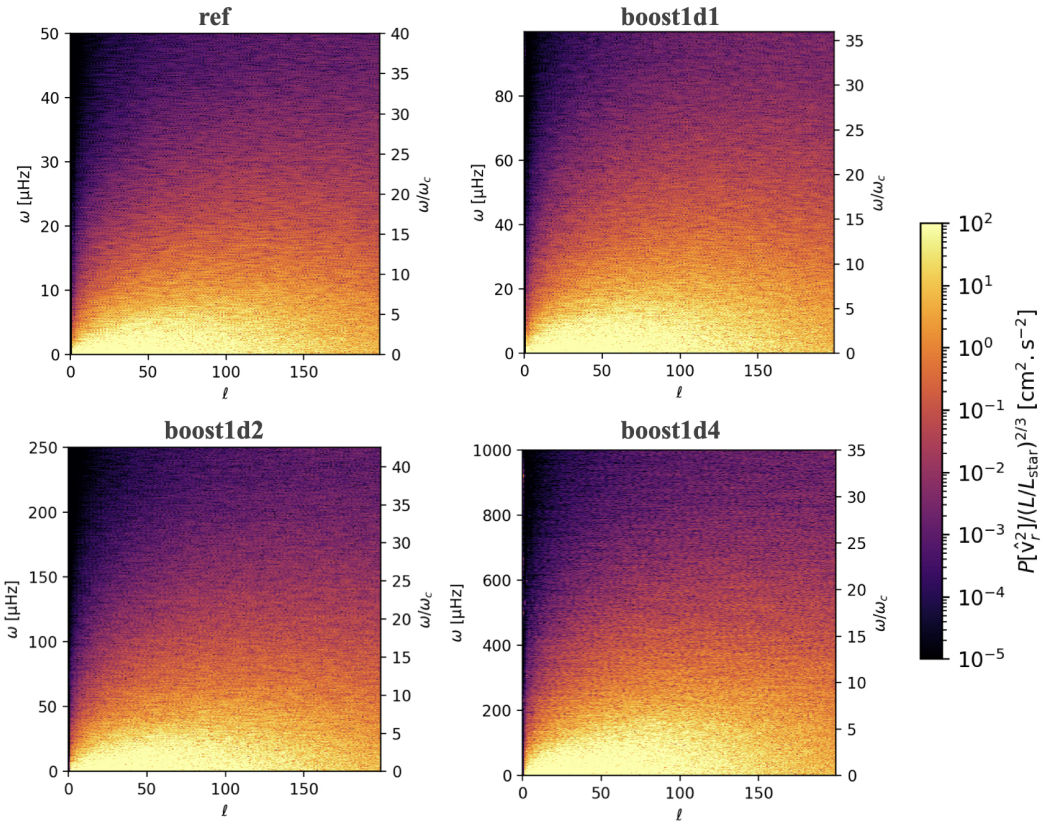

Fig. 6.4 Power spectra of the radial velocity for the four stellar simulations *ref*, *boost1d1*, *boost1d2,* and *boost1d4,* respectively, in the convective zone at depth $r = 0.762R_{\rm tot}$. The spectra were obtained via mode projection on the spherical harmonics basis and a temporal Fourier transform of the radial velocity. The radial velocities are normalised by $(L/L_{\rm star})^{1/3}$ (see text Sect. 6.4.1).

plumes is negligible. Velocities are not rescaled, and the magnitudes represented by the colour bar are different for each simulation in Fig. 6.5.

A pattern of bright ridges of high energy is present in the four panels of Fig. 6.5. This structure is similar to the one obtained by linear theory, see Fig. 3.2, and by other numerical simulations of solar-like stars (Alvan et al., 2014, 2015) and of more massive stars with a convective core (Horst et al., 2020). These bright ridges present a discrete nature, and the observed bright dots correspond to g modes that form in the radiative zone. The g mode patterns have similar structures for the four numerical models, even if they are only visible at low ℓ in *boost1d4*. As will be shown in Sect. 6.4.3, the eigenfrequencies of the g modes are not affected

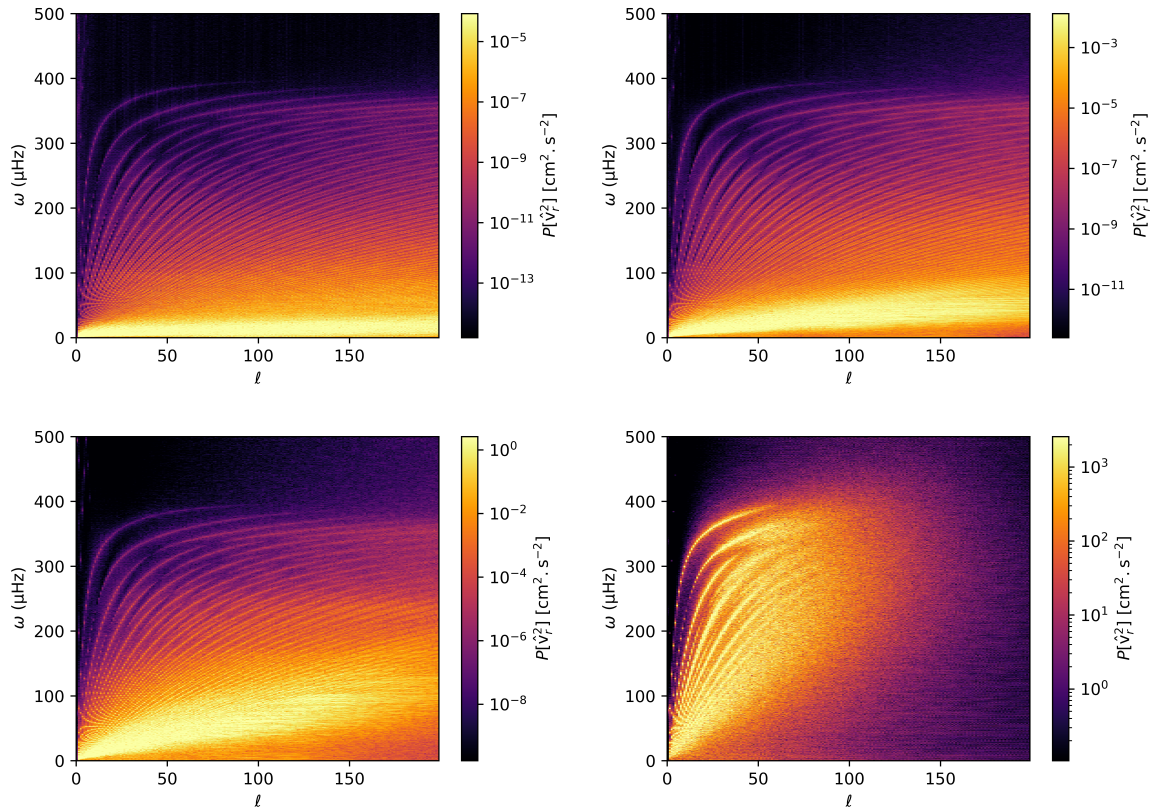

Fig. 6.5 Power spectra of the radial velocity for the four stellar simulations *ref* (top left), *boost1d1* (top right), *boost1d2* (bottom left), and *boost1d4* (bottom right) at depth $r = 0.494R_{\rm star} \simeq r_{\rm conv} - 2H_{p,{\rm conv}}$. They were obtained via mode projection on the spherical harmonics basis and a temporal Fourier transform of the radial velocity. Velocities are not rescaled, and the magnitudes represented by the colour bar are different for each simulation.

by the artificial enhancement of the luminosity over the simulated time. These frequencies depend only on the stratification and the geometry of the resonant cavity limited by the inner boundary, located at $r_{\rm in} = 0.4R_{\rm star}$ in present simulations, and by the radiative/convective boundary $r_{\rm conv}$.

The power spectra in Fig. 6.5 are displayed for frequencies ranging from 0 to 500 μHz and for degrees ℓ from 0 to 200. In order to reach such high frequencies, the simulation data need to be sampled at a fixed time interval that is short enough ($\leq 10^3$s) to capture the full spectrum of the waves up to the Brunt-Väisälä frequency. According to the right panel of Fig. 6.1, the maximal frequency for IGWs propagating at radius $r = 0.494R_{\rm tot}$ is $\simeq 370\,\mu$Hz. We thus identify the modes observed at low degrees, $\ell \simeq 1, 2$ or 3, and at frequencies of $\sim 400\,\mu$Hz or above as standing acoustic waves, or p-modes. The study of p-modes is beyond the scope of this work. Figure 6.5 clearly shows that the larger the luminosity enhancement factor, the higher the energy of high frequency waves. This trend is consistent with theoretical models. For waves excited by turbulent Reynolds stress, Lecoanet and Quataert (2013) predict a peak of the IGW flux for waves with frequencies close to the convective turnover frequency, $\omega_{\rm conv}$, which increases with the luminosity enhancement factor. For waves generated by penetrative plumes, Pinçon et al. (2016) suggest that when the frequency associated with the lifetime of the plumes increases, there is a redistribution of the wave energy from low frequencies towards higher frequencies. The lifetime of the plumes can be linked to their velocities in the overshooting layer, which significantly increase with the luminosity enhancement factor (see Sect. 6.3.1 and Baraffe et al. (2021)).

In terms of length scales, Fig. 6.5 shows that most of the energy tends to be concentrated in waves of lower degree ℓ for increasing luminosity enhancement factors. The higher the enhancement factor is, the lower the energy in waves of small length scales (high ℓ) compared to the larger ones (low ℓ). This can also be expected from theory, eddies with characteristic degree $\ell_{\rm eddy}$ will excite waves of degree $\ell \leq \ell_{\rm eddy}$ (Lecoanet and Quataert, 2013). This assumption comes from the statistical properties of stellar convection using Kolmogorov turbulence and is often used to model convection in the context of IGW excitation (Goldreich and Keeley, 1977; Goldreich and Kumar, 1990; Stein, 1967; Zahn et al., 1997). It can be expressed as

$$\ell_{\rm eddy} \sim H\left(\frac{\omega}{\omega_{\rm conv}}\right)^{3/2}, \tag{6.4}$$

where H corresponds to the size of the largest convective eddies. Based on a comparison of the flow for all simulations, we assume that H is the same for the four numerical models; thus, the value of $\ell_{\rm eddy}$ for a given frequency is smaller for a more boosted simulation.

The results presented in this section highlight that the waves that bear most of the energy have different frequency and spatial ranges for each simulation. In the *ref* simulation most of the energy is below $\sim 30\,\mu$Hz and spread over all ℓ (up to 200) while it is above $\sim 50\,\mu$Hz and for $0 \leq \ell \leq 100$ for the *boost1d4* simulation. In addition to Sect. 6.4.1, these results confirm the theoretical expectations that convective eddies with higher frequencies excite IGWs with higher frequencies (Kumar et al., 1999; Lecoanet and Quataert, 2013). This should be kept in mind when studying IGWs, and particularly energy and angular momentum transport, as they strongly depend on the frequencies and angular degrees of the waves that can be excited (see for example Zahn et al., 1997).

6.4.3 g modes

In order to confirm that the bright dots patterns of Fig. 6.5 are indeed g modes, we compare their frequencies along ℓ slices to the results of a linear stability analysis using the stellar oscillation code GYRE (Version 6.0)[1] (Goldstein and Townsend, 2020; Townsend et al., 2018; Townsend and Teitler, 2013). This code solves the oscillation equations given by Eq. (3.23) - (3.25), and provides the eigenfrequencies and eigenfunctions characteristic of a one-dimensional stellar structure model. As an input to GYRE, we used the initial one-dimensional radial profile common to all four simulations, with a domain geometry corresponding to the radially truncated domain of our simulations.

Figure 6.6 shows slices of the spectra of Fig. 6.5 for harmonic degree $\ell = 5$. The peaks in the spectra correspond to the bright dots of Fig. 6.5. Those peaks obtained from the four MUSIC simulations closely match the predictions of GYRE (vertical dashed lines) for the g-mode frequencies. For better visibility, we do not plot the GYRE predictions for modes with frequency lower than $12\,\mu$Hz. The degree $\ell = 5$ is chosen arbitrarily; we also found a good match for the other angular degree we tested, such as $\ell = 1$, 2, and 10. For each numerical model, the energy spectrum peaks at a different frequency. For the *ref* simulation, the peak is visually identified at $\simeq 2\,\mu$Hz, for *boost1d1* at $\simeq 3.5\,\mu$Hz, for *boost1d2* at $\simeq 6\,\mu$Hz and for *boost1d4* at $\simeq 25\,\mu$Hz. These frequencies are rather close to the convective turnover frequency of the corresponding simulation (see Table 6.1). The location of the maximum power is linked to the excitation of IGWs as analysed in the next section.

[1] https://gyre.readthedocs.io/

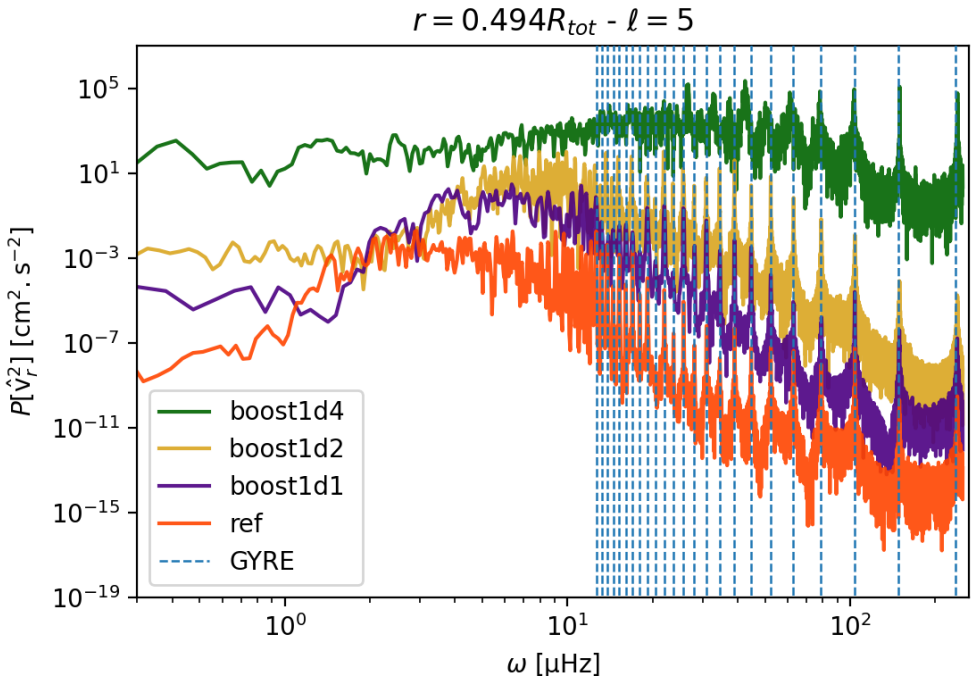

Fig. 6.6 Power spectrum of the radial velocity as a function of frequency at degree $\ell = 5$ for the four simulations *ref*, *boost1d1*, *boost1d2,* and *boost1d4* at depth r = 0.494 $R_{\rm star} \simeq r_{\rm conv} - 2H_{p,\rm conv}$. The vertical dashed blue lines correspond to g-mode frequencies predicted by GYRE.

6.5 Excitation and damping of internal gravity waves

6.5.1 Radial evolution of power spectra

Next, the aim is to understand the impact of the luminosity enhancement on the excitation of IGWs and their propagation in the radiative zone. To do so, we analyse in this section the evolution with depth of the power spectral density (PSD) of the radial velocity summed over the harmonic degree ℓ, which determines which frequencies contribute the most to the energy. The relation between the power spectrum, $P[\hat{v}_r^2]$, and the PSD, $\mathrm{PSD}[\hat{v}_r^2]$, is given in our conventions by

$$P[\hat{v}_r^2] = \frac{\mathrm{PSD}[\hat{v}_r^2]}{T_{\rm s}}, \tag{6.5}$$

with $T_{\rm s}$ the sampling time that corresponds to the total time span used for the computations of the spectra. In order to compare the amount of power in log-sized, non-uniform frequency bins, we look at $\mathrm{PSD}_{\ln\omega}$, the PSD in terms of $\ln\omega$, defined by

$$\mathrm{PSD}_{\ln\omega} \mathrm{d}\ln\omega = \mathrm{PSD}\mathrm{d}\omega. \tag{6.6}$$

Figure 6.7 shows

$$\mathrm{PSD}_{\ln\omega}[\hat{\mathrm{v}}_r^2](r,\omega) = \sum_{\ell} \omega\,\mathrm{PSD}[\hat{\mathrm{v}}_r^2](r,\ell,\omega) \tag{6.7}$$

at selected radii in the convective and radiative zones for the four simulations. The spectra are computed over a simulated time of $200\times\tau_{\mathrm{conv}}$ for *ref*, *boost1d1* and *boost1d2* and $500\times\tau_{\mathrm{conv}}$ for *boost1d4*. This is because τ_{conv} is short for simulation *boost1d4* compared to other simulations (see Table 6.1). For each simulation the frequency range covered by the spectra are different as we focus on the range that bears most of the energy (see Sect. 6.4.2). Moreover, the flattening of the slope of the spectra close to the maximal frequency for each simulation results from numerical aliasing. This does not impact our analysis, as we focus on frequencies below the affected range.

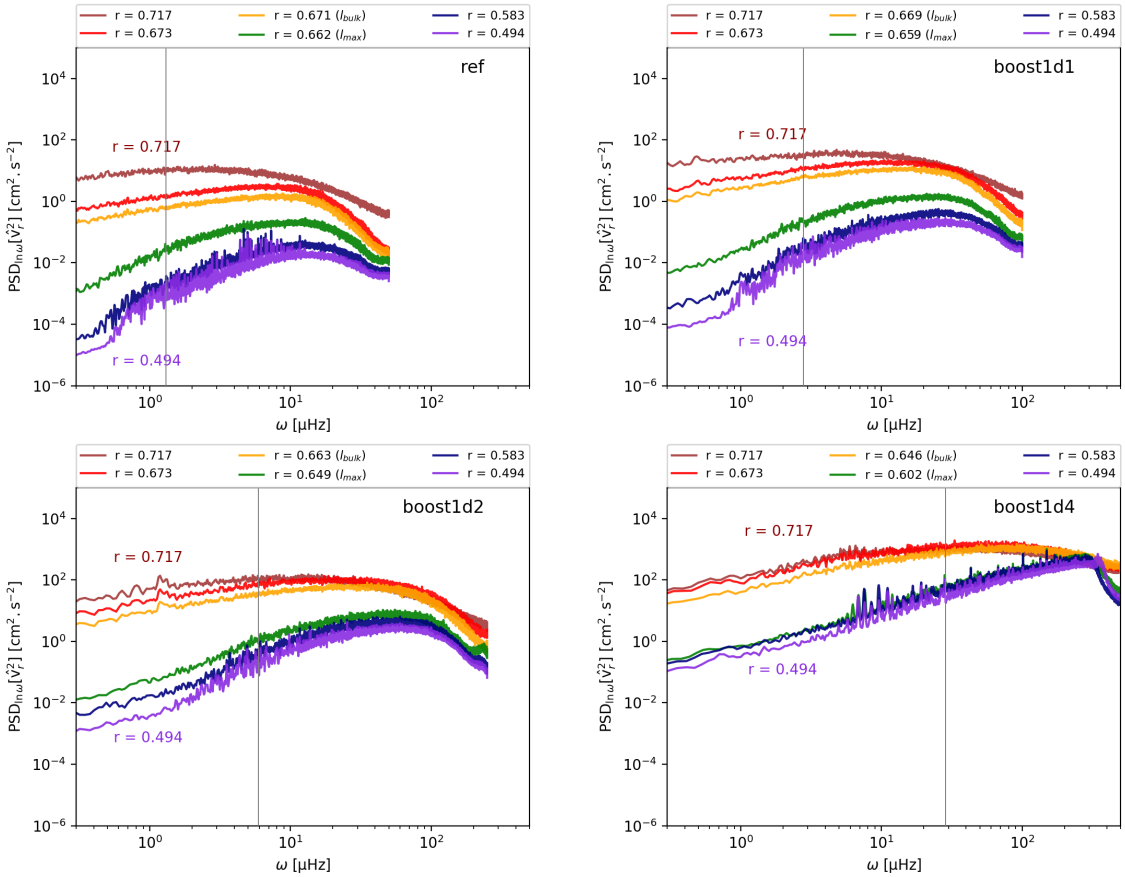

Fig. 6.7 PSD of the radial velocity as a function of frequency for the four simulations *ref* (top left), *boost1d1* (top right), *boost1d2* (bottom left), and *boost1d4* (bottom right) at different depths. The vertical grey line indicates the convective frequency for each simulation. The spectra are obtained via mode projection on the spherical harmonics basis and a temporal Fourier transform of the radial velocity.

Table 6.2 Characteristics lengths $l_{\rm bulk}$ and $l_{\rm max}$ derived in Baraffe et al. (2021).

Simulation	$l_{\rm bulk}/R_{\rm star}$	$l_{\rm bulk}/H_{p,\rm conv}$	$l_{\rm max}/R_{\rm star}$	$l_{\rm max}/H_{p,\rm conv}$
ref	2.35×10^{-3}	2.62×10^{-2}	1.12×10^{-2}	0.124
boost1d1	4.72×10^{-3}	5.24×10^{-2}	1.45×10^{-2}	0.161
boost1d2	1.04×10^{-2}	0.115	2.47×10^{-2}	0.275
boost1d4	2.82×10^{-2}	0.313	7.1×10^{-2}	0.787

Values of $l_{\rm bulk}$ and $l_{\rm max}$ based on the vertical heat flux.

We show in Fig. 6.7 that in the bulk of the convective zone, at $r = 0.717R_{\rm star} \simeq r_{\rm conv} + H_{p,\rm conv}$ (brown curve), the energy of all four simulations is increasing with frequency up to approximately the convective frequency, $\omega_{\rm conv}$, which is indicated by the vertical grey line. Then, the energy decreases towards higher frequencies, consistent with the results presented in Sect. 6.4.1. Just below the convective boundary, velocities are the result of a mix of convective penetration and waves.

In Baraffe et al. (2021), we define a layer of characteristic length $l_{\rm bulk}$ as the distance that convective plumes typically penetrate, and a larger penetration length $l_{\rm max}$ characterised by the most vigorous convective plumes. These lengths are estimated using an approach developed by Pratt et al. (2017) based on a statistical analysis of the depth reached by all convective plumes that penetrate in the radiative region. They use two different criteria to compute $l_{\rm bulk}$ and $l_{\rm max}$ but the method is identical for both. The depth reach by a penetrative plume r_0 at a given angle θ and time t is defined as the first zero below the convective boundary of an energy flux. The first criterion uses the vertical kinetic energy flux $\mathbf{f}_k(r,\theta,t) = \frac{1}{2}\rho\mathbf{v}^2\mathbf{v}_r$, and the second one considers instead the vertical heat flux $\mathbf{f}_{\delta T}(r,\theta,t) = \rho c_p(\delta T)\mathbf{v}_r$. In this work, we consider the criterion based on the vertical heat flux. Therefore, the penetration length l_0 is defined as

$$l_0(\theta,t) = r_{\rm conv} - r_0(\theta,t). \tag{6.8}$$

We then define characteristic length $l_{\rm bulk}$ where convective plumes frequently penetrate as

$$l_{\rm bulk} = \langle l_0(\theta,t)\rangle_{\mathcal{S},t}\,, \tag{6.9}$$

and the maximal length of penetration of plumes $l_{\rm max}$ as

$$l_{\rm max} = \left\langle \max_{\theta}\left(l_0(\theta,t)\right)\right\rangle_t. \tag{6.10}$$

The values of $l_{\rm bulk}$ and $l_{\rm max}$ derived in Baraffe et al. (2021) and used in this work are given in Table 6.2.

Figure 6.7 shows spectra in the radiative - convective transition region, at $r = 0.673 R_{\rm star}$ (red curve), and at $r = r_{\rm conv} - l_{\rm bulk}$ (yellow curve) for all simulations.

We first discuss simulations *ref*, *boost1d1* and *boost1d2*. Compared to spectra above the convective boundary, the energy increases up to some characteristic frequency and sharply drops beyond. As the luminosity enhancement factor increases, the knee of the spectrum shifts to higher frequencies; in addition, the spectra above and just below the convective boundary (brown, red, yellow curves) become closer to each other, indicating that vigorous convection increasingly dominates at the top of the penetration region.

Finally, at even deeper layers inside the radiative zone, the PSDs are dominated by waves, excited from above and propagating in the radiative zone of the star while also undergoing damping (Press, 1981), which we analyse in Sect. 6.6.2. The deepest spectra displayed in Fig. 6.7 correspond to the depths $r = 0.583 R_{\rm star} \simeq r_{\rm conv} - H_{p,\rm conv}$ (blue) and $r = 0.494 R_{\rm star} \simeq r_{\rm conv} - 2H_{p,\rm conv}$ (purple curve). In this region, the spectra present high-amplitude narrow peaks corresponding to g modes. The amplitude of these spectra is also decreasing towards low frequencies, reaching a peak for some ω, which corresponds approximately to the frequency at which the spectra computed just below the convective boundary (red and yellow curves) reach their maxima. However, at low frequency we can observe a modification of the aspect of the spectra. In this range there are no more g modes, due to the stronger damping of low-ω waves (see Sect. 6.6.2).

The PSD computed at a distance $l_{\rm max}$ from the convective boundary (green curve) is a mix of the spectra just below the convective boundary (red and yellow) and the ones deeper in the radiative zone (blue and purple). Indeed, very little of the convective motions penetrate that deep in the radiative zone, and below a depth of $l_{\rm max}$, the wave signal dominates the spectra.

In Fig. 6.7, the most boosted numerical model *boost1d4* is qualitatively different and deserves special discussion. Firstly, its spectra just below the convective boundary (red, yellow) are very similar to the spectrum in the convection zone (brown). This could result from the layer becoming very close to convective below the boundary: as noted in Baraffe et al. (2021), the thermal background in the overshooting layer of this model is significantly modified during the course of the simulation, with the temperature profile getting steeper and closer to the adiabatic gradient. Secondly, in the region $r \leq r_{\rm conv} - l_{\rm max}$ of the radiative zone where only waves remain, the spectra are monotonically increasing, compared to their less boosted counterparts, up until the Brunt-Väisälä frequency ($N \simeq 370\,\mu$Hz at $r = 0.494 R_{\rm star}$), after which the energy drops suddenly, since IGWs are evanescent above this frequency. The energy spectra are therefore 'clipped' at high frequencies $\omega \geq N$, resulting in a significant redistribution of wave energies.

6.5.2 Amplitude of oscillatory motions across the convective boundary

In this subsection, we analyse the decrease in the radial velocity amplitude between the convective zone and the radiative zone. To this end, we study the IGWs wave luminosity as a function of depth. The luminosity associated with a monochromatic IGW is defined as

$$L_{\rm wave}(r,\ell,\omega) = 4\pi r^2 F_{\rm wave}(r,\ell,\omega), \tag{6.11}$$

with $F_{\rm wave}$ the wave energy flux for the considered wave. In order to calculate wave fluxes from our numerical simulations and compare them to theoretical predictions, we estimate the wave energy flux for a monochromatic IGW (ω, ℓ) as (Lecoanet and Quataert, 2013; Press, 1981)

$$F_{\rm wave} \sim \rho |\hat{\rm v}_{\rm h}|^2 u_{{\rm g},r}, \tag{6.12}$$

where we have assumed that $\mathrm{v_h} \gg \mathrm{v}_r$ in the radiative zone, which is true for low frequency waves. We recall that in our two-dimensional case, we identify $\mathrm{v_h} = \mathrm{v}_\theta$. The radial component of the group velocity has been derived in Eq. (4.6) and using the dispersion relation of IGWs Eq. (4.2) we can rewrite as (Unno et al., 1989)

$$u_{{\rm g},r} \simeq \frac{\omega^2}{N k_{\rm h}}, \tag{6.13}$$

where it is assumed that $\omega \ll N$. Moreover, from Press (1981), we have (see Eq. 4.31

$$\mathrm{v_h} \simeq \frac{N}{\omega}\hat{\mathrm{v}}_r. \tag{6.14}$$

The wave flux is thus

$$F_{\rm wave} \sim \rho \frac{N}{k_{\rm h}} |\mathrm{v}_r|^2. \tag{6.15}$$

Following our definition Eq. (B.5) of the power spectrum

$$|\mathrm{v}_r|^2 \sim \frac{P[\hat{\mathrm{v}}_r^2]}{2}, \tag{6.16}$$

our final expression for the flux for an individual IGW mode (ω, ℓ) at radius r is

$$F_{\rm wave}(r,\ell,\omega) \sim \frac{1}{2}\rho \frac{N}{k_{\rm h}} P[\hat{\mathrm{v}}_r^2](r,\ell,\omega). \tag{6.17}$$

This expression is equivalent to the one from (Press, 1981) given by Eq. (4.33) in the low frequency limit. The horizontally averaged luminosity of a superposition of modes, Eq. (6.11), is therefore given, through Eq. (6.17), by the total power summed across all ℓ.

Figure 6.8 shows the radial evolution of the horizontally averaged IGW luminosity at six different frequencies for the four simulations. The luminosities are normalised by their value at the convective boundary (horizontal solid black line), allowing us to compare the depth dependence across the different frequencies. In the absence of damping effects, the wave luminosity of propagating IGWs is conserved, making it a useful quantity for studying the decay of the wave amplitudes as they travel inwards, away from the convective boundary.

All four numerical models show a peak of the wave luminosity at $r \sim r_{\rm conv} - l_{\rm bulk}$ (horizontal green dashed line), which is located deeper towards the centre as the luminosity of the simulation increases. We suggest that the peaks indicate the region where the excitation of the waves is maximum. Below $r \sim r_{\rm conv} - l_{\rm bulk}$, there is a strong decrease in energy towards the centre of the star. This drop is the result of the transition from convective motions to waves, in which the majority of the convective kinetic energy is not transferred to IGWs but rather to horizontal flows and to local heating (see Baraffe et al., 2021).

After reaching approximately $r \sim r_{\rm conv} - l_{\rm max}$ (horizontal dotted blue line), the energy is still decreasing but at slower rate over some distance for *ref* and *boost1d1*. Below this radius, the wave luminosity is approximately constant. In the case of *boost1d2* and *boost1d4*, the wave luminosity is constant from $r \sim r_{\rm conv} - l_{\rm max}$. The behaviour of the wave luminosity just below the convective boundary shows that the larger the model luminosity enhancement factor, the more energy is transmitted to the waves. The two expected wave excitation mechanisms, namely turbulent Reynolds stress at the convective boundary and penetrating plumes below the boundary, directly depend on the model luminosity enhancement factor because of the increase in the convective and penetrating plume velocities (see Sect. 6.3.1 and Baraffe et al. (2021)). Trying to disentangle the impact of one mechanism from the other or to determine if one is dominating over the other is a difficult task, since both are enhanced with the luminosity of the simulation. But the changes of behaviour of the spectra (see Fig. 6.7) and of the rate of energy decrease (see Fig. 6.8) linked to the positions of $l_{\rm bulk}$, where the bulk of the plumes penetrate, and of $l_{\rm max}$ reached by the most vigorous plumes, suggest that convective penetration plays a non-negligible role on the energy spectra of IGWs in the radiative zone.

We also note that the efficiency of the decay of the wave luminosity just below $r \sim r_{\rm conv} - l_{\rm bulk}$ depends on the frequency of the waves. For a given simulation, the decrease in amplitude of lower frequency waves is larger compared to higher frequency waves. Compared to their initial amount of energy at the convective boundary, low frequency motions thus have less energy as they propagate towards the centre of the star.

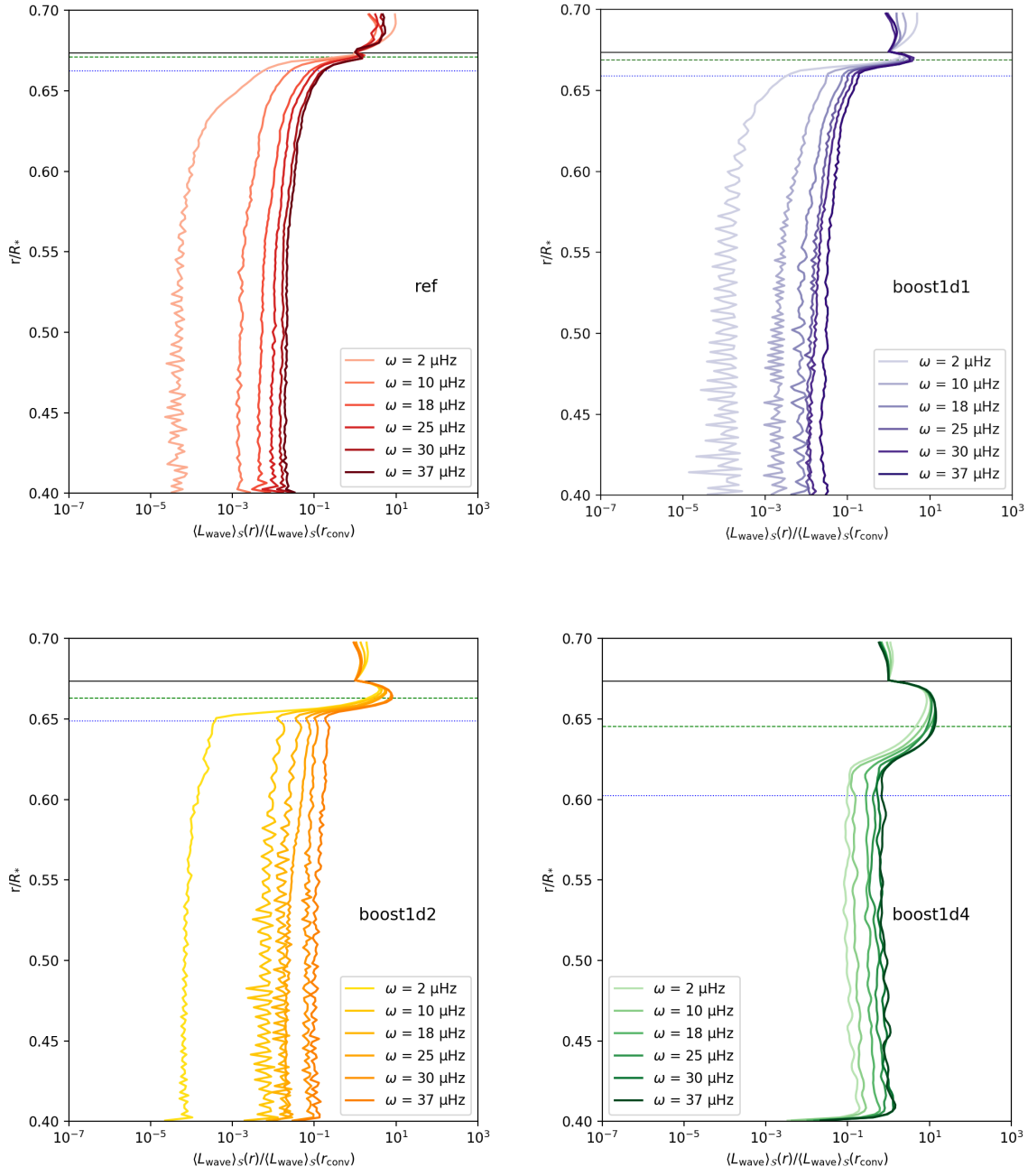

Fig. 6.8 Radial profile of the horizontally averaged luminosity associated with the waves for the four simulations *ref* (top left), *boost1d1* (top right), *boost1d2* (bottom left), and *boost1d4* (bottom right) at six different frequencies. The power spectra are normalised by their value at the convective boundary $L_{\rm wave}(r_{\rm conv})$. The horizontal solid black line indicates the radiative–convective boundary as defined by the Schwarzschild criterion for the initial model. The horizontal dashed green and dotted blue lines indicate the radii $r = r_{\rm conv} - l_{\rm bulk}$ and $r = r_{\rm conv} - l_{\rm max}$, respectively. The horizontal average $\langle . \rangle_S$ is defined in Eq. (A.2).

From theory, it is expected that the amplitude of the waves, represented by $P[\hat{v}_r^2]$, decreases as they propagate towards the centre of the star, see Eq. (7.2), due to damping and geometrical effects. One of the benefits of working with the wave luminosity is that it is supposed to be constant in the absence of damping effects. As we can see on Fig. 6.8, the wave luminosity at a distance larger than $l_{\max}$ from the convective boundary is approximately constant and thus there is no frequency-dependent variations of the luminosity, i.e. we do not see the impact of radiative damping. We suggest that the horizontal averaging masks the effect of radiative damping, with non-damped waves that dominate in the average.

The situation for *boost1d4* is less clear. Because of the very vigorous convection in this model, waves in the radiative zone reach very large amplitudes shifted towards larger ω (see Fig. 6.5), resulting in significant reflections at the bottom boundary with almost no visible damping; the problem is further aggravated by the larger overshooting depth of this model. Waves can also reach strongly non-linear regimes where linear theory breaks down. The comparison to the other models highlights the limitations of strongly boosted simulations for the analysis of IGW properties.

6.6 Comparison with theory

6.6.1 Radial wave energy flux

The wave energy flux is central to determining the efficiency of angular momentum transport in stellar interiors, and can be used to predict the detectability of IGWs in stars. Based on the pioneering work of Stein (1967), several models have been developed for the calculation of the wave energy flux, assuming that the excitation mechanism is due to Reynolds stresses, but these models result in differences in the predicted flux; this is the subject of Sect. 4.3.1.

For our simulations, we estimate the total wave energy flux F using a method similar to the one of Couston et al. (2018). The total flux F is obtained by summing the fluxes F_{wave} of all individual IGW modes:

$$F(r) \simeq \sum_{\omega,k_{\text{h}}} \frac{F_{\text{wave}}}{\delta\omega\,\delta k_{\text{h}}}\,\delta\omega\,\delta k_{\text{h}}, \tag{6.18}$$

where $\delta\omega$ and δk_{h} are the spacing of modes in spectral space, which are defined as

$$\delta\omega = \frac{1}{T_{\text{s}}} \quad ; \quad \delta k_{\text{h}} = \frac{1}{r}, \tag{6.19}$$

where T_s is the sampling time. Then replacing $F_{\rm wave}$ by its expression given by Eq. (6.17), we have

$$F(r) \simeq \sum_{\omega,k_h} \frac{\frac{1}{2}\rho\frac{N}{k_h}P[\hat{v}_r^2](r,\omega,\ell)}{\delta\omega\,\delta k_h}\delta\omega\,\delta k_h. \tag{6.20}$$

We can now introduce the discrete version of the wave energy flux:

$$\sum_{\omega,k_h} \frac{\frac{1}{2}\rho\frac{N}{k_h}P[\hat{v}_r^2](r,\omega,\ell)}{\delta\omega\,\delta k_h}\delta\omega\,\delta k_h := \sum_{\omega,k_h} \frac{\delta F}{\delta\omega\,\delta k_h}\delta\omega\,\delta k_h. \tag{6.21}$$

This last form can be related to a continuous form of the differential wave energy flux:

$$\sum_{\omega,k_h} \frac{\delta F}{\delta\omega\,\delta k_h}\delta\omega\,\delta k_h \simeq \int \frac{\mathrm{d}F}{\mathrm{d}\omega\mathrm{d}k_h}\mathrm{d}\omega\mathrm{d}k_h. \tag{6.22}$$

In order to compare our estimation to the analytical expressions introduced above, we identify from Eqs. (6.21) and (6.22)

$$\frac{\mathrm{d}F}{\mathrm{d}\omega\mathrm{d}k_h} = \frac{1}{2}\rho\frac{N}{k_h}\frac{P[\hat{v}_r^2]}{\delta\omega\,\delta k_h}. \tag{6.23}$$

Then, using the expressions introduced in Eq. (6.19) we finally obtain

$$\frac{\mathrm{d}F}{\mathrm{d}\ln\omega\mathrm{d}\ln k_h} = \omega k_h\frac{\mathrm{d}F}{\mathrm{d}\omega\mathrm{d}k_h} \sim \frac{1}{2}\rho T_s r N\omega P[\hat{v}_r^2]. \tag{6.24}$$

The fluxes are calculated at a radius far away from the convective boundary ($r \sim r_{\rm conv} - l_{\rm max}$) to ensure that $\hat{v}_r$ only captures the wave motions and not additional motions due to convective penetration. These fluxes extracted from the numerical data can then be compared to the theoretical spectra predicted for excitation by turbulent convective eddies and penetrative convection. For the former we use the model of Reynold's stress excitation by Lecoanet and Quataert (2013) and consider the three different cases for the temperature gradient at the convective boundary: discontinuous Eq. (4.26), piecewise linear Eq. (4.27) and hyperbolic tangent Eq. (4.28). Note that the theory used to derive Eqs. (4.26)–(4.28) relies on three-dimensional assumptions, for example on the counting of modes and the turbulence spectrum. Even though we should not expect these results to hold in two-dimensions, they were still found to provide a good match to numerical spectra from two-dimensional simulations (Lecoanet et al., 2021). For the penetrative convection excitation mechanism, we use the model from Pinçon et al. (2016) described by Eq. (4.45). For both models, we only compare the frequency dependence of the spectra. The results are shown in Fig. 6.9 for $\ell = 10$. We recall that the relation between k_h and ℓ is defined by Eq. (4.1).

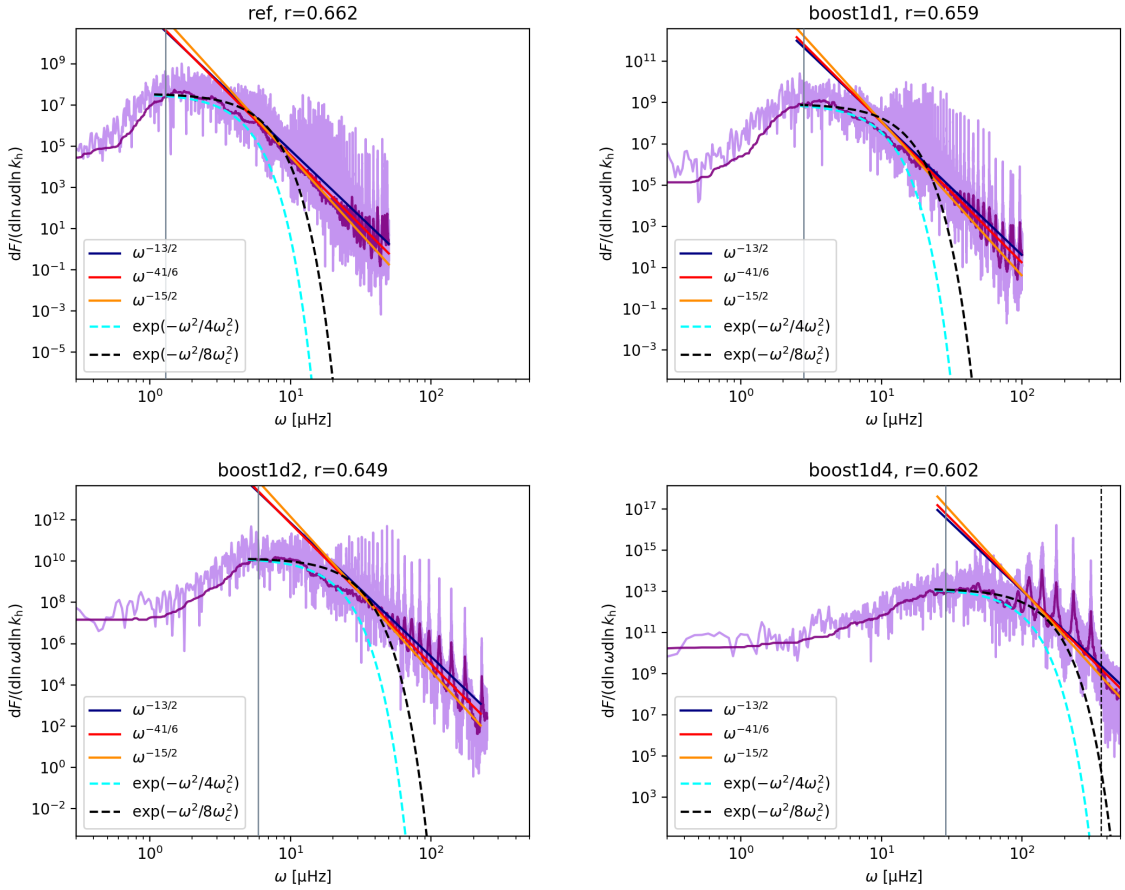

Fig. 6.9 Wave energy flux (light purple line) for the four simulations *ref* (top left), *boost1d1* (top right), *boost1d2* (bottom left), and *boost1d4* (bottom right). The spectra are computed at $r = r_{\rm conv} - l_{\rm max}$ (i.e. at a distance l_{max} from the convective boundary) and for angular degree $\ell = 10$. The grey vertical lines indicate the convective turnover frequency, $\omega_{\rm conv}$, and the blue, red, and orange lines correspond to functions with slope $\omega^{-13/2}$, $\omega^{-41/6}$, and $\omega^{-15/2}$, respectively. The dashed curves represent two Gaussian spectra with characteristic frequencies $\omega_{\rm conv}$ (cyan) and $\sqrt{2}\omega_{\rm conv}$ (black). The dark purple line is a running 25th percentile of the flux over 100 frequency bins.

The four spectra present similar shapes, with a flat part at low frequencies and a peak that is shifted towards higher frequencies with increasing luminosity enhancement factor. The peak follows the convective turnover frequency, which is indicated by the vertical grey line. For a better visual comparison with theoretical predictions, we also compute and plot a running median on the 25th percentile of the flux with a window of 100 frequency bins (dark purple line). According to Lecoanet and Quataert (2013), the scaling relationships Eqs. (4.26)–(4.28) are only valid for frequencies $\omega \geq \omega_{\text{conv}}$. In the high frequency part, the baseline of the spectra approximately follows a scaling between $\omega^{-13/2}$ and $\omega^{-15/2}$, broadly consistent with the theoretical predictions; however, determining the precise slope is difficult because of the presence of strong g modes, which appear as 'combs' of high-energy peaks. We find similar behaviours for other values of ℓ. Following the arguments of Lecoanet and Quataert (2013) and given the increase in the overshooting length characterising the convective-radiative transition with the luminosity enhancement factor, one would expect the high-ω slope to evolve as luminosity increases, from the discontinuous case of Eq. (4.26) to the smoother case of Eq. (4.28). However, given that the theoretical slopes are quite close to each other, it is difficult to determine the exact slope of the calculated spectra beyond ω_{conv} from such a comparison.

In Fig. 6.9, we have also plotted part of the theoretical spectrum predicted by Pinçon et al. (2016), taking $\nu_{\text{p}} = \omega_{\text{conv}}$. To observe the effect of varying this characteristic frequency, we have also plotted a spectrum with $\nu_{\text{p}} = \sqrt{2}\omega_{\text{conv}}$; as expected, increasing ν_{p} increases the width of the spectrum. The spectrum of Pinçon et al. (2016) is consistent with the shape of our simulated spectra in the vicinity of ω_{conv}. The agreement seems to improve as the luminosity enhancement factor is increased and could thus suggest that excitation by plumes slightly takes over in boosted simulations

This result suggests that both Reynolds stresses and plume penetration play a role in IGW generation. Moreover, the excitation by penetrative convection at low frequencies and by Reynolds stress at higher frequencies agree with the predictions from Pinçon et al. (2016) presented in Fig. 4.2.

We note that the larger the luminosity enhancement factor of the stellar model, the closer the peak of the spectrum lies to the Brunt-Väisälä frequency. The luminosity enhancement thus limits the range of frequencies over which numerical models can be compared to theoretical predictions. As noted in Baraffe et al. (2021), very large enhancement factors for the luminosity, with factors $> 10^6$, will produce unrealistic results because of convective velocities in the outer part of the domain that could become close to the speed of sound. In addition, that paper highlights that for such large factors the convective turnover frequencies, which scale as $L^{1/3}$, would become higher than the Brunt-Väisälä frequency.

We also analyse the horizontal wavenumber dependence of the wave flux derived from the simulations. In Fig. 6.10, the wave energy flux of Eq. (6.24) is displayed for the four simulations as a function of k_h at a frequency $\omega = 10\omega_\mathrm{conv}$ for the relevant simulation. This allows a meaningful comparison between the different simulations. Figure 6.10 shows that the four numerical models present similar features.

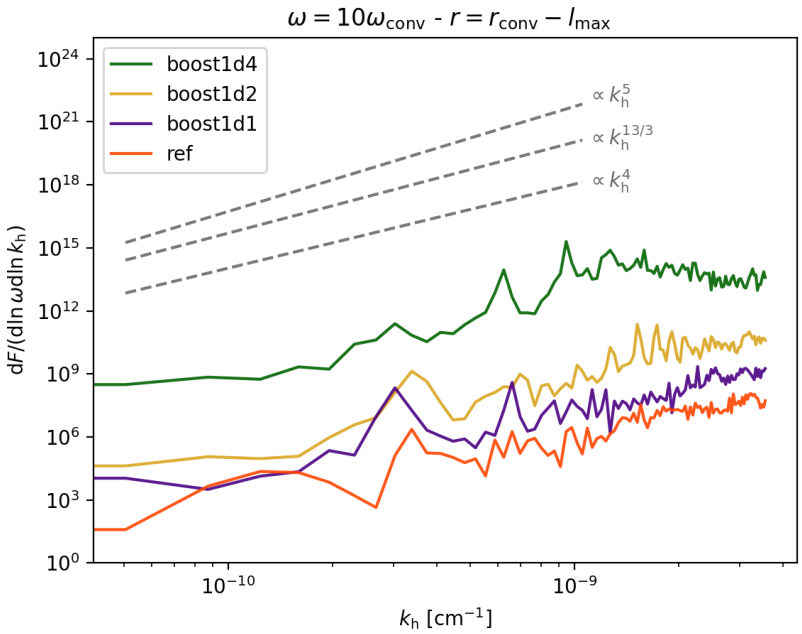

Fig. 6.10 Wave energy flux as a function of the horizontal wavenumber for the four simulations at depth $r = r_\mathrm{conv} - l_\mathrm{max}$. The frequency is fixed at $\omega = 10\omega_\mathrm{conv}$. The dashed lines represent the three theoretical scaling laws, Eqs. (4.26)–(4.28), from Lecoanet and Quataert (2013).

The scaling relationships Eqs. (4.26)–(4.28) from Lecoanet and Quataert (2013) are also displayed in Fig. 6.10. The derivation of their expressions is valid for $k_\mathrm{h} \lesssim k_\mathrm{h,max} \propto \omega_\mathrm{conv}^{-3/2}$ (see Eq. (6.4)). The low-ω slope of the simulated spectra is roughly consistent with these theoretical scalings, even though the large statistical variance of the spectra prevents an accurate comparison without running over very long simulation times, or averaging over many ensemble simulations.

In this section, we have showed that the wave fluxes in the radiative zone obtained from present simulations obey scaling laws with frequency and wavenumber that are broadly consistent with the ones predicted by theoretical models. However, discriminating or constraining the theoretical models with precise measurement of slopes from simulations remains challenging. In particular, even though our simulations are consistent with theoretical predictions, we caution

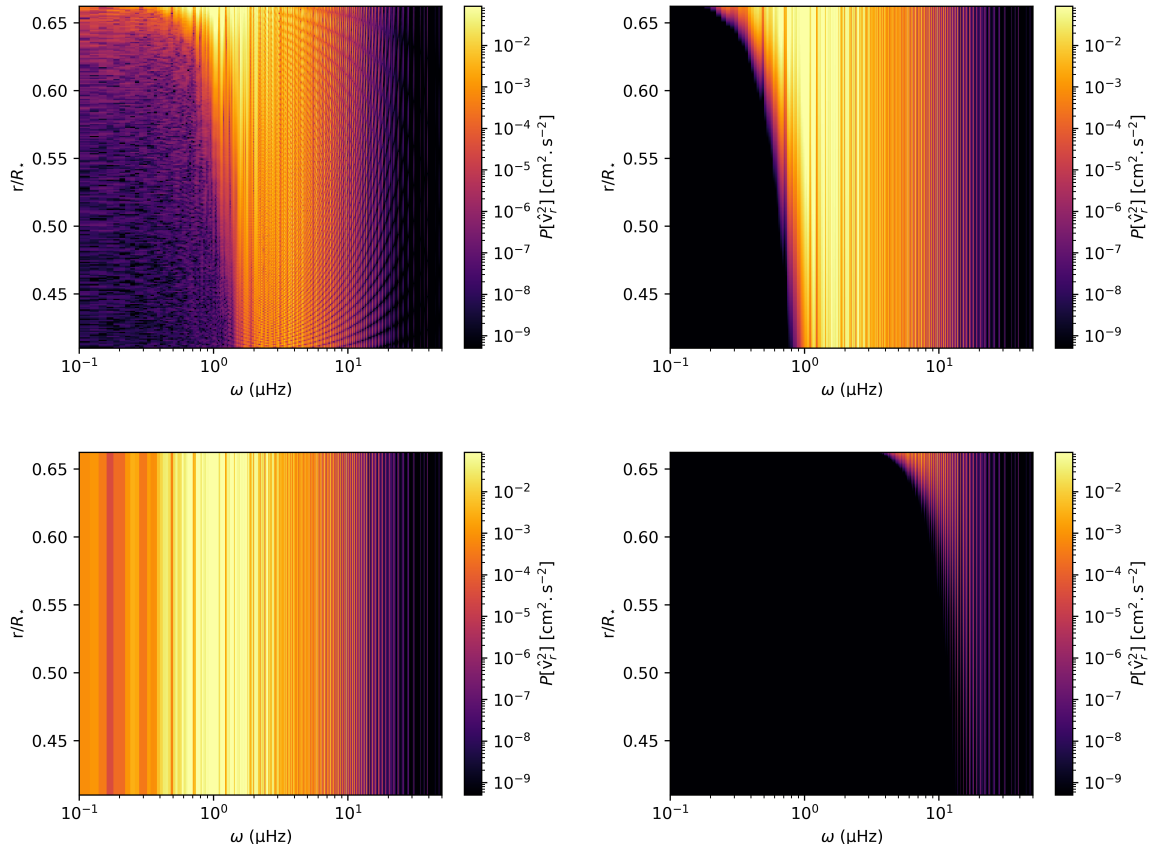

Fig. 6.11 Power spectra of the radial velocity for the simulation *ref* obtained from MUSIC (top left) and the theoretical prediction using Eq. (4.14) with the dependence on frequency, ω^{-n}, which varies: $n = 4$ (top right), $n = 3$ (bottom left), and $n = 5$ (bottom right). The angular degree is fixed at $\ell = 5$. For the theoretical spectra, a minimal threshold is set at a value of 10^{-7} for better visibility.

that these simulations are not fully turbulent and that the two-dimensional geometry does not allow us to resolve realistic plumes.

6.6.2 Spatial damping of IGWs

Internal gravity waves propagating in stably stratified stellar interiors are expected to be damped by radiative diffusion. Their amplitude exponentially decays with a factor $\exp(-\tau)$, with τ given by (4.14).

In order to verify that the damping of the waves in the simulations is consistent with the theoretical expectations, in Fig. 6.11 we use a similar method as Alvan et al. (2014) to compare the evolution of the computed power spectrum of the radial velocity, $P[\hat{v}_r^2]$ (see Eq. (B.5)), to

the one predicted theoretically $P_{\text{theory}}[\hat{\mathrm{v}}_r^2]$, for a fixed harmonic degree $\ell_0 = 5$, which is defined as

$$P_{\text{theory}}[\hat{\mathrm{v}}_r^2](r, \ell_0, \omega) = P[\hat{\mathrm{v}}_r^2](r_{\text{conv}} - l_{\max}, \ell_0, \omega) \times \mathrm{e}^{-\tau(r,\ell_0,\omega)}. \tag{6.25}$$

The depth $r = r_{\text{conv}} - l_{\max}$ is chosen in order to avoid any contribution to the radial velocity from convective penetration. In the integral (4.14), the upper bound r_{e} is thus set to $r_{\text{conv}} - l_{\max}$.

To visually compare the spectral density plots, we set an identical colour scale for all panels of Fig. 6.11, adjusted to the noise floor of the simulation. The simulation (top left panel) and theoretical ω^{-4} scaling (top right panel) spectra in Fig. 6.11 show similar patterns, with g modes (vertical bright lines) formed in the radiative zone for frequencies $\gtrsim 1\,\mu$Hz, as well as the absence of modes below $\sim 0.5\,\mu$Hz. To form g modes, propagating IGWs generated by convection travel towards the centre of the star until they reflect at their inner turning point or at the bottom of the simulation domain. A turning point is defined as the radius where $k_r^2 = 0$, or equivalently $\omega = N$, from Eq.(4.2). Travelling back towards the surface, they again reflect at their outer turning point. Travelling back and forth, propagating waves of a given frequency and angular degree interfere with themselves and form standing waves.

The radial profile of the spectra between $\sim 0.5\,\mu$Hz and $\sim 10\,\mu$Hz are also similar in both top panels of Fig. 6.11, with waves propagating deeper as the frequency increases; in addition, both spectra reach the noise floor (darkest colour) at comparable frequencies for each given radius in both top panels. As expected from the radiative damping formulation given by Eq. (4.14), the damping is stronger for low frequency waves. In the MUSIC spectrum, the nodes of the g modes are visible as dark spots of low energy spaced in radius along a given mode; they are not visible on the theoretical reconstructions, as expected from our definition of $P_{\text{theory}}[\hat{\mathrm{v}}_r^2]$.

In previous studies of IGWs using hydrodynamical simulations, the radiative damping of the waves was found to have a scaling with frequency closer to ω^{-3}, instead of ω^{-4} (Alvan et al., 2014; Rogers et al., 2013). In order to directly compare our results with Alvan et al. (2014); Rogers et al. (2013) and to keep τ dimensionless when changing only the exponent of ω, we replace $N^3\omega^{-4}$ in (4.14) with $N^3\omega^{-q} \times (1\ \text{Hz})^{q-4}$ for $q = 3, 4, 5$. We plot in Fig. 6.11 the theoretical spectra calculated using a dependence of ω^{-3} and ω^{-5}. We can exclude these scaling laws for the MUSIC spectrum, which has a dependence in ω closer to ω^{-4}, as predicted by Eq. (4.14).

Figure 6.12 shows that Eq.(4.14) also holds for the three boosted simulations, provided that radiative diffusivity is increased with the same enhancement factor as the luminosity. In addition to simulation *ref*, we also checked for these boosted simulations that damping laws scaling as ω^{-3} and ω^{-5} can be excluded. The MUSIC spectra thus provide a good agreement with the theoretical predictions of radiative damping.

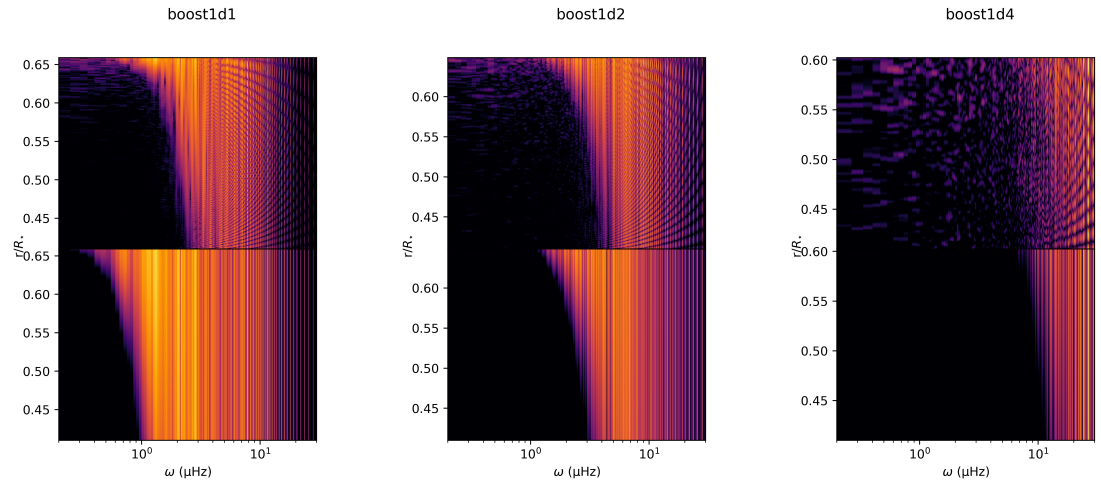

Fig. 6.12 Power spectra of the radial velocity for simulations *boost1d1* (left), *boost1d2* (middle), and *boost1d4* (right) obtained from MUSIC (top row) and the theoretical prediction using Eq. (4.14) with the dependence on frequency, ω^{-4} (bottom row). The angular degree is fixed at $\ell = 5$. For the theoretical spectra, a minimal threshold is set for better visibility.

These results show that if both the luminosity and the radiative diffusivity are enhanced by the same factor, the damping of the waves follows similar scaling for all enhancement factors, and is in agreement with the theoretical prediction for radiative damping. The boosting factor will have an important effect on the spectrum of surviving g modes. Since g modes can only appear with waves propagating in the whole domain, they can only be observed when waves are able to travel down to the inner boundary without being fully damped. Because increasing the luminosity enhancement factor shifts the IGW excitation spectrum towards higher frequencies, the frequency of waves surviving at the inner boundary will increase with the boosting factor. Indeed, for *ref* in Fig. 6.11, the lowest frequency g modes that are formed have a frequency of $\omega \sim 1.0\,\mu\text{Hz}$. In Fig. 6.12, we can see that for *boost1d1*, *boost1d2,* and *boost1d4*, the minimum frequency of the surviving g modes is $\omega \sim 2.0\,\mu\text{Hz}$, $\omega \sim 3.0\,\mu\text{Hz}$, and $\omega \sim 8.0\,\mu\text{Hz}$, respectively, for the harmonic degree $\ell = 5$. Below these frequencies, waves are either damped before being able to propagate back and forth in the radiative zone or not excited, and thus are unable to form g modes.

6.7 Numerical resolution of IGWs

Finally, we would like to draw attention to a numerical resolution issue related to the study of IGW damping in simulations. The condition of propagation of IGWs in a stably stratified

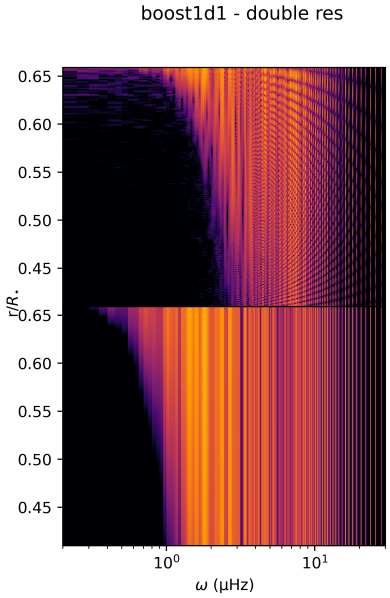

Fig. 6.13 Power spectra of the radial velocity for the simulation *boost1d1* with double resolution (1024x1024) obtained from MUSIC (top) and the theoretical prediction using Eq. (4.14) with the dependence on frequency, ω^{-4} (bottom). The angular degree is fixed at $\ell = 5$. For the theoretical spectra, a minimal threshold is set for better visibility.

medium is set by their dispersion relation given by Eq.(4.2). It predicts that the radial wavelength becomes small as $\omega \to 0$. For a given spatial grid, there is a maximal radial wavenumber, or equivalently a minimal wavelength, that can be resolved on the grid. As the wavelength approaches the grid resolution, numerical dissipation of the numerical scheme is expected to increase; ultimately, as the radial wavelength approaches twice the length of a grid cell, it becomes impossible to represent the wave on the grid, and aliasing occurs. This is potentially problematic for the study of IGW damping, which requires looking at very low frequencies.

Using the dispersion relation Eq. (4.2) and considering a given spatial resolution of the mesh, we can define a corresponding minimal frequency, given in the limit $\omega \ll N$

$$\omega_{\min} = \frac{\sqrt{\ell(\ell+1)}}{r} \frac{\lambda_{r,min}}{2\pi} N, \tag{6.26}$$

with $\lambda_{r,\min}$ the minimal radial wavelength that can be resolved with a given radial resolution. In order to give an idea of the minimal frequency that we can resolve we arbitrarily set $\lambda_{r,\min} \sim 5\Delta r$, where Δr is the radial resolution. It means that we consider a minimum of five radial grid cells per radial wavelength. As mentioned in Sect. 6.2.2 the radial resolution of our simulations is constant with $\Delta r \simeq 5.5 \times 10^7$ cm. This gives a minimal frequency for IGW of 0.62 μHz at low degree ℓ but it is even larger as ℓ increases.

For our simulations, we can see in Figs. 6.11 and 6.12 that some aliasing is present in the g modes around 1 μHz, which is close to our estimation $\omega_{\min}$. In order to confirm our results, we performed a test with a simulation identical to *boost1d1* but with double resolution $N_r \times N_\theta = 1024\times1024$. Figure 6.13 shows the power spectrum from MUSIC together with the theoretically predicted one. There is no more aliasing at low frequencies, and more importantly, the spectrum is still very similar to the one shown in Fig. 6.12 for simulation *boost1d1* with lower resolution. This gives us thus some confidence that the damping we observe in our simulations is indeed radiative damping.

Finally, we draw attention to a maximum frequency that also exists because of the mesh size. Since we are working in spherical geometry, the size of the grid cells in the θ-direction is not constant, it depends on radius as

$$\Delta\theta(r) = \frac{r\pi}{N_\theta}. \tag{6.27}$$

In the whole domain considered in our simulations we have $\Delta\theta > \Delta r$. Consequently, even if the horizontal wavelength is larger than the radial one, the horizontal direction could also be a limiting factor for the resolution of IGWs via the condition

$$\omega_{\max}(r) = \frac{N}{\sqrt{\frac{a_\theta^2\pi^2r^2}{N_\theta^2\lambda_r^2}+1}} \tag{6.28}$$

with a_θ an integer that is the number of grid cells per horizontal wavelength we want to set as minimal resolution, $\lambda_{h,\min} \sim a_\theta\Delta\theta$. In the limit $a_\theta\pi r/(N_\theta\lambda_r) \to 0$, we obtain the classical condition $\omega_{max} = N$. This latter condition is then fulfilled for large radial wavelength, simulations with very high resolution and near the centre of the star. It is interesting to note that also in this case the limiting wavelength is the radial one. For most of the waves in our simulations, we found that $\omega_{\max}(r) \geq 0.9N(r)$. However, for a wave with radial wavelength close to $\lambda_{r,\min}$, the maximal frequency $\omega_{\max}(r)$ can be close to half the Brunt-Väisälä frequency.

6.8 Discussion & Outlook

In this chapter, we have focused on the impact of enhanced luminosity and thermal diffusivity on IGWs excited by convection in hydrodynamical simulations of stellar interiors. Our main results are listed below.

- Increasing the luminosity of a simulation decreases the convective turnover time, τ_{conv}, and thus increases the convective turnover frequency, ω_{conv}. The larger the luminosity,

the higher $\omega_{\rm conv}$. Typical dynamical quantities such as velocities scale with the luminosity in the convective zone.

- We show that an appropriate rescaling of the frequencies with $\omega_{\rm conv}$ and of the velocities with $L^{1/3}$ provides a kinetic energy spectrum in the convective zone that is independent of the luminosity enhancement factor. But firstly, such rescaling does not hold in the radiative zone. Secondly, our results highlight that the relevant frequency range of IGWs that are excited and propagating strongly depends on the luminosity enhancement factor. The waves that bear most of the energy are not in the same frequency and spatial ranges for simulations with different luminosities. As the luminosity increases, the frequency distribution is shifted towards higher ω, whereas the angular degree distribution is shifted towards lower ℓ (larger wavelengths).

- Our simulated energy flux spectra are broadly consistent with IGWs being generated from a combination of two excitation mechanisms: Reynolds stresses and penetrative convection. At high ω, we observe scaling laws for the flux that are compatible with the Reynolds stress excitation models from Lecoanet and Quataert (2013). While those authors predict different expressions for the wave energy flux depending on the stratification at the radiative–convective boundary, it is difficult to compare the slopes obtained from the simulations with the ones predicted by theoretical models given the variance of the spectra and the presence of high-amplitude g modes. As ω decreases, the radial energy flux departs from a power law and reaches a maximum for $\omega \simeq \omega_{\rm conv}$. In this range, the flux is more consistent with the predictions from Pinçon et al. (2016) from penetrative convection. However, we are aware that with global two-dimensional simulations of stellar interiors, flows cannot present a real state of turbulence, feature well-identified plumes, or finely resolve penetrating convection. Therefore, we cannot expect the analytical models of Lecoanet and Quataert (2013) and Pinçon et al. (2016) to apply precisely and quantitatively. Nevertheless, our results qualitatively support a picture where IGWs are simultaneously excited by Reynolds-like stresses at high ω and by penetrating convection around $\omega_{\rm conv}$.

- Our work therefore suggests an important consequence for boosted luminosity simulations: as the luminosity enhancement factor increases, the wave flux is shifted towards higher ω. This also implies that the peak of the wave flux will be closer to the Brunt-Väisälä frequency, limiting the extent of the frequency range of excited IGWs. Furthermore, larger enhancement factors could impact the local stratification (see Baraffe et al., 2021, for more details), further interfering with wave excitation processes. Consequently, while it is difficult with present simulations to conclude on the impact of the luminosity

enhancement factor on the detailed shape of the wave flux spectrum, our results highlight that the artificial boosting of a simulation has a noticeable impact on the wave flux by changing the location of the peak of the spectra in terms of frequency and horizontal wavenumber.

- For radiative damping at low frequencies, in contrast to results reported by other groups, our simulations present a decay in the amplitude of waves in the radiative zone, which closely decreases as $\propto \exp\left(-\omega^{-4}\right)$ as predicted by theory (Press, 1981). This dependence of the damping on frequency holds in the boosted simulations on the condition that the radiative diffusivity is increased by the same amount as the luminosity. We also show that the waves that reach the inner boundary of the domain are affected by the boost as a result of a change in the wave excitation spectrum and with fewer g modes surviving with higher luminosity enhancement factors. This could have some importance when studying angular momentum transport in stellar interiors. We want to stress that radiative damping is difficult to study numerically because it is more efficient at low frequencies, at which the radial wavelength of the IGWs becomes close to the radial grid resolution due to the dispersion relation. Our test simulation at double resolution strengthens our confidence that we are actually observing radiative damping.

In summary, our analysis shows that artificially increasing the luminosity of a stellar model can be a useful technique. It can be justified in particular for studies restricted to the dynamics in a convective zone, since appropriate rescaling laws can apply. However, it has to be used with great caution to predict the spectra of IGWs and g modes in stars. These spectra will define how waves interact with the dynamics and internal structure of stars. Consequently, making predictions for more realistic systems, in particular when related to mixing and angular momentum transport, is not straightforward when using simulations with artificially enhanced luminosity.

Chapter 7

Waves analysis in a zero-age-main-sequence 5 $M_\odot$ star model

Unlike main sequence low-mass stars, such as the model studied in the Chapt. 6, where the radiative zone is located in the inner part of the star, more massive main sequence stars with $M \gtrsim 2M_\odot$ present a radiative envelope. Internal gravity waves generated at the edge of the convective core propagate towards the surface through a medium of decreasing density, which tend to increase their amplitude. These waves are also damped by radiative diffusion as they travel, and are suggested to transport energy and angular momentum and mix chemical elements through this mechanism (Schatzman, 1993). Thus, the evolution of IGWs amplitude will depend on the interplay between growth due to decreasing density and decay due to radiative damping. It remains unclear if these waves should be able to propagate up to the surface. More than a decade ago, Blomme et al. (2011) observed a low frequency power excess in the spectra of O type stars observed by the CoRoT (Auvergne et al., 2009) mission. They concluded that the physical origin of this power excess was unclear but give three possible explanations: granulation, stellar wind and subsurface convective zone. In recent studies, Bowman et al. (2019, 2020) claim that a similar low frequency power excess in the spectrum of O and B type stars observed by the CoRoT and TESS (Ricker et al., 2015) satellites is due to IGWs excited by turbulent core convection. This hypothesis is supported by hydrodynamical simulations in three (Edelmann et al., 2019) and two dimensions (Ratnasingam et al., 2020). However, theoretical work by Lecoanet et al. (2019) and numerical simulations by Lecoanet et al. (2021) do not agree with this conclusion and state that the origin of this power excess is more probably due to a near surface convection zone (Cantiello et al., 2021). This question will remain difficult to answer while the properties of IGWs in such stars remain poorly known.

Hydrodynamical simulations offer a great opportunity to test theoretical models and guide observations. In particular, numerical modelling of internal waves, is a good way to get

Table 7.1 Properties of the initial stellar model used for the 2D hydrodynamical simulations.

$M/M_\odot$	$L_{\rm star}/L_\odot^{(a)}$	$R_{\rm star}$ (cm)	$r_{\rm conv}/R_{\rm star}$	$H_{P,\rm conv}$ (cm)
5	523	1.8424×10^{11}	0.1814	1.828×10^{10}

With mass M, luminosity $L_{\rm star}$, radius $R_{\rm star}$, size of the convective core $r_{\rm conv}$ and pressure scale height at the convective boundary $H_{p,\rm conv}$.
[a] We use $L_\odot = 3.839 \times 10^{33}$ erg/s.

constraints on the spectrum generated by convection, their amplitude and damping rate within the star. This has already proven to be efficient in simulations of solar-like stars (see for example Alvan et al., 2014; Rogers and Glatzmaier, 2005a) as well as stars with convective cores (see for example Horst et al., 2020; Rogers et al., 2013). In this chapter, we present two-dimensional simulations of a 5 solar mass star with different enhancement factors for the luminosity and the radiative diffusivity. We focus mainly on the damping of IGWs and the impact of boosting on these waves, but we neglect the effect of rotation, even though most OB stars may be moderate to fast rotators.

7.1 Numerical simulations

We performed two-dimensional simulations of the interior of a $5M_\odot$ star model at zero-age-main-sequence (ZAMS) with the MUSIC code (see Sect. 6.2.1).

7.1.1 Initial stellar model

The initial one-dimensional model has an initial helium abundance in mass fraction Y=0.28 and solar metallicity Z=0.02 and is evolved through the pre-main-sequence and the early main-sequence. The initial structure of the simulations have burnt 1% of their hydrogen since the ZAMS. An analysis of a similar $5M_\odot$ star model but at later stages of evolution with a steeper gradient of molecular weight at the core boundary is currently underway (Morison et al. [incl. Le Saux], in prep). There is no overshooting or diffusion considered during the computation of the one-dimensional model. In the MUSIC simulations, the energy generated by nuclear reactions are taken into account in the energy equation as a source term and the nuclear energy profile is the one from the one-dimensional model. As the nuclear timescale is orders of magnitude larger than the time scales considered in the simulations (see Sect. 2.1), the nuclear energy is assumed to remain constant during the run of the MUSIC simulations. The properties of the initial one-dimensional model are summarised in Table 7.1.

Table 7.2 Summary of the two-dimensional simulations.

Simulation	$L/L_{\rm star}$	$\tau_{\rm conv}^{(a)}$ (s)	$N_{\rm conv}^{(b)}$	$\omega_{\rm conv}^{(c)}$ (μHz)
ref	1	1.5×10^6	52	0.7
boost1d1	10^1	6.0×10^5	35	1.7
boost1d2	10^2	3.0×10^5	58	3.4
boost1d4	10^4	6.5×10^4	54	15.4

[a] Convective turnover time (see Eq. (4.14) for its definition), measured from our simulations.
[b] Number of convective turnover times used for this work.
[c] Convective turnover frequency associated with $\tau_{\rm conv}$

7.1.2 Spherical-shell geometry and boundary conditions

Two-dimensional simulations are performed in a spherical shell using spherical coordinates, namely r the radius and the polar angle θ, and assuming azimuthal symmetry in the ϕ-direction. For all simulations, the inner radius $r_{\rm in}$ is set at 0.02 $R_{\rm star}$ and the outer radius $r_{\rm out}$ at 0.91 $R_{\rm star}$. Note that extension of the numerical domain to the photosphere ($r = R_{\rm star}$) is an open challenge for stellar hydrodynamical simulations, given the sharp decrease of the pressure scale height with increasing radius. The domain in the co-latitudinal direction ranges from 0 to π. We use a uniform grid resolution of $N_r \times N_\theta = 1322 \times 668$ cells. This provides a good resolution of the pressure scale height at the convective boundary $H_{p,\rm conv}/\Delta r \sim 147$, with $\Delta r = 1242$ km, the size of a radial grid cell.

The boundary conditions used and the method to boost a model are the same as the ones described in Sect. 6.2.1 and Sect. 6.2.3 respectively. The characteristics of the four numerical models used for this study are presented in Table 7.2. The definition we use for the convective turnover time $\tau_{\rm conv}$ and associated frequency $\omega_{\rm conv}$ are given by Eq. (6.2). Aerts et al. (2021) provide observed values of the convective turnover frequency for Slowly-Pulsating B (SPB) stars with mass approximately between $3M_\odot$ and $9M_\odot$. They found typical values of $\omega_{\rm conv}$ in the range 0.2 to 0.5 μHz, which is close to the value of 0.7 μHz in our reference model. We consider the stellar model studied in this chapter to be a template of intermediate-mass stars with a convective core, with mass between 3 and 20 $M_\odot$. Therefore, our conclusions regarding wave damping and propagation could be applied, at least qualitatively, to other stellar masses in this range.

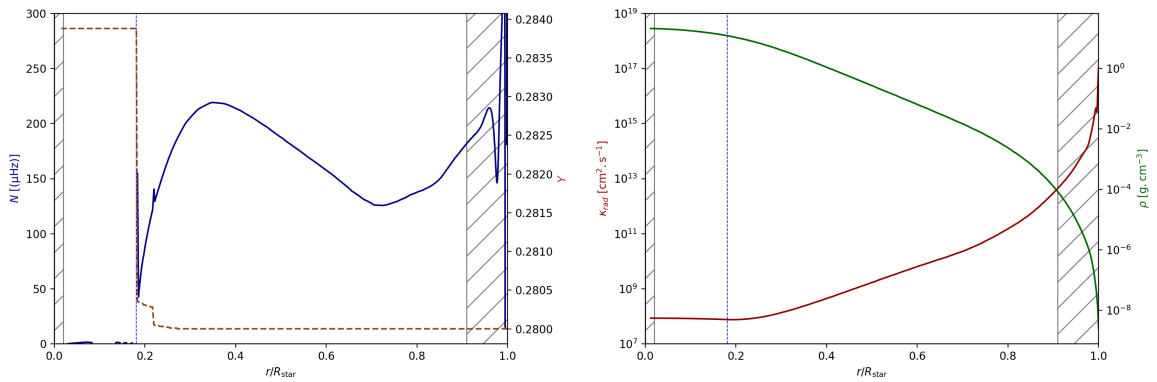

Fig. 7.1 Radial profile of the Brunt-Väisälä frequency in the radiative zone (left panel) and of radiative diffusivity $\kappa_{\rm rad}$ (red, left y-axis) and density ρ (green right x-axis) (right panel) for the initial 1D model. The hatched regions are not considered in the two-dimensional simulations.

7.1.3 Stratification and radiative diffusivity

Internal gravity waves are able to propagate in radiative zones and are evanescent in convective zones. As explained in Chapt. 3, this means they can travel in region where $N^2 > 0$, with the condition on their frequency $\omega < N$.

The left panel of Fig. 7.1 shows the radial profile of the Brunt-Väisälä frequency (left y-axis, blue curve) and the helium mass fraction Y (right y-axis, brown dashed curve) in the initial one-dimensional model. The peak of the Brunt-Väisälä frequency just above the convective core is a result of the small gradient of Y in this region. In our simulations, the hatched regions are excluded. From this plot, we can see that an IGW of frequency ω might not propagate in the whole radiative envelope. For instance, in the considered model, a wave with a frequency of 150 μHz may only propagate between $r \sim 0.25 R_{\rm star}$ and $r \sim 0.6 R_{\rm star}$.

As explained in Sect. 4.2, radiative diffusivity is of major importance in stellar interiors, as it is supposed to be the main mechanism that damps internal waves. In our reference simulation, model *ref*, we use a realistic profile of radiative diffusivity for a $5 M_\odot$ model. This allows modelling of a realistic damping of IGWs, as we showed in Sect. 6.6.2. This profile is displayed in the right panel of Fig. 7.1 (red, left y-axis). This figure also shows the radial profile of the density in our model (green, right y-axis). Note that the profiles displayed in Fig. 7.1 left panel are the ones used in our simulation *ref*. This is important as these two quantities define the propagation properties of IGWs.

Indeed, as they propagate towards the surface, IGWs amplitudes grow due to decreasing density and decay due to radiative damping. The variation of both the radiative diffusivity and the density is very large in a star, by 9 orders of magnitude between the centre and the surface.

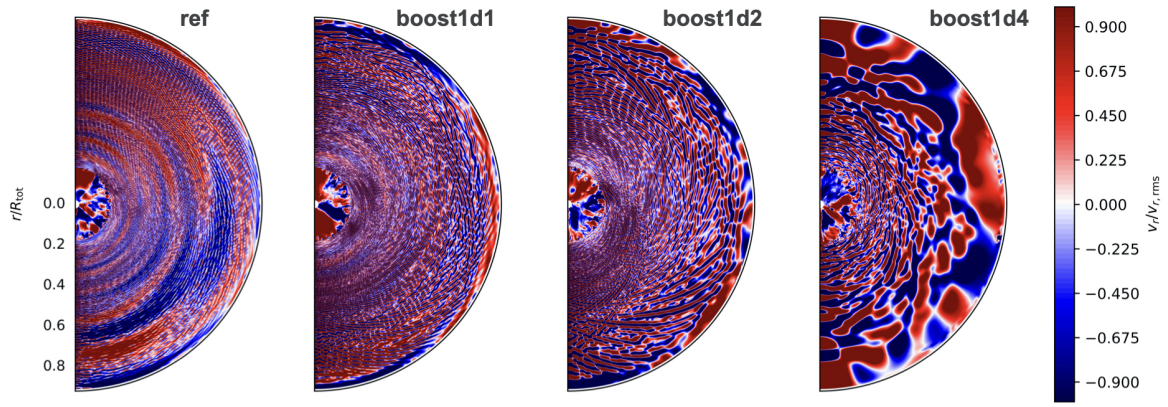

Fig. 7.2 Visualisation of the radial velocity for the four stellar simulations *ref*, *boost1d1*, *boost1d2,* and *boost1d4* as a function of radius r and co-latitude θ. The radial velocity is normalised by the rms radial velocity. Positive values of the radial velocity (ref) are outward and negative (blue) are inward.

This is one of the main challenges that hydrodynamical simulations have to deal with (see Sect. 5.2). In our simulations, that exclude the 9% outer layers, these variations are restricted to approximately 5 orders of magnitude. These variations have to be taken into account in hydrodynamical simulations because they significantly impact propagation of IGWs as we will see in the next sections

7.2 Velocities

Internal gravity waves manifest themselves as perturbations in density, temperature, luminosity or velocity. In this section, we focus on the radial velocity amplitude to study IGWs properties.

7.2.1 Radial velocity pattern

Figure 7.2 shows snapshots of the radial velocity v_r for the four simulations. For better visualisation, the radial velocity is normalised by the root-mean-square value of the radial velocity $\mathrm{v}_{r,\mathrm{rms}}$. The convective core extends from the centre up to $r_{\mathrm{conv}} = 0.1814 R_{\mathrm{star}}$. In this region, the structure of the flows is similar in the four snapshots, with large coherent upflows (red) and downflows (blue).

The three simulations *ref*, *boost1d1* and *boost1d2* present similar patterns in the radiative envelope with the classical spiral structure corresponding to wavefronts of IGWs. Figure 7.2 suggests that the angle α between the total and the horizontal wave vectors (see Eq. (4.3))

decreases with the boosting factor. Therefore, waves of higher frequencies dominate in the radiative zone when the luminosity is increased. This was also observed in Fig. 6.3 for the solar-like star simulations presented in Chapt. 6. The structure of the radiative envelope of *boost1d4* does not present the classical spiral IGWs wavefronts pattern. The structure in this most boosted case is larger scale and not periodic any more. Similar patterns are observed in other simulations of intermediate-mass stars using the same or larger artificial boosting factors for the luminosity and the radiative diffusivity (see for example Edelmann et al., 2019; Horst et al., 2020).

7.2.2 Radial evolution of the velocity amplitude

According to linear theory, the evolution of the amplitude of an IGW is expected to depend on the stratification of the supporting medium and on spatial damping due to radiative effects as well as on the frequency and wavelength of the wave. The analytical formula that expresses these dependences is given by Eq. (4.13). It is important to keep in mind that in boosted simulations, the radiative diffusivity is enhanced by the same amount as the luminosity. Consequently, wave damping by radiative diffusion is enhanced in a boosted simulation, as shown in Sect. 6.6.2. In Eq. (4.13), we have introduced a constant C that fixes the amplitude. In this work, we chose to fix it such as the analytical velocity amplitude of a wave at $r = r_e$ matches the amplitude of the velocity in the simulations, i.e. $\mathrm{v}_0(\ell,\omega) = \mathrm{v}_r(r_e,\ell,\omega)$. We recall that r_e is the radius at which waves are excited. Therefore, we obtain

$$C = \mathrm{v}_0(\ell,\omega)\rho_0^{1/2}k_{\mathrm{h},0}^{-3/2}\left(\frac{N_0^2-\omega^2}{\omega^2}\right)^{1/4}, \tag{7.1}$$

with $k_{\mathrm{h},0} = \sqrt{\ell(\ell+1)}/r_e$, $\rho_0 = \rho(r_e)$, $N_0 = N(r_e)$ and by definition $\tau(r_e,\ell,\omega) = 0$ (see Eq. (4.14)). Finally, we can write the analytical expression of the norm of the radial velocity as

$$|\mathrm{v}_r|(r,\ell,\omega) = \mathrm{v}_0(\ell,\omega)\left(\frac{\rho}{\rho_0}\right)^{-1/2}\left(\frac{k_\mathrm{h}}{k_{\mathrm{h},0}}\right)^{3/2}\left(\frac{N^2-\omega^2}{N_0^2-\omega^2}\right)^{-1/4}\mathrm{e}^{-\tau/2}. \tag{7.2}$$

In the following we will drop the norm notation $|.|$ and will refer to v_r as the norm of the radial velocity. Equation (7.2) is similar to the one obtained by Ratnasingam et al. (2019) (see their Eq. (13)). In our simulations, we determine the amplitude of the radial velocity at a given frequency ω and angular degree ℓ using a temporal Fourier transform and a decomposition on the spherical harmonic basis of the velocities computed by MUSIC. The definition we are using for spherical harmonics and Fourier transform are defined in Appendix B. We obtain the power

spectrum of the radial velocity $P[\hat{v}_r^2](r, \ell, \omega)$, which scales as the amplitude squared of a given wave (ℓ, ω).

Figure 7.3 compares the analytical expression from Eq. (7.2) (dotted lines) to the corresponding wave velocity amplitude from MUSIC simulations, $\sqrt{P[\hat{v}_r^2]}$ (solid lines), as a function of normalised radius for the four numerical models. We have also included the analytical velocity amplitude without the damping term (dashed lines), i.e. we are neglecting the term $e^{-\tau/2}$ in Eq. (7.2). The spatial boundaries of the simulation domain at $r_{\rm in} = 0.02 R_{\rm star}$ and $r_{\rm out} = 0.91 R_{\rm star}$ are specified by the vertical black dashed lines, and the convective boundary $r_{\rm conv} = 0.1814 R_{\rm star}$ is indicated by the vertical blue dashed line. For the analytical expressions, we need to set the initial velocity amplitude of the waves in the excitation region, i.e. close to the convective boundary. We arbitrarily chose for v_0, the value of the radial velocity in the simulations at $r_e = 0.183 R_{\rm star}$, just above the convective core. This to avoid having a component of the velocity due to penetrative convection.

Figure 7.3 presents the velocity amplitude of a wave with angular degree $\ell = 5$ and frequency $\omega = 45.2$ μHz. In the four simulations, the wave amplitude shows a similar oscillatory pattern, where the troughs are the radial nodes of the corresponding g mode. For the mode observed in Fig. 7.3, the oscillation code GYRE predicts a radial order [1] $n = -9$, which is also the number of nodes observed in the simulations. This confirms that we see g modes in Fig. 7.3.

Compared with the analytical predictions from Eq. (7.2) (dotted lines in Fig. 7.3), the simulation velocities present a very similar global evolution of their amplitude from the convective boundary up to the top of the simulation domain. Except for the oscillations but these are not taken into account in the linear analytical expression of the velocity amplitude. However, there are notable differences between the four numerical models. Firstly, as expected, the velocity amplitude of the waves increases with the enhancement of the luminosity. Secondly, the analytical amplitudes predict a sharp drop at a given radius close to the surface, which corresponds to the location where the wave is totally damped out, i.e. the location where the wave will deposit most of its energy. This abrupt drop is indeed due to radiative damping, as it is not present in the case with no damping (dashed lines). For models *ref*, *boost1d1* and *boost1d2* this abrupt drop is approximately at $r \simeq R_{\rm star}$, but for model *boost1d4* it is located around $r \simeq 0.91 R_{\rm star}$. By looking at Eq. (7.2) we can see the radiative diffusivity, which is enhanced by the same amount as the luminosity, is included in the expression of τ. As a result, damping of waves by radiative diffusion increases in a boosted model. This is why the sharp drop of the dotted lines is not located at the same radius for the four cases. However, for the waves considered, with $\ell = 5$ and $\omega = 45.2$ μHz, this sharp drop is located at radii $r \geq 0.91 R_{\rm star}$, thus they are able to reach the top of the simulation domain.

[1] By convention, the radial order n is negative for a g mode and positive for a p mode (standing acoustic waves).

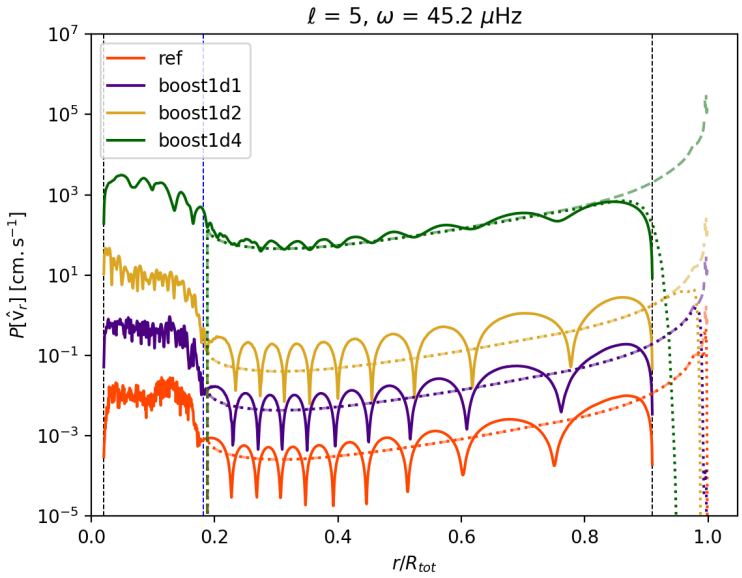

Fig. 7.3 Wave amplitude as a function of normalised radius for the four simulations *ref* (orange), *boost1d1* (indigo), *boost1d2* (yellow), and *boost1d4* (green) for angular degree $\ell = 5$ and frequencies $\omega = 45.2$ μHz. The vertical black lines indicate the boundaries of the simulation domain and the vertical blue line indicate the convective boundary. The solid lines are the velocity measured in the simulations. Dotted and dashed lines are the theoretical velocity amplitudes computed with Eq. (7.2) with and without the damping term, respectively.

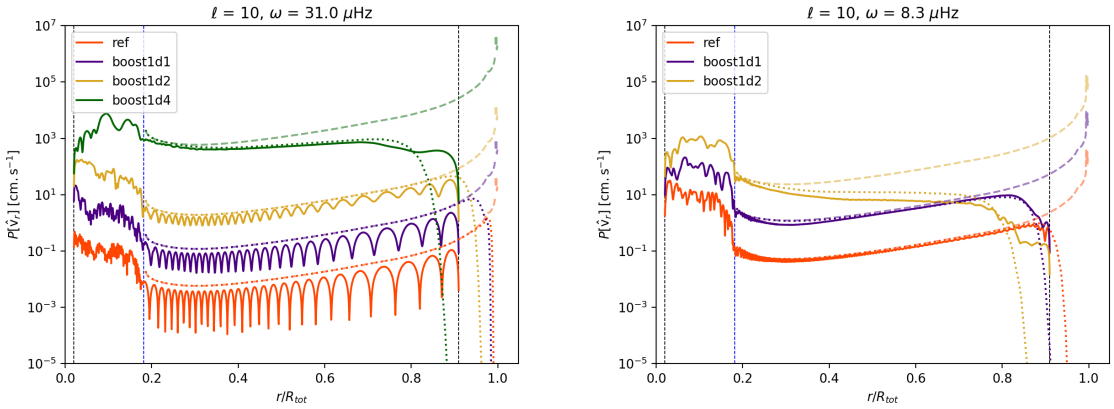

Fig. 7.4 Same as Fig. 7.3 but for waves with $\ell = 10$ and $\omega = 31.0$ µHz (left panel) and with $\ell = 10$ and $\omega = 8.3$ µHz (right panel)

7.2.3 Influence of the boost

From Eqs. (4.14) and (7.2), it is clear that when the angular degree ℓ and the frequency ω are changed, the amplitude and the damping of the corresponding wave are impacted. Indeed, Eq. (7.2) shows that wave amplitude depends on ℓ and ω and Eq. (4.14) shows that waves with higher ℓ and smaller ω will be damped more efficiently. The radial velocity amplitude for a wave with $\ell = 10$ and $\omega = 31.0$ µHz is plotted on the left panel of Fig. 7.4. As expected, the damping is more important than for the wave with $\ell = 5$ and $\omega = 45.2$ µHz (see Fig. 7.3). This is highlighted by the abrupt drop of the theoretical amplitude (dotted lines) which is shifted towards smaller radii in the three boosted models. Indeed, for this wave the drop is located at $r \simeq 0.95 R_{\rm star}$ in model *boost1d1*, $r \simeq 0.91 R_{\rm star}$ in model *boost1d2* and $r \simeq 0.8 R_{\rm star}$ in model *boost1d4*. However, for model *ref* the location of the drop is not changed, meaning that the effect of radiative damping remains weak for this wave with $\ell = 10$ and $\omega = 31.0$ µHz. Note that for the four simulations, the agreement with theory is still relatively good. The case with no damping (dashed lines) is now clearly different from the other two (solid and dotted lines). In that case, the shape of the curves remains the same as in Fig. 7.3. Neglecting the damping for these waves would imply that they would be able to propagate up to the surface for all models, yielding an erroneous prediction.

On the right panel of Fig. 7.4, the angular degree and frequency are set to $\ell = 10$ and $\omega = 8.3$ µHz respectively, implying more efficient damping. Model *boost1d4* is not plotted here, as we do not expect such low frequency IGWs to be excited in this simulation. Indeed, the frequency $\omega = 8.3$ µHz is smaller than the convective frequency, $\omega_{\rm conv} = 15.4$ µHz, for this simulation (see Table 7.2). A convective region with associated frequency $\omega_{\rm conv}$ is expected to generate waves with frequencies $\omega \geq \omega_{\rm conv}$ (Lecoanet and Quataert, 2013). On this plot, the

abrupt drop of the analytically predicted velocity amplitude (dotted lines) for models *boost1d1* and *boost1d2* is located at $r \simeq 0.9R_{\rm star}$ and $r \simeq 0.85R_{\rm star}$, respectively. We thus observe a similar phenomenon as for model *boost1d4* in the left panel of Fig. 7.4. Namely, that the waves in the simulations are damped before the top of the numerical domain and do not form g modes.

Our results highlight that the artificial enhancement of the luminosity and the radiative diffusivity of a numerical model impacts not only the amplitude of the waves, but also their spatial damping. This is particularly important at low frequencies, as expected from Eq. (4.14). This enhanced damping of waves in the low frequency regime in boosted simulations was already suggested by Horst et al. (2020). When the luminosity is boosted, the increased damping means that waves over a smaller range of frequencies reach the top of the cavity. Particularly, low frequency g modes are fully damped in boosted simulations compared to the one with realistic luminosity. In addition, waves of given frequency and angular degree will be damped out in different locations in boosted simulations, therefore depositing their energy in different regions. In a case where the luminosity is artificially enhanced but not the radiative diffusivity, as in the simulation of Horst et al. (2020), the location where IGWs are damped out is not modified. However, because of the higher luminosity, the dominant frequency range of excited waves will be different from in a non boosted case (Sect. 6.4 and 7.3). Therefore, in simulations with different enhancement factors for the luminosity and radiative diffusivity, we do not expect the propagation of IGWs to be identical as in a model with realistic luminosity.

Finally, comparison between the two analytical cases with and without damping also highlights that running simulations with unrealistic radiative diffusivity may not capture the proper propagation properties of IGWs. Particularly for low frequency waves, which are the ones more impacted by radiative diffusion. In these simulations, transport by IGWs should be studied with caution, as well as their ability to propagate up to the surface or not.

7.2.4 Radial kinetic energy density

Figure 7.5 presents the power spectrum of the radial velocity $P[\hat{\mathrm{v}}_r^2]$, as a function of normalised radius and frequency, for an angular degree $\ell = 20$. This quantity $P[\hat{\mathrm{v}}_r^2]$ is equivalent to the radial kinetic energy density. This plot offers a general overview on the dependence of radiative damping of IGWs on frequency and radius. In the convective core, between the bottom of the plot and $r_{\rm conv}$, the spectrum is relatively homogeneous at all frequencies and characteristic of a convective zone. The bright ridges observed in the radiative zone, at $r \geq 0.1814R_{\rm star}$, are high amplitude g modes. The dark knots observed in the bright ridges are the radial nodes of the considered mode. The number of nodes for a given mode defines the radial order n of the mode, and it increases as the frequency decreases. This is an important characteristic of g modes (Aerts et al., 2010).

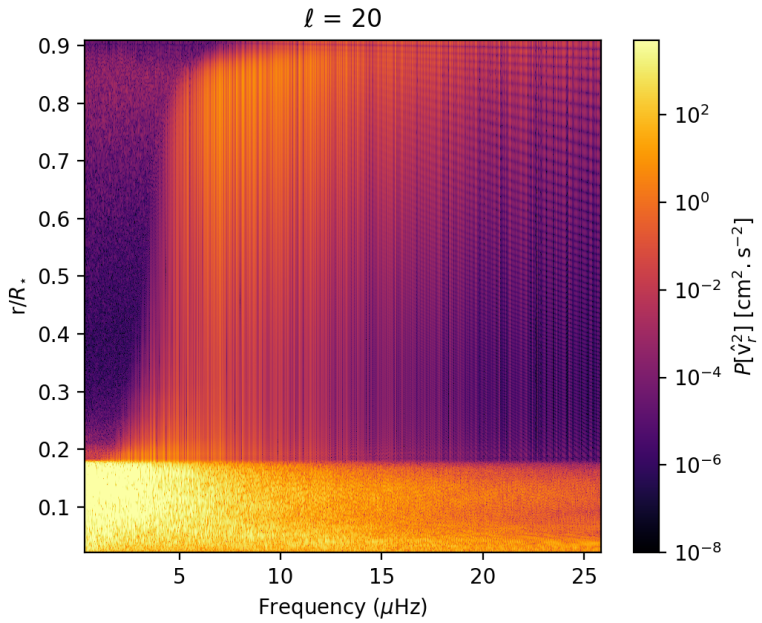

Fig. 7.5 Power spectrum of the radial velocity for the simulation *ref*. The angular degree is fixed at ℓ= 20. The power spectrum is obtained via mode projection on the spherical harmonics basis and a temporal Fourier transform of the radial velocity.

The properties displayed in Fig. 7.5 for model *ref* are common to the three boosted simulations. We find that IGWs are dampened by radiative effects and more importantly that the damping strength depends on the location in radius, as can be expected from the radiative diffusivity profile showed in the right panel of Fig. 7.1. The damping rate seems relatively constant between the convective boundary and $r \simeq 0.8 R_{\rm star}$, but above this radius, wave damping appears to be strengthened. This means that waves deposit their energy in the radiative cavity, but there are regions where this deposition will be more important, particularly close to the top of the simulation domain. This will be further investigated in Sect. 7.5.

7.3 Wave energy flux

In this section, we study the radial wave energy flux in its differential form as given by Eq. (6.24) in order to compare with theoretical predictions (see Sect. 6.6.1 for details).

Figure 7.6 presents the dependence of the differential wave energy flux given by Eq. (6.24) with frequency at two radii, $r = r_{\rm conv} + 0.5 H_{p,\rm conv} \simeq 0.231 R_{\rm star}$ (purple curves) and $r = r_{\rm conv} + 6 H_{p,\rm conv} \simeq 0.777 R_{\rm star}$ (green curves). The two vertical dashed lines indicate the Brunt-Väisälä frequencies at the radii with the same colour code. The wave fluxes are plotted

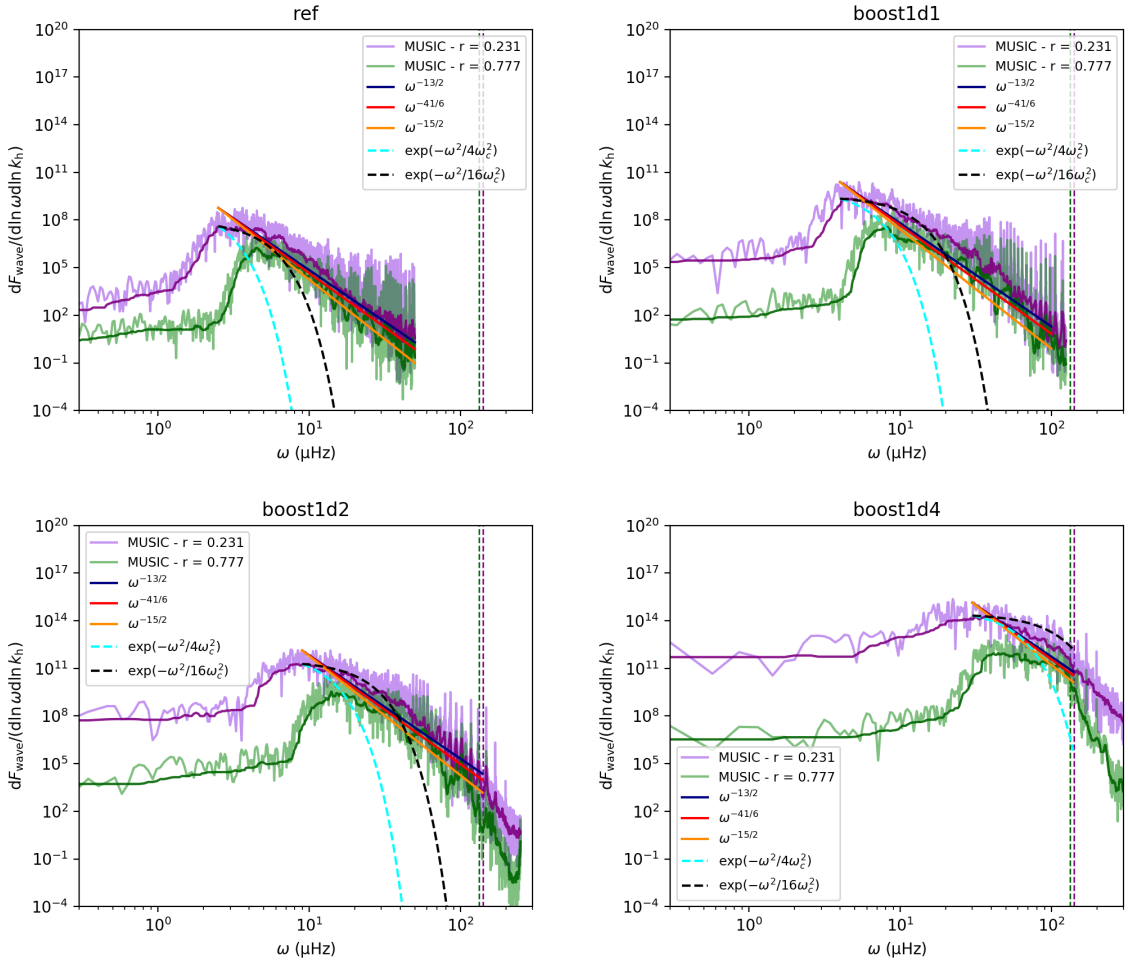

Fig. 7.6 Wave energy flux as a function of frequency for an angular degree $\ell = 10$ for the four simulations *ref* (top left), *boost1d1* (top right), *boost1d2* (bottom left), and *boost1d4* (bottom right) at two radii, $r = r_{\rm conv} + 0.5H_{p,\rm conv} \simeq 0.231R_{\rm star}$ (purple curves) and $r = r_{\rm conv} + 6H_{p,\rm conv} \simeq 0.777R_{\rm star}$ (green curves). The vertical dashed lines indicate the values of the Brunt-Väisälä at $r \simeq 0.231R_{\rm star}$ (purple curves) and $r \simeq 0.777R_{\rm star}$ (green curves). The spectra are obtained via mode projection on the spherical harmonics basis and a temporal Fourier transform of the radial velocity.

for an angular degree $\ell = 10$. Note that for each simulation, Fig. 7.6 shows a different frequency range as we focus on the range that bears most of the energy. The spectra present a relatively flat structure at low frequencies, then peak around a given frequency $\omega_{\rm peak}$ and finally decrease towards higher frequencies. As in Sect. 6.6.1, these fluxes are compared with theoretical predictions for waves generation by Reynolds stress (blue, red and orange straight lines) and penetrative convection (cyan and black dashed curves). The analytical model used for Reynolds stress excitation is the one from Lecoanet and Quataert (2013) and for penetrative convection excitation it is the one from Pinçon et al. (2016). These models are described in details in Sect. 4.3. For both models, the excitation mechanism is expected to generate waves with frequencies larger than the convective frequencies, $\omega \geq \omega_{\rm conv}$. This is why we compare the wave flux from MUSIC to these analytical models in the range of frequencies $\omega \geq \omega_{\rm peak}$. For a better visual comparison with theoretical predictions, we also compute and plot a running median on the $25^{\rm th}$ percentile of the fluxes with a window of 100 frequency bins (dark purple and green lines superimposed on the corresponding flux).

After IGWs are excited at the boundary by convection in the core at frequencies $\omega \geq \omega_{\rm conv}$, they propagate away towards the surface. At the radius where they are excited, the excitation is more efficient at $\omega = \omega_{\rm conv}$, i.e. the wave flux peaks at $\omega_{\rm peak} = \omega_{\rm conv}$. During their propagation, low frequency waves are damped much more rapidly than their higher-frequency counterparts. Indeed, as explained in Sect. 4.2 radiative damping of IGWs is modelled by Eq. (4.14) which scales as ω^{-4}. At a given radius r, IGWs with frequencies in the range $[\omega_{\rm conv}, \omega_{\rm peak}(r)]$ are already damped. Consequently, the peak of the flux is shifted towards higher frequencies at larger radii. This is illustrated in Fig. 7.6, when comparing the fluxes at two locations. For model *ref* the peak is located at $\omega_{\rm peak} \sim 2.5$ µHz at $r = 0.231 R_{\rm star}$ (purple curve) and at $\omega_{\rm peak} \sim 5$ µHz at $r = 0.777 R_{\rm star}$ (green curve). Waves with frequencies between 2.5 and 5 µHz have been damped before being able to reach $r = 0.777 R_{\rm star}$. For models *boost1d1*, *boost1d2* and *boost1d4* the shift is from 4 to 7 µHz, 7 to 10 µHz and 11 to 13 µHz respectively.

For frequencies larger than $\omega_{\rm peak}$, the fluxes of the four simulations are decreasing towards higher frequencies up to the Brunt-Väisälä frequency (vertical dashed lines in Fig. 7.6). Because of the high amplitude g modes, it is not possible to precisely measure the slope of the spectra. However, for models *ref*, *boost1d1* and *boost1d2* the wave flux measured in MUSIC is broadly consistent with analytical prediction for Reynolds stress excitation from Lecoanet and Quataert (2013) and for plumes excitation from Pinçon et al. (2016), but in different frequency ranges. Close to the peak the excitation seems to be dominated by penetrative convection, whereas the Reynolds stress takes over at larger frequencies. This result was already suggested by the theoretical work of Pinçon et al. (2016) as illustrated by Fig. 4.2 and by the simulations of the solar-like model presented in Chapt. 6. In addition, it seems that the fit is better when using

$\nu_p = 2\omega_{conv}$. However, it is difficult to disentangle the two mechanisms since Reynolds stress and penetrative convection act simultaneously to excite waves in the same frequency range, namely between ω_{conv} and N. However, our results suggest that the excitation efficiency of each mechanism is not homogeneous in this whole frequency range.

Model *boost1d4* shows a different behaviour. The MUSIC flux has a Gaussian shape that is broadly consistent with the plumes excitation, but the proximity of the peak of the flux to the Brunt-Väisälä frequency makes the comparison difficult. Nevertheless, it seems that for this simulation the excitation by penetrative convection is more efficient on a larger frequency range. The shape of the curve is no longer consistent with any of the three predictions from Lecoanet and Quataert (2013) in any frequency range. This suggests that the excitation of IGWs by penetrative flows is strengthened when the luminosity is increased, and seems to dominate over Reynolds stress excitation in the most boosted simulation. Interestingly, this shape of spectrum is similar to results from other multidimensional simulations, such as the ones from Rogers et al. (2013) or Edelmann et al. (2019). In both these studies, it is suggested that the excitations of IGWs is dominated by penetrative convection. Note that the authors artificially increase the luminosity of their models by factors up to 10^7. This suggests that enhancing the luminosity by large factors tend to increase the efficiency of plume excitation.

Finally, for the three models *ref*, *boost1d1* and *boost1d2* the slope of the wave flux remains similar close to the convective boundary (purple curve) and at the top of the domain (green curve). However, it is difficult to draw conclusions about the slope up to the stellar surface because of the wave damping that is significantly increasing from $r \simeq 0.8 R_{star}$ as shown in Fig. 7.5 and also because of the complexity of the near surface layers that will affect the waves. Moreover, when analysing hydrodynamical simulations with different values for the luminosity enhancement factor, waves of different frequencies would be able to reach the stellar surface. As we have shown, higher frequencies waves will be excited with a larger amplitude and low frequencies waves are more strongly damped, when a larger enhancement factor is used. Comparing results from luminosity enhanced models with observations requires caution, since the former predict the wrong range of frequencies for waves that could reach the stellar surface. Extrapolation of spectra measured in the interior of the stellar model to the surface of the star may not be straightforward due to the strong impact of the near surface layers on waves propagation. Indeed, there is a very important increase of the radiative diffusivity and the Brunt-Väisälä frequency in this region. Consequently, we suggest that quantitative direct comparison between observations and simulations would require to run simulations as close as possible to the stellar surface. Moreover, observations of stellar oscillations do not resolve

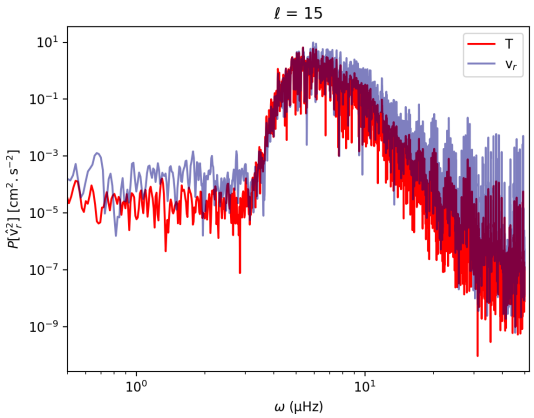

Fig. 7.7 Power spectrum of the radial velocity (blue) and of the temperature (red) for simulation *ref*. The angular degree and radius are fixed at ℓ= 15 and $r = 0.777 R_{\rm star}$. The power spectrum is obtained via mode projection on the spherical harmonics basis and a temporal Fourier transform of the radial velocity.

the surface of stars and consequently the signal is averaged in a way that makes it difficult to compare to simulations.

In our work, we use radial velocity spectra. Lecoanet et al. (2021) suggest that it should be equivalent to use any local wave perturbation variable. We have checked this suggestion by computing the temperature perturbations spectra and find a very good agreement with the one computed with the radial velocity. This is illustrated on Fig. 7.7 for model *ref* at given angular degree $\ell = 15$ and radius $r = 0.777 R_{\rm star}$. The two spectra differ only in amplitude. From an observational perspective, it can be interesting to estimate the ratio of horizontal to radial velocities. At a location $r = 0.85 R_{\rm star}$ in model *ref*, we calculate $\mathrm{v_h}/\mathrm{v}_r \sim 270$ for $\omega = 10\,\mu$Hz and $\mathrm{v_h}/\mathrm{v}_r \sim 13$ for $\omega = 40\,\mu$Hz. This decrease with frequency is expected from the dispersion relation of IGWs, which predicts that the ratio $\mathrm{v_h}/\mathrm{v}_r$ varies as N/ω, with the Brunt-Väisälä frequency N which is fixed at a given radius. The values we obtain for the ratio of the velocities are in agreement with the ones determined in the simulations of Horst et al. (2020) in the same frequency range. At lower frequency, the value of the ratio keeps increasing, and for $\omega = 2\,\mu$Hz we obtain $\mathrm{v_h}/\mathrm{v}_r \sim 7800$. This value is larger than the ones calculated by Horst et al. (2020) at similar frequency. We suspect that this discrepancy is the result of the lack of independent data points from their simulations for the temporal Fourier transform, as suggested by the authors. Such high value of $\mathrm{v_h}/\mathrm{v}_r$ is in agreement with the value calculated from the two-dimensional simulations of Aerts and Rogers (2015). In their simulations of rotating intermediate-mass stars, Aerts and Rogers (2015) obtain ratio up to 10^4 at $r = 0.99 R_{\rm star}$. In the observational community, this ratio is known as the K value which is approximated by $K \simeq GM/4\pi^2\nu^2R^3$, with ν the observed intrinsic frequency of a given star and G is the gravitational constant. In their study,

De Cat and Aerts (2002) measure this K value for SPB stars, which are mid-B type stars pulsating in high-order g modes. They obtain typical values between ∼10 and ∼100. However, note that this approximated K value is only defined at the stellar surface. Consequently, direct comparison with simulated velocity amplitudes determined deeper in the stellar interior should be taken very cautiously.

In their study, Bowman et al. (2019) are using luminosity perturbations, which is equivalent to look at the perturbations of the effective temperature $T_{\rm eff}^4$ as we have the relation $L \propto T_{\rm eff}^4$. First, in both spectra, observed and modelled, we note the presence of g modes, appearing as high amplitude narrow peaks. In the observed spectra, these peaks are present at frequencies larger than the so-called low-frequency power excess. We suggest that if this low-frequency power excess results from IGWs excited by core convection, we should expect to see g modes (i.e. narrow peaks in the spectra) in this low-frequency range. Indeed, in the spectrum of model *ref*, there are g modes starting to appear from 10 µHz. As we will see in Sect. 7.4, in this simulation, waves with frequencies lower than 10 µHz are damped before being able to reach the stellar surface. However, as suggested by Edelmann et al. (2019) and Horst et al. (2020) it is also possible that the small frequency spacing between modes of different radial order and different angular degree "hides" these individual narrow peaks. To confirm this suggestion would require simulations with a radial domain extending to layers close to the stellar surface. Note that the radial extent in Edelmann et al. (2019) and Horst et al. (2020) is at 90% and 91% of the stellar radius, respectively. Second, the simulation spectrum shape peaks around $\omega_{\rm peak}$ and decreases towards lower frequencies. This feature is not observed, and the spectra inferred from observations remains mostly flat at low frequencies. This difference was already reported by Edelmann et al. (2019) and Lecoanet et al. (2021). In their study, Horst et al. (2020) state that this drop towards low frequencies is not present in the spectra measured in their simulations. They suggest that this could be attributed to the low viscosity and thermal diffusivity used in their simulations. However, our results show that this feature should be present even for non boosted simulations. We suggest that this drop is still present in the simulation of Horst et al. (2020) but it has a very low amplitude (see their Fig. 16). This is a consequence of boosting only the luminosity and not the radiative diffusivity, which will results in less damping in the frequency range close to $\omega_{\rm peak}$. Concerning the observed spectra from Bowman et al. (2019, 2020), this drop at low frequency is not observed. This could be the result of rotational effects that could shift wave frequency to lower values. In this case, rotation could help reconcile our simulations and observations. Rogers et al. (2013) indeed suggest an important impact of differential rotation for frequencies below 10 µHz, based on simulations which initially impose some differential rotation. Further work including rotation and an appropriate modelling of

the radiative damping of waves as close as possible to the surface layers would be required to confirm this effect of rotation.

7.4 Non-linear effects of IGWs

Linear theory for wave propagation is based on the assumption that the displacement amplitude of a wave is small compared to its wavelength. As the amplitude increases, non-linear effects can arise, such that the advection terms in the material derivative of the momentum equation start to play an important role (Sutherland, 2010). These non-linear effects can modify wave properties and evolution. To quantify the impact of non-linear effects, we use a non-linear parameter ϵ, defined as (Press, 1981)

$$\epsilon := \xi_\mathrm{h} k_\mathrm{h} = \xi_r k_r, \tag{7.3}$$

where ξ_h (resp. ξ_r) is the horizontal (resp. radial) displacement of a fluid particle associated with an IGW. This definition is basically the ratio of the horizontal (resp. radial) amplitude of a wave to its horizontal (resp. radial) wavelength. According to Press (1981), the displacement may be approximated as $\xi_i = \mathrm{v}_i/\omega$ where $i = r, \mathrm{h}$. We thus have for the non-linearity parameter

$$\epsilon = \frac{\mathrm{v}_\mathrm{h}}{\omega} k_\mathrm{h} = \frac{\mathrm{v}_r}{\omega} k_r. \tag{7.4}$$

From this definition, an IGW is non-linear if $\epsilon \geq 1$. In the following, we compute ϵ using the definition based on the radial component of velocity and wavenumber. Using Eq. (7.2), an analytical expression for ϵ can be inferred

$$\epsilon = \mathrm{v}_0(\ell, \omega)\omega^{-1} \left(\frac{\rho}{\rho_0}\right)^{-1/2} \left(\frac{k_\mathrm{h}}{k_{\mathrm{h},0}}\right)^{3/2} \left(\frac{N^2 - \omega^2}{N_0^2 - \omega^2}\right)^{-1/4} \mathrm{e}^{-\tau/2} k_r. \tag{7.5}$$

Using the dispersion relation Eq. (4.2) for IGWs, we also have an expression for the radial wavenumber

$$k_r = k_\mathrm{h} \left(\frac{N^2}{\omega^2} - 1\right)^{1/2}. \tag{7.6}$$

Figure 7.8 presents the dependence of this non-linear parameter ϵ on frequency and radius for an angular degree $\ell = 4$, calculated from the MUSIC simulations (left column) and as predicted from theory (right column) using Eq. (7.5). We chose to analyse the angular degree $\ell = 4$ as it is for this degree that Horst et al. (2020) predict that the non-linear effects should be most important. We have performed the same analysis for angular degrees $\ell = 1, 2, 5, 10$ and

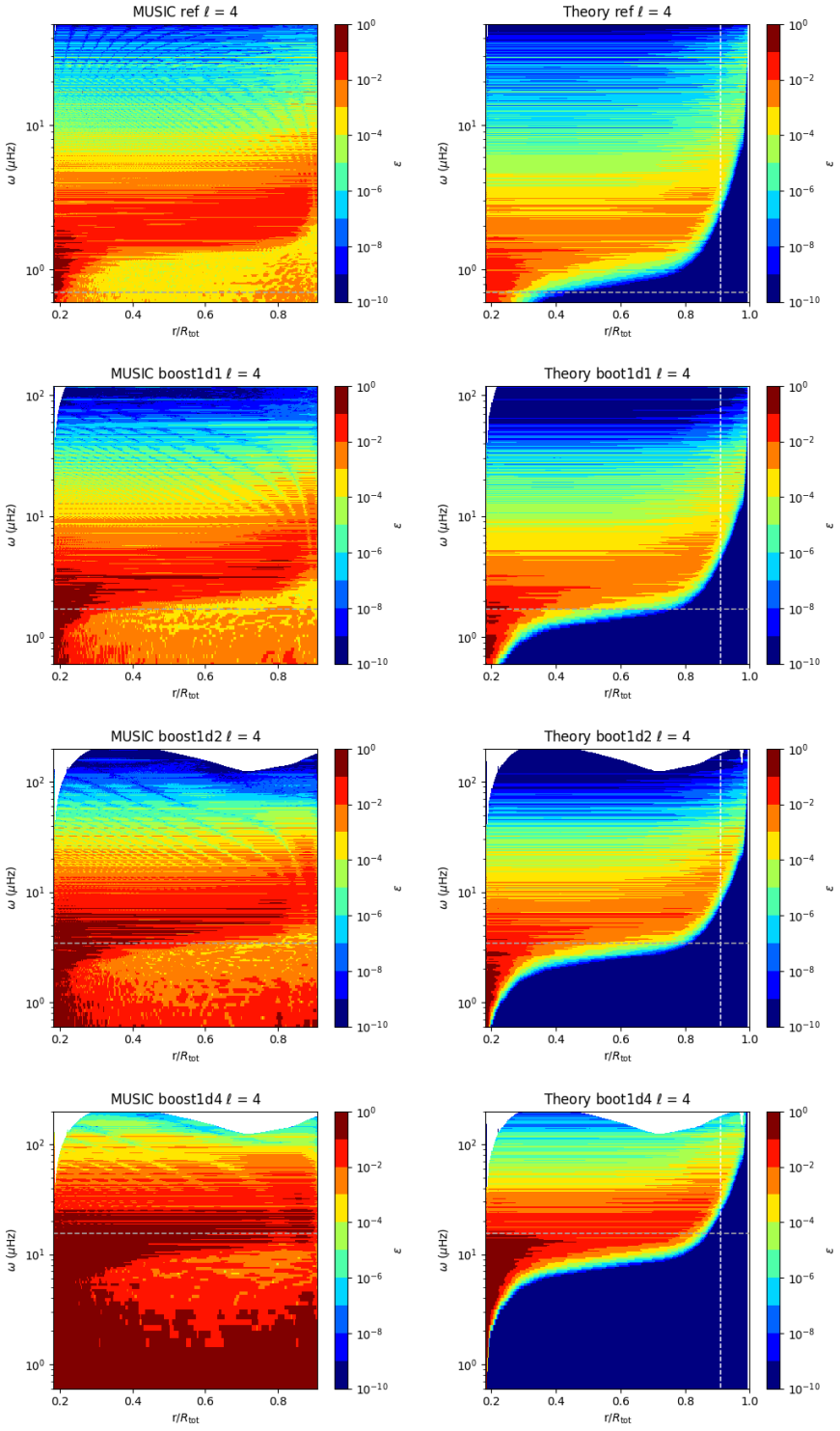

Fig. 7.8 Dependence of the non-linear parameter ϵ on frequency and normalised radius for the four simulations *ref* (top row), *boost1d1* (second row), *boost1d2* (third row), and *boost1d4* (bottom row). The angular degree is fixed $\ell = 4$. The left column presents ϵ as measured in MUSIC and the right column comes from the analytical expression given by Eq. (7.5), normalised with the value of the velocity in the simulations at $r = r_N$, where r_N is the smallest radius such as $\omega = N(r_N)$. The vertical white line in the analytical plots indicates the top of the numerical domain. The horizontal grey dashed line indicates the convective frequency $\omega_{\rm conv}$ for each simulation.

20, and we obtained similar results. Note that the radial range (x-axis) is different in the two columns, in the left one it extends to the top of the numerical domain $r_{\rm out} = 0.91 R_{\rm star}$ and in the right one it extends up to the surface $r = R_{\rm star}$. For the theoretical plots, the value of v_0 needed to normalise the amplitude of the velocity is the value of the radial velocity $v(r_N, \ell, \omega)$ where r_N is the smallest radius, such as $\omega = N(r_N)$ for a given frequency ω. For frequencies up to ~ 50 μHz, $r_N \simeq 0.183 R_{\rm star}$, as in Sect. 7.2.2. For frequency between ~ 50 μHz and the maximal value of the Brunt-Väisälä, $N_{max} \sim 220$ μHz, this radius r_N increases with frequency (see Fig. 7.1 left panel). We introduce r_N because of the condition for IGWs propagation $\omega < N$, this allows ϵ to only take real values (see Eq. (7.5)). Note also that the frequency range (x-axis) available for each simulation is different. The lower frequency is set to 0.6 μHz for the four simulations whereas the maximal frequencies are 50, 100, 200 and 200 μHz for *ref*, *boost1d1*, *boost1d2* and *boost1d4* respectively. This is because we focus on the frequency range that bears most of the energy in each simulation. We have also set a minimum threshold for ϵ at 10^{-10} as the actual value can become very small due to the exponential damping term.

All plots present a similar general aspect, with horizontal ridges corresponding to waves of a given frequency and for which the value of ϵ varies with radius. For each simulation, there is a clearly defined range of frequencies above the convective frequency (horizontal dashed grey line) with $\epsilon \geq 10^{-3}$. This occurs in different frequency ranges for each simulation. These ranges are approximately $[0.7, 5.0]$ μHz, $[1.2, 10.0]$ μHz, $[3.0, 20.0]$ μHz and $[10.0, 60.0]$ μHz for models *ref*, *boost1d1*, *boost1d2* and *boost1d4* respectively. Most of these waves seem to conserve their structure in the whole envelope, suggesting that no non-linear effects occur (no energy transfer, mode coupling, etc...).

This is not the case for the lowest frequencies in the bottom region of the radiative envelope, just above the convective core. Indeed, in this region for frequencies close to the convective frequency, we can see that $\epsilon \geq 10^{-2}$, and even $\epsilon \geq 10^{-1}$ for some frequencies, both in the simulations and the theoretical plots. Ratnasingam et al. (2019) suggested that we can observe non-linear effects when $\epsilon \sim 0.1$. Therefore, we may expect non-linear effects to be relevant just above the convective core. It is possible that some IGWs generated at these frequencies have too large amplitudes and break close to the boundary.

However, if we compare the simulations and theoretical plots, there is a major difference at very low frequencies $\omega \leq \omega_{\rm conv}$. The simulations plots indicate high values of ϵ in the whole radiative zone for this frequency range, which do not appear on the theoretical plots and do not present the structure of horizontal ridges as at higher frequencies. This signal with large values of ϵ is difficult to analyse as it is localised at very low frequencies, for which the wavelengths of IGWs approach the spatial resolution of our grid. Indeed, as the radial wavelength approaches

twice the length of a grid cell, it is not possible any more to represent the wave on the grid. Refer to Sect. 6.7 for more discussion on this topic.

If we compare the four simulations, ϵ is larger as the luminosity enhancement factor is increased. This is expected as the amplitude of the waves increase with the boost. Consequently, we should expect non-linear effects to be more relevant in boosted simulations. This could result in more mixing (see for example Jermyn, 2022), angular momentum transport (see for example Gervais et al., 2018) and/or wave-wave interactions.

Finally, by looking at the analytical predictions for ϵ up to $r = R_{\text{star}}$, we can see that non-linear effects are not expected close to the surface of the star. Most of the waves in the range of frequencies with values of $\epsilon \geq 10^{-3}$ are damped before even reaching $r = 0.91R_{\text{star}}$, the top of the MUSIC radial domain. For waves that can propagate further, the maximal values of the non-linear parameter close to the surface are smaller than 10^{-5}. This is consistent with the results of Ratnasingam et al. (2019) who computed a non-linearity parameter from the analytical spectra of Kumar et al. (1999) and Lecoanet and Quataert (2013) for Reynolds stress excitation of IGWs and found that $\epsilon < 10^{-2}$ in a $3M_\odot$ star for the angular degree $\ell = 10$. According to the theoretical plots, some waves may reach the surface of the star, but these are relatively high frequency waves compared to the excitation frequency ω_{conv}. The predictions, however, are based on linear theory, which neglects the interaction with a possible subsurface convection zone (see for example Cantiello and Braithwaite, 2019) and near-surface layers that are difficult to accurately model (see for example Basu and Chaplin, 2017).

7.5 Wave heating in the upper layers

Often overlooked, thermal effects of IGWs can be significant. In the Earth atmosphere, they are known to irreversibly convert kinetic energy into internal energy (see for example Medvedev and Klaassen, 2003). Through this mechanism, they can heat up the thermosphere (Yiğit and Medvedev, 2009). Almost always neglected in main sequence stars, these thermal effects of acoustic and internal gravity waves have recently been accounted for in evolved stars in order to explain outbursts in supernova progenitors (Fuller, 2017; Wu and Fuller, 2022) and in an attempt to explain the lithium enhancement of clump stars (Jermyn and Fuller, 2022). In these studies, waves deposit heat through radiative diffusion.

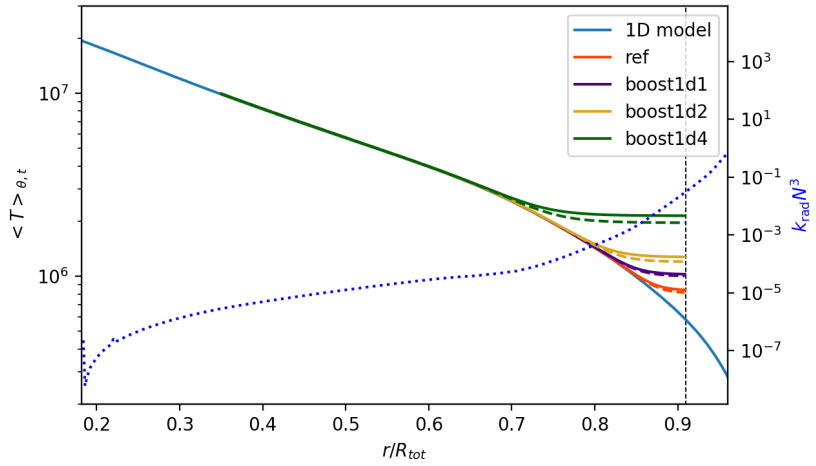

Fig. 7.9 Spatially average temperature profile in the four simulations *ref* (orange), *boost1d1* (indigo), *boost1d2* (yellow), *boost1d4* (green). The dashed curves are the temperature profiles obtained at time t_0, and the plain curves at $t_0 + \Delta t$, where Δt is different for each simulation (see text for values). The temperature profile from the 1D initial model is represented by the plain blue curve. The outer boundary of the MUSIC numerical domain is indicated by the vertical dashed black line. The right axis corresponds to the term $k_{\rm rad}N^3$ (blue dotted curve) computed from the 1D model.

7.5.1 Temperature increase in the simulations

In our simulations, we observe a significant increase of the temperature in the upper layers of the model. Figure 7.9 presents the evolution of the radial profile of the average temperature in our four simulations *ref* (orange), *boost1d1* (indigo), *boost1d2* (yellow), *boost1d4* (green). The average is performed horizontally, as defined by Eq. (A.2). A first average is performed at time t_0 (dashed curves) and a second one on $t_0 + \Delta t$ (solid curves), with $\Delta t = 7.0 \times 10^7$ s, 1.6×10^7 s, 1.2×10^7 s and 1.8×10^6 s for models *ref*, *boost1d1*, *boost1d2* and *boost1d4* respectively. We can clearly see an increase of the temperature close to the top of the domain in the four simulations, from $r \simeq 0.75 R_{\rm tot}$ up to $r = 0.91 R_{\rm tot}$. The heated region corresponds to the one with strong wave damping observed in Fig. 7.5 and 7.8. The temperature increase is more important when the enhancement factor of the luminosity is larger. The term $k_{\rm rad}N^3$ (blue dotted curve) computed from the one-dimensional model is also plotted in Fig. 7.9. In the heated region, this term increases sharply. By looking at Eq. (4.14) it is clear that this term drives the radiative damping of a wave at fixed ω and ℓ. Therefore, IGWs are strongly damped in this region and will deposit a significant amount of energy. We suggest that the observed heating results from this damping by radiative diffusion.

7.5.2 Theoretical estimate of heat added by waves

In order to test this hypothesis, we analytically estimate the amount of heat $\epsilon_{\rm heat}$ added by waves in these layers in model *ref* through radiative damping. Following Fuller (2017), an IGW is damped by radiative diffusion at a rate γ given by

$$\gamma \simeq k_r^2 \kappa_{\rm rad}. \tag{7.7}$$

Using Eq. (7.7), we can define a damping length for a given wave

$$l_{\rm damp} = \frac{u_{\rm g,r}}{\gamma}, \tag{7.8}$$

As in Sect. 6.5.2 we rewrite the radial group velocity given by Eq. (4.6) as

$$u_{\rm g,r} \simeq \frac{\omega^2}{N^2 k_{\rm h}} \left(N^2 - \omega^2\right)^{1/2}. \tag{7.9}$$

but here we do not assume the low frequency limit, i.e. we do not consider that ω is negligible in front of N. Using Eq. (7.7) and (7.9) and the dispersion relation of IGWs given by Eq. (4.2), the damping length expression becomes

$$l_{\rm damp} = \frac{\omega^3}{N^2 k_{\rm h}^3 \kappa_{\rm rad}} \left(\frac{N^2}{\omega^2} - 1\right)^{-1/2}. \tag{7.10}$$

The amount of heat deposited per unit mass per unit time by a single wave (ℓ, ω) is given by

$$\epsilon_{\rm heat} = -\frac{{\rm d}L_{\rm wave}(\ell,\omega)}{{\rm d}M} = \frac{L_{\rm wave}}{M_{\rm damp}}, \tag{7.11}$$

with $L_{\rm wave}$ the wave luminosity and $M_{\rm damp} = 4\pi r^2 \rho l_{\rm damp}$ the mass through which the waves pass before being damped. The wave luminosity in Eq. (7.11) corresponds to the luminosity initially injected by convection in a given wave, i.e. it corresponds to the initial amplitude of the wave when it is excited. Finally, radiative damping of IGWs produces a heating by unit time and unit mass for a single wave (ℓ, ω) estimated by

$$\epsilon_{\rm heat}(r,\ell,\omega) = \frac{N^2 k_{\rm h}^3 \kappa_{\rm rad}}{4\pi r^2 \rho \omega^3} \left(\frac{N^2}{\omega^2} - 1\right)^{1/2} L_{\rm wave}(r,\ell,\omega) \tag{7.12}$$

Using Eq. (7.12) we can thus estimate an order of magnitude for the amount of heat theoretically added to the region between $r = 0.75 R_{\rm star}$ and $r = 0.91 R_{\rm star}$. To do this, we estimate the wave

luminosity $L_{\rm wave}$ for a wave (ℓ, ω) as

$$L_{\rm wave}(r,\ell,\omega) = L_{\rm wave}(r_{\rm e},\ell,\omega)\mathrm{e}^{-\tau(\mathrm{r},\ell,\omega)}. \tag{7.13}$$

with $L_{\rm wave}(r_{\rm e},\ell,\omega)$ measured in our simulation *ref* using

$$L_{\rm wave}(r_{\rm e},\ell,\omega) = 4\pi r^2 F_{\rm wave}(r_{\rm e},\ell,\omega) \tag{7.14}$$

where $r_{\rm e}$ is the radius at which waves are excited and $F_{\rm wave}$ has been defined in Eq. (6.17), except here we do not assume the low frequency limit. In addition, as we are interested quantitatively in the amplitude of the flux, we multiply $F_{\rm wave}$ by a $3.28/4\pi$ to compensate for the loss of power due to FFT windowing and normalisation of the spherical harmonics. We chose $r_{\rm e} \simeq 0.183 R_{\rm star}$ as in Sect. 7.2.2 and 7.4. We consider contribution of waves with frequency ω in the range $[\omega_{\rm conv};\omega_{\rm max}]$, with $\omega_{\rm max} = 50$ μHz being the maximal frequency available for the simulation. The minimal frequency is set to $\omega_{\rm conv}$ as we do not expect waves with lower frequencies to be excited (Lecoanet and Quataert, 2013). Similarly, we consider in the estimation the contribution of waves with angular degree ℓ from 1 to 200.

Finally, the total amount of heat $Q_{\rm theory}$ added in the region between $r = 0.75 R_{\rm star}$ and $r = 0.91 R_{\rm star}$ during the time Δt is

$$Q_{\rm theory} = \sum_{N_{r_1,r_2}} q_{\rm th}(r), \tag{7.15}$$

where N_{r_1,r_2} is the number of radial grid cells in our simulation between $r_1 = 0.75 R_{\rm star}$ and $r_2 = 0.91 R_{\rm star}$ and $q_{\rm th}(r)$ is the amount of heat added in each radial grid cell, which is defined as

$$q_{\rm th}(r) = \sum_{\ell=0}^{200} \sum_{\omega=\omega_{\rm conv}}^{N_{\rm max}} \rho \epsilon_{\rm heat}(r,\ell,\omega) \mathcal{V}_{\rm shell} \Delta t, \tag{7.16}$$

with $\mathcal{V}_{\rm shell}$ the volume of the shell between radii r and $r + \Delta r$ where Δr is the size of a numerical grid cell in the radial direction. In Eq. (7.15), Δt is the same time interval as the one used in Fig. 7.9, which is $\Delta t = 7.0 \times 10^7$ s for model *ref*. We obtain $Q_{\rm theory} = 3.3 \times 10^{41}$ erg.

Now, in order to compare with the results from the simulations, we measure the total added heat $Q_{\rm MUSIC}$ at the top of the numerical domain using the expression

$$Q_{\rm MUSIC} = \sum_{N_{r_1,r_2}} \rho c_p \Delta T \mathcal{V}_{\rm shell} \tag{7.17}$$

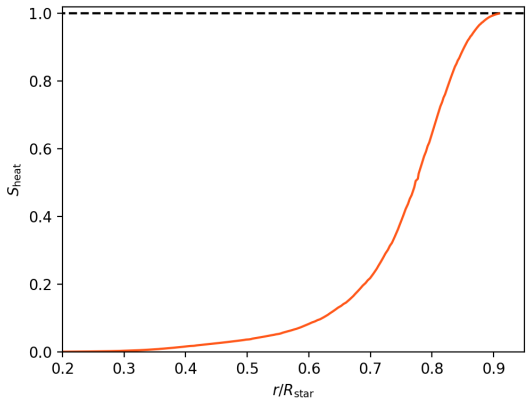

Fig. 7.10 Cumulative sum of the theoretical estimate of the heat deposited by waves, $S_{\rm heat}$, as a function of normalised radius. The horizontal dashed line indicate the value $S_{\rm heat} = 1.0$.

with c_p the specific heat capacity at constant pressure and ΔT the temperature difference after the same interval of time Δt. The total added heat in model *ref* is $Q_{\rm MUSIC} = 1.0 \times 10^{43}$ erg. This value is larger than $Q_{\rm theory}$, but this can be expected. In the simulations, the top boundary $r_{\rm out} = 0.91 R_{\rm star}$ is reflecting IGWs, therefore waves that would be damped in the region between $r_{\rm out}$ and the stellar surface in an actual star are damped in the region between $r_1 = 0.75 R_{\rm tot}$ and $r_{\rm out}$ in our simulation. Therefore, this heating could be strengthened due to boundary conditions. The issue of the impact of boundary conditions on hydrodynamical simulations is an open challenge that affects all stellar simulations (see for example Vlaykov et al., 2022). We thus consider that the value of $Q_{\rm MUSIC}$ is in relatively good agreement with the value estimated from linear theory $Q_{\rm theory}$. This strengthens our confidence that the heating observed in the simulations results from the damping of IGWs by radiative diffusion.

The estimation of $Q_{\rm theory}$ is performed between $r_1 = 0.75 R_{\rm star}$ and $r_2 = 0.91 R_{\rm star}$. However, the location of the inner boundary of this domain has a limited influence on the computation of $Q_{\rm theory}$. This is highlighted in Fig. 7.10. This figure presents the radial cumulative sum of added heat by IGWs, $S_{\rm heat}$, estimated with the analytical expression given by Eq. (7.15). It is defined as

$$S_{\rm heat}(r) = \frac{\sum_{N_{r_0,r}} q_{\rm th}(r)}{\sum_{N_{r_0,r_{\rm max}}} q_{\rm th}(r)} \tag{7.18}$$

where $N_{r_0,r}$ is the number of radial grid cells between $r_0 = 0.2 R_{\rm star}$ and a given radius r, and $r_{\rm max} = r_2$. We can see that most of the heat that waves can deposit is at radii $r \geq 0.7 R_{\rm star}$. This corresponds to the region where we observe an increase of the temperature in Fig. 7.9 for model *ref*.

In this section, our results show an increase of the temperature in the upper layers of the star. The amount of heating is comparable to the theoretical predictions of heat added by IGWs damped by radiative diffusion. This thermal impact of IGWs may thus be relevant in main sequence stars and is currently under investigation.

7.6 Discussion & Outlook

This chapter presents an analysis of the properties of IGWs excited by convection in a two-dimensional fully compressible simulation of a 5 solar mass star model at zero-age-main-sequence. Our reference simulation is run with a luminosity that is not artificially enhanced and with a realistic radiative diffusivity profile. The simulation radial domain extends from $r_{\rm in} = 0.02 R_{\rm star}$ to $r_{\rm out} = 0.91 R_{\rm star}$.

- A key highlight from this analysis is the importance of including radiative diffusion in stellar hydrodynamical simulations. Indeed, we have shown that waves propagating in the radiative envelope of such stars are strongly damped due to radiative diffusion. In our truncated model, the radiative diffusivity varies radially by 5 orders of magnitude. In the region not modelled in this work, between $r_{\rm out}$ and $R_{\rm star}$, we expect the effect of radiative damping to be enhanced, since the radiative diffusivity varies by more than 4 orders of magnitude in this region. This is particularly important if the goal is to analyse the waves that can reach the stellar surface and to establish a link with observations or to study their transport properties.

- A limitation of our work is that we do not include rotation in our simulations, since the primary goal is to analyse the effect of radiative damping with realistic radiative diffusivity profiles. A relevant comparison of simulated spectra with observations is a challenge as it would require a proper description of the surface layers and including rotation. Indeed, many OB stars observed showing photometric variability are rotating (e.g. Pedersen et al., 2021; Szewczuk et al., 2021). In addition to the dynamical effects of rotation on convection (e.g. impacting $\omega_{\rm conv}$ and the plume dynamics) and thus on wave excitation, rotation may produce a shift in the wave frequencies. As already mentioned, Rogers et al. (2013) suggest a large impact of differential rotation on the low frequency power spectrum. But these conclusions are based on an imposed differential rotation profile and would need confirmation with further numerical simulations. Interestingly, the shape and structure of the power excess observed in these stars(e.g. Bowman et al., 2019; Szewczuk et al., 2021) is very similar for most stars in their sample. Since the rotation rates of B dwarfs vary by more than one order of magnitude, it is compelling to

observe such similarity, since the expected frequency shift would depend on the rotation rate.

- In the simulations presented in this chapter, we observe an increase of the temperature close to the top of the numerical domain. In this region, the damping of IGWs is strong, due to the simultaneous increase of stratification and radiative diffusivity. Using the linear theory of IGWs, we have estimated an order of magnitude for the amount of heat that could be added by waves in these upper layers. This value is comparable to the value inferred from the MUSIC simulations, suggesting that IGWs may be at the origin of the observed heating. Since the radiative diffusivity can vary steeply with radius, wave damping is not uniform throughout the star and waves will deposit different amounts of energy at different radii. Once again, this highlights the importance of using a realistic radiative diffusivity profile. However, this heating induced by waves is, to our knowledge, always neglected in main-sequence stars. This may not be always justified and thermal effects of IGWs may be relevant in some cases, particularly as this occurs in the outer part of the star.

- We have also studied non-linear effects linked to IGWs propagating in the radiative envelope of intermediate mass stars. Our results suggest that non-linear effects may be relevant only above the convective core, close to where waves are excited. In this region, waves with frequencies close to the convective frequency appear to be strongly damped or to break in MUSIC simulations. More precisely, these waves have a non-linear parameter ϵ close to 1, meaning that they may be highly non-linear. A possible explanation could be that these waves are generated with a very large amplitude and that they likely break almost immediately due to non-linear effects, just above the convective core. This could result in mode coupling and/or generation of lower frequency waves. However, we cannot exclude that the signal in this very low frequency range results from aliasing, as the associated wavelengths may not be resolved properly on the numerical grid of our model. This is a common issue in hydrodynamical simulations that is difficult to quantify.

- The results obtained for our reference model are compared with three simulations for which the luminosity has been increased by factors 10, 10^2 and 10^4. As in Chapt. 6, this comparison highlights the impact of this artefact on the generation and propagation of IGWs. In our simulation with realistic luminosity and radiative diffusivity, the wave flux measured is broadly consistent with excitation by penetrative convection at low frequency and with Reynolds stress at higher frequencies. This is similar in the two less boosted models, but not in the most boosted one. In the latter, the wave energy flux is approximately consistent with an excitation by penetrative convection but not by

Reynolds stress. This suggests that the efficiency of these two excitation mechanisms is also impacted by an enhancement of the luminosity and radiative diffusivity. We have also shown that the heating close to the top of the domain and non-linear effects are more important when the luminosity is artificially increased. In addition, this should also impact the transport of angular momentum, which depends on the radiative damping of IGWs and on their amplitude. Results are thus quantitatively modified by an enhancement of the luminosity, and any prediction based on simulations using this artefact should be taken with caution.

- Concerning the surface manifestation of IGWs excited by core convection, our main conclusion is that extrapolating simulated spectra determined at an internal radius to the surface in order to compare to observations is likely meaningless. Such a comparison would require numerical simulations extending up to the surface layers, to properly describe the radiative damping in these layers, which is a formidable challenge for stellar hydrodynamics simulations. Finally, we can identify two additional challenges regarding the comparison between observations and numerical simulations. First, simulations require physical simplifications and are thus far from realistic stellar conditions. As shown in this work, these assumptions can impact the physics of waves. Second, observations do not resolve stellar surface and thus only consider global variations of luminosity. Further efforts are thus needed in order to improve the reliability of comparisons between observations and the predictions of numerical simulations.

Chapter 8

Perspectives: looking for the missing physics in stellar evolution

One of the overall objectives of this thesis is to demonstrate how we can use numerical modelling to understand physical processes occurring in stellar interiors. This is a complementary approach to observations, which will reveal what phenomenon we can not explain with current theories. In this context, I am currently working on an asteroseismology project to look for the missing physics in stellar evolution and structure theory. This project was initiated during the Kavli Summer Program 2021, in collaboration with Dr. Earl Bellinger (Max Planck Institute for Astrophysics, Germany) and Prof. Sarbani Basu (Yale University, USA). We are aiming to develop an innovative tool to perform non-linear inversions of stellar structure. This project is presented in Sect. 8.1 and will be the subject of a publication (Le Saux, Bellinger & Basu, in prep.)

In addition, all hydrodynamical simulations used for the work presented in this thesis are two-dimensional. A natural next step will then be to move towards three-dimensional simulations. This will allow a more realistic modelling of stellar interiors and thus a better comparison with observations. However, this presents a challenge when the objective is to study waves in the spectral domain. Indeed, with MUSIC full three-dimensional spheres are too expensive to run, so we are running pieces of spheres, called wedges. This makes it impossible to use the spherical harmonics basis to describe waves. We are therefore developing a new basis, called wedge harmonics, which is adapted to our geometry. This is the subject of Sect. 8.2.

8.1 Non-linear inversions for stellar structure

Seismic inversion methods aim to build a model of the internal structure of a given star constrained by all available observational data, seismic or not. In general, it is based on the effects, i.e. observations, to determine the causes, i.e. stellar structure. From a mathematical perspective, an inversion consists of solving the equations of the stellar structure taking into account all available observational constraints (Buldgen et al., 2022). The challenge of inversion problems comes in part from the fact that they are ill-posed, i.e. in particular that the solution is not unique. Consequently, the resulting solution is uncertain and degenerate. Physical arguments are therefore needed to choose the most likely solution.

8.1.1 Linear methods and their limitations

As mentioned in Sect. 3.1, we know that theory of stellar evolution is still missing or at least incorrectly modelling some physics. In the solar case, it has been highlighted that Standard Models of the Sun (see Sect. 3.1) are significantly discrepant with the helioseismic observations of the Sun (see for example Basu, 2016; Christensen-Dalsgaard, 2021). For instance, there are still some unexplained discrepancies between the helioseismic sound speed and density profiles and the modelled one as shown on Fig. 5.1. It has also been shown that diffusion and gravitational settling of all elements heavier than hydrogen play a very important role when building solar models (Basu, 2016; Christensen-Dalsgaard et al., 1993). These results were obtained thanks to helioseismic structure inversion methods, which consist in inferring an internal structure of the Sun using the observed frequencies of its modes of oscillation (see Sect. 3.1). As illustrated on Fig. 8.1 left panel, the oscillation frequencies of the Sun and the ones of a Standard Solar Model such as model S do not match. The discrepancies between the two can be large, particularly at high frequencies. The main reason for this frequency dependent discrepancy is that we currently do not know how to model accurately the near surface layers of the Sun (e.g. Basu and Chaplin, 2017; Houdek et al., 2017). Higher frequency acoustic waves have their lower turning point that is more shallow, so they propagate less in the deeper layers. Consequently, these effects are more important for those waves. In order to compensate for these surface effects, empirical methods have been developed (see for example Gruberbauer et al., 2012; Kjeldsen et al., 2008; Roxburgh and Vorontsov, 2003). However, these corrections do not solve the whole problem. Despite the fact that they improve the agreement with the observations, there are still discrepancies. These differences result from uncertainties in the physics of stellar interiors, as we will see.

In this work, we use the more recent correction introduced by Ball and Gizon (2014) because it has been shown to be the (so far) most favourable treatment of the surface term

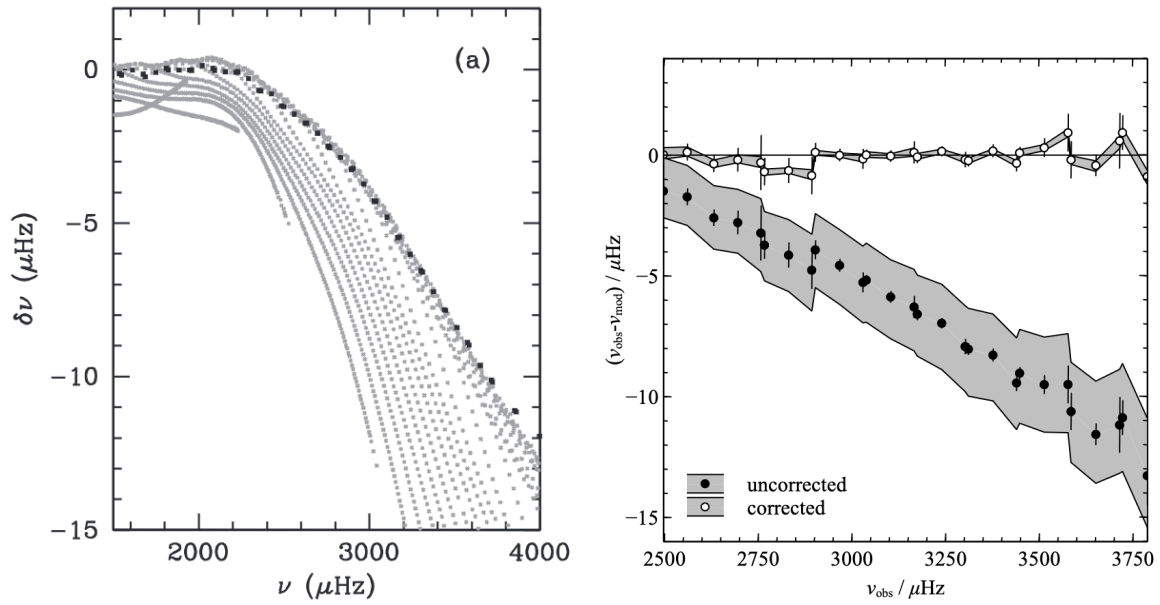

Fig. 8.1 Left panel: Frequency differences between the Sun (mode set BiSON-13 of Basu et al. (2009)) and Model S of Christensen-Dalsgaard et al. (1996) as a function of frequency. (Credits Schmitt and Basu, 2015). Right panel: Uncorrected (black symbols) and corrected (white symbols) frequency differences between observed frequencies for the BiSON solar data and MESA models. Error bars that correspond to the observed uncertainties are also showed. The shaded regions show the spread of the modelled frequencies. i.e. taken from the 100 fits to random realizations of the observations (see Ball and Gizon, 2014, for details)

(Ong et al., 2021; Schmitt and Basu, 2015). It suggests adding to the modelled frequencies the following parametrization

$$\delta\omega = \left(a_{-1}(\nu/\nu_{\rm ac})^{-1} + a_3(\nu/\nu_{\rm ac})^3\right)/\mathcal{I} \tag{8.1}$$

with a_{-1} and a_3 being coefficients that are fit for a given stellar model (hence the dependence of the frequency shift on the model), $\nu_{\rm ac}$ is the acoustic cut-off frequency, and $\mathcal{I}$ is the normalized mode inertia. The results of this correction are presented on the right panel of Fig. 8.1. We can see that there are no remaining trends in the corrected data. However, there are still some discrepancies which are larger than the error bars. These remaining differences between the Sun and the standard solar model do not belong to the surface effects. The discrepancies suggest that solar models are not totally right and are still missing or incorrectly modelling some physics. They are thus used to perform inversions of the internal structure of the Sun. Indeed, as mentioned, the frequencies of normal modes of oscillations depends on this internal

structure. These methods have been proven powerful as they give deep insight into the solar interior (see Buldgen et al., 2022, for a recent review).

Current and past spatial telescopes have already provided data on hundreds of thousands of stars, and millions more are expected in the coming years. The diversity of the observed stars offer a unique laboratory to determine precisely the stellar structure of a wide variety of stars. We are no longer limited to one star, but now have access to many stars at almost every step of stellar evolution. This presents an incredible opportunity to test stellar evolution theory.

To date, most methods used to perform inversions have been linear. This type of inversion methods are based on the variational principle of adiabatic stellar oscillations. This principle links perturbations of oscillation frequencies to perturbations of the internal structure. Starting from the perturbed equations of hydrodynamics (see Eq. (3.23)-(3.25)) we can obtain an eigenvalue equation of the form

$$\mathcal{L}(\xi_{n,\ell}) = -\omega^2_{n,\ell}\xi_{n,\ell}, \tag{8.2}$$

with $\mathcal{L}$ a linear differential operator (see Eq. (3.111) in Basu and Chaplin, 2017, for its definition). This eigenvalue value problem is Hermitian under the boundary conditions $\rho = P = 0$ (Chandrasekhar, 1964). This allows us to apply a variational principle to compute the eigenfrequencies $\omega^2_{n,\ell}$ corresponding to a given eigenfunction $\xi_{n,\ell}$, as

$$-\omega^2_{n,\ell} = \frac{< \xi_{n,\ell}, \mathcal{L}(\xi_{n,\ell}) >}{< \xi_{n,\ell}, \xi_{n,\ell} >}, \tag{8.3}$$

with $< . >$ the inner product operator defined over the functional space of the solutions of the adiabatic oscillation equations (Buldgen et al., 2022). Frequencies calculated using Eq. 8.3 are usually called *variational frequencies*. Next, we consider a small perturbation around a *reference model*. Then the linear operator, eigenfunctions and eigenfrequencies can be written as $\mathcal{L} + \delta\mathcal{L}$, $\xi_{n,\ell} + \delta\xi_{n,\ell}$ and $\omega_{n,\ell} + \delta\omega_{n,\ell}$ respectively, with δ the variational perturbation. This is the linearisation step responsible for the name of this method. Finally, we can express the relative perturbation to the eigenfrequencies as a function of relative perturbation of the inner structure of the star (Basu and Chaplin, 2017), as

$$\frac{\delta\omega_{n,\ell}}{\omega^2_{n,\ell}} = \int K^{n,\ell}_{f_1,f_2} \frac{\delta f_1}{f_1} \mathrm{d}x + \int K^{n,\ell}_{f_2,f_1} \frac{\delta f_2}{f_2} \mathrm{d}x + \frac{F_{\mathrm{surf}}(\omega_{n,\ell})}{\mathcal{I}_{n,\ell}} + O(\delta^2), \tag{8.4}$$

with f_1 and f_2 two structural variable (e.g. density, sound speed, pressure...), $K^{n,\ell}_{f_1,f_2}$ and $K^{n,\ell}_{f_2,f_1}$ are two inversions kernels which are functions of the reference model. The term before the last on the RHS takes into account the surface term correction F_{surf}, which we define using Eq. 8.1.

Finally, the inversion kernels, are computed using the reference unperturbed model (see Chapt. 10 of Basu and Chaplin, 2017, for a detail description). Recently Bellinger et al. (2020, 2021) pointed out that these linear methods could introduce errors, especially for more evolved stars that change on relatively short timescales. Indeed, by definition, in the linearisation introduce to derive Eq. 8.4, all terms of order larger than one are neglected, which may not be justified in some cases. In these cases the last term of Eq. 8.4, which takes into account terms of higher order than one, might not be negligible. This will introduce errors in the relation between the eigenfrequencies and the stellar structure. In the case of evolved stars, it is known that mode coupling from mixed oscillation modes introduces errors in the inversions results (Ong et al., 2021). In addition, linear methods also require a manual adjustment for numerous free parameters. This motivates us to study and develop a non-linear inversion technique, i.e. a method that will solve the full system of oscillations equations. This will allow applying seismic inversions to subgiant and red giant stars.

8.1.2 A new self-consistent inversion method

The goal of this ongoing project is to obtain better constraints on stellar interiors by developing a non-linear inversion technique. The objective is to build static stellar models with a flexible composition profile and to use the MESA stellar evolution code (Jermyn et al., 2022; Paxton et al., 2011, 2013, 2015, 2018, 2019) to relax these models, i.e. to solve the full non-linear equations of stellar structure. In MESA, a snapshot of the composition profile is set with the radial evolution of 3 variables: the hydrogen mass fraction X, the helium mass fraction Y and the heavy elements mass fraction Z. The elements contained in Z depend on which network is chosen. In this work, we are using two different networks: 'basic.net' and 'pp_cno_extras.net'. The former contains 8 chemical species, and the latter 25. Using one or the other depends on the information we have on the star we aim to model. Particularly, stars more massive than the Sun and stars at later phases of evolution need more detailed nuclear networks. The relative abundance of each element is taken from the solar photospheric composition, as determined by Magg et al. (2022). Because of the constraint X+Y+Z=1, we only need to parametrize 2 of these 3 variables. Due to the burning of hydrogen in the core of the star during the main sequence, the X profile is strictly increasing from the centre toward the surface in main sequence stars. Thus, to ensure this constraint, we chose X as our first independent variable. The second one can either be Y or Z. In this work, we will use Z, unless stated otherwise. We chose to parametrise the perturbation to the composition profile, δA, instead of the composition profile itself, A. Then the new profile will be $A' = A + \delta A$, with $A = X,\ Y$or Z. This is to avoid any problem with discontinuities, particularly the one at the convective-radiative boundary.

In MESA models, the composition profile is usually discretised in 1500–2000 points. This is way too much to parametrise the compositions profiles using all of them. Indeed, in our method we would like to perturb the composition profile to build a model with a structure that allows to get oscillations frequencies as close as possible to the observational data. If we keep these 1500–2000 points for the composition profile, it means that the algorithm will need to work with two times much input parameters. Consequently, in order to reduce this dimensionality, we use a P-splines representation of the composition profile. P-splines, or Penalized B-splines, were developed by Eilers and Marx (1996). The concept is based on B-splines, but with addition of a parameter to control the smoothness of the representation. This smoothness parameter, λ, is optimized using the equation:

$$Q = \sum_i (o_i - b_i)^2 + \lambda \sum_i (b_i - b_{i-1})^2 \tag{8.5}$$

where o_i is the value of X, Y or Z at a given point i in radius in the initial MESA model and b_i is the build value from the P-splines method. The main advantage of the technique is that it allows to obtain a faithful representation of the composition profile with only a limited number of parameters. These parameters, also called knots, will be regularly spaced in terms of acoustic depth, which is defined as (Gough, 1990)

$$\tau_{\mathrm{d}}(r) = \int_r^{R_{\mathrm{star}}} \frac{\mathrm{d}r}{c_{\mathrm{s}}} \tag{8.6}$$

By definition acoustic waves travel at the sound speed. We determined the optimal number of knots as 65 by analysing the convergence of the cumulative error on the rebuild profile compare to the initial. This value was already used in Basu and Chaplin (2017). We are going to consider that the value of the perturbation of all the knots in a given convective zone is equal. This means we consider a very efficient chemical mixing by convection, which is true on evolutionary time scales. Then, the number of parameters used to parametrise a profile will be reduced to 25, as there is 40 knots in the convection zone.

This method gives us a total of 50 parameters to perturb the composition profile. We use an extra parameter to build our static models, which is the mixing length parameter α_{MLT}, already introduced in Eq. (2.21). Indeed, this parameter influence strongly the value of the radius R_{star} and luminosity L_{star} of the star, as showed on Fig. 8.2 for a solar model.

Now that we are able to build flexible static models of stars, the next step is to determine which structure allows the best fit to observations. This step will be automated using a Basin-Hopping optimisation algorithm (Wales and Doye, 1997). The main benefit of this algorithm is that it has been designed to find the global minimum of a non-linear function with multiple

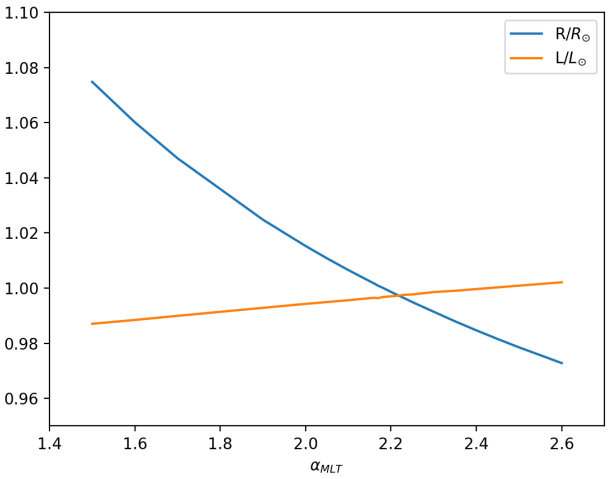

Fig. 8.2 Evolution of radius, R, and luminosity, L, with the mixing length parameter $\alpha_{\rm MLT}$ for our Standard Solar Model built with MESA.

minima. The optimiser has then to minimise a likelihood for a given combination of parameters. The likelihood we chose is a χ^2 function. Thus, we have

$$\chi^2(\alpha_{\rm MLT}, X_1, \ldots, X_N, Z_1, \ldots, Z_N) = \sum_j \frac{(O_j - M_j)^2}{\sigma_j^2}. \tag{8.7}$$

with O_j and M_j that are respectively the observed and modelled values of oscillation frequencies ν_i, radius $R_{\rm star}$, luminosity $L_{\rm star}$, and metal abundance at the surface $[Z/X]$. The σ_j are the uncertainties on the observed values.

8.1.3 Preliminary results

As the Sun is the best known star, we have chosen to develop our method using an analysis of this star. This allows for precise comparison not only with observations but with previous studies that used different methods to get similar results (e.g., linear inversion techniques). Indeed, for low-mass main-sequence stars linear inversion methods appear to be mostly valid, thus we should expect both linear and non-linear methods to give similar results. The full potential of our new self-consistent method lies in applying inversions to evolved or massive stars.

The main observational characteristics of the Sun we are using are summarised in Table 8.1. These values are taken from Prša et al. (2016), except for the surface abundances that are from Magg et al. (2022). The estimation of the mass of the Sun is done by measuring its product

Table 8.1 Observed characteristics of the Sun.

Variables	Sun	Uncertainties
Age (Gyr)	4.59	± 0.006
$M_\odot$ (g)	1.988×10^{33}	–
$R_\odot$ (cm)	6.957×10^{10}	0.00140×10^{10}
$L_\odot$ (erg.s^{-1})	3.828×10^{33}	0.0014×10^{33}
$[Z/X]_\odot$	0.0225	± 0.0014
$T_{\mathrm{eff},\odot}$ (K)	5772.0	± 0.8

Table 8.2 Characteristics of solar numerical models.

Model	M ($M_\odot$)	R ($R_\odot$)	L ($L_\odot$)	[Z/X] ($[Z/X]_\odot$)
Evolutionary	1.0	0.99767	1.00236	0.97
Non-evolutionary	1.0	1.00023	1.00003	1.10

with the gravitational constant, which is known with very high accuracy. Therefore, we keep its value fixed at the one given in Table 8.1. The observational oscillations frequencies for the Sun used in this project are from the Birmingham Solar Oscillations Network (BiSON) (Broomhall et al., 2009; Davies et al., 2014; Hale et al., 2016).

To initiate our non-linear method, we need to start from an initial 1D model of the considered star. This model can be build using non asteroseismic observational data such as its radius, age, surface abundances and luminosity. Then, we build a Standard Solar Model using MESA. The characteristic of this model, called evolutionary model, are given in Table 8.2. In order to test the feasibility of our idea, we are first performing a test of our algorithm with only 5 parameters: α_{MLT}, δX_{RZ}, δZ_{RZ}, δX_{CZ} and δZ_{CZ}, which are respectively the mixing length parameter, the value of the perturbations to the X and Z profiles in the radiative zone, and the perturbations to the X and Z profiles in the convective zone. As an initial guess for the parameters, we use a random number generator following a normal distribution around the mean value 2.0 and variance 0.3 for α_{MLT} and with mean value 0.0 and variance 0.09 for the perturbations. We recall that the function that is then minimised by the algorithm is given by Eq. (8.7).

The characteristics of the resulting optimised static solar model, which we call non-evolutionary model in the following, are given in Table 8.2. We can see that the radius and luminosity are in better agreement with the observed values. However, the agreement of the surface abundance of heavy elements is less good, as it is now 10% too high. This is an indication that we need more flexibility, i.e. more knots, to parametrise the composition profile.

Next, we can compare the oscillations frequencies of the initial and the optimised models to the observed values for the Sun. This is presented on the left panel of Fig. 8.3. This plot presents the oscillations frequencies as a function of frequency modulo the large frequency

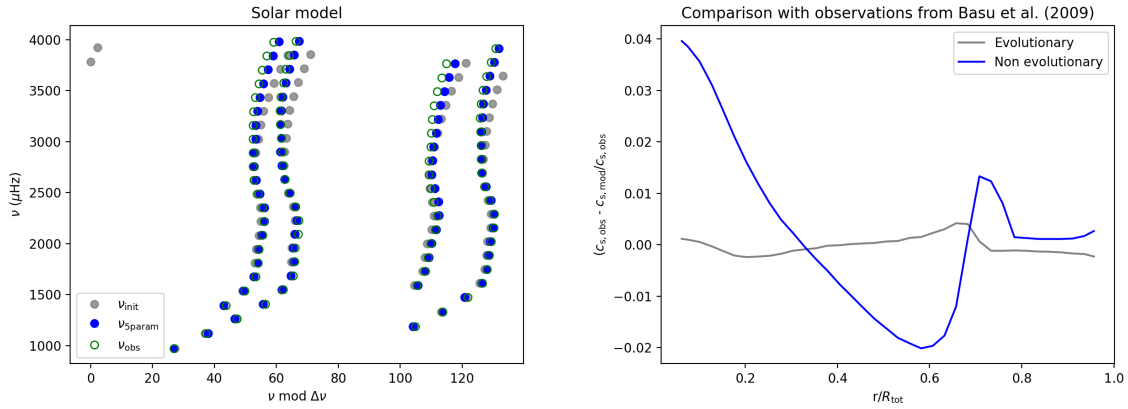

Fig. 8.3 Left panel: Echelle diagrams comparing the frequencies of the initial model (grey filled circle) and the optimised model (blue filled circles), with observations (green empty circles) of harmonic degrees $\ell = 0, 1, 2$ and 3. Right panel: Comparison of the sound speed radial profiles between the initial (grey) and optimised (blue) 1D model of the Sun.

separation $\Delta\nu$ (see Eq. (3.50) for definition). This kind of representation is called an echelle diagram and is convenient to quickly identify low degree oscillation modes. Indeed, each dot corresponds to an eigenfrequency and each 'column' of dots to an angular degree. On this plot, from left to right, we have the angular degrees $\ell = 2, 0, 3, 1$. Echelle diagrams are widely used by observers, as they are convenient to visually compare the eigenfrequencies of the Sun to our different one-dimensional models. We can see that our non-evolutionary model (blue dots) is in better agreement with the solar observations (green circles), compare to the initial evolutionary model (grey dots).

Thanks to the optimisation process, the values of all the parameters used to compute the cost function are now in better agreement with the observed values. This confirms the efficiency of our algorithm. However, the right panel of Fig. 8.3 shows the limitations we are currently facing. This plot shows the radial profile of the relative difference in sound speed between one-dimensional models and observations from Basu et al. (2009). We can see that the agreement is worse for our non-evolutionary model. This is most probably due to the fact that we use only 5 parameters instead of the 51 required for an ideal optimisation.

8.1.4 Futur work

As mentioned, the final objective of this work is to perform non-linear inversion of the structure of massive and evolved stars, for which the linear methods fail. The motivation is that thanks to observational data, I am getting information on physical processes occurring in specific location within a star which remain poorly described by current theories. It allows me to determine which

regions to focus on when I run simulations. For instance, by inferring the compositional profile of a star, I can infer information about mixing. This will help to understand the discrepancies between theoretical predictions and observations in terms of life-time of stars in their different evolutionary stages or surface abundances of chemical elements, for instance.

In this Sect. 8.1, we present an innovative method which allow performing non-linear inversion of stellar structure. Despite that we only run the optimisation with 5 parameters for the moment, instead of the 51 required, our algorithm gives promising results. Indeed, the frequencies, radius and luminosity of the evolutionary model are in better agreement with observations. The next step is thus to confirm the efficiency of our method with more parameters to constrain composition profiles. The main obstacle we are currently facing is the time required for computation. Indeed, when increasing the number of parameters, the time required to run the optimisation increases importantly. Reducing the computation time is not simple, as most of it is due to MESA and GYRE computations. However, a solution we are currently investigating is to parametrise the composition profiles with polynomial functions instead of P-splines. This could reduce the number of parameters down to ~ 21.

8.2 Towards three-dimensional simulations

From observations, we know that all stars rotate and are magnetised, event though the amplitude of these two phenomena may vary by orders of magnitude from one star to another. For some stars, neglecting one, or both, of these physical processes may not be justified. For instance, most of F type stars are known to rotate quite rapidly, typically 5 times the rotation rate of the Sun (Santos et al., 2021), and there is a particular class of A type stars that are particularly magnetic, the roAp stars. To model such physical phenomena, three spatial dimensions are needed. Concerning waves modelling in stellar interiors, the addition of rotation and magnetic field to simulation is important for two main reasons. First, waves could impact physically these two phenomena through transport of angular momentum, energy and chemical elements. For instance, they are supposed to transport angular momentum (e.g. Zahn et al., 1997), which would impact the rotational profile and could possibly affect a dynamo generated magnetic field. Second, waves can be used as probes of these two phenomena thanks to asteroseismology. As mentioned in Sect. 8.1, very good constraints on stellar rotational profile have been obtained thanks to inverse methods. Very recently, Li et al. (2022) have presented the first detection of internal magnetic fields in red giants thanks to mixed modes.

Therefore, a logical continuation of this work is to carry out three-dimensional simulations of stellar interiors that include rotation and magnetic fields. This present two major challenge: computation is way more expensive and spherical geometry creates singularities at the poles.

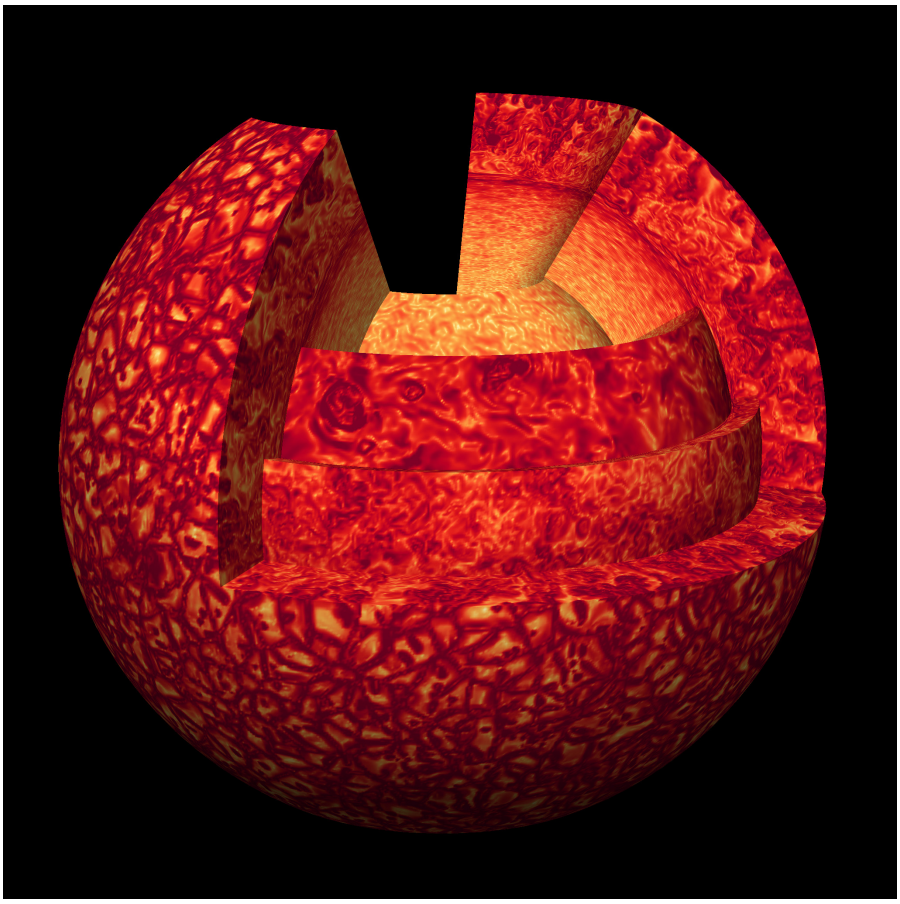

Fig. 8.4 Visualisation of the radial velocity in a three-dimensional solar model run with MUSIC. Credits: D. G. Vlaykov (University of Exeter).

As mentioned earlier, with MUSIC we are consequently running simulations with a wedge geometry. The wedge geometry reduces the size of the numerical domain and therefore the computational cost of the simulation. It also avoids the singularity at the poles. An illustration of three-dimensional simulations of a solar model run using a wedge geometry with MUSIC is presented in Fig. 8.4. To perform spectral analysis of waves in simulations with a wedge geometry, we developed the wedge harmonics basis. This basis allows a decomposition of any variable using an effective angular degree ℓ_{eff}, which takes real values, unlike the usual integer angular degree ℓ from the spherical harmonics basis. The decomposition corresponding to the ϕ component is performed using the same azimuthal order m as the spherical harmonics. Appendix C describes how we constructed this wedge harmonics basis.

8.2.1 Numerical simulations

In order to test our new wedge harmonics basis, I have run three different simulations of a solar model in two dimensions with different co-latitudinal range. In this chapter we consider a realistic solar model, i.e. we do not enforce a fully adiabatic convection as is the case in Chapt. 6. The initial one dimensional model is the same as the solar model introduced in Sect. 6.2.2. The first model, *wide*, is a full hemisphere ranging from 0 to π, similar to the simulations presented in Chapt. 6 and 7. The two others are wedges with a co-latitudinal extent ranging from $\pi/12$ to $11\pi/12$. These two simulations differs in their boundary conditions in the θ-direction. One has periodic boundary conditions, model *wedge-P*, and the other one reflective boundary conditions, model *wedge-R*. The reflective boundary conditions are described in Sect. 6.2.1 and the periodic ones are defined as

- $\mathrm{v}_r(\theta_{\min}) = \mathrm{v}_r(\theta_{\max})$,
- $\mathrm{v}_\theta(\theta_{\min}) = \mathrm{v}_\theta(\theta_{\max})$,

with the co-latitudinal domain ranging from $\theta_{\min} = \pi/12$ to $\theta_{\max} = 11\pi/12$ in our case. Thanks to this study, we will thus also be able to test the influence of boundary conditions in the θ-direction. In these three simulations, the radial extent is the same, ranging from $r_{\text{in}} = 0.4R_{\text{star}}$ to $r_{\text{out}} = 0.9R_{\text{star}}$.

Figure 8.5 presents snapshots of the radial velocity v_r for the three simulations. The values of the radial velocities have been normalised by the rms of the radial velocity $\mathrm{v}_{r,\text{rms}}$ to allow better visualisation. Values of v_r in the radiative zone are indeed orders of magnitude smaller than in the convective zone (see Chapt. 6). In the three models, the envelope structure is very similar, with large up flows (red) and down flows (blue) characteristic of convection. The radiative interior present a structure in concentric circles characteristic of IGWs wavefronts. At first glance, the three simulations looks very similar. Let us study that in more details in the next section.

8.2.2 Preliminary results

As already well-used in Chapt. 6 and 7, the spectral space is very convenient for waves analysis. In the present section, it will also allow testing our wedge harmonics basis. Figure 8.6 presents the power spectrum of the radial velocity as a function of frequency and angular degree for the three simulations. In the following, we will indifferently call ℓ and ℓ_{eff} angular degree. We will therefore only use one common notation ℓ. For model *wide* we are using a decomposition on the spherical harmonics basis, whereas for model *wedge-R* and *wedge-P* we use the wedge harmonics basis. The structure of the power spectra is similar to the one presented in Fig.

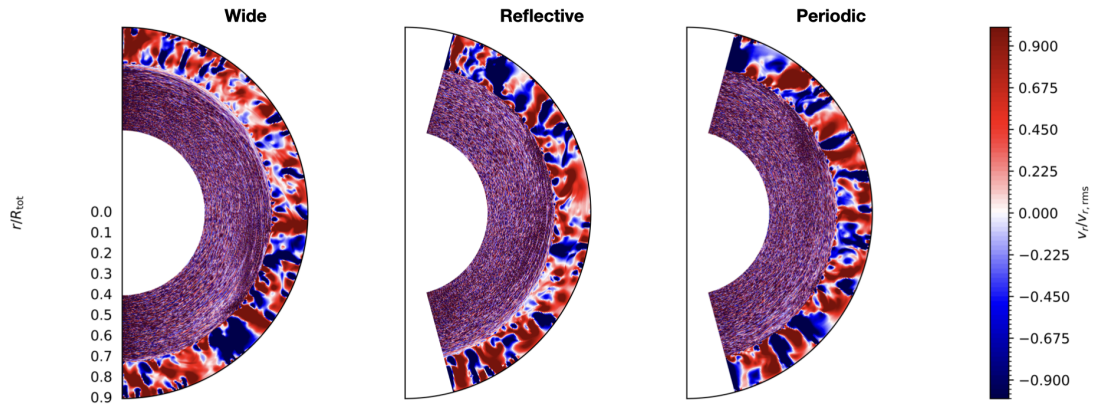

Fig. 8.5 Visualisation of the radial velocity, v_r for the three solar simulations *wide*, *wedge-R* and *wedge-P* as a function of radius r and co-latitude θ. The radial velocity is normalised by the rms value of the radial velocity. Positive values of the radial velocity (red) are outward and negative (blue) are inward.

6.5 for a solar-like model, with the discrete bright ridges corresponding to g modes. The fact that we observe the same g mode patterns for the three models confirms the validity of our wedge harmonics decomposition. However, one main difference between spherical and wedge harmonics is that the eigenvalues are different (see Appendix C for details). In the spherical harmonics case, the angular degree ℓ values are integer. However, for wedge harmonics we can only estimate an equivalent of the angular degree, whose values are real and not equally spaced. The value of this equivalent angular degree depends on the numerical grid in the θ-direction. This is part of the reason why the "resolution" in ℓ on Fig. 8.6 looks different.

This is further illustrated on Fig. 8.7. This figure presents the power spectra of the radial velocity as a function of radius and frequency. As indicated in the title of each panel, the angular degree is not the same for model *wide* and the other two. For the former, the angular degree is $\ell = 9$, whereas for the two wedge simulations, the angular degree is the closest to 9 that is available, $\ell = 9.14$. The three spectra present a very similar structure, with a monotonically decreasing amplitude with increasing frequency in the convective zone ($r \geq 0.72 R_{\rm star}$) and bright ridges corresponding to g modes in the radiative zone ($r \leq 0.72 R_{\rm star}$). On these high amplitude ridges, the low amplitude dots correspond to the knots of the modes. On the three plots, we can see that the number of knots is increasing with decreasing frequency, which is a

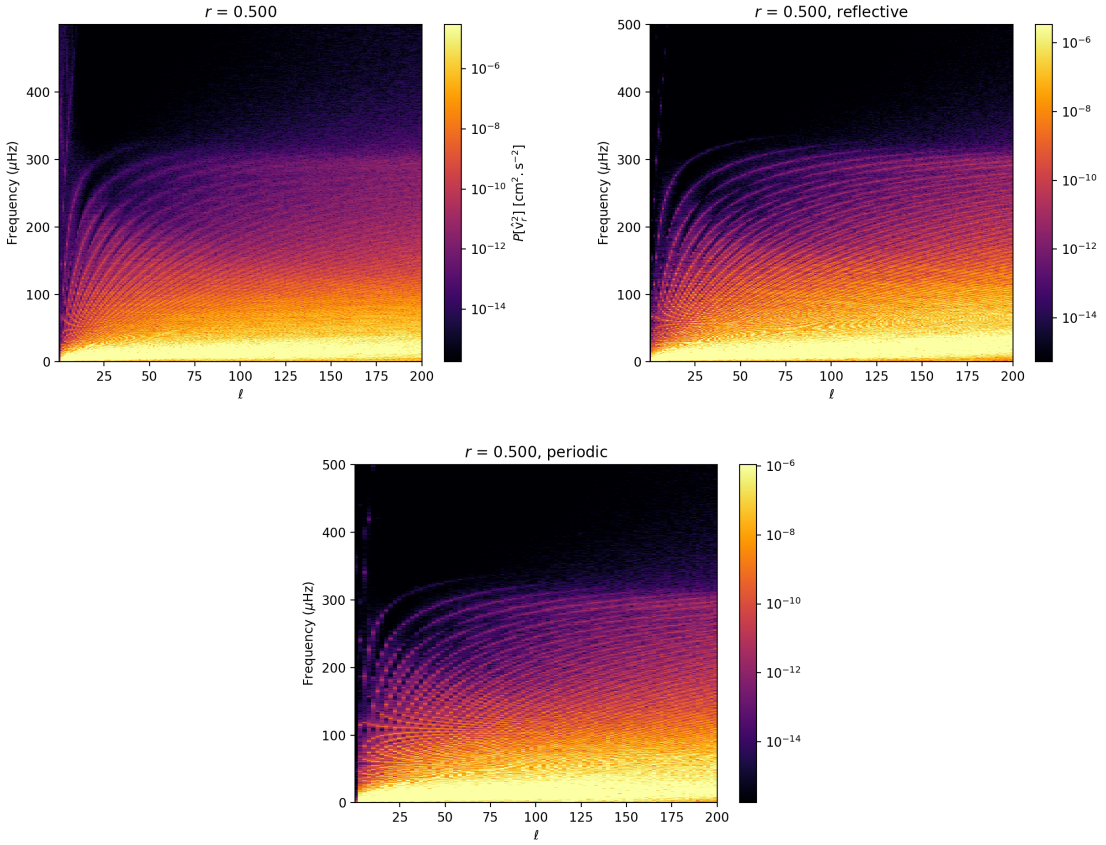

Fig. 8.6 Power spectra of the radial velocity for the three solar simulations *wide* (top), *wedge-R* (middle), *wedge-P* (bottom) as a function of frequency and angular degree at depth $r = 0.5R_{\text{star}}$ in the middle of the radiative zone. They were obtained via mode projection on the spherical and wedge harmonics basis and a temporal Fourier transform of the radial velocity.

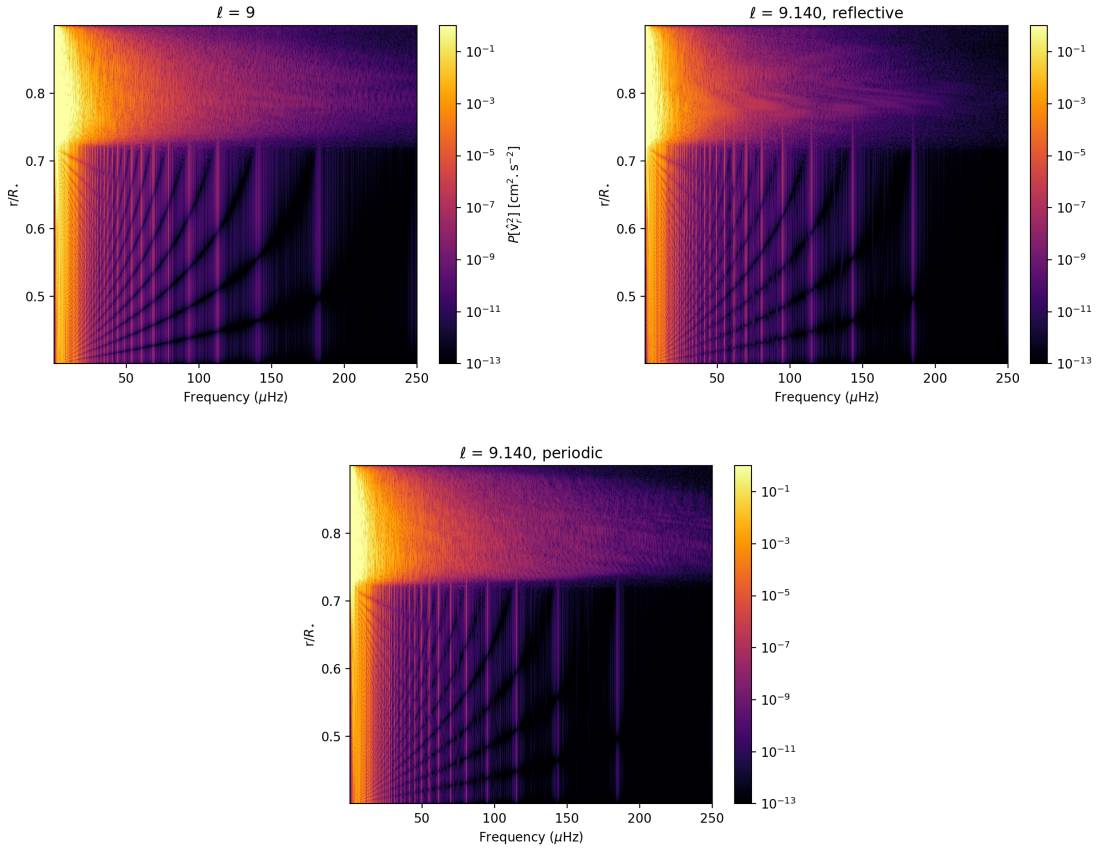

Fig. 8.7 Power spectra of the radial velocity for the three solar simulations *wide* (top), *wedge-R* (middle), *wedge-P* (bottom) as a function of frequency and radius. The spectra are computed for angular degree $\ell = 9$ for mode *wide* and effective angular degree ell_{eff} the closet to 9 for model *wedge-R* and *wedge-P*. They were obtained via mode projection on the spherical harmonics and wedge basis and a temporal Fourier transform of the radial velocity.

property of g modes (Aerts et al., 2010). The structure of these modes, particularly the position of the knots, and their frequency do not appear to be affected by the change in co-latitudinal extent or in the boundary conditions in the θ-direction. From Eq. (3.45) and (3.47) we can see that the eigenfrequencies and eigenfunctions of g modes depends mostly on quantities that only vary with radius. Nevertheless, we need to confirm that by comparing more precisely the frequencies with the predictions from oscillations code GYRE.

8.2.3 Futur work

Running three-dimensional simulations is a natural follow-up to the work presented in this thesis. We have showed that the MUSIC code is well suited to model internal gravity waves with realistic properties, particularly related to their excitation and damping by radiative

diffusion. These two mechanisms remains poorly constrained in stellar interiors, therefore hydrodynamical simulations give valuable information to describe them. Next, to model more realistic IGWs, rotation and magnetism need to be added in the simulations as they will both affect the excitation and propagation of the waves. This will help to guide and analyse observations, as well as studying the role played by IGWs in angular momentum and energy transport in stellar interiors.

The work presented in Sect. 8.2 is a first step towards three-dimensional simulations with MUSIC. As mentioned, running simulations of the full three-dimensional sphere is computationally too expensive with MUSIC at the moment. Thus, we are running simulations on portions of a sphere called wedge (see Fig. 8.4). As the spherical harmonics basis can not be used in this case, we developed a new basis called wedge harmonics, which allow studying waves in the spectral domain. We showed that this basis works and is adapted to a two-dimensional wedge geometry.

The next step is to test it with a three-dimensional simulation. Note that the validity of the wedge harmonics basis in three dimensions is almost straightforward. Indeed, the decomposition in ϕ-direction, which corresponds to the m component in the spectral space, is the same as for the spherical harmonics basis as explained in Appendix C. We already have two sets of simulations running with a three-dimensional geometry that we will be able to analyse soon. We have a set of solar models with different rotation rates and a set of 20 $M_\odot$ star model, also with different rotation rates. The addition of magnetic field is currently in development by the MUSIC team.

Finally, the three simulations presented in this section are also interesting to study the influence of boundary conditions in the θ-direction and the co-latitudinal extent of the numerical grid. This work will be complementary to the study presented in Vlaykov et al. (2022), which analyses the impact of radial truncations on two-dimensional simulations of a solar model.

Chapter 9

Conclusion

This thesis has explored the properties of internal gravity waves (IGWs) in stellar interiors using hydrodynamical simulations. On the one hand, we have highlighted that it is possible to model realistic IGWs with a fully compressible hydrodynamical code. On the other hand, we have showed that numerical simulations set up can impact the properties of IGWs, thus one has to be careful when interpreting the results from these simulations. In addition, theoretical and numerical models can present a good agreement in the linear regime, which will help to constrain observations in the quest for IGWs or g modes in stars. After some introductory chapters (Chapt. 2 - Chapt. 5) on the general context of the study, this thesis is divided in two parts presenting the results. The first part focuses on IGWs properties in two-dimensional simulations of a solar-like model, and particularly on the impact of an artificial enhancement of the luminosity of the numerical model (Chapt. 6). The second part is devoted to intermediate-mass stars which possess a convective core, and where IGWs propagate towards the surface of the star (Chapt. 7).

The first problem we are interested in is related to the challenge of thermal relaxation in hydrodynamical simulations. This open challenge is a consequence of the length of the thermal timescale compared to the other timescales relevant to the simulations. In the context of hydrodynamical simulations, this timescale represents the characteristic time to reach thermal equilibrium. The thermal timescale is estimated with the Kelvin-Helmholtz time, which corresponds to the time for the star to radiate away all its gravitational energy in absence of any energy source (see Eq. (2.6)). For the Sun, it is approximately 20 Myr, and for a $5M_{\odot}$ star 0.4 Myr. With computational time step of the order of several seconds (see Sect. 5.2), it is not possible to run simulations for that long with current computational resources. One common solution to deal with this issue, known as *boosting*, is to artificially increase the luminosity of the stellar model by several orders of magnitude. As showed in Eq. (2.6), the thermal timescale is inversely proportional to the stellar luminosity. The enhancement factor can take value up to

10^7 (e.g. Edelmann et al., 2019), thus decreasing equivalently the thermal timescale and making it computationally reachable. However, despite being used for almost two decades (e.g. Rogers and Glatzmaier, 2005a), the impact of this artificial technique on physical processes has never been quantified. Consequently, the first question we wanted to address was to quantify **the impact of the artificial enhancement of the luminosity in hydrodynamical simulations of stellar interiors on internal gravity waves**. Our results, presented in Chapt. 6 and published in Le Saux et al. (2022), highlight that

- the enhancement of the luminosity increases the convective velocity and therefore the characteristic frequency $\omega_{\rm conv}$ associated with convection. From theory, we know that a given excitation mechanism will generate waves with frequencies $\omega \geq \omega_{\rm conv}$. Therefore, the lowest frequency waves are "lost" in boosted simulations.

- eigenfrequencies of g modes in a given stellar model are not impacted by the luminosity enhancement for boosting factors up to 10^4. This is because the frequency of g modes depends on the stratification and the geometry of the stellar model, which are not modified in boosted simulations. However, there is a dependence on the enhancement factor with a redistribution of most of the energy in high frequency modes. This is a result of the increase of the convective frequency $\omega_{\rm conv}$.

- the two previous points imply, and explain why we observe, a shift of the wave flux towards higher frequencies in boosted simulations. Nevertheless, an important consequence of this is the reduction of the size of the range of frequencies excited. This is because the Brunt-Väisälä frequency N is fixed, and therefore the interval between $\omega_{\rm conv}$ and N is smaller.

- there is an impact of the boost on radiative damping of IGWs. In boosted simulations, radiative diffusivity is increased by the same amount as the luminosity to be consistent and to keep the stellar structure identical as in the reference model. Therefore, damping by radiative diffusion is increased in boosted simulations compared to non-boosted ones. This can have important consequences on angular momentum transport.

These results do not rule out the boosting method, they are a warning about their use and the interpretation of boosted simulation results. In a companion paper, Baraffe et al. (2021) we also study the impact of this technique on convective penetration. The analysis of these two-dimensional simulations have also highlighted that we can model realistic IGWs with the MUSIC code. Indeed, we have showed that

- the wave flux computed in our hydrodynamical simulations are broadly consistent with theoretical predictions for waves excitation by Reynolds stress (Lecoanet and Quataert, 2013) and by penetrative convection (Pinçon et al., 2016).
- the eigenfrequencies of g modes observed in MUSIC simulations compare very well with the analytical predictions from the oscillation code GYRE (Townsend et al., 2018; Townsend and Teitler, 2013).
- damping of IGWs measured in simulations follow the predictions from damping by radiative diffusion predicted by Press (1981).

This encourages us towards three-dimensional modelling to study the transport properties of IGWs, linked to transport of angular momentum, chemical elements and energy.

The second problem we focus on concerns the properties of IGWs in intermediate-mass stars. In these stars, IGWs are excited near the convective core and propagate in the radiative envelope towards the stellar surface. This should offer a better opportunity to detect convectively excited IGWs and associated g modes, and therefore to get information on the inner part of these stars. The inner structure of this type of stars remain poorly known at the moment, and having new constraints will thus help to test stellar evolution theory. However, there are no confirmed detection of IGWs excited by core convection in intermediate-mass stars. More than a decade ago, Blomme et al. (2011) reported the detection of a low-frequency power excess in the observed power spectra of O type stars whose origin was unknown. The authors speculate on three possible explanations for this origin: sub-surface convection, granulation, or stellar wind inhomogeneities. However, they did not conclude on the more probable one. More recently, Bowman et al. (2019, 2020) found a similar power excess at low-frequency in power spectra of OB stars observed by CoRoT (Auvergne et al., 2009) and TESS (Ricker et al., 2015). In these studies, the authors conclude that this power excess results from propagating IGWs excited by core convection that reach the surface of the stars. To draw such a conclusion, they measure the slopes of the observed spectra and obtain a dependence on frequency between ω^{-1} and $\omega^{-3.5}$ for a majority of stars. The authors state that these values are relatively close to the slopes measured in the hydrodynamical simulations of Edelmann et al. (2019); Horst et al. (2020); Ratnasingam et al. (2020); Rogers et al. (2013). However, these findings have been challenged by the theoretical work of Lecoanet et al. (2019) and the simulations from Couston et al. (2018); Lecoanet et al. (2021). In these studies, the authors show that if the observed spectra were resulting from IGWs generated by core convection we should observe high amplitude g modes in the frequency range of the power excess, and a decrease in power towards lower frequencies. They conclude that the likely origin of this power excess is a sub-surface convection zone

(Cantiello et al., 2021). To date, the actual physical origin of this low-frequency power excess is still a matter of debate. It will remain difficult to answer this question as long as the properties of IGWs in intermediate-mass stars are not well known. In this context, the second challenge we want to face is to **bring new constraints on the properties of IGWs propagating in the radiative envelope of intermediate-mass stars**. Our findings are presented in Chapt. 7 and published in Le Saux et al. (2023). Using two-dimensional simulations of a 5 $M_\odot$ stellar model at Zero-Age Main-Sequence (ZAMS), we have highlighted the following properties of IGWs.

- To model realistic IGWs propagating in radiative zone of stars, it is crucial to include a realistic profile of radiative diffusion in hydrodynamical simulations. Indeed, the propagation of IGWs, and thus the evolution of their amplitude, depends strongly on the density and radiative diffusivity profiles. In our 5 $M_\odot$ stellar model, the latter varies by 9 order of magnitudes between the centre and the surface of the star. This strongly impacts the waves amplitude as they propagate, and will determine whether it can reach the surface or not. In addition, it is through damping by radiative diffusion that waves can transport energy and angular momentum. Therefore, to model a realistic transport, it requires a realistic damping mechanism.

- Non-linear effects resulting from high amplitude IGWs may be relevant only above the convective core. In this region, where waves are excited, it appears that IGWs with frequency close to the convective frequency, are excited with amplitude large enough for non-linear effects to occur. In our simulations, these waves seem to be damped very efficiently. Another possible explanation is that these IGWs are generated with a very large amplitude and thus break almost immediately. This could result in additional mixing and/or wave-wave interactions.

- Thermal effects linked to IGWs may be relevant in stellar interiors. Indeed, through damping by radiative diffusion, IGWs can add heat into a given region, but this is almost always neglected in main-sequence stars. In our simulations, we observe an increase of the temperature in the upper layers in a region where radiative damping is particularly efficient. We suggest that IGWs damped by radiative diffusion could explain the temperature increase. Using linear theory, we show that IGWs can explain the amount of heat added in this region during the time of the simulation. This highlights again the importance of using a realistic radiative diffusivity profile in hydrodynamical simulations.

- The actual IGWs spectrum in stellar interiors is still unknown. This is part of the reason why their detection is challenging. Theoretical predictions predict different spectra depending on the excitation mechanism, i.e. penetrative convection or Reynolds stress.

Our results suggest that both mechanisms are present, with the former being more efficient at low frequencies, close to the excitation frequency, and the latter becoming more efficient at higher frequencies. However, in simulations run with artificially enhanced luminosity, the IGWs spectrum is impacted by the boost. Particularly, the efficiency of both mechanisms is affected. In our most boosted simulations, with an enhancement factor of 10^4, the excitation by penetrative convection totally dominates. This casts doubts on the comparison of Bowman et al. (2020) between observed spectra and the ones computed from the boosted simulations.

- Direct comparison between observations and hydrodynamical simulations is not straightforward. Particularly, we cannot easily extrapolate spectra from an internal radius to the surface of the star. In order to compare with observations, one would have to simulate as close as possible to the stellar surface ($r > 0.99 R_{\rm star}$). Indeed, the upper layers of a star will strongly impact the propagation of IGWs. There are also two additional obstacles to this comparison. First, hydrodynamical simulations require physical simplifications that could impact IGWs as we have seen in the work presented in this thesis. Second, during observations, the surface of a star is not resolved. The light received from a star is only collected by a couple of pixels. This will average the signal in such a way that only large scale oscillations are detected.

The results presented in this second part of the thesis have highlighted the complexity of modelling IGWs with hydrodynamical simulations. These waves are particularly sensitive to the physical simplifications needed to run hydrodynamical simulations of stellar interiors. Consequently, making predictions on the ability of IGWs to reach the stellar surface and/or making comparison with observations require caution.

The work presented in this thesis offers several perspectives. I have identified at least three major direction to continue this work.

First, the more evident development is to run more realistic simulations with the MUSIC code. As shown in this thesis, this code is particularly well suited to model IGWs. Their excitation and damping properties are consistent with theoretical predictions. The next step is thus to study their transport properties in further details. In Chapt. 7 we have started to determine the ability of IGWs to transport heat, i.e. energy. This needs to be confirmed with more simulations, both extending closer to the stellar surface and of stellar model with different masses. To analyse the transport of chemical species, two-dimensional simulations are still very efficient. A powerful method for this analysis is to run simulations with Lagrangian particle tracers. A post-processing study including such particles is currently under way using the $5 M_\odot$

model presented in Chapt. 7 and simulations of a $20M_\odot$ star model. This work is done in collaboration J. Morton, new PhD student in Exeter who will work on waves modelling using MUSIC, I. Baraffe, T. Guillet and the MUSIC team. Then, studying the transport properties of angular momentum by IGWs require three-dimensional simulations including rotation. Several simulations are currently running for a solar model (see Fig. 8.4) and a $20M_\odot$ star model with different rotation rates. Waves analysis in the spectral domain in three-dimensional simulations required the development of a new basis, similar to the spherical harmonics but adapted to our wedge geometry, i.e. portions of spheres (see Sect. 8.2). This is the wedge harmonics basis (see Appendix C). The analysis of these rotating simulations will be started in the next couple of months. The last development towards more realistic and complex simulations will be to include magnetic fields to run magneto-hydrodynamical simulations. This development is currently tested and benchmarked by the MUSIC team.

Second, a very interesting perspective is to run simulations of stellar models at different stages of evolution. Indeed, all the models presented in this thesis are at ZAMS. This is a bit restrictive to generalise the properties of IGWs in stellar interiors, as the internal structure of stars evolve a lot during its life. In this context, in collaboration with A. Morison, postdoctoral researcher in Exeter, we are analysing IGWs in evolved $5M_\odot$ star models. The set of simulations used for this study is composed of a reference model, similar to the model *ref* introduced in Chapt. 7, and two evolved models. The reference model has a helium central mass fraction $Y_c = 0.28$, and the two evolved have $Y_c = 0.56$ and $Y_c = 0.70$. The main interest of these evolved models lies in the fact that they present a strongly stratified zone just above the convective core. This phenomenon is due to the retreat of the convective core during the evolution of the star on the main-sequence. Another ongoing analysis focuses on a two-dimensional simulation of a $1.3M_\odot$ subgiant star model. This model is similar to the model M0 presented in Belkacem et al. (2015). Besides the analysis of IGWs, the other main motivation for this study is to model mixed modes. These modes result from the coupling between p and g modes (see Sect. 3.4.4). This work fully exploits the potential of the MUSIC code. Indeed, MUSIC solves the fully compressible equations of hydrodynamics and thus offers the possibility to model acoustic waves, and consequently mixed modes. To my knowledge, this has never been done with hydrodynamical simulations. We have already been able to model and identify one mixed mode in this simulation, as presented in Fig. 9.1. To identify this mode I have used the oscillations code GYRE, which can predict the eigenfrequencies and eigenfunctions of normal modes of a one-dimensional model, but also the nature of these normal mode (acoustic, gravity or mixed mode). However, mixed modes are particularly complex to model. The g mode part, located in the core of the star, has a very short radial wavelength (see inset in Fig. 9.1). Consequently, to model most of the mixed modes of this star will require a very thin mesh in this region. A

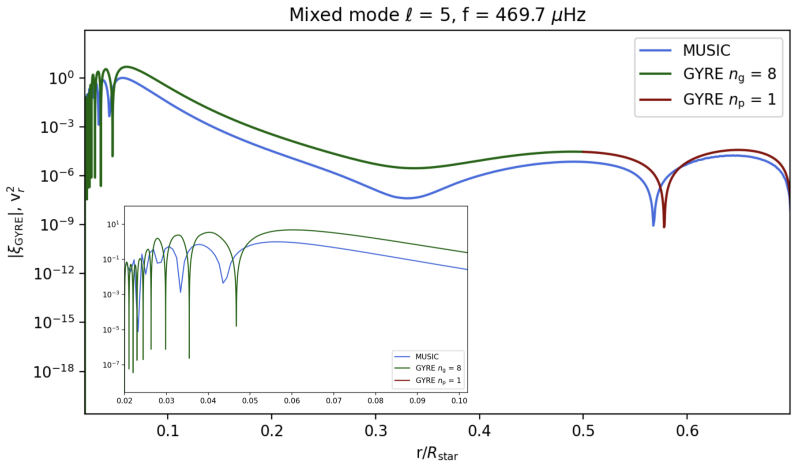

Fig. 9.1 Identification of a mixed mode in a MUSIC simulation of $1.3M_\odot$ subgiant star model (blue curve). Using the oscillations code GYRE it has been possible to identify the nodes corresponding to the g mode part (green curve) and of the p mode part (red curve). The plot present the wave amplitude as a function of normalised radius. The inset is a zoom on the central region of the star.

major issue with this is that such a fine grid close to the centre of the stellar model would imply a too large number of grid points in the radial directions to model a large portion of the star. A solution to this problem is currently developed by T. Guillet, and consists in using static mesh refinement. With this, we will be able to create spatial mesh with a non-uniform spacing.

The third perspective I have identified is to make additional efforts to develop a synergy between observations and simulations. As showed in Chapt. 7, this is challenging mostly because of the physical simplifications used in hydrodynamical simulations and of the unknown physics present in actual stars. However, it will be of major interest for the stellar physics community, and therefore for most astrophysics research fields. This development axis can be divided in two complementary projects. On the one hand, it is possible to use observations to get information on the missing, or incorrectly modelled, physics from stellar evolution and structure theories. An ongoing project with this objective is presented in Sect. 8.1. The aim is to develop a non-linear inversion method for stellar structure. It will help me determine on which region to focus on when setting up and running new hydrodynamical simulations in order to explain observations. On the other hand, it is also possible to use simulations to interpret observations. This is not straightforward, as showed in Chapt. 7. Particularly, hydrodynamical simulations run with radial truncation below $r = 0.99R_{\rm star}$ are not well suited for this purpose. Extrapolation of IGWs' amplitude from an internal radius to the stellar surface can not be done easily due to the complexity of the near-surface layers. Moreover, new comparison methods are required to take into account the spatial average of the stellar surface resulting

from observational acquisition in photometry. These two projects will undoubtedly strengthen the synergy between observations and simulations. We believe that this will become more and more essential with the continuously increasing amount of data received from present and future space telescopes.

I will conclude by pointing out that the results of this thesis could have a wider application than stellar physics. The properties of IGWs presented in this work are not specific to stellar interiors, in the sense that they can be studied as the properties of waves in a fluid, to echo the famous book by Lighthill (1978). Indeed, any fluid, including the plasma inside stars, may be characterised by several fluid dynamics dimensionless parameters, describing the dominant effects or forces. The values taken by these parameters can also give an idea of the dominant properties of IGWs. For instance, the value of Prandtl number, quantifying the effects of viscosity to radiative diffusion, is an indication of the dominant damping mechanism of IGWs. If it becomes larger than one, unlike in stellar interiors, viscous effects dominate and dampen the waves rather than radiative diffusion. Furthermore, the value taken by the Prandtl number is the main difference between geophysical and stellar fluids. On Earth, it is of the order of unity, whereas in stars it is much smaller, typically 10^{-5} or lower. Despite this, geophysical and stellar fluids share a lot of common properties. Both are rotating spheroids that contain stably stratified and convective regions. In addition, stellar and geophysical fluid dynamics are facing similar problems, such as wave-induced transport or convective boundary mixing.

In any case, a generic definition of IGWs is that they are perturbations to a stably stratified fluid, which can transport angular momentum, energy and chemical elements. Therefore, the results obtained in this thesis can be applied and/or tested in multidimensional simulations of planetary atmospheres. This could have multiple benefits such as extending our knowledge of IGWs properties in a general way, helping to understand physical phenomena in these planetary atmospheres, but also give new insights on the interpretation of the results presented in this thesis. This is one of the objectives that I will aim for during my postdoctoral position at the Laboratoire de Météorologie Dynamique (Sorbonne Université, Paris, France). For the next two years, I will be studying the atmospheric dynamics of Neptune and Uranus using a General Circulation Model, which is a kind of hydrodynamical simulations applied to planetary atmospheres. The initial objectives are to test a gravity wave parametrization and study its impact on stratospheric thermal structure and dynamics, and to account for convective plumes and study their impact on the general circulation of the atmospheres of these two planets. These are phenomena that are also present in stellar interiors. I believe that working on both, stellar interiors and planetary atmospheric dynamics, will be valuable for both communities.

Appendix A

Calculation of the root-mean-square velocity

This appendix presents different definitions of the root-mean-square (rms) velocity, v_{rms} that can be found in the literature. In principle, all those definitions are identical, but in practice some differences may arise. Consequently, one should be careful on which definition to use in a specific application. It is not always clear what is the meaning behind each definition, and the purpose of this section is to try to clarify this a little.

A.1 Averages

In hydrodynamic systems, variables are functions of position (r, θ, ϕ) in spherical coordinates, and time t. In the context of multidimensional simulations of a stratified system, it makes sense to look at the radial profile of rms velocity. It is thus necessary to perform angular, i.e. spatial, and temporal averages of the relevant variables. Different averages can be used, depending on whether one is working in the real or spectral domain. Moreover, the order in which these averages are performed is not insignificant.

The general definition for averaging is to perform a statistical averaging. To do so the same experiment need to be repeated many times providing independent realisations (see e.g. Bailly and Comte-Bellot, 2015). In our case, this would mean running a large ensemble of simulations with different initial conditions. Because simulations are computationally very expensive, this not achievable. Hence, two other methods are used to perform averages. First, assuming that the system is stationary, one can use a temporal average. Once a steady-state is achieved, trajectories in phase space quickly forget about their past, and all trajectories wander around a same steady-state configuration. This is the hypothesis of ergodicity. Under this assumption,

the integration become independent of the initial conditions, and we do not need to repeat the same simulation many times! Then, if the time of integration, T, is large enough, the temporal average will be close enough to the statistical one. Temporal average is defined as

$$\langle f(t)\rangle_t \coloneqq \frac{1}{T}\int_0^T f(t)\mathrm{d}t\,. \tag{A.1}$$

The lower limit of the integral $t = 0$ corresponds to the time from which convection is in steady state. After a relaxation phase characterised by the propagation of strong acoustic waves and the onset of convection reaches a plateau which characterises the steady state for the convection (see Baraffe et al., 2021, for more details). Secondly, assuming a homogeneous system one can use a spatial, or angular, averaging. In order to have the spatial average to be equivalent to the statistical one, we need some sort of ergodicity across space points. This property is used in simulations where far-away locations in the simulation domain are uncorrelated, and are effectively close to independently probing phase space. One condition for that is that the volume $\mathcal{V}$ of the system has to be large compare to any length scale. Angular average over the whole unit sphere is defined as

$$\langle g(\theta,\phi)\rangle_{\mathcal{S}} \coloneqq \frac{1}{4\pi}\int_{\mathcal{S}} g(\theta,\phi)\,\sin\theta\mathrm{d}\theta\mathrm{d}\phi, \tag{A.2}$$

with $\mathcal{S}$ the surface of the sphere.

A.2 Mass-weighted squared velocity

First, let's introduce a definition of the rms velocity through the kinetic energy density, e_k,

$$\mathrm{v}_{\mathrm{rms}}^2 \coloneqq \frac{\left\langle \rho \mathrm{v}^2\right\rangle_{\mathcal{S},t}}{\langle\rho\rangle_{\mathcal{S},t}} = \frac{2\langle e_k\rangle_{\mathcal{S},t}}{\langle\rho\rangle_{\mathcal{S},t}}. \tag{A.3}$$

This definition is the most relevant for comparison with analytical models which define a $\mathrm{v}_{\mathrm{rms}}$ and a kinetic energy density base on mass-weighted quantities (see e.g. eq. (47) in Goldreich and Keeley, 1977). In this definition $\rho\mathrm{v}^2\mathrm{d}\mathcal{V}$ is an energy, and $\rho\mathrm{d}\mathcal{V}$ is a mass, so the volume-weighted integrands are all extensive quantities. This metric is a physically motivated measure of the *central tendency* of the kinetic energy content at radius r. That is, it measures what $\langle e_k(r)\rangle_{\mathcal{S}}$ we'd expect to find in a typical star.

In this work, we chose to use this first definition (A.3).

A.3 Spatial average first

Secondly, here is a definition with the $\mathrm{v}_{\mathrm{rms}}$ calculated in real space with the spatial average performed first

$$\mathrm{v}^2_{\mathrm{rms},S}(r) \coloneqq \sum_i \left\langle \left\langle \mathrm{v}_i^2(r,\theta,\phi,t) \right\rangle_{\mathcal{S}} - \langle \mathrm{v}_i(r,\theta,\phi,t)\rangle^2_{\mathcal{S}} \right\rangle_t , \tag{A.4}$$

where $i = r,\theta,\phi$ and v_r, v_θ and v_ϕ being the radial, co-latitudinal and longitudinal velocity components respectively. This definition can be found for example in Samadi et al. (2003) and in Beeck et al. (2012).

Note that in (A.4), the term $\langle\cdot\rangle^2$ reminds us that this type of formula measures the *dispersion of a distribution around its mean*; the distribution in question is related to *uncertainty about (or ignorance of) what we're averaging over*. In this particular definition, we're measuring the dispersion of the distribution of velocities, where the distribution is over θ,ϕ. This tells us *the ensemble-averaged uncertainty on* v *caused by ignorance of* θ,ϕ.

We can define an equivalent $\mathrm{v}_{\mathrm{rms}}$ expression using a decomposition on the Spherical Harmonics (SH) only

$$\mathrm{v}^2_{\mathrm{rms},SH1} = \frac{1}{4\pi} \sum_i \sum_{\ell,m\neq(0,0)} \left\langle \mathrm{v}^2_{i,\ell,m} \right\rangle_t \tag{A.5}$$

or combined with a temporal Fourier transform

$$\mathrm{v}^2_{\mathrm{rms},FS1}(r) = \frac{1}{4\pi}\frac{1}{N} \sum_{i,\omega} \sum_{\ell,m\neq(0,0)} \hat{\mathrm{v}}^2_{i,\ell,m}(\omega,r) \tag{A.6}$$

where $i = r,\theta,\phi$ and we have introduced $\ell \geq 0$ the spherical harmonic degree, m the azimuthal order with $-\ell \leq m \leq \ell$, ω the frequency and N the number of frequency bins. Note that in this method, the sum over SH coefficient play the role of angular averaging and sum over frequency of time averaging. Moreover, neglecting the term associated with $(\ell,m) = (0,0)$ is equivalent to subtracting the spatial average of the velocity. Indeed, we have $\langle \mathrm{v}_i(r,\theta,\phi,t)\rangle^2_{\mathcal{S}} = v^2_{i,\ell=0,m=0}(t,r)$.

This variance only tells us about how homogeneous on average the velocity field is in the angular directions. Angular averages could make sense as an approximation to ensemble averages, in a context where we also have some form of ergodicity across space points. This is not the case for IGW low-ℓ modes, which have dominant energy, induce spatial correlations over the whole domain. Consequently, the second term in Eq. (A.4) may not be negligible.

A.4 Temporal average first

In this third definition, we perform the temporal average first. The definition in real space is

$$\mathrm{v}^2_{\mathrm{rms},T}(r) = \sum_i \left\langle \left\langle \mathrm{v}_i^2(r,\theta,\phi,t) \right\rangle_t - \langle \mathrm{v}_i(r,\theta,\phi,t) \rangle_t^2 \right\rangle_{\mathcal{S}} , \tag{A.7}$$

where $i = r,\theta,\phi$. Just as in the previous section, this expression has equivalents in the spectral domain, using a decomposition on SH only

$$\mathrm{v}^2_{\mathrm{rms},SH2} = \frac{1}{4\pi} \sum_{i,\ell,m} \left(\left\langle v^2_{i,\ell,m} \right\rangle_t - \langle v_{i,\ell,m} \rangle_t^2 \right) \tag{A.8}$$

or combining it with a temporal Fourier transform

$$\mathrm{v}^2_{\mathrm{rms},FS2}(r) = \frac{1}{4\pi} \frac{1}{N} \sum_{i,\ell,m} \sum_{\omega \neq 0} \hat{v}^2_{i,\ell,m}(\omega, r) . \tag{A.9}$$

Note that neglecting the term associated with $\omega = 0$ is equivalent to subtracting the time average. Indeed, we have $\hat{u}_{i,\ell,m}(\omega = 0, r) = \langle v_{i,\ell,m} \rangle_t$. These two equations (A.8) and (A.9) are similar to the definitions given in Belkacem et al. (2009). Here, we compute the ensemble dispersion of the velocity for each space point, and average this dispersion over spherical shells. However, in our case the time average of the velocity is close to zero, particularly in the radiative zone where velocities due to waves tend to cancel out over long periods of time.

A.5 Raw second moment of the velocity

Alternative definitions for Eqs. (A.4) and (A.7) that can be found in the literature are the cases where the $\langle v_{i,\ell,m} \rangle^2$ term is omitted. Then the averages can commute so the definitions given in the Sect. A.4 and A.3 are equivalent

$$\mathrm{v}^2_{\mathrm{rms},R} := \left\langle \left\langle \mathrm{v}^2 \right\rangle_{\mathcal{S}} \right\rangle_t = \left\langle \left\langle \mathrm{v}^2 \right\rangle_t \right\rangle_{\mathcal{S}} := \left\langle \mathrm{v}^2 \right\rangle_{\mathcal{S},t} . \tag{A.10}$$

In our case, we expect that $\left\langle \mathrm{v}^2_{i,\ell,m} \right\rangle \gg \langle \mathrm{v}_{i,\ell,m} \rangle^2$, so this definition is supposed to be equivalent to Eqs. (A.4) and (A.7). Nevertheless, the physical meaning is not the same. In this case, we are looking at the rms of the total velocity (raw output of the simulation) and in the previous two we were looking at the rms of the fluctuations of the velocity.

However, this last definition, although better than the two previous ones, is still not great because it does not make physical sense to compute volume-weighted averages of v^2: $\mathrm{v}^2 \mathrm{d}\mathcal{V}$ is

not an extensive quantity (it has units of energy per unit of mass), so it does not make sense to add up their contributions in an integral over a shell or volume.

A.6 Comparison

Figure A.1 compares the four methods introduced in this appendix, i.e. Eqs. (A.4), (A.7), (A.10) and (A.3). The radial profiles plotted are for the simulation *ref* of the solar-like model introduced in Chapt. 6, but the comparison results are similar for the other simulations used in this thesis. It can be highlighted that the second term on the RHS of Eqs. (A.4) and (A.7) are not negligible. It is the case in the convection zone with the definition (A.7) but not in the radiative zone. And vice versa with the definition given by Eq. (A.4), the second term on the RHS in the radiative region but not in the convective one. Thus, it is important to define precisely how rms values are computed in order to allow comparison of different results.

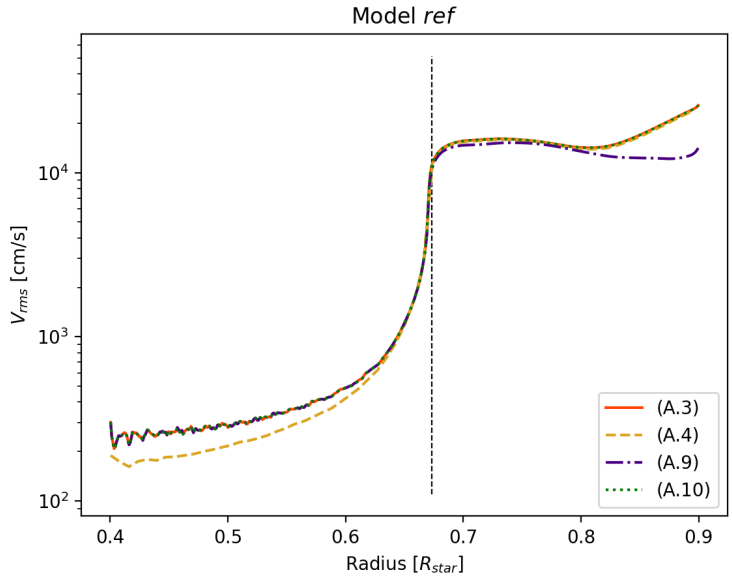

Fig. A.1 Comparison of the rms velocity profile for *ref* using the four definitions (A.3), (A.4), (A.7) and (A.10). The convective boundary corresponding to the Schwarzschild boundary from the 1D initial model is indicated by the vertical dashed line.

Finally, the two other definitions, Eqs. (A.10) and (A.3), are equivalent. Following the arguments presented in Sect. A.2, we chose to work with the corresponding rms velocity definition, i.e. Eq. (A.3).

Appendix B

Spherical harmonics and Fourier amplitudes for simulations

In two-dimensional spherical geometry, on the unit axisymmetric sphere $\mathcal{S}$ parameterised by the polar angle θ, we define the spherical harmonics coefficients $\hat{f}_\ell$ of a function $f(\theta)$ from the expansion

$$f(\theta) = \sum_{\ell \geq 0} \hat{f}_\ell \, Y_\ell^0(\theta), \tag{B.1}$$

$$Y_\ell^0(\theta) = \sqrt{\frac{2\ell+1}{4\pi}} P_\ell(\cos\theta), \tag{B.2}$$

where P_ℓ is the ℓ-th Legendre polynomial. This expansion is identical to the usual spherical harmonics on the sphere, but restricted to the axisymmetric mode $m = 0$. The choice of normalisation makes the Y_ℓ^0 an orthonormal basis for the L^2 inner product on $\mathcal{S}$

$$\int_{\mathcal{S}} Y_\ell^{0*} \, Y_{\ell'}^0 \, \mathrm{d}\Omega = 2\pi \int_0^\pi Y_\ell^0 \, Y_{\ell'}^0 \sin\theta \, \mathrm{d}\theta = \delta_{\ell\ell'}. \tag{B.3}$$

The Fourier coefficients $\tilde{f}_k$ of a temporal signal $f(t)$ over a period T are defined from the expansion

$$f(t)W(t/T) = \sum_k \tilde{f}_k \, e^{2i\pi kt/T}. \tag{B.4}$$

where W is the Blackman window function, used for apodisation of the spectra of non-periodic signals f. In the above formula, mode k corresponds to a physical frequency $\omega_k = 2\pi|k|/T$.

The corresponding Fourier power spectrum $P[f]_n$ is defined from the $\tilde{f}_k$ for all non-negative frequency mode integers n as

$$P[f]_n = \sum_{|k|=n} |\tilde{f}_k|^2 = \begin{cases} |\tilde{f}_0|^2 & \text{if } n = 0, \\ |\tilde{f}_n|^2 + |\tilde{f}_{-n}|^2 & \text{if } n > 0. \end{cases} \tag{B.5}$$

We note that for a real-valued signal f, $\forall k, |\tilde{f}_k|^2 = |\tilde{f}_{-k}|^2$.

Appendix C

Wedge Harmonics

A natural follow-up to the work presented in this thesis is to run three-dimensional simulations. With MUSIC, we can not (for now) run simulations of a full sphere. Therefore, we model a portion of a sphere, which we call a wedge. As explained in Chapt. 8, a challenge for waves analysis in this geometry is that the usual spherical harmonics basis cannot be used to expand variables. Therefore, in collaboration with Thomas Guillet and Mathieu Sylvain, former summer student in Exeter, we have developed a new basis, called the wedge harmonics basis, which is the basis of eigenfunctions of the Laplacian on the wedge (much like the spherical harmonics are the eigenfunctions of the Laplacian on the sphere). This allows to perform analysis in spectral space when analysing waves in a wedge simulation. The objective is to solve on the wedge the eigenvalue problem

$$\Delta u + \lambda u = 0, \tag{C.1}$$

with $\Delta = \nabla^2$ the Laplacian operator, u the eigenfunctions associated to the eigenvalues λ.

C.1 Wedge domain

Consider a spherical system of coordinates on the surface of the unit sphere $\mathcal{S}$, with colatitude θ and longitude ϕ. We define the wedge $\mathcal{W}_{\alpha,\beta}$ as the region of the sphere delimited by $\alpha \leq \theta \leq \pi - \alpha$ and $-\beta \leq \phi \leq \beta$.

$$\mathcal{W}_{\alpha,\beta} = \{x \in \mathcal{S} | (\theta(x), \phi(x)) \in [\alpha, \pi - \alpha] \times [-\beta, \beta]\}, \tag{C.2}$$

with $0 < \alpha < \pi/2$ and $0 < \beta < \pi$. Concerning boundary conditions for the wedge, we will always assume periodic domain in the ϕ-direction. In the θ-direction, the domain can be either periodic

or reflective. An example of a wedge domain is illustrated on Fig. C.1 for $\alpha = \pi/6$ and $\beta = \pi/6$. Furthermore, we assume that the wedge inherits the metric from a sphere

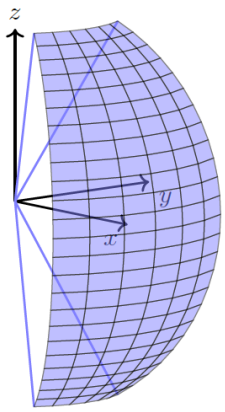

Fig. C.1 Wedge domain for $\alpha = \pi/6$ and $\beta = \pi/6$, discretized in uniform cells of angular extension 5 degrees in both the θ and ϕ directions. Credits: T. Guillet (University of Exeter).

$$\mathrm{d}\Omega = \sin\theta \mathrm{d}\phi \mathrm{d}\theta \tag{C.3}$$

C.2 Eigenfunctions of the Laplacian operator on a wedge

On the unit sphere, and therefore on a wedge $\mathcal{W}_{\alpha,\beta}$ of unit radius, the Laplacian operator is given by

$$\Delta u = \frac{1}{\sin\theta}\left[\frac{\partial}{\partial\theta}\left(\sin\theta\frac{\partial u}{\partial\theta}\right) + \frac{\partial}{\partial\phi}\left(\frac{1}{\sin\theta}\frac{\partial u}{\partial\phi}\right)\right] \tag{C.4}$$

In our case, the geometry of the domain permits the use of separation of variable to look for solutions of Eq. (C.1), which may be written

$$u(\theta,\phi) = f(\theta)g(\phi). \tag{C.5}$$

Substituting this decomposition in Eq. (C.1), we can obtain

$$\Delta u + \lambda u = \frac{1}{\sin\theta}\left[\frac{\partial}{\partial\phi}\left(\frac{1}{\sin\theta}\frac{\partial u}{\partial\phi}\right) + \frac{\partial}{\partial\theta}\left(\frac{\partial u}{\partial\theta}\sin\theta\right)\right] + \lambda u = 0, \tag{C.6}$$

and u has a continuous solution of the wedge surface. Therefore, this solution must be periodic in ϕ and regular at boundaries in θ, i.e. at these points the solution must approach a limit independent of ϕ (Courant and Hilbert, 1966). In the case of the spherical harmonics, the

solutions are the spherical harmonics functions $Y_{\ell m}(\theta,\phi)$ and $\lambda = \ell(\ell+1)$. These solutions are not directly applicable in the case of a wedge, but by adapting the method used for the spherical case we can obtain the wedge solutions. With the considered separation of variables Eq. (C.5), the eigenvalue problem is

$$\frac{\sin\theta}{f}\left[\frac{\mathrm{d}}{\mathrm{d}\theta}\left(\sin\theta\frac{\mathrm{d}f}{\mathrm{d}\theta}\right)\right] + \lambda\sin^2\theta = -\frac{1}{g}\frac{\mathrm{d}^2 g}{\mathrm{d}\phi^2}. \tag{C.7}$$

By the usual argument of separation of variables, since the left-hand side of Eq. (C.7) depends only on θ and the right-hand side only on ϕ, both must be equal to some common constant, which we write as B^2, with $B \in \mathbb{C}$.

From Eq. (C.7), we have

$$\frac{\mathrm{d}^2 g}{\mathrm{d}\phi^2} = -B^2 g \tag{C.8}$$

and therefore the solution takes the form $g \propto \mathrm{e}^{iB\phi}$. Enforcing the periodicity of g on the wedge in the ϕ direction, we find that B must be of the form

$$B = \eta m, \qquad m \in \mathbb{Z}, \qquad \eta := \frac{2\pi}{2\beta}, \tag{C.9}$$

to ensure 2β-periodicity along ϕ. Therefore, the solutions are the modes defined by

$$g_m(\phi) = \frac{1}{\sqrt{2\beta}}\mathrm{e}^{i\eta m\phi}, \qquad m \in \mathbb{Z}, \tag{C.10}$$

where the normalisation is chosen so that the g_m are orthonormal for the inner product

$$\langle g, g'\rangle_\phi := \int_{-\beta}^{\beta} g^* g' \mathrm{d}\phi, \tag{C.11}$$

where the superscript $*$ denotes the complex conjugate.

Going back to Eq. (C.7) and using results for $g(\phi)$, we find for f

$$\frac{\sin\theta}{f}\left[\frac{\mathrm{d}}{\mathrm{d}\theta}\left(\sin\theta\frac{\mathrm{d}f}{\mathrm{d}\theta}\right)\right] + \lambda\sin^2\theta = \eta^2 m^2, \tag{C.12}$$

which may be rewritten as

$$\frac{1}{\sin\theta}\frac{\mathrm{d}}{\mathrm{d}\theta}\left(\sin\theta\frac{\mathrm{d}f}{\mathrm{d}\theta}\right) - \frac{\eta^2 m^2}{\sin^2\theta} f = -\lambda f. \tag{C.13}$$

This is very similar to the eigenproblem appearing in the derivation of the spherical harmonics, for which the solutions for f are the associated Legendre polynomials in $\cos\theta$. Unfortunately, in our case, there is a major difference: we have the $\eta \neq 1$ factor.

We have chosen to solve this eigenproblem in the θ-direction numerically. In order to do so, it is useful to formulate the problem in a weak form that is manifestly symmetric. Let $\mathcal{E}$ be the vector space of (complex-valued) functions of θ that satisfy the chosen boundary conditions (either periodic, zero value, or zero derivative). We use the inner product of the sphere, which for functions of E writes:

$$\forall f, f' \in \mathcal{E}, \qquad \langle f, f' \rangle_\theta \coloneqq \int_\alpha^{\pi-\alpha} \sin\theta \mathrm{d}\theta f^* f'. \tag{C.14}$$

To establish the weak formulation of the eigenproblem given by Eq. (C.13), we take the inner product of this equation with an arbitrary test function f', and require that the identity holds for all f'

$$\forall f' \in \mathcal{E}, \qquad \left\langle f', \frac{1}{\sin\theta}\frac{\mathrm{d}}{\mathrm{d}\theta}\left(\sin\theta\frac{\mathrm{d}f}{\mathrm{d}\theta}\right)\right\rangle_\theta - \left\langle f', \frac{\eta^2 m^2}{\sin^2\theta} f\right\rangle_\theta = -\lambda\langle f', f\rangle_\theta. \tag{C.15}$$

Using integration by parts, one can easily obtain

$$\left\langle f', \frac{1}{\sin\theta}\frac{\mathrm{d}}{\mathrm{d}\theta}\left(\sin\theta\frac{\mathrm{d}f}{\mathrm{d}\theta}\right)\right\rangle_\theta = -\left\langle \frac{\mathrm{d}f'}{\mathrm{d}\theta}, \frac{\mathrm{d}f}{\mathrm{d}\theta}\right\rangle_\theta \tag{C.16}$$

where we have used the fact that, for all the boundary conditions we consider (periodic, zero value, zero derivative), the boundary terms vanish. Equation (C.15) therefore writes

$$\forall f' \in \mathcal{E}, \qquad \left\langle \frac{\mathrm{d}f'}{\mathrm{d}\theta}, \frac{\mathrm{d}f}{\mathrm{d}\theta}\right\rangle_\theta + \left\langle \frac{\eta m}{\sin\theta} f', \frac{\eta m}{\sin\theta} f\right\rangle_\theta = \lambda\langle f', f\rangle_\theta. \tag{C.17}$$

In this form, the problem can be directly discretized into matrix form:

$$\forall F', \quad (DF')^\dagger B(DF) + \eta^2 m^2 (S^{-1}F')^\dagger B(S^{-1}F) = \lambda F'^\dagger BF \tag{C.18}$$

where $M^\dagger$ denotes the conjugate transpose of the matrix M, and where:

- F, F' are the column vectors formed by the discrete values of f, f' at the points of the simulation θ grid,
- B is the (real) matrix corresponding to a discrete approximation of the inner product, i.e.: $\langle f', f\rangle_\theta \approx F'^\dagger BF$. We derive B by approximating the integral of the inner product using a second-order midpoint rule with the point-wise values stored F and F', accounting for the metric term $\sin\theta$,

- The D matrix represents the derivation operator on functions of θ. To ensure that D is anti-Hermitian, we derive D by taking the matrix square root of a finite difference discretization of the Laplacian D^2. The chosen discretization for D^2 accounts for the desired boundary conditions in θ (periodic, zero value, or zero derivative),
- S is the matrix corresponding to a point-wise multiplication by $\sin\theta$.

The problem above amounts to solving the generalized eigenvalue problem:

$$\left(D^\dagger BD + \eta^2 m^2 (S^{-1})^\dagger B(S^{-1})\right)F = \lambda BF \tag{C.19}$$

which we solve numerically for eigenvalues λ and eigenvectors F, using solvers making use of the Hermitian character of the formulation. For a fixed given m, each of the λ, F are labelled with an integer q, so the modes are indexed by (m,q).

C.3 Angular scales with the wedge and spherical harmonics

In the case of spherical harmonics, i.e. $\alpha = 0$ and $\beta = \pi$, the eigenvalues are $\lambda^{\mathrm{SH}}_{|m|,q} = (|m| + q)(|m| + q + 1)$ and depend only on $|m| + q$, so we can index them alternatively with

$$\ell = |m| + q \tag{C.20}$$

and use (ℓ, m) to index the corresponding eigenfunctions $Y_{m,\ell}$. In this case, the constraints $|m| \geq 0$ and $q \geq 0$ translates to the usual $\ell \geq 0$ and $|m| \leq \ell$. For many physical applications where quantities on the sphere are expanded into spherical harmonics, the spectrum dependence on ℓ provides rich information about the angular scales present in the signal, because the modes with eigenvalue $\lambda^{\mathrm{SH}}_\ell$ probe angular scales $\sim \pi/\sqrt{\lambda^{\mathrm{SH}}_\ell} \simeq \pi/\ell$.

For wedge harmonics, the angular scales probed by given modes (m,q) will depend on the extent of the wedge, i.e. on α and β. In addition, the wedge eigenvalues now cannot be expressed as a function of only $\ell = |m| + q$. However, by analogy with spherical harmonics, we can define an "effective" $\ell_{|m|,q}$ which informs about the angular scales probed by wedge modes $(\pm m, q)$ by equating the eigenvalues of the spherical and wedge harmonics, which indicate what angular scale is being probed by a given mode:

$$\lambda^{\mathrm{SH}}_\ell = \tilde{\ell}(\tilde{\ell} + 1) = \lambda_{|m|,q}, \tag{C.21}$$

with

$$\tilde{\ell}_{|m|,q} = \sqrt{\lambda_{|m|,q} + \frac{1}{4}} - \frac{1}{2}. \tag{C.22}$$

References

Aerts, C., Augustson, K., Mathis, S., Pedersen, M. G., Mombarg, J. S. G., Vanlaer, V., Van Beeck, J., and Van Reeth, T. (2021). Rossby numbers and stiffness values inferred from gravity-mode asteroseismology of rotating F- and B-type dwarfs. Consequences for mixing, transport, magnetism, and convective penetration. *A&A*, 656:A121.

Aerts, C., Christensen-Dalsgaard, J., and Kurtz, D. W. (2010). *Asteroseismology*.

Aerts, C. and Rogers, T. M. (2015). Observational Signatures of Convectively Driven Waves in Massive Stars. *ApJ*, 806(2):L33.

Aizenman, M., Smeyers, P., and Weigert, A. (1977). Avoided Crossing of Modes of Non-radial Stellar Oscillations. *A&A*, 58:41.

Alvan, L., Brun, A. S., and Mathis, S. (2014). Theoretical seismology in 3D: nonlinear simulations of internal gravity waves in solar-like stars. *A&A*, 565:A42.

Alvan, L., Strugarek, A., Brun, A. S., Mathis, S., and Garcia, R. A. (2015). Characterizing the propagation of gravity waves in 3D nonlinear simulations of solar-like stars. *A&A*, 581:A112.

Alvan, S. (2014). *Ondes internes de gravite dans les etoiles de type solaire. Excitation, propagation et transport de moment cinetique.* PhD thesis, Universite Paris- Diderot.

Anders, E. H., Brown, B. P., and Oishi, J. S. (2018). Accelerated evolution of convective simulations. *Physical Review Fluids*, 3(8):083502.

Andersen, B. N. (1994). Excitation of Solar Gravity Waves. *Sol. Phys.*, 152(1):241–246.

Andersen, B. N. (1996). Theoretical amplitudes of solar g-modes. *A&A*, 312:610–614.

Ando, H. and Osaki, Y. (1975). Nonadiabatic nonradial oscillations: an application to the five-minute oscillation of the sun. *PASJ*, 27(4):581–603.

Andrassy, R., Herwig, F., Woodward, P., and Ritter, C. (2020). 3D hydrodynamic simulations of C ingestion into a convective O shell. *MNRAS*, 491(1):972–992.

Antia, H. M. and Basu, S. (1994). Nonasymptotic helioseismic inversion for solar structure. *A&AS*, 107:421–444.

Auvergne, M., Bodin, P., Boisnard, L., Buey, J. T., Chaintreuil, S., Epstein, G., Jouret, M., Lam-Trong, T., Levacher, P., Magnan, A., Perez, R., Plasson, P., Plesseria, J., Peter, G., Steller, M., Tiphène, D., Baglin, A., Agogué, P., Appourchaux, T., Barbet, D., Beaufort, T., Bellenger, R., Berlin, R., Bernardi, P., Blouin, D., Boumier, P., Bonneau, F., Briet, R., Butler,

B., Cautain, R., Chiavassa, F., Costes, V., Cuvilho, J., Cunha-Parro, V., de Oliveira Fialho, F., Decaudin, M., Defise, J. M., Djalal, S., Docclo, A., Drummond, R., Dupuis, O., Exil, G., Fauré, C., Gaboriaud, A., Gamet, P., Gavalda, P., Grolleau, E., Gueguen, L., Guivarc'h, V., Guterman, P., Hasiba, J., Huntzinger, G., Hustaix, H., Imbert, C., Jeanville, G., Johlander, B., Jorda, L., Journoud, P., Karioty, F., Kerjean, L., Lafond, L., Lapeyrere, V., Landiech, P., Larqué, T., Laudet, P., Le Merrer, J., Leporati, L., Leruyet, B., Levieuge, B., Llebaria, A., Martin, L., Mazy, E., Mesnager, J. M., Michel, J. P., Moalic, J. P., Monjoin, W., Naudet, D., Neukirchner, S., Nguyen-Kim, K., Ollivier, M., Orcesi, J. L., Ottacher, H., Oulali, A., Parisot, J., Perruchot, S., Piacentino, A., Pinheiro da Silva, L., Platzer, J., Pontet, B., Pradines, A., Quentin, C., Rohbeck, U., Rolland, G., Rollenhagen, F., Romagnan, R., Russ, N., Samadi, R., Schmidt, R., Schwartz, N., Sebbag, I., Smit, H., Sunter, W., Tello, M., Toulouse, P., Ulmer, B., Vandermarcq, O., Vergnault, E., Wallner, R., Waultier, G., and Zanatta, P. (2009). The CoRoT satellite in flight: description and performance. *A&A*, 506(1):411–424.

Bailly, C. and Comte-Bellot, G. (2015). *Turbulence*. Springer International Publishing.

Baldwin, M. P., Gray, L. J., Dunkerton, T. J., Hamilton, K., Haynes, P. H., Randel, W. J., Holton, J. R., Alexander, M. J., Hirota, I., Horinouchi, T., Jones, D. B. A., Kinnersley, J. S., Marquardt, C., Sato, K., and Takahashi, M. (2001). The quasi-biennial oscillation. *Reviews of Geophysics*, 39(2):179–229.

Ball, W. H. and Gizon, L. (2014). A new correction of stellar oscillation frequencies for near-surface effects. *A&A*, 568:A123.

Baraffe, I., Chabrier, G., Allard, F., and Hauschildt, P. H. (1998). Evolutionary models for solar metallicity low-mass stars: mass-magnitude relationships and color-magnitude diagrams. *A&A*, 337:403–412.

Baraffe, I. and El Eid, M. F. (1991). Evolution of massive stars with variable initial compositions. *A&A*, 245(2):548–560.

Baraffe, I., Pratt, J., Goffrey, T., Constantino, T., Folini, D., Popov, M. V., Walder, R., and Viallet, M. (2017). Lithium Depletion in Solar-like Stars: Effect of Overshooting Based on Realistic Multi-dimensional Simulations. *ApJ*, 845(1):L6.

Baraffe, I., Pratt, J., Vlaykov, D. G., Guillet, T., Goffrey, T., Le Saux, A., and Constantino, T. (2021). Two-dimensional simulations of solar-like models with artificially enhanced luminosity. I. Impact on convective penetration. *A&A*, 654:A126.

Basu, S. (1997). Seismology of the base of the solar convection zone. *MNRAS*, 288(3):572–584.

Basu, S. (2016). Global seismology of the Sun. *Living Reviews in Solar Physics*, 13(1):2.

Basu, S. and Chaplin, W. J. (2017). *Asteroseismic Data Analysis: Foundations and Techniques*.

Basu, S., Chaplin, W. J., Elsworth, Y., New, R., and Serenelli, A. M. (2009). Fresh Insights on the Structure of the Solar Core. *ApJ*, 699(2):1403–1417.

Bedding, T. R., Butler, R. P., Kjeldsen, H., Baldry, I. K., O'Toole, S. J., Tinney, C. G., Marcy, G. W., Kienzle, F., and Carrier, F. (2001). Evidence for Solar-like Oscillations in β Hydri. *ApJ*, 549(1):L105–L108.

Beeck, B., Collet, R., Steffen, M., Asplund, M., Cameron, R. H., Freytag, B., Hayek, W., Ludwig, H. G., and Schüssler, M. (2012). Simulations of the solar near-surface layers with the CO5BOLD, MURaM, and Stagger codes. *A&A*, 539:A121.

Belkacem, K., Marques, J. P., Goupil, M. J., Mosser, B., Sonoi, T., Ouazzani, R. M., Dupret, M. A., Mathis, S., and Grosjean, M. (2015). Angular momentum redistribution by mixed modes in evolved low-mass stars. II. Spin-down of the core of red giants induced by mixed modes. *A&A*, 579:A31.

Belkacem, K., Pinçon, C., and Buldgen, G. (2022). Amplitudes of Solar Gravity Modes: A Review. *Sol. Phys.*, 297(11):147.

Belkacem, K., Samadi, R., Goupil, M. J., Dupret, M. A., Brun, A. S., and Baudin, F. (2009). Stochastic excitation of nonradial modes. II. Are solar asymptotic gravity modes detectable? *A&A*, 494(1):191–204.

Bellinger, E. P., Basu, S., and Hekker, S. (2020). Inverse Analysis of Asteroseismic Data: A Review. *Astrophysics and Space Science Proceedings*, 57:171–183.

Bellinger, E. P., Basu, S., Hekker, S., and Ball, W. H. (2017). Model-independent Measurement of Internal Stellar Structure in 16 Cygni A and B. *ApJ*, 851(2):80.

Bellinger, E. P., Basu, S., Hekker, S., Christensen-Dalsgaard, J., and Ball, W. H. (2021). Asteroseismic Inference of the Central Structure in a Subgiant Star. *ApJ*, 915(2):100.

Biermann, L. (1932). Untersuchungen über den inneren Aufbau der Sterne. IV. Konvektionszonen im Innern der Sterne. (Veröffentlichungen der Universitäts-Sternwarte Göttingen, Nr. 27.) Mit 5 Abbildungen. *ZAp*, 5:117.

Blomme, R., Mahy, L., Catala, C., Cuypers, J., Gosset, E., Godart, M., Montalban, J., Ventura, P., Rauw, G., Morel, T., Degroote, P., Aerts, C., Noels, A., Michel, E., Baudin, F., Baglin, A., Auvergne, M., and Samadi, R. (2011). Variability in the CoRoT photometry of three hot O-type stars. HD 46223, HD 46150, and HD 46966. *A&A*, 533:A4.

Böhm-Vitense, E. (1958). Über die Wasserstoffkonvektionszone in Sternen verschiedener Effektivtemperaturen und Leuchtkräfte. Mit 5 Textabbildungen. *ZAp*, 46:108.

Borucki, W. J., Koch, D., Basri, G., Batalha, N., Brown, T., Caldwell, D., Caldwell, J., Christensen-Dalsgaard, J., Cochran, W. D., DeVore, E., Dunham, E. W., Dupree, A. K., Gautier, T. N., Geary, J. C., Gilliland, R., Gould, A., Howell, S. B., Jenkins, J. M., Kondo, Y., Latham, D. W., Marcy, G. W., Meibom, S., Kjeldsen, H., Lissauer, J. J., Monet, D. G., Morrison, D., Sasselov, D., Tarter, J., Boss, A., Brownlee, D., Owen, T., Buzasi, D., Charbonneau, D., Doyle, L., Fortney, J., Ford, E. B., Holman, M. J., Seager, S., Steffen, J. H., Welsh, W. F., Rowe, J., Anderson, H., Buchhave, L., Ciardi, D., Walkowicz, L., Sherry, W., Horch, E., Isaacson, H., Everett, M. E., Fischer, D., Torres, G., Johnson, J. A., Endl, M., MacQueen, P., Bryson, S. T., Dotson, J., Haas, M., Kolodziejczak, J., Cleve, J. V., Chandrasekaran, H., Twicken, J. D., Quintana, E. V., Clarke, B. D., Allen, C., Li, J., Wu, H., Tenenbaum, P., Verner, E., Bruhweiler, F., Barnes, J., and Prsa, A. (2010). Kepler planet-detection mission: Introduction and first results. *Science*, 327(5968):977–980.

Bouchy, F. and Carrier, F. (2001). P-mode observations on α Cen A. *A&A*, 374:L5–L8.

Bowman, D. M., Burssens, S., Pedersen, M. G., Johnston, C., Aerts, C., Buysschaert, B., Michielsen, M., Tkachenko, A., Rogers, T. M., Edelmann, P. V. F., Ratnasingam, R. P., Simón-Díaz, S., Castro, N., Moravveji, E., Pope, B. J. S., White, T. R., and De Cat, P. (2019). Low-frequency gravity waves in blue supergiants revealed by high-precision space photometry. *Nature Astronomy*, 3:760–765.

Bowman, D. M., Burssens, S., Simón-Díaz, S., Edelmann, P. V. F., Rogers, T. M., Horst, L., Röpke, F. K., and Aerts, C. (2020). Photometric detection of internal gravity waves in upper main-sequence stars. II. Combined TESS photometry and high-resolution spectroscopy. *A&A*, 640:A36.

Broomhall, A.-M., Chaplin, W. J., Davies, G. R., Elsworth, Y., Fletcher, S. T., Hale, S. J., Miller, B., and New, R. (2009). Definitive Sun-as-a-star p-mode frequencies: 23 years of BiSON observations. *Monthly Notices of the Royal Astronomical Society: Letters*, 396(1):L100–L104.

Brown, T. M. and Morrow, C. A. (1987). Depth and Latitude Dependence of Solar Rotation. *ApJ*, 314:L21.

Brun, A. S., Miesch, M. S., and Toomre, J. (2011). Modeling the Dynamical Coupling of Solar Convection with the Radiative Interior. *ApJ*, 742(2):79.

Brun, A. S., Strugarek, A., Varela, J., Matt, S. P., Augustson, K. C., Emeriau, C., DoCao, O. L., Brown, B., and Toomre, J. (2017). On Differential Rotation and Overshooting in Solar-like Stars. *ApJ*, 836(2):192.

Bugnet, L. (2020). *Caractérisation globale des étoiles et magnétisme interne le long de leur évolutionIntelligence artificielle en support de l'astérosismologie et nouvelles contraintes théoriques pour les champs magnétiques internes*. Theses, Université de Paris.

Buldgen, G., Bétrisey, J., Roxburgh, I. W., Vorontsov, S. V., and Reese, D. R. (2022). Inversions of Stellar Structure From Asteroseismic Data. *Frontiers in Astronomy and Space Sciences*, 9:942373.

Buldgen, G., Salmon, S., and Noels, A. (2019). Progress in global helioseismology: a new light on the solar modelling problem and its implications for solar-like stars. *Frontiers in Astronomy and Space Sciences*, 6:42.

Buzasi, D., Catanzarite, J., Laher, R., Conrow, T., Shupe, D., Gautier, T. N., I., Kreidl, T., and Everett, D. (2000). The Detection of Multimodal Oscillations on α Ursae Majoris. *ApJ*, 532(2):L133–L136.

Cantiello, M. and Braithwaite, J. (2019). Envelope convection, surface magnetism, and spots in a and late b-type stars. *The Astrophysical Journal*, 883(1):106.

Cantiello, M., Lecoanet, D., Jermyn, A. S., and Grassitelli, L. (2021). On the Origin of Stochastic, Low-Frequency Photometric Variability in Massive Stars. *ApJ*, 915(2):112.

Canuto, V. M. (2009). Turbulence in Astrophysical and Geophysical Flows. In Hillebrandt, W. and Kupka, F., editors, *Interdisciplinary Aspects of Turbulence*, volume 756, page 107.

Castro, N., Fossati, L., Langer, N., Simón-Díaz, S., Schneider, F. R. N., and Izzard, R. G. (2014). The spectroscopic Hertzsprung-Russell diagram of Galactic massive stars. *A&A*, 570:L13.

Catelan, M. and Smith, H. A. (2015). *Pulsating Stars*.

Chandrasekhar, S. (1939). *An introduction to the study of stellar structure*.

Chandrasekhar, S. (1964). A General Variational Principle Governing the Radial and the Non-Radial Oscillations of Gaseous Masses. *ApJ*, 139:664.

Christensen-Dalsgaard, J. (1984). What Will Asteroseismology Teach us. In Mangeney, A. and Praderie, F., editors, *Space Research in Stellar Activity and Variability*, page 11.

Christensen-Dalsgaard, J. (1988). An Overview Of Helio- and Asteroseismology. In Christensen-Dalsgaard, J. and Frandsen, S., editors, *Advances in Helio- and Asteroseismology*, pages 3–19. Springer Netherlands.

Christensen-Dalsgaard, J. (2002). Helioseismology. *Rev. Mod. Phys.*, 74:1073–1129.

Christensen-Dalsgaard, J. (2014). *Lecture notes on stellar oscillations*. Aarhus University.

Christensen-Dalsgaard, J. (2021). Solar structure and evolution. *Living Reviews in Solar Physics*, 18(1):2.

Christensen-Dalsgaard, J., Dappen, W., Ajukov, S. V., Anderson, E. R., Antia, H. M., Basu, S., Baturin, V. A., Berthomieu, G., Chaboyer, B., Chitre, S. M., Cox, A. N., Demarque, P., Donatowicz, J., Dziembowski, W. A., Gabriel, M., Gough, D. O., Guenther, D. B., Guzik, J. A., Harvey, J. W., Hill, F., Houdek, G., Iglesias, C. A., Kosovichev, A. G., Leibacher, J. W., Morel, P., Proffitt, C. R., Provost, J., Reiter, J., Rhodes, E. J., J., Rogers, F. J., Roxburgh, I. W., Thompson, M. J., and Ulrich, R. K. (1996). The Current State of Solar Modeling. *Science*, 272(5266):1286–1292.

Christensen-Dalsgaard, J., Gough, D. O., and Thompson, M. J. (1991). The Depth of the Solar Convection Zone. *ApJ*, 378:413.

Christensen-Dalsgaard, J., Monteiro, M. J. P. F. G., Rempel, M., and Thompson, M. J. (2011). A more realistic representation of overshoot at the base of the solar convective envelope as seen by helioseismology. *MNRAS*, 414(2):1158–1174.

Christensen-Dalsgaard, J., Proffitt, C. R., and Thompson, M. J. (1993). Effects of Diffusion on Solar Models and Their Oscillation Frequencies. *ApJ*, 403:L75.

Claverie, A., Isaak, G. R., McLeod, C. P., van der Raay, H. B., and Roca Cortes, T. (1979). Solar structure from global studies of the 5-minute oscillation. *Nature*, 282:591–594.

Cohen-Tannoudji, C., Diu, B., and Laloe, F. (1986). *Quantum Mechanics, Volume 2*, volume 2.

Courant, R., Friedrichs, K., and Lewy, H. (1928). Über die partiellen Differenzengleichungen der mathematischen Physik. *Mathematische Annalen*, 100:32–74.

Courant, R. and Hilbert, D. (1966). *Methods of Mathematical Physics*. New York: Interscience Publishers.

Couston, L. A., Lecoanet, D., Favier, B., and Le Bars, M. (2017). Dynamics of mixed convective-stably-stratified fluids. *Physical Review Fluids*, 2(9):094804.

Couston, L.-A., Lecoanet, D., Favier, B., and Le Bars, M. (2018). The energy flux spectrum of internal waves generated by turbulent convection. *Journal of Fluid Mechanics*, 854:R3.

Couvidat, S., Turck-Chièze, S., and Kosovichev, A. G. (2003). Solar Seismic Models and the Neutrino Predictions. *ApJ*, 599(2):1434–1448.

Cowling, T. G. (1941). The Non-radial Oscillations of Polytropic Stars. *Monthly Notices of the Royal Astronomical Society*, 101(8):367–375.

Cristini, A., Meakin, C., Hirschi, R., Arnett, D., Georgy, C., Viallet, M., and Walkington, I. (2017). 3D hydrodynamic simulations of carbon burning in massive stars. *MNRAS*, 471(1):279–300.

Däppen, W., Gough, D. O., Kosovichev, A. G., and Thompson, M. J. (1991). A New Inversion for the Hydrostatic Stratification of the Sun. In Gough, D. and Toomre, J., editors, *Challenges to Theories of the Structure of Moderate-Mass Stars*, volume 388, page 111.

Davies, G. R., Broomhall, A. M., Chaplin, W. J., Elsworth, Y., and Hale, S. J. (2014). Low-frequency, low-degree solar p-mode properties from 22 years of Birmingham Solar Oscillations Network data. *MNRAS*, 439(2):2025–2032.

De Cat, P. and Aerts, C. (2002). A study of bright southern slowly pulsating B stars. II. The intrinsic frequencies. *A&A*, 393:965–981.

Deheuvels, S. and Michel, E. (2010). New insights on the interior of solar-like pulsators thanks to CoRoT: the case of HD 49385. *Ap&SS*, 328(1-2):259–263.

Deubner, F. L. (1975). Observations of low wavenumber nonradial eigenmodes of the sun. *A&A*, 44(2):371–375.

Dintrans, B., Brandenburg, A., Nordlund, Å., and Stein, R. F. (2005). Spectrum and amplitudes of internal gravity waves excited by penetrative convection in solar-type stars. *A&A*, 438(1):365–376.

Eddington, A. S. (1916). On the radiative equilibrium of the stars. *MNRAS*, 77:16–35.

Edelmann, P. V. F., Ratnasingam, R. P., Pedersen, M. G., Bowman, D. M., Prat, V., and Rogers, T. M. (2019). Three-dimensional Simulations of Massive Stars. I. Wave Generation and Propagation. *ApJ*, 876(1):4.

Eilers, P. H. C. and Marx, B. D. (1996). Flexible smoothing with B-splines and penalties. *Statistical Science*, 11(2):89 – 121.

Ekman, V. W. (1904). On dead water. *Norwegian North Polar Expedition, 1893-1896*, pages 1–150.

Evans, J. W. and Michard, R. (1962). Observational Study of Macroscopic Inhomogeneities in the Solar Atmosphere. III. Vertical Oscillatory Motions in the Solar Photosphere. *ApJ*, 136:493.

Fath, E. A. (1935). A photometric study of Delta Scuti. *Lick Observatory Bulletin*, 479:175–177.

Fourdrinoy, J., Dambrine, J., Petcu, M., Pierre, M., and Rousseaux, G. (2020). The dual nature of the dead-water phenomenology: Nansen versus ekman wave-making drags. *Proceedings of the National Academy of Sciences*, 117(29):16770–16775.

Fuller, J. (2017). Pre-supernova outbursts via wave heating in massive stars - I. Red supergiants. *MNRAS*, 470(2):1642–1656.

Fuller, J., Lecoanet, D., Cantiello, M., and Brown, B. (2014). Angular Momentum Transport via Internal Gravity Waves in Evolving Stars. *ApJ*, 796(1):17.

García, R. A., Turck-Chièze, S., Jiménez-Reyes, S. J., Ballot, J., Pallé, P. L., Eff-Darwich, A., Mathur, S., and Provost, J. (2007). Tracking Solar Gravity Modes: The Dynamics of the Solar Core. *Science*, 316(5831):1591.

Garcia Lopez, R. J. and Spruit, H. C. (1991). Li Depletion in F Stars by Internal Gravity Waves. *ApJ*, 377:268.

Geroux, C., Baraffe, I., Viallet, M., Goffrey, T., Pratt, J., Constantino, T., Folini, D., Popov, M. V., and Walder, R. (2016). Multi-dimensional structure of accreting young stars. *A&A*, 588:A85.

Gervais, A. D., Swaters, G. E., van den Bremer, T. S., and Sutherland, B. R. (2018). Evolution and Stability of Two-Dimensional Anelastic Internal Gravity Wave Packets. *Journal of Atmospheric Sciences*, 75(10):3703–3724.

Glatzmaier, G. A. (2013). *Introduction to Modelling Convection in Planets and Stars*.

Goffrey, T., Pratt, J., Viallet, M., Baraffe, I., Popov, M. V., Walder, R., Folini, D., Geroux, C., and Constantino, T. (2017). Benchmarking the Multidimensional Stellar Implicit Code MUSIC. *A&A*, 600:A7.

Goldreich, P. and Keeley, D. A. (1977). Solar seismology. II. The stochastic excitation of the solar p-modes by turbulent convection. *ApJ*, 212:243–251.

Goldreich, P. and Kumar, P. (1990). Wave Generation by Turbulent Convection. *ApJ*, 363:694.

Goldreich, P., Murray, N., and Kumar, P. (1994). Excitation of Solar p-Modes. *ApJ*, 424:466.

Goldstein, J. and Townsend, R. H. D. (2020). The Contour Method: a New Approach to Finding Modes of Nonadiabatic Stellar Pulsations. *ApJ*, 899(2):116.

Gough, D. (1990). Comments on helioseismic inference. In Osaki, Y. and Shibahashi, H., editors, *Progress of Seismology of the Sun and Stars*, pages 281–318, Berlin, Heidelberg. Springer Berlin Heidelberg.

Gough, D. O. (1969). The Anelastic Approximation for Thermal Convection. *Journal of Atmospheric Sciences*, 26(3):448–456.

Gough, D. O. (1977). Mixing-length theory for pulsating stars. *ApJ*, 214:196–213.

Gruberbauer, M., Guenther, D. B., and Kallinger, T. (2012). Toward a New Kind of Asteroseismic Grid Fitting. *ApJ*, 749(2):109.

Haberreiter, M., Schmutz, W., and Kosovichev, A. G. (2008). Solving the discrepancy between the seismic and photospheric solar radius. *The Astrophysical Journal*, 675(1):L53.

Hale, S. J., Howe, R., Chaplin, W. J., Davies, G. R., and Elsworth, Y. P. (2016). Performance of the Birmingham Solar-Oscillations Network (BiSON). *Sol. Phys.*, 291(1):1–28.

Hayashi, C. (1961). Stellar evolution in early phases of gravitational contraction. *PASJ*, 13:450–452.

Hekker, S. and Mazumdar, A. (2014). Solar-like oscillations in subgiant and red-giant stars: mixed modes. In Guzik, J. A., Chaplin, W. J., Handler, G., and Pigulski, A., editors, *Precision Asteroseismology*, volume 301, pages 325–331.

Henyey, L. G., Lelevier, R., and Levée, R. D. (1955). The Early Phases of Stellar Evolution. *PASP*, 67(396):154.

Hevelius, J. and Horrocks, J. (1662). *Iohannis Hevelii Mercurius in Sole visus Gedani, anno christiano observationibus, rarisque phaenomenis : Cui annexa est, Venus in Sole MDCLXI, d. III Maii, St. n. cum aliis quibusdam rerum coelestium pariter visa, anno 1639, d. 24 Nov. St. V. ... a Ieremia Horroxio ... : quibus accedit succincta historiola, novae illius, ac mirae stellae in collo Ceti, certis anni temporibus clare admodum affulgentis, rursus omnino evanescentis ...*

Holton, J. R. (2004). Chapter 7 atmospheric oscillations: Linear perturbation theory. In *An Introduction to Dynamic Meteorology*, volume 88 of *International Geophysics*, pages 182 – 227. Academic Press.

Horst, L., Edelmann, P. V. F., Andrássy, R., Röpke, F. K., Bowman, D. M., Aerts, C., and Ratnasingam, R. P. (2020). Fully compressible simulations of waves and core convection in main-sequence stars. *A&A*, 641:A18.

Hotta, H. (2017). Solar Overshoot Region and Small-scale Dynamo with Realistic Energy Flux. *ApJ*, 843(1):52.

Hotta, H. and Kusano, K. (2021). Solar differential rotation reproduced with high-resolution simulation. *Nature Astronomy*, 5:1100–1102.

Houdek, G., Trampedach, R., Aarslev, M. J., and Christensen-Dalsgaard, J. (2017). On the surface physics affecting solar oscillation frequencies. *MNRAS*, 464(1):L124–L128.

Howe, R. (2009). Solar Interior Rotation and its Variation. *Living Reviews in Solar Physics*, 6(1):1.

Huber, D., Chaplin, W. J., Christensen-Dalsgaard, J., Gilliland, R. L., Kjeldsen, H., Buchhave, L. A., Fischer, D. A., Lissauer, J. J., Rowe, J. F., Sanchis-Ojeda, R., Basu, S., Handberg, R., Hekker, S., Howard, A. W., Isaacson, H., Karoff, C., Latham, D. W., Lund, M. N., Lundkvist, M., Marcy, G. W., Miglio, A., Silva Aguirre, V., Stello, D., Arentoft, T., Barclay, T., Bedding, T. R., Burke, C. J., Christiansen, J. L., Elsworth, Y. P., Haas, M. R., Kawaler, S. D., Metcalfe, T. S., Mullally, F., and Thompson, S. E. (2013). Fundamental Properties of Kepler Planet-candidate Host Stars using Asteroseismology. *ApJ*, 767(2):127.

Hurlburt, N. E., Toomre, J., and Massaguer, J. M. (1986). Nonlinear Compressible Convection Penetrating into Stable Layers and Producing Internal Gravity Waves. *ApJ*, 311:563.

Iglesias, C. A. and Rogers, F. J. (1996). Updated Opal Opacities. *ApJ*, 464:943.

Jermyn, A. S. (2022). Nonlinear Mixing driven by Internal Gravity Waves. *arXiv e-prints*, page arXiv:2209.08344.

Jermyn, A. S., Bauer, E. B., Schwab, J., Farmer, R., Ball, W. H., Bellinger, E. P., Dotter, A., Joyce, M., Marchant, P., Mombarg, J. S. G., Wolf, W. M., Wong, T. L. S., Cinquegrana, G. C., Farrell, E., Smolec, R., Thoul, A., Cantiello, M., Herwig, F., Toloza, O., Bildsten, L., Townsend, R. H. D., and Timmes, F. X. (2022). Modules for Experiments in Stellar Astrophysics (MESA): Time-Dependent Convection, Energy Conservation, Automatic Differentiation, and Infrastructure. *arXiv e-prints*, page arXiv:2208.03651.

Jermyn, A. S. and Fuller, J. (2022). Wave heating during the helium flash and lithium-enhanced clump stars. *arXiv e-prints*, page arXiv:2206.13479.

Käpylä, P. J. (2019). Overshooting in simulations of compressible convection. *A&A*, 631:A122.

Käpylä, P. J. (2021). Star-in-a-box simulations of fully convective stars. *A&A*, 651:A66.

Käpylä, P. J., Mantere, M. J., Cole, E., Warnecke, J., and Brandenburg, A. (2013). Effects of Enhanced Stratification on Equatorward Dynamo Wave Propagation. *ApJ*, 778(1):41.

Kennicutt, R. C. and Evans, N. J. (2012). Star formation in the milky way and nearby galaxies. *Annual Review of Astronomy and Astrophysics*, 50(1):531–608.

Kippenhahn, R. and Weigert, A. (1990). *Stellar Structure and Evolution*. Springer-Verlag.

Kippenhahn, R., Weigert, A., and Hofmeister, E. (1967). Methods for Calculating Stellar Evolution. *Methods in Computational Physics*, 7:129–190.

Kippenhahn, R., Weigert, A., and Weiss, A. (2013). *Stellar Structure and Evolution*.

Kiraga, M., Jahn, K., Stępień, K., and Zahn, J. P. (2003). Direct NumeriSimulations of Penetrative Convection and Generation of Internal Gravity Waves. *Acta Astron.*, 53:321–339.

Kiraga, M., Stepien, K., and Jahn, K. (2005). Generation and Propagation of Internal Gravity Waves: Comparison between Two- and Three-Dimensional Models at Low Resolution. *Acta Astron.*, 55:205–217.

Kjeldsen, H., Bedding, T. R., and Christensen-Dalsgaard, J. (2008). Correcting Stellar Oscillation Frequencies for Near-Surface Effects. *ApJ*, 683(2):L175.

Kolmogorov, A. (1941). The Local Structure of Turbulence in Incompressible Viscous Fluid for Very Large Reynolds' Numbers. *Akademiia Nauk SSSR Doklady*, 30:301–305.

Kosovichev, A. G. (2011). Advances in Global and Local Helioseismology: An Introductory Review. In Rozelot, J.-P. and Neiner, C., editors, *Lecture Notes in Physics, Berlin Springer Verlag*, volume 832, page 3.

Kumar, P., Talon, S., and Zahn, J.-P. (1999). Angular Momentum Redistribution by Waves in the Sun. *ApJ*, 520(2):859–870.

Kumar, Y. B., Reddy, B. E., Campbell, S. W., Maben, S., Zhao, G., and Ting, Y.-S. (2020). Discovery of ubiquitous lithium production in low-mass stars. *Nature Astronomy*, 4:1059–1063.

Kupka, F. and Muthsam, H. J. (2017). Modelling of stellar convection. *Living Reviews in Computational Astrophysics*, 3(1):1.

Le Bars, M., Lecoanet, D., Perrard, S., Ribeiro, A., Rodet, L., Aurnou, J. M., and Le Gal, P. (2015). Experimental study of internal wave generation by convection in water. *Fluid Dynamics Research*, 47(4):045502.

Le Saux, A., Baraffe, I., Guillet, T., Vlaykov, D. G., Morison, A., Pratt, J., Constantino, T., and Goffrey, T. (2023). Two-dimensional simulations of internal gravity waves in a 5 $m_\odot$ zero-age-main-sequence model.

Le Saux, A., Guillet, T., Baraffe, I., Vlaykov, D. G., Constantino, T., Pratt, J., Goffrey, T., Sylvain, M., Réville, V., and Brun, A. S. (2022). Two-dimensional simulations of solar-like models with artificially enhanced luminosity. II. Impact on internal gravity waves. *A&A*, 660:A51.

Leavitt, H. S. and Pickering, E. C. (1912). Periods of 25 Variable Stars in the Small Magellanic Cloud. *Harvard College Observatory Circular*, 173:1–3.

Lebonnois, S., Garate-Lopez, I., Le Saux, A., and Plougonven, R. (2019). Wave activity below the clouds of Venus with the IPSL Venus GCM. In *EGU General Assembly Conference Abstracts*, EGU General Assembly Conference Abstracts, page 14183.

Lebonnois, S., Sugimoto, N., and Gilli, G. (2016). Wave analysis in the atmosphere of Venus below 100-km altitude, simulated by the LMD Venus GCM. , 278:38–51.

Lecoanet, D., Cantiello, M., Anders, E. H., Quataert, E., Couston, L.-A., Bouffard, M., Favier, B., and Le Bars, M. (2021). Surface manifestation of stochastically excited internal gravity waves. *MNRAS*, 508(1):132–143.

Lecoanet, D., Cantiello, M., Quataert, E., Couston, L.-A., Burns, K. J., Pope, B. J. S., Jermyn, A. S., Favier, B., and Le Bars, M. (2019). Low-frequency Variability in Massive Stars: Core Generation or Surface Phenomenon? *ApJ*, 886(1):L15.

Lecoanet, D. and Quataert, E. (2013). Internal gravity wave excitation by turbulent convection. *MNRAS*, 430(3):2363–2376.

Leibacher, J. W. and Stein, R. F. (1971). A New Description of the Solar Five-Minute Oscillation. *Astrophysical Letters*, 7:191–192.

Leighton, R. B., Noyes, R. W., and Simon, G. W. (1962). Velocity Fields in the Solar Atmosphere. I. Preliminary Report. *ApJ*, 135:474.

Li, G., Deheuvels, S., Ballot, J., and Lignières, F. (2022). Magnetic fields of 30 to 100 kG in the cores of red giant stars. *Nature*, 610(7930):43–46.

Lighthill, J. (1978). *Waves in fluids*.

Lighthill, M. J. (1952). On Sound Generated Aerodynamically. I. General Theory. *Proceedings of the Royal Society of London Series A*, 211(1107):564–587.

Lorenz, R. D., Young, L. A., and Ferri, F. (2014). Gravity waves in titan's lower stratosphere from huygens probe in situ temperature measurements. *Icarus*, 227:49–55.

Magg, E., Bergemann, M., Serenelli, A., Bautista, M., Plez, B., Heiter, U., Gerber, J. M., Ludwig, H.-G., Basu, S., Ferguson, J. W., Gallego, H. C., Gamrath, S., Palmeri, P., and Quinet, P. (2022). Observational constraints on the origin of the elements. IV. Standard composition of the Sun. *A&A*, 661:A140.

Marques, J. P., Goupil, M. J., Lebreton, Y., Talon, S., Palacios, A., Belkacem, K., Ouazzani, R. M., Mosser, B., Moya, A., Morel, P., Pichon, B., Mathis, S., Zahn, J. P., Turck-Chièze, S., and Nghiem, P. A. P. (2013). Seismic diagnostics for transport of angular momentum in stars. I. Rotational splittings from the pre-main sequence to the red-giant branch. *A&A*, 549:A74.

Martić, M., Schmitt, J., Lebrun, J. C., Barban, C., Connes, P., Bouchy, F., Michel, E., Baglin, A., Appourchaux, T., and Bertaux, J. L. (1999). Evidence for global pressure oscillations on Procyon. *A&A*, 351:993–1002.

Meakin, C. A. and Arnett, D. (2007). Turbulent Convection in Stellar Interiors. I. Hydrodynamic Simulation. *ApJ*, 667(1):448–475.

Medvedev, A. S. and Klaassen, G. P. (2003). Thermal effects of saturating gravity waves in the atmosphere. *Journal of Geophysical Research: Atmospheres*, 108(D2):ACL 4–1–ACL 4–18.

Miczek, F., Röpke, F. K., and Edelmann, P. V. F. (2015). New numerical solver for flows at various Mach numbers. *A&A*, 576:A50.

Montalbán, J. and Schatzman, E. (2000). Mixing by internal waves. III. Li and Be abundance dependence on spectral type, age and rotation. *A&A*, 354:943–959.

Mosser, B., Goupil, M. J., Belkacem, K., Michel, E., Stello, D., Marques, J. P., Elsworth, Y., Barban, C., Beck, P. G., Bedding, T. R., De Ridder, J., García, R. A., Hekker, S., Kallinger, T., Samadi, R., Stumpe, M. C., Barclay, T., and Burke, C. J. (2012). Probing the core structure and evolution of red giants using gravity-dominated mixed modes observed with Kepler. *A&A*, 540:A143.

Muthsam, H. J., Kupka, F., Mundprecht, E., Zaussinger, F., Grimm-Strele, H., and Happenhofer, N. (2011). Simulations of stellar convection, pulsation and semiconvection. In Brummell, N. H., Brun, A. S., Miesch, M. S., and Ponty, Y., editors, *Astrophysical Dynamics: From Stars to Galaxies*, volume 271, pages 179–186.

Nansen, F. and Sverdrup, O. N. (1897). *Farthest North: Being the Record of a Voyage of Exploration of the Ship" Fram" 1893-96, and of a Fifteen Month's Sleigh Journey by Dr. Nanson and Lieut*. Archibald Constable & Company.

Nikurashin, M. and Ferrari, R. (2013). Overturning circulation driven by breaking internal waves in the deep ocean. *Geophysical Research Letters*, 40(12):3133–3137.

Nomoto, K., Tominaga, N., Umeda, H., Kobayashi, C., and Maeda, K. (2006). Nucleosynthesis yields of core-collapse supernovae and hypernovae, and galactic chemical evolution. , 777:424–458.

Ong, J. M. J., Basu, S., and McKeever, J. M. (2021). Differential Modeling Systematics across the HR Diagram from Asteroseismic Surface Corrections. *ApJ*, 906(1):54.

Paxton, B., Bildsten, L., Dotter, A., Herwig, F., Lesaffre, P., and Timmes, F. (2011). Modules for Experiments in Stellar Astrophysics (MESA). *ApJS*, 192(1):3.

Paxton, B., Cantiello, M., Arras, P., Bildsten, L., Brown, E. F., Dotter, A., Mankovich, C., Montgomery, M. H., Stello, D., Timmes, F. X., and Townsend, R. (2013). Modules for Experiments in Stellar Astrophysics (MESA): Planets, Oscillations, Rotation, and Massive Stars. *ApJS*, 208(1):4.

Paxton, B., Marchant, P., Schwab, J., Bauer, E. B., Bildsten, L., Cantiello, M., Dessart, L., Farmer, R., Hu, H., Langer, N., Townsend, R. H. D., Townsley, D. M., and Timmes, F. X. (2015). Modules for Experiments in Stellar Astrophysics (MESA): Binaries, Pulsations, and Explosions. *ApJS*, 220(1):15.

Paxton, B., Schwab, J., Bauer, E. B., Bildsten, L., Blinnikov, S., Duffell, P., Farmer, R., Goldberg, J. A., Marchant, P., Sorokina, E., Thoul, A., Townsend, R. H. D., and Timmes, F. X. (2018). Modules for Experiments in Stellar Astrophysics (MESA): Convective Boundaries, Element Diffusion, and Massive Star Explosions. *ApJS*, 234(2):34.

Paxton, B., Smolec, R., Schwab, J., Gautschy, A., Bildsten, L., Cantiello, M., Dotter, A., Farmer, R., Goldberg, J. A., Jermyn, A. S., Kanbur, S. M., Marchant, P., Thoul, A., Townsend, R. H. D., Wolf, W. M., Zhang, M., and Timmes, F. X. (2019). Modules for Experiments in Stellar Astrophysics (MESA): Pulsating Variable Stars, Rotation, Convective Boundaries, and Energy Conservation. *ApJS*, 243(1):10.

Pedersen, M. G., Aerts, C., Pápics, P. I., Michielsen, M., Gebruers, S., Rogers, T. M., Molenberghs, G., Burssens, S., Garcia, S., and Bowman, D. M. (2021). Internal mixing of rotating stars inferred from dipole gravity modes. *Nature Astronomy*, 5:715–722.

Peralta, J., Hueso, R., Sánchez-Lavega, A., Piccioni, G., Lanciano, O., and Drossart, P. (2008). Characterization of mesoscale gravity waves in the upper and lower clouds of Venus from VEX-VIRTIS images. *Journal of Geophysical Research (Planets)*, 113(2):E00B18.

Pinçon, C., Belkacem, K., and Goupil, M. J. (2016). Generation of internal gravity waves by penetrative convection. *A&A*, 588:A122.

Plumb, R. A. and McEwan, A. D. (1978). The Instability of a Forced Standing Wave in a Viscous Stratified Fluid: A Laboratory Analogue of .the Quasi-Biennial Oscillation. *Journal of the Atmospheric Sciences*, 35(10):1827–1839.

Porter, D. H. and Woodward, P. R. (2000). Three-dimensional Simulations of Turbulent Compressible Convection. *ApJS*, 127(1):159–187.

Prandtl, L. (1925). 7. bericht über untersuchungen zur ausgebildeten turbulenz. *ZAMM - Journal of Applied Mathematics and Mechanics / Zeitschrift für Angewandte Mathematik und Mechanik*, 5(2):136–139.

Pratt, J., Baraffe, I., Goffrey, T., Constantino, T., Viallet, M., Popov, M. V., Walder, R., and Folini, D. (2017). Extreme value statistics for two-dimensional convective penetration in a pre-main sequence star. *A&A*, 604:A125.

Pratt, J., Baraffe, I., Goffrey, T., Geroux, C., Viallet, M., Folini, D., Constantino, T., Popov, M., and Walder, R. (2016). Spherical-shell boundaries for two-dimensional compressible convection in a star. *A&A*, 593:A121.

Press, W. H. (1981). Radiative and other effects from internal waves in solar and stellar interiors. *ApJ*, 245:286–303.

Prša, A., Harmanec, P., Torres, G., Mamajek, E., Asplund, M., Capitaine, N., Christensen-Dalsgaard, J., Depagne, É., Haberreiter, M., Hekker, S., Hilton, J., Kopp, G., Kostov, V., Kurtz, D. W., Laskar, J., Mason, B. D., Milone, E. F., Montgomery, M., Richards, M., Schmutz, W., Schou, J., and Stewart, S. G. (2016). Nominal Values for Selected Solar and Planetary Quantities: IAU 2015 Resolution B3. , 152(2):41.

Quataert, E. and Shiode, J. (2012). Wave-driven mass loss in the last year of stellar evolution: setting the stage for the most luminous core-collapse supernovae. *MNRAS*, 423(1):L92–L96.

Ratnasingam, R. P., Edelmann, P. V. F., and Rogers, T. M. (2019). Onset of non-linear internal gravity waves in intermediate-mass stars. *MNRAS*, 482(4):5500–5512.

Ratnasingam, R. P., Edelmann, P. V. F., and Rogers, T. M. (2020). Two-dimensional simulations of internal gravity waves in the radiation zones of intermediate-mass stars. *MNRAS*, 497(4):4231–4245.

Rauer, H., Catala, C., Aerts, C., Appourchaux, T., Benz, W., Brandeker, A., Christensen-Dalsgaard, J., Deleuil, M., Gizon, L., Goupil, M. J., Güdel, M., Janot-Pacheco, E., Mas-Hesse, M., Pagano, I., Piotto, G., Pollacco, D., Santos, Ċ., Smith, A., Suárez, J. C., Szabó, R., Udry, S., Adibekyan, V., Alibert, Y., Almenara, J. M., Amaro-Seoane, P., Eiff, M. A.-v., Asplund, M., Antonello, E., Barnes, S., Baudin, F., Belkacem, K., Bergemann, M., Bihain, G., Birch, A. C., Bonfils, X., Boisse, I., Bonomo, A. S., Borsa, F., Brandão, I. M., Brocato, E., Brun, S., Burleigh, M., Burston, R., Cabrera, J., Cassisi, S., Chaplin, W., Charpinet, S., Chiappini, C., Church, R. P., Csizmadia, S., Cunha, M., Damasso, M., Davies, M. B., Deeg, H. J., Díaz, R. F., Dreizler, S., Dreyer, C., Eggenberger, P., Ehrenreich, D., Eigmüller, P., Erikson, A., Farmer, R., Feltzing, S., de Oliveira Fialho, F., Figueira, P., Forveille, T., Fridlund, M., García, R. A., Giommi, P., Giuffrida, G., Godolt, M., Gomes da Silva, J., Granzer, T., Grenfell, J. L., Grotsch-Noels, A., Günther, E., Haswell, C. A., Hatzes, A. P., Hébrard, G., Hekker, S., Helled, R., Heng, K., Jenkins, J. M., Johansen, A., Khodachenko, M. L., Kislyakova, K. G., Kley, W., Kolb, U., Krivova, N., Kupka, F., Lammer, H., Lanza, A. F., Lebreton, Y., Magrin, D., Marcos-Arenal, P., Marrese, P. M., Marques, J. P., Martins, J., Mathis, S., Mathur, S., Messina, S., Miglio, A., Montalban, J., Montalto, M., Monteiro, M. J. P. F. G., Moradi, H., Moravveji, E., Mordasini, C., Morel, T., Mortier, A., Nascimbeni, V., Nelson, R. P., Nielsen, M. B., Noack, L., Norton, A. J., Ofir, A., Oshagh, M., Ouazzani, R. M., Pápics, P., Parro, V. C., Petit, P., Plez, B., Poretti, E., Quirrenbach, A., Ragazzoni, R., Raimondo, G., Rainer, M., Reese, D. R., Redmer, R., Reffert, S., Rojas-Ayala, B., Roxburgh, I. W., Salmon, S., Santerne, A., Schneider, J., Schou, J., Schuh, S., Schunker, H., Silva-Valio, A., Silvotti, R., Skillen, I., Snellen, I., Sohl, F., Sousa, S. G., Sozzetti, A., Stello, D., Strassmeier, K. G., Švanda, M., Szabó, G. M., Tkachenko, A., Valencia, D., Van Grootel,

V., Vauclair, S. D., Ventura, P., Wagner, F. W., Walton, N. A., Weingrill, J., Werner, S. C., Wheatley, P. J., and Zwintz, K. (2014). The PLATO 2.0 mission. *Experimental Astronomy*, 38(1-2):249–330.

Rempel, M. (2004). Overshoot at the Base of the Solar Convection Zone: A Semianalytical Approach. *ApJ*, 607(2):1046–1064.

Rhodes, E. J., J., Ulrich, R. K., and Simon, G. W. (1977). Observations of nonradial p-mode oscillations on the sun. *ApJ*, 218:901–919.

Ricker, G. R., Winn, J. N., Vanderspek, R., Latham, D. W., Bakos, G. Á., Bean, J. L., Berta-Thompson, Z. K., Brown, T. M., Buchhave, L., Butler, N. R., Butler, R. P., Chaplin, W. J., Charbonneau, D., Christensen-Dalsgaard, J., Clampin, M., Deming, D., Doty, J., De Lee, N., Dressing, C., Dunham, E. W., Endl, M., Fressin, F., Ge, J., Henning, T., Holman, M. J., Howard, A. W., Ida, S., Jenkins, J. M., Jernigan, G., Johnson, J. A., Kaltenegger, L., Kawai, N., Kjeldsen, H., Laughlin, G., Levine, A. M., Lin, D., Lissauer, J. J., MacQueen, P., Marcy, G., McCullough, P. R., Morton, T. D., Narita, N., Paegert, M., Palle, E., Pepe, F., Pepper, J., Quirrenbach, A., Rinehart, S. A., Sasselov, D., Sato, B., Seager, S., Sozzetti, A., Stassun, K. G., Sullivan, P., Szentgyorgyi, A., Torres, G., Udry, S., and Villasenor, J. (2015). Transiting Exoplanet Survey Satellite (TESS). *Journal of Astronomical Telescopes, Instruments, and Systems*, 1:014003.

Rieutord, M. (1987). Linear theory of rotating fluids using spherical harmonics part I: Steady flows. *Geophysical and Astrophysical Fluid Dynamics*, 39(3):163–182.

Rieutord, M. (2015). *Fluid Dynamics: An Introduction*.

Rieutord, M. and Zahn, J. P. (1995). Turbulent plumes in stellar convective envelopes. *A&A*, 296:127.

Rogers, F. J. and Nayfonov, A. (2002). Updated and Expanded OPAL Equation-of-State Tables: Implications for Helioseismology. *ApJ*, 576(2):1064–1074.

Rogers, T. M. (2015). On the Differential Rotation of Massive Main-sequence Stars. *ApJ*, 815(2):L30.

Rogers, T. M. and Glatzmaier, G. A. (2005a). Gravity waves in the Sun. *MNRAS*, 364(4):1135–1146.

Rogers, T. M. and Glatzmaier, G. A. (2005b). Penetrative Convection within the Anelastic Approximation. *ApJ*, 620(1):432–441.

Rogers, T. M. and Glatzmaier, G. A. (2006). Angular Momentum Transport by Gravity Waves in the Solar Interior. *ApJ*, 653(1):756–764.

Rogers, T. M., Glatzmaier, G. A., and Jones, C. A. (2006). Numerical Simulations of Penetration and Overshoot in the Sun. *ApJ*, 653(1):765–773.

Rogers, T. M., Lin, D. N. C., McElwaine, J. N., and Lau, H. H. B. (2013). Internal Gravity Waves in Massive Stars: Angular Momentum Transport. *ApJ*, 772(1):21.

Rogers, T. M. and McElwaine, J. N. (2017). On the Chemical Mixing Induced by Internal Gravity Waves. *ApJ*, 848(1):L1.

Roxburgh, I. W. and Vorontsov, S. V. (2003). The ratio of small to large separations of acoustic oscillations as a diagnostic of the interior of solar-like stars. *A&A*, 411:215–220.

Samadi, R. and Goupil, M. J. (2001). Excitation of stellar p-modes by turbulent convection. I. Theoretical formulation. *A&A*, 370:136–146.

Samadi, R., Nordlund, Å., Stein, R. F., Goupil, M. J., and Roxburgh, I. (2003). Numerical constraints on the model of stochastic excitation of solar-type oscillations. *A&A*, 403:303–312.

Santos, A. R. G., Breton, S. N., Mathur, S., and García, R. A. (2021). Surface Rotation and Photometric Activity for Kepler Targets. II. G and F Main-sequence Stars and Cool Subgiant Stars. *ApJS*, 255(1):17.

Schatzman, E. (1993). Transport of angular momentum and diffusion by the action of internal waves. *A&A*, 279(2):431–446.

Schmitt, J. R. and Basu, S. (2015). Modeling the Asteroseismic Surface Term across the HR Diagram. *ApJ*, 808(2):123.

Schwarzschild, M. (1958). *Structure and evolution of the stars.*

Shibahashi, H. (1979). Modal Analysis of Stellar Nonradial Oscillations by an Asymptotic Method. *PASJ*, 31:87–104.

Spiegel, E. A. (1963). A Generalization of the Mixing-Length Theory of Turbulent Convection. *ApJ*, 138:216.

Stein, R. F. (1967). Generation of Acoustic and Gravity Waves by Turbulence in an Isothermal Stratified Atmosphere. *Solar Physics*, 2(4):385–432.

Sutherland, B. (2010). *Internal Gravity Waves*. Cambridge University Press.

Szewczuk, W., Walczak, P., and Daszyńska-Daszkiewicz, J. (2021). Variability of newly identified B-type stars observed by Kepler. *MNRAS*, 503(4):5894–5928.

Takata, M. (2016). Physical formulation of mixed modes of stellar oscillations. *PASJ*, 68(6):91.

Talon, S. and Charbonnel, C. (2005). Hydrodynamical stellar models including rotation, internal gravity waves, and atomic diffusion. I. Formalism and tests on Pop I dwarfs. *A&A*, 440(3):981–994.

Tassoul, M. (1980). Asymptotic approximations for stellar nonradial pulsations. *ApJS*, 43:469–490.

Thielemann, F.-K., Nomoto, K., and Hashimoto, M.-A. (1996). Core-Collapse Supernovae and Their Ejecta. *ApJ*, 460:408.

Thompson, M. J., Christensen-Dalsgaard, J., Miesch, M. S., and Toomre, J. (2003). The Internal Rotation of the Sun. *ARA&A*, 41:599–643.

Tian, C.-L., Deng, L.-C., and Chan, K.-L. (2009). Numerical simulations of downward convective overshooting in giants. *MNRAS*, 398(2):1011–1022.

Townsend, A. A. (1966). Internal waves produced by a convective layer. *Journal of Fluid Mechanics*, 24:307–319.

Townsend, R. H. D., Goldstein, J., and Zweibel, E. G. (2018). Angular momentum transport by heat-driven g-modes in slowly pulsating B stars. *MNRAS*, 475(1):879–893.

Townsend, R. H. D. and Teitler, S. A. (2013). GYRE: an open-source stellar oscillation code based on a new Magnus Multiple Shooting scheme. *MNRAS*, 435(4):3406–3418.

Turner, J. S. (1986). Turbulent entrainment - The development of the entrainment assumption, and its application to geophysical flows. *Journal of Fluid Mechanics*, 173:431–471.

Uckert, K., Chanover, N., Olkin, C., Young, L., Hammel, H., Miller, C., and Bauer, J. (2014). An investigation of the temperature variations in neptune's upper stratosphere including a july 2008 stellar occultation event. *Icarus*, 232:22–33.

Ulrich, R. K. (1970). The Five-Minute Oscillations on the Solar Surface. *ApJ*, 162:993.

Unno, W., Osaki, Y., Ando, H., Saio, H., and Shibahashi, H. (1989). *Nonradial oscillations of stars*.

Vallis, G. K. (2017). *Atmospheric and Oceanic Fluid Dynamics: Fundamentals and Large-Scale Circulation*. Cambridge University Press.

Viallet, M., Baraffe, I., and Walder, R. (2011). Towards a new generation of multi-dimensional stellar evolution models: development of an implicit hydrodynamic code. *A&A*, 531:A86.

Viallet, M., Baraffe, I., and Walder, R. (2013). Comparison of different nonlinear solvers for 2D time-implicit stellar hydrodynamics. *A&A*, 555:A81.

Viallet, M., Goffrey, T., Baraffe, I., Folini, D., Geroux, C., Popov, M. V., Pratt, J., and Walder, R. (2016). A Jacobian-free Newton-Krylov method for time-implicit multidimensional hydrodynamics. Physics-based preconditioning for sound waves and thermal diffusion. *A&A*, 586:A153.

Vlaykov, D. G., Baraffe, I., Constantino, T., Goffrey, T., Guillet, T., Le Saux, A., Morison, A., and Pratt, J. (2022). Impact of radial truncation on global 2D hydrodynamic simulations for a Sun-like model. *MNRAS*, 514(1):715–727.

von Neuman, J. and Wigner, E. (1929). Uber merkwürdige diskrete Eigenwerte. Uber das Verhalten von Eigenwerten bei adiabatischen Prozessen. *Physikalische Zeitschrift*, 30:467–470.

Wales, D. J. and Doye, J. P. K. (1997). Global optimization by basin-hopping and the lowest energy structures of lennard-jones clusters containing up to 110 atoms. *The Journal of Physical Chemistry A*, 101(28):5111–5116.

Watkins, C. and Cho, J. Y. K. (2010). Gravity Waves on Hot Extrasolar Planets. I. Propagation and Interaction with the Background. *ApJ*, 714(1):904–914.

Wu, S. C. and Fuller, J. (2022). Wave-driven Outbursts and Variability of Low-mass Supernova Progenitors. *ApJ*, 930(2):119.

Yiğit, E. and Medvedev, A. S. (2009). Heating and cooling of the thermosphere by internal gravity waves. *Geophysical Research Letters*, 36(14).

Young, L. A., Yelle, R. V., Young, R., Seiff, A., and Kirk, D. B. (1997). Gravity waves in jupiter's thermosphere. *Science*, 276(5309):108–111.

Zahn, J. P. (1991). Convective penetration in stellar interiors. *A&A*, 252:179–188.

Zahn, J. P., Talon, S., and Matias, J. (1997). Angular momentum transport by internal waves in the solar interior. *A&A*, 322:320–328.